INTEGRATED ANTENNAS ON ORGANIC PACKAGES AND CAVITY FILTERS FOR MILLIMETER-WAVE AND MICROWAVE COMMUNICATIONS SYSTEMS

A Dissertation
Presented to
The Academic Faculty

by

Arnaud L. Amadjikpè

In Partial Fulfillment
of the Requirements for the Degree
Doctor of Philosophy in the
School of Electrical and Computer Engineering

Georgia Institute of Technology
May 2012

INTEGRATED ANTENNAS ON ORGANIC PACKAGES AND CAVITY FILTERS FOR MILLIMETER-WAVE AND MICROWAVE COMMUNICATIONS SYSTEMS

Approved by:

Professor John Papapolymerou, Advisor
School of Electrical and Computer Engineering
Georgia Institute of Technology

Professor Emmanouil Tentzeris
School of Electrical and Computer Engineering
Georgia Institute of Technology

Professor John Cressler
School of Electrical and Computer Engineering
Georgia Institute of Technology

Professor Christos Alexopoulos
School of Industrial and Systems Engineering
Georgia Institute of Technology

Professor Andrew Peterson
School of Electrical and Computer Engineering
Georgia Institute of Technology

Date Approved: January 9th, 2012

To my beloved family.

ACKNOWLEDGEMENTS

At first, I would like to express my sincere gratitude to my advisor Prof. John Papapolymerou who gave me the opportunity to join the Microwave Circuit Technology (MircTech) group in my first months at Georgia Tech. Prof. Papapolymerou trusted my ambitions and devotion for hard work very early, as well as I quickly gained confidence in him as a great teacher and leader. Throughout the four years I spent in his research group, he inspired both my work and attitude as a graduate student. He taught me *creative thinking* and *perseverance* in a unique way that guided me toward my achievements.

I am particularly grateful to Dr. Debabani Choudhury from Intel Corporation who was my industry mentor for the project on 60-GHz antenna design and wireless platform integration. The greatest values I learnt from her are *method* and *rigor*. The quality of my work has significantly improved thanks to her sound comments and guidance. I also thank Dr. Choudhury for always being available to discuss my research work inspite of her busy agenda.

I also thank Philippe Eudeline from Thales Air Systems and Afshin Ziaei from Thales Research and Technology for supporting my work on RF-MEMS tunable cavity filters.

I thank Dr. George E. Ponchak from the NASA Glenn Research Center for the invaluable assistance he gave me in characterizing 60-GHz antennas in the NASA far-field range setup. He also provided technical guidance to my work and suggestions to build our own antenna range setup.

At Georgia Tech, we are blessed to have a top-notch nanotechnology research cleanroom facility with a great staff who trained me on most of the thin-film processing equipments. I also express many thanks to Dennis Brown and Dennis Denney from the Georgia Tech Research Institute machine shop for helping with metal cavities fabrication.

I would like to thank my dear alumni and current colleagues Nickolas Kingsley, Matt Morton, Pete Kirby, Ramanan Subramanian, Symeon Nikolaou, Bo Pan, Yuan Li, Richard

Daigler, David Chung, Negar Tavassolian, Chad Patterson, Carlos Donado, Aida Lopez, Ann Trippe, Ana Yepes, Wasif Khan, Fan Cai, Spyridon Pavlidis, John Poh, Eric Juntunen, and Christiane Kameni.They all made my journey in the MircTech group enriching socially and technically. Our alumni and current post-doctoral fellows Dr. Swapan Bhattacharya, Dr. Kim Huyngrak, Dr. Stanis Courreges, and Dr. Benjamin Lacroix were of great assistance to me in sharing their knowledge and experience.

I will always be grateful to my friends Nevin Altunyurt from the Mixed Signal Design group, Milap Dalal, Mauricio Pardo, Roozbeh Tabrizian, and Jenna Fu from the Integrated MEMS group, Stan Philipps and Stephen Horst from the SiGe Devices and Circuits group, Amin Rida from the Athena group, Florian Herrault from the MSMA group at Georgia Tech, and George Shaker from the University of Waterloo for insightful technical discussions.

My friends Nefertari N'Diour, Oumou Ba, Illenin Kondo, Rodrigue Ngueyep, Ibrahima N'Diour, Mamadou Diao, Seydou Ba, Thymour Legba, Marcel Sossou, Poitiers Donald, and Raoul Akpovo consistently brought happiness in my life during off-campus time.

My deepest appreciation undoubtedly goes to my wife Nadia who has been of exceptional support during my entire doctoral studies. Nadia's daily encouragements and advice contributed in making this journey a success to our family as we have recently welcomed in our life, our first and lovely daughter, Zoe. I owe a lot to Nadia and I will always keep giving my best to our family. Zoe undeniably brought with her job opportunities towards the end of my PhD. My parents Elena and Gilbert are those who educated me and always convinced me that nothing should be taken for granted in this life. I thus owe them a lot in reaching this level of education. My uncle Sylvain Akpamagbo never stopped encouraging me. My sister Katherina and brother-in-law Boris are simply the greatest people around me; they have been so supportive morally.

Most importantly, I thank God for all his blessings and making me what I am for my family, my friends, and colleagues.

TABLE OF CONTENTS

DEDICATION . . . . . **iii**

ACKNOWLEDGEMENTS . . . . . **iv**

LIST OF TABLES . . . . . **x**

LIST OF FIGURES . . . . . **xi**

SUMMARY . . . . . **xviii**

1 INTRODUCTION **1**

1.1 Millimeter-Wave Integrated Antennas on Organic Packages for Multi-Gigabit Wireless Communications 1

1.2 Microwave Cavity Resonator Filters for Air Traffic Control Radars 4

PART I MILLIMETER-WAVE INTEGRATED ANTENNAS ON ORGANIC PACKAGES

2 BACKGROUND **7**

2.1 Challenges 7

2.1.1 Performance 7

2.1.2 Cost 9

2.1.3 Form-Factor 10

2.2 Literature Survey 11

2.2.1 Antenna-on-Chip 11

2.2.2 Antenna-in-Package 12

2.3 Proposed Approach 18

3 PLANAR END-FIRE ANTENNAS ON ORGANIC PACKAGES . . **21**

3.1 Switched-Beam Planar Yagi-Uda Antenna Array Module 22

3.1.1 Single Element Planar Yagi-Uda Antenna 22

3.1.2 Four-Element Planar Yagi-Uda Antenna Array 25

3.1.3 Switched-Beam Planar Yagi-Uda Antenna Array 27

3.2 Switched-Beam Tapered Slot Antenna Module with Novel Microstrip to Slot Transition 33

3.2.1 Novel Microstrip-to-Slot Transition 34

3.2.2 End-Fire Tapered Slot Antenna Module 38

4 BROADSIDE ANTENNA ON MULTILAYER ORGANIC PACKAGES 43

4.1 High Directivity Dipole Antenna on MLO Package 46

4.2 Dipole Antenna Array on MLO Package 51

5 INTEGRATED ANTENNA ON MULTILAYER ORGANIC PACKAGES WITH BROADSIDE AND END-FIRE RADIATION 56

5.1 Integrated Antenna Design on MLO Package 58

5.1.1 Broadside Dipole Radiator 58

5.1.2 End-Fire Folded Dipole Radiator 64

5.2 Fabrication of the Integrated Antenna Module 77

5.3 Input Impedance Characterization of the Passive Integrated Antenna Module 77

5.3.1 Broadside Radiator 79

5.3.2 End-Fire Radiator 79

5.3.3 Isolation Between Broadside and End-Fire Radiators 80

5.4 Characterization of Active Transmit and Receive Integrated Antenna Modules 81

5.4.1 Packaged dies performance 81

5.4.2 Transmit Antenna Module 85

5.4.3 Receive Antenna Module 89

5.5 Passive Antenna Module with Simultaneous Broadside and End-Fire Radiation 90

5.5.1 Wilkinson Divider Design and Fabrication 91

5.5.2 Characterization of the Packaged Simultaneous Beam Antenna Module 93

6 LOCATION SPECIFIC COVERAGE WITH WIRELESS PLATFORM INTEGRATED 60-GHZ ANTENNA SYSTEMS 96

6.1 Wireless Platform Chassis Modeling 97

6.1.1 Laptop Computer Lid Mounted Antenna 98

6.1.2 Laptop Computer Base Mounted Antenna 99

6.2 Review of 60-GHz Antennas for Wireless Platform Integration 99

6.2.1 3-dB Average Gain 100

6.2.2 Rectangular Patch Antenna 100

6.2.3 Switched-Beam Directive Planar Yagi-Uda Antenna Array 102

6.3 Characterization of 60-GHz Platform Embedded Antennas 103

6.3.1 Measurement Setup Description 103

6.3.2 Rectangular Patch inside the Laptop Lid . . . 104
6.3.3 Rectangular Patch in the Front of the Laptop Base . . . 106
6.3.4 Switched-Beam Planar Yagi-Uda Array in the Back of the Laptop Base . . . 107
6.4 Summary and Discussion . . . 110
7 CONTRIBUTIONS . . . 115
PART II MICROWAVE CAVITY RESONATOR FILTERS
8 BACKGROUND . . . 117
8.1 Challenges . . . 117
8.2 Literature Survey . . . 118
8.3 Proposed Approach . . . 120
9 FREQUENCY TUNABLE EVANESCENT-MODE CAVITY FILTER WITH OHMIC RF-MEMS SWITCHES . . . 121
9.1 Evanescent-Mode Waveguide Resonator . . . 122
9.2 Evanescent-Mode Filter with RF-MEMS Ohmic Switches . . . 124
9.2.1 Filter design . . . 124
9.2.2 Filter Fabrication . . . 126
9.2.3 Filter Characterization . . . 128
9.2.4 On the Improvement of the Tunable Filter Performance . . . 131
9.3 Comparison with Other Concepts for High-Q (≥ 400) Tunable Filters . . . 132
10 FOLDED CAVITY RESONATOR FILTERS WITH MAGNETIC SOURCE-LOAD CROSS COUPLING . . . 134
10.1 Theory of Magnetic Source-Load Cross Coupling . . . 136
10.1.1 Admittance Transfer Function . . . 136
10.1.2 Two Finite Transmission Zeros . . . 137
10.1.3 Three Finite Transmission Zeros . . . 138
10.2 Folded Cavity Bandpass Filter Design and Characterization . . . 138
11 CONTRIBUTIONS . . . 142
12 OPEN TOPICS FOR FUTURE RESEARCH . . . 143
APPENDIX A — MICROELECTRONIC FABRICATION . . . 144

PUBLICATIONS **146**

REFERENCES **148**

LIST OF TABLES

1 Combined ($G_t + G_r$) antenna gain in dBi required for LOS path [108] . . . 8

2 Frequency bands and limits on transmit power and antenna gain levels . . . 9

3 Summary of most recent mm-wave AoC solutions from the literature 12

4 Comparison of LTCC, PTFE, and LCP 14

5 Summary of most recent mm-wave AiP solutions from the literature 16

6 Comparison between AoC and AiP solutions 19

7 Comparison of tunable filters technologies for Q over 400 132

LIST OF FIGURES

1 Schematics of (a) Yagi-Uda antenna; (b) Tapered slot antenna. 21

2 Planar Yagi-Uda antenna with three directors. 23

3 Four-element planar Yagi-Uda antenna array. 24

4 Fabricated four-element planar Yagi-Uda antenna array. 24

5 Simulated and measured magnitude of S_{11} of the four-element planar Yagi-Uda array. 25

6 Antenna radiation pattern measurement setup from the GTRI. 27

7 Photograph of the GTRI far-field range setup. 28

8 Normalized radiation pattern of the four-element Yagi-Uda array: (a) E plane; (b) H plane. 28

9 Schematic of the switched-beam planar Yagi-Uda array fabricated on LCP and integrated with the HMC-SDD112 SPDT GaAs switch. 29

10 Simulated and measured magnitude of S_{11} of the switched-beam planar Yagi-Uda antenna array. 30

11 Simulated and measured normalized radiation pattern of the switched beam planar Yagi-Uda antenna array at 60 GHz: (a) E plane; (b) H plane. 30

12 Proposed 10 mm $\times$ 10 mm end-fire tapered slot antenna module with switch and power amplifier recessed in a 4 mil thick LCP substrate: (a) bottom layer with patterned slot antennas in the ground plane; (b) top layer with integrated chips and feed/bias networks. 34

13 Proposed novel microstrip-to-slot transition: schematic and photograph of the transition structure. 34

14 Simulated magnitude of S_{11} of a conventional transition from a uniform open ended 50 Ω microstrip line to a $Z_{s,th}$ slot line: $Z_{s,th}$ varies from 60 to 110 Ω. 35

15 Equivalent circuit model of the proposed microstrip-to-slot transition. . . . 36

16 Edge currents flow on the microstrip-to-slot transition. 36

17 Simulated and measured magnitude of S-parameters of the proposed microstrip-to-slot transition. 37

18 Conceptual drawing of the proposed end-fire antenna module. 38

19 Measured magnitude of S_{11} of the active antenna module in both $+45^\circ$ and -45° transmit modes. 39

20 Measured normalized E plane radiation pattern of the active antenna module at 56, 58 and 60 GHz: the E plane is parallel to the antenna module plane, that is $\theta = 90^\circ$. 41

21 Measured normalized H plane radiation pattern of the active antenna module at 56, 58 and 60 GHz: only the $\phi = +45°$ transmit mode is measured (ANT-1 is ON and ANT-2 is OFF) with the isolation corresponding to the H plane scan looking into ANT-2. 41

22 Schematic of a horizontal dipole antenna printed on top of a grounded dielectic substrate. 43

23 Image theory as applied to an infinitesimal horizontal dipole above a grounded dielectric medium. 44

24 Conceptual drawing of the proposed dipole antenna integrated with a 60-GHz chip: (a) flip-chip or embedded die; (b) wire bonded die. 46

25 Conventional dipole antenna above ground plane with integrated balun. . . 47

26 Schematic of the proposed package-integrated dipole. 48

27 Stack-up of the proposed package-integrated dipole. 49

28 Variation of directivity and efficiency of the horizontal dipole at a height h above a finite ground plane. 49

29 Simulated antenna parameters of the package-integrated dipole: (a) Magnitude of S_{11}; (b) Normalized radiation pattern at 60 GHz. 50

30 Schematic and photograph of the proposed package-integrated dipole array. 53

31 Eight-element dipole antenna array: (a)Simulated magnitude of S_{11}; (b) Photograph of the CPW-to-GPPO launcher transition. 53

32 Simulated and measured normalized radiation pattern of the 8-element dipole array at 58, 61 and 64 GHz. 54

33 Dipole antenna array: (a) Measured normalized E plane pattern at 58 GHz with extended microstrip line effects; (b) Simulated and measured peak gain variation with frequency. 54

34 Example of mm-wave WPAN with Wireless HDMI and 3D sound system. . 56

35 Spherical coordinates system showing broadside radiation at elevation angles and end-fire radiation at azimuth angles. 57

36 Conceptual drawing of the integrated antenna on MLO package with broadside and end-fire radiation. 58

37 Stackup of the integrated antenna on MLO package. 59

38 Simulated normalized E plane radiation pattern of the broadside radiator: effects of balun symmetry on E plane (ϕ=90°) pattern over frequency. . . . 60

39 Schematic of broadside dipole antenna with a post wall cavity: (a) view of the dipole on vias, balun, and micro-via through ground plane; (b) view of air cavity created inside the superstrate layer. 61

40 Effects of PWC height and aperture size on boresight directivity and radiation efficiency: (a) variations with H; (b) variations with A. 62

41 Implementation of a PWC with 4:1 aspect ratio through vias. 63

42 Micro-via transition between layers M3 and M5 with a ground plane void. . 64

43 Impedance matching of the micro-via transition between layers M3 and M5 as a function of the void diameter: (a) Return loss; (b) Insertion loss. . . . 65

44 Schematic of a printed asymmetric folded dipole: (a) Perspective view; (b) Planar view. 66

45 Schematic of a uniplanar end-fire dipole backed with a truncated ground plane. 66

46 TE_0 dielectric slab surface wave mode excitation mechanism. 68

47 E and H fields distribution of the TE_0 dielectric slab surface wave mode: (a) E field; (b) H field. 68

48 Effects of dielectric slab relative permittivity (or effective thickness) on radiator directivity and efficiency: solid lines correspond to dipole with single slab layer; dotted lines correspond to dipole with slab layers on both sides. . 70

49 Equivalent transmission line circuit model of the asymmetric folded dipole antenna; V represents the voltage at the input of the folded dipole branch. 71

50 Microstrip-to-slot transition used to provide an external feed on layer M5 for the end-fire radiator. 73

51 Isolation between two adjacents folded dipole end-fire radiators: the solid line represents the dipole with slabs on both sides; the dotted line represents the dipole with slab only on one side. 75

52 Compensation techniques to correct for the end-fire beam squinting: normalized H plane radiation pattern of the end-fire radiator. 75

53 Multilayer integrated antenna fabrication process flow with organic materials. 76

54 Photograph of the fabricated integrated antenna module on MLO package for return loss and isolation measurements. 78

55 Simulated and measured return loss of the integrated passive broadside radiator. 78

56 Simulated and measured input impedance of the integrated passive broadside radiator. 79

57 Simulated and measured return loss of the integrated passive end-fire radiator. 80

58 Simulated and measured input impedance of the integrated passive end-fire radiator. 80

59 Simulated and measured isolation between the integrated passive broadside and end-fire radiators. 81

60 Photograph of packaged dies: (a) SPDT switch with by pass capacitors; (b) LNA with by pass capacitors and a series 10 Ω resistor to the gate 100 pF capacitor. 82

61 Measured return loss and gain of the packaged power amplifier: V_{gg} = -0.1V, V_{dd} = +5.0V, I_{dd} = 72 mA. 82

62 Measured return loss and gain of the packaged low-noise amplifier: V_{gg} = -0.2V, V_{dd} = +2.5V, I_{dd} = 67 mA. 83

63 Measured return loss and insertion loss of the packaged single pole double throw switch: V^{+}_{dd} = +5.0V, V^{-}_{dd} = -5.0V, I_{dd} = 24 mA. 83

64 Photograph of the fabricated integrated transmit antenna module on MLO package. 84

65 Measured return loss of the packaged transmit antenna module: (PA) V_{gg} = -0.1V, V_{dd} = +5.0V, I_{dd} = 72 mA; (SPDT) V^{+}_{dd} = +5.0V, V^{-}_{dd} = -5.0V, I_{dd} = 24 mA. 84

66 Photographs of the antenna pattern measurement setup belonging to the MircTech group at Georgia Tech. 86

67 Simulated and measured radiation patterns at 60 GHz of the packaged transmit antenna module in broadside radiation mode: (PA) V_{gg} = -0.1V, V_{dd} = +5.0V, I_{dd} = 72 mA; (SPDT) V^{+}_{dd} = +5.0V, V^{-}_{dd} = -5.0V, I_{dd} = 24 mA. . . 87

68 Simulated and measured radiation patterns at 60 GHz of the packaged transmit antenna module in end-fire radiation mode: (PA) V_{gg} = -0.1V, V_{dd} = +5.0V, I_{dd} = 72 mA; (SPDT) V^{+}_{dd} = +5.0V, V^{-}_{dd} = -5.0V, I_{dd} = 24 mA. . . 88

69 Measured return loss of the packaged receive antenna module: (LNA) V_{gg} = -0.2V, V_{dd} = +2.5V, I_{dd} = 67 mA; (SPDT) V^{+}_{dd} = +5.0V, V^{-}_{dd} = -5.0V, I_{dd} = 24 mA. 89

70 Simulated and measured radiation patterns at 60 GHz of the packaged receive antenna module in broadside radiation mode: (LNA) V_{gg} = -0.2V, V_{dd} = +2.5V, I_{dd} = 67 mA; (SPDT) V^{+}_{dd} = +5.0V, V^{-}_{dd} = -5.0V, I_{dd} = 24 mA. . . 90

71 Simulated and measured radiation patterns at 60 GHz of the packaged receive antenna module in end-fire radiation mode: (LNA) V_{gg} = -0.2V, V_{dd} = +2.5V, I_{dd} = 67 mA; (SPDT) V^{+}_{dd} = +5.0V, V^{-}_{dd} = -5.0V, I_{dd} = 24 mA. . . 91

72 Measured peak gains of the integrated transmit and receive antenna module on MLO package: (PA) V_{gg} = -0.1V, V_{dd} = +5.0V, I_{dd} = 72 mA; (LNA) V_{gg} = -0.2V, V_{dd} = +2.5V, I_{dd} = 67 mA; (SPDT) V^{+}_{dd} = +5.0V, V^{-}_{dd} = -5.0V, I_{dd} = 24 mA. 92

73 Design structure and photograph of the fabricated wilkinson power divider on a 4 mil thick LCP substrate. 93

74 Simulated magnitude of S-parameters of the wilkinson power divider. 94

75 Photograph of the fabricated antenna package module integrated with a wilkinson power divider or a regular T-junction. 95

76 Measured return loss of the simultaneous beam antenna module with a wilkinson power divider or a regular T-junction. 95

77 Antenna integration in the laptop lid: (a) back view with the center of the coordinates system aligned with the iAUT location; (b) lateral zoom on the antenna mounted behind the LCD screen. Large arrows indicate possible directions of radiation. iAUT denotes the internal antenna under test. . . . 98

78 Antenna integration in the laptop base: (a) the antenna is mounted in the front left corner; (b) the antenna is mounted in the back left corner. In all cases, the antenna location coincides with the center of the coordinates system. Large arrows indicate possible directions of radiation. 98

79 Rectangular patch antenna: (a) Schematic of the patch antenna; (b) Measured magnitude of S_{11} for the rectangular patch antenna in free space. . . 101

80 Simulated and measured normalized radiation pattern of the rectangular patch antenna in free space, at 60 GHz: (a) E plane; (b) H plane. 101

81 Photograph of measurement setup. This picture was taken during the measurement of the embedded switched-beam antenna. The laptop is re-positioned each time for a new measurement run to align the iAUT with the receiving horn antenna. 102

82 Rectangular patch antenna inside the laptop lid: (a) Magnitude of electric field distribution on the surface of the laptop lid, showing surface waves excitation on the interface of the plastic cover. This is a view from the back of the laptop with a zoom into the area surrounding the patch; (b) Normalized H plane co-pol radiation pattern of the patch antenna; (c) Normalized E plane co-pol radiation pattern of the patch antenna. The antenna beam is directed toward -x. 104

83 Simulated and measured normalized radiation pattern of the patch antenna: (a) H plane co-polarization; (b) E plane co-polarization. The antenna beam is directed toward -y. The E plane cut could not be measured. Standalone and integration in the front of the base are compared. 105

84 Magnitude of electric field distribution on the surface of the laptop base: (a) patch at 2.5 cm from the inner vertical plastic obstacle; (b) patch at 0.5 cm from the base vertical wall; (c) patch at 0.5 cm from the base vertical wall without slots in the cover. The antenna location in the coordinates system is represented by a "Υ" in the plots. 106

85 Simulated normalized radiation pattern of the patch antenna for different configurations: (a) H plane co-polarization; (b) E plane co-polarization. The antenna beam is directed toward -y. 106

86 Measured normalized radiation pattern of the switched-beam array mounted in the back left corner of the laptop base: (a) H plane co-polarization -x; (b) E plane co-polarization -x; (c)H plane co-polarization -y; (d) E plane co-polarization -y. 108

87 Simulated normalized radiation pattern of the switched-beam antenna array when located 0.5 or 2.5 cm away from the vertical plastic cover of the base: (a) H plane co-polarization -x; (b) E plane co-polarization -x; (c)H plane co-polarization -y; (d) E plane co-polarization -y. 109

88 Magnitude of electric field distribution on the surface of the laptop lid and base: (a) switched-beam array "-x" at 0.5 cm from the base vertical wall; (b) switched-beam array "-x" at 2.5 cm from the base vertical wall; (c) switched-beam array "-y" at 0.5 cm from the base vertical wall; (d) switched-beam array "-y" at 2.5 cm from the base vertical wall. The antenna location in the coordinates system is represented by a "Υ" in the plots. 110

89 Summary of waves scattering phenomena that occur with platform integrated 60-GHz antenna systems. 111

90 Proposed electronically frequency switchable evanescent-mode cavity resonator: (a) Structure of the cavity with the inserted capacitors; (b) Structure of the variable capacitor; (b) Equivalent circuit model of the proposed frequency reconfigurable resonator. 122

91 Measured evanescent-mode cavity resonator with three different capacitor networks inserts. 123

92 Proposed two-pole evanescent-mode cavity filter with inserted switchable capacitor network: (a) 3D view; (b) Top view. 124

93 Switchable capacitor network: (a) Transversal view showing the capacitor network inserted between the top and bottom ridges of a resonator; (b) 3D view of one digitally switched capacitor with an RF-MEMS cantilever. . . . 125

94 Biasing scheme for the switchable capacitor network: (a) Surface current distribution on the bias line of one digitally tunable capacitor; (b) Photograph of the fabricated tuning element showing the location of the resistors. . . . 125

95 Evanescent mode cavity filter prototype: (a) Photograph of the fabricated tunable bandpass filter; (b) Photograph of the fabricated tuning element illustrating one of the RF-MEMS switches in up state (see color gradient). . 127

96 Simulated response of the two-pole digitally RF-MEMS tunable evanescent-mode waveguide bandpass filter: (a) Return loss; (b) Insertion Loss. 128

97 Measured response of the two-pole digitally RF-MEMS tunable evanescent-mode waveguide bandpass filter: (a) Return loss; (b) Insertion Loss. 128

98 Fabricated low-stress gradient RF-MEMS switch: (a) SEM photograph with a side view of the released cantilever; (b) Top view of the switch. 130

99 Measured response of the tunable evanescent-mode filter with a low stress gradient cantilever: (a) Return loss; (b) Insertion Loss. 130

100 Folded cavity resonator filter: (a) Coupling scheme of cross coupled folded resonators filters; (b) proposed folded cavity resonator filter with magnetic source-load cross coupling. 134

101 Circuit model of proposed filter concept: (a) Equivalent circuit model of a folded resonator filter with magnetic source-load cross coupling; (b) real transformer and its equivalent cantilever circuit model. 135

102 Circuit model filter response: (a) Variations of normalized functions of FTZs with the transformer coupling coefficient k_e: C_0 = 0.05pF, C_m = 0.002fF, C_e = 1.4fF, and L_0 = 57.5nH; (b) Transfer functions of $Y_{21}(s)$ and -$sC_{SL}(s)$: C_0 = 0.05pF, C_m = 0.002fF, C_e = 1.34fF, C_{SL} = 0.037aF, L_0 = 57.5nH, L_e = 3.9nH, and k_e = 0.028. 137

103 Folded waveguide cavity bandpass filter: (a) Half of the folded cavity filter full-wave model; (b) even and odd mode resonant frequencies as a function of coupling aperture h_{ap}. 139

104 Simulated and measured S-parameters of the second order bandpass filter with magnetic source-load cross coupling. The filter is fabricated with brass material. 140

SUMMARY

This dissertation presents novel designs of millimeter-wave integrated antennas on organic packages for wireless personal area networks applications and designs of microwave cavity filters for air traffic control radars.

Driven by the ever growing consumer wireless electronics market and the need for higher speed communications, the 60-GHz technology gifted with an unlicensed 9 GHz frequency band in the millimeter-wave (mm-wave) spectrum has emerged as the next-generation Wi-Fi for short-range wireless communications. High-performance, cost-effective, and small form-factor 60-GHz antenna systems for portable devices are key enablers of this technology. This work presents various antenna architectures built on low-cost organic packages. Planar end-fire switched beam antenna modules that can easily conform to various surfaces inside a wireless device platform are developed. The planar antenna package is realized on thin flexible LCP dielectrics. One design is based on a planar Yagi-Uda antenna element and the second on a tapered slot antenna element. A low-loss microstrip-to-slot via transition is designed to provide wide impedance matching for end-fire antenna paradigms. The novel transition utilizes the slow-wave concept to provide unbalanced to balanced mode conversion as well as impedance matching. It is demonstrated that the planar antenna packages may be even integrated with active circuits that are cavity recessed inside the thin dielectric. A compact switched-beam antenna module is developed to fit into a 10 mm $\times$ 10 mm $\times$ 0.1 mm package, with a bandwidth larger than 55-67 GHz, and a 19 dBi active peak gain (7 dBi passive). The first-ever integrated mm-wave active antenna module on organic package capable of generating both broadside and end-fire radiation is also developed in this work. Both broadside and end-fire radiators are co-designed and integrated into a single multilayer package to achieve optimal directivity, efficiency and frequency bandwidth and yet maintain excellent isolation between the two radiators. Post-wall cavities, image theory and dielectric slab modes concepts are invoked to optimize these functions. Active circuitry is integrated

into the same package to add control functions such as beam switching, and also amplify the packaged-antenna gain when operated either as a transmitter or a receiver. The versatile multilayer integration approach that is presented paves the way to smart high-performance mm-wave antenna systems and yet cost-effective owing to the low manufacturing costs of the combined IC/antenna package. This antenna module fits in a 12.5 mm $\times$ 10 mm $\times$ 1.3 mm package, covers a bandwidth of 56-64 GHz, achieves as high as 9 dBi passive gain, and illuminates in both azimuth and elevation planes owing to the integration of broadside and end-fire dipole radiators in a single package. A transmit module achieving up to 21 dBi peak gain in the broadside direction and 29.1 dBi in the end-fire direction is demonstrated. Likewise, a receive module achieving up to 31.7 dBi in the broadside direction and 38.9 dBi in the end-fire direction is designed. The proposed architecture results in a single antenna package solution with 3D radiation capability. A significant challenge in the design of antenna systems for wireless platforms is the assessment of embedded antenna performance, that is, the proximity effects of the platform chassis on the embedded antenna. Various antennas are mounted at different locations inside a laptop computer chassis: modeling and experimental studies are carried out to characterize this problem that is apparent to an antenna behind a radome. To the best of our knowledge, it is the first time that such studies are conducted with 60-GHz antennas inside wireless platforms. The outcomes of these experiments remain valid for other wireless platforms such as tablets and smartphones.

Air traffic control radars usually require cavity filters that can handle high power and low in-band insertion loss while providing enough out-band rejection to prevent interference with neighboring channels. Such radars that operate in the S-band consist of filter banks with switching devices at the filter bank I/O to select individual filters that cover individual channels. Although this approach guarantees performance within each channel, the main drawback is a resulting bulky filter bank. This is the main motivation for replacing such filter banks with a single frequency reconfigurable filter capable of tuning its frequency between channels and, ideally, meeting all required specifications throughout every channel. The first topic in this section is the development of a frequency tunable cavity filter using contact radio frequency micro electromechanical systems (RF-MEMS) switches. Evanescent-mode

mode cavity resonators are loaded with RF-MEMS tuning capacitance networks to control the resonant frequency of a second-order bandpass filter. The reported quality factor of this filter is between 315-460 with 1.1-2.1 dB in-band insertion loss in the 2.96-3 GHz frequency range. The second part is the design of a novel cavity filter architecture for enhanced selectivity near the passband. It is a second-order folded cavity resonator bandpass filter with magnetic source-load cross coupling. This filter can have at least two finite transmission zeros near the passband that increase its selectivity while maintaining better than 0.65 dB insertion loss at 2.94 GHz in a 1 dB bandwidth of 1.15%. The source-load cross coupling is achieved with proximity coupled coaxial probe connectors. A theoretical analysis of the concept of magnetic source-load cross coupling is derived based on the admittance transfer function of the filter. Variable capacitance networks utilizing RF-MEMS switches can eventually be integrated with this novel filter architecture to achieve frequency tuning between multiple channels.

CHAPTER 1

INTRODUCTION

Antennas and filters are fundamental components of any radio frequency (RF) transmission chain. To put it simple, a transmitting antenna converts currents (RF signal) flowing on its conductors into electromagnetic fields that are further radiated into the free space. Likewise, a receiving antenna converts the electromagnetic fields that couple to its conductors into RF currents that are further processed by the RF receiving stage. Although most antennas (standing wave antennas for instance) are frequency selective, they often do not provide enough rejection to undesired spectral components. This is where filters (bandpass filters for instance) play a prominent role because they can be designed to precisely reject spurious RF signals while passing the in-band frequencies with minimum insertion loss. As a result, antennas and filters appear to be both indispensable stages of RF transceivers. Design specifications for these functions are highly dependant on the type of applications. In this dissertation, the focus is to develop cost-effective antenna solutions for the emerging 60-GHz technology for wireless consumer electronics, and develop S-band cavity filters for air traffic control radars.

1.1 Millimeter-Wave Integrated Antennas on Organic Packages for Multi-Gigabit Wireless Communications

Millimeter-wave technology for the 60-GHz band is one of the most promising opportunities for the consumer wireless communications systems. This technology that is currently being standardized by the Wireless HD, the ECMA-387, the IEEE 802.15.3c and 802.11ad task groups, and the WiGig will enable short-range (up to 10 m) high data rate communications (up to 8 Gbps) for usage with most mobile devices including smartphones, tablets, e-books, and laptop computers [6,7,9–11]. Owing to the high atmospheric attenuation (15 dB/km at 60 GHz) and the increased propagation loss factor at mm-wave frequencies, 60-GHz enabled devices may only communicate within a few meters to meet error rate criteria under an

acceptable signal-to-noise ratio (SNR). However, this property may be used advantageously to increase immunity to interferers in highly dense environments because power levels would ebb off much quicker in less illuminated directions.

Another major attribute of 60-GHz is the license-free 9 GHz (57-66 GHz) spectrum that is available. The spectrum is subdivided into four channels, each as wide as 2.16 MHz, which indicates that unprecedent data rates may be achieved, either in the single carrier (SC) or the orthogonal frequency-division multiplexing (OFDM) mode. Thinking about multiple radios integration into mobile platforms, adopting mm-wave technologies is definitely key to avoid co-existence issues that are prominent in the 800 MHz-6 GHz range. These are symbolic characteristics of 60-GHz that drive the wireless consumer electronics industry to quickly embrace this novel technology.

A number of challenges arise however as we try to scale available circuits and systems to operate at mm-wave frequencies. In fact, power consumption scales linearly with frequency and is one the greatest challenges that researchers are currently addressing. This issue may be addressed either with smart design of the integrated circuits (IC) or by scaling down the transistor gate length into deep sub-micron levels, which is actually the current trend in both research and industry. Since these are more IC and process/technology related issues, we will leave it to our RFIC and lithography engineering experts. The next challenge is chips packaging and interconnects between 60-GHz dies and RF signal traces that lie on the packaging substrate. Power dissipation through the package is one part of the problem that needs to be address as we know that 60-GHz ICs are power hungry and thus dissipate a lot of heat. Heat dissipation may be addressed with heat sinks, or packaging materials with good thermal conductivity to alleviate heat flow away from dies. Again, this is more of a mechanical/thermal related aspects; we will work closely with mechanical and materials science engineers to meet this challenge. The point of interest for me as a microwave engineer is the electrical design aspect of interconnects and die-to-package assembly. Interconnect reactances are highly pronounced at mm-wave frequencies because of the much smaller wavelength (5 mm in free space and much less for IC or package integrated interconnects). Mm-wave interconnects design and die-to-package assembly will

thus be part of the work covered in this dissertation. We also mentioned above that power loss at 60-GHz is incredibly high which in turns means that high transmit power levels would be required to cover even short-range distances. Power amplifiers may be used, but at the cost of higher direct current (DC) power consumption. Alternatively, high gain antennas are used to boost the effective isotropic radiated power (EIRP) for much less cost. In order to maximize an antenna gain, both directivity and efficiency must be simultaneously enhanced. The directivity, as will be shown later in this work, is directly proportional to the antenna physical area or aperture. Therefore, it is clear that highly directive antennas occupy a large area. For slim devices, size is a critical parameter hence this criterion must be taken into account by the antenna designer. Needless to say, a power amplifier will most likely be required in case only moderate size antennas can be afforded. To maximize the antenna efficiency, the substrate carrying the antenna must have extremely low loss and relative dielectric constant as close as possible to unity. High-k dielectrics actually store a significant amount of the electromagnetic energy leaving a small amount for radiation. Lossy dielectrics dissipate substantial RF power at higher frequencies. Both of these reasons make silicon ($\epsilon_r = 11.9$) and gallium arsenide ($\epsilon_r = 13$) based on-chip antennas less efficient on one side, and FR-4 epoxy ($\tan\delta = 0.02$) unsuitable to carry RF power in package on the other side.

Fortunately, researchers including teams at the Georgia Institute of Technology have extensively worked on characterizing next generation high frequency materials and liquid crystalline polymer (LCP) is one these materials with excellent electrical properties ($\epsilon_r = 3.0 \pm 0.2$ and $\tan\delta = 0.002$-0.004 [97]) to carry RF signals and most importantly accomodate the antenna itself in a technology called Antenna-in-Package. AiP is defined as an antenna that is built on the packaging material used to carry the IC. Ferro A6-S LTCC ($\epsilon_r = 5.9$ and $\tan\delta = 0.002$), polytetrafluoroethylene (PTFE) commonly known as teflon ($\epsilon_r = 2.1$ and $\tan\delta = 0.0008$), and fused silica ($\epsilon_r = 3.8$ and $\tan\delta = 0.0003$) are other materials with excellent electrical performance but less attractive than LCP for many reasons such as cost, thermal properties, and hermeticity that will be further discussed in this work. Note that relative dielectric constant and loss tangent values given above are reported at 60 GHz.

The first objective of this dissertation is to develop integrated 60-GHz antenna solutions on organic materials such as LCP to meet cost, performance, and size constraints. Chapter II reviews the literature and identifies challenges. Planar structures and multilayer architectures on organic packages are developed in chapters III, IV, and V. Emphasis is given to switched-beam modules integrated with switches, power amplifier, low-noise amplifier, and wilkinson dividers to expand the antenna field-of-view from 2D to even 3D illumination. Meticulous benchmarking is performed with the state-of-the-art to clearly demonstrate originality and superiority of the proposed concepts. Chapter VI approaches systems level aspects where designed 60-GHz antennas are actually embedded inside a laptop computer platform to evaluate embedded antenna performance. Ultimately, the goal is to mount 60-GHz radios inside mobile platform for commercial usage. We demonstrate with EM modeling and experiments that the platform chassis must be taken into account in the antenna development process, and that embedded 60-GHz antennas may suffer from drastic radiation pattern deterioration unless they are mounted within a wavelength from the platform chassis, which must also be free of discontinuities. Chapter VII recapitulates contributions on this topic.

1.2 Microwave Cavity Resonator Filters for Air Traffic Control Radars

The second objective of this dissertation is the development of S-band cavity resonator bandpass filters for air traffic control (ATC) radars. ATC radars for commercial air traffic control are usually operated in the 2.7-2.9 GHz band where high power handling (500 mW) is required along with sharp selectivity and narrow bandwidth (as low as 1%). These specifications clearly put planar technologies aside as their limited quality factor or unloaded Q_u (less than 200) will inevitably harm the in-band insertion loss. Traditionally, coaxial cavity resonator filters (with $Q_u \geq$ 1,000-5,000 depending on size) are utilized but they suffer from bad spurious response because of higher order modes excitation. Well-proven techniques to improve stopband performance include evanescent-mode cavities and the insertion of finite attenuation poles, that is, finite transmission zeros in the transfer function of the filter. Evanescent-mode resonators are chosen because of their increased spurious-free

range compared to coaxial cavity resonators. An evanescent-mode resonator is composed of a waveguide loaded with a post, and operated at a frequency well below the cut-off frequency of the waveguide [37, 91]. Because the operating frequency is well below the cut-off, any higher order mode will not be excited unless it is higher than the cut-off frequency. In other words, wide sprurious-free bandpass filters can be designed with evanescent-mode cavity resonators, and the lower the operating frequency with respect to the cut-off, the wider the spurious-free range. On the other side, filters with transmission zeros have the unique feature of increasing the frequency selectivity with control of the zeros location. Among techniques available in the literature, source-load cross coupled filters are particularly attractive because compact size canonical filters with sharp roll-off can be designed [21, 28, 30, 71].

Practical implementations of source-load cross coupled resonator filters often utilize an electric source-load cross coupling scheme where the resonators are magnetically coupled to each other [62, 79, 90]. Alternatively, the source-load cross coupling is magnetic while the inter-resonator coupling is electric [34]. Besides design techniques related to filtering functions, a recent trend is the development of frequency reconfigurable filters. The need for such devices is simply justified by the increased level of integration required by most wireless applications. For instance, smartphones today contain multiple RF transceivers which perform each a specific function at various frequencies. If each function is to be assigned a distinct filter to provide enough isolation between adjacent modules, the size and cost of the RF board in the mobile device could quickly increase to unacceptable limits for the consumer market. Likewise, radar systems that operate at multiple frequency channels quickly become bulky if each channel is allocated a single filter. With the recent development of tuning semiconductor and MEMS devices such as p-i-n diode varactors, schottky diodes, radio frequency micro electromechanical systems (RF-MEMS) switches, ferroelectric thin-film barium strontium titanate (BST) varactors, and piezoelectric actuators it is now possible develop frequency reconfigurable filters integrated with these devices. An appropriate comparison between these technologies (except piezoelectric actuators) is provided in [86]. It is shown that RF-MEMS switches have the highest Q_u (about 400), linearity (≥ 60

dBm) and power handling (100-1,000 mW) to date. For applications requiring greater than 1,000 quality factors, RF-MEMS and piezoelectric actuators are prominent candidates.

Chapter VIII reviews the literature and identifies challenges. In chapter IX of this dissertation, ohmic RF-MEMS switches are monolitically integrated on low-loss fused silica substrate with fixed high-Q capacitors. Therefore, the tunable capacitor banks (diced as chips) are mounted inside a second order evanescent-mode cavity resonator filter to achieve frequency tuning. Chapter X describes the design of a novel folded cavity filter architecture with finite transmission zeros using magnetically coupled coaxial probes connectors. In the literature, it has so far been necessary to add either surface mount devices (SMDs) or sections of transmission lines to properly implement the required source-load cross coupling. Although SMDs can be easily added to planar filter topologies, they are not recommended for cavity filters because of their limited quality factor. Besides, additional lengths of transmission lines (or waveguide sections) increase the size and complexity of the filter topology, especially when it comes to prototyping mass-producible cavity filters at low costs. This chapter demonstrates how the same features are achieved using standard coaxial probe connectors. Chapter XI recapitulates contributions on this topic.

INTEGRATED ANTENNAS ON ORGANIC PACKAGES AND CAVITY FILTERS FOR MILLIMETER-WAVE AND MICROWAVE COMMUNICATIONS SYSTEMS

PART I

Millimeter-Wave Integrated Antennas on Organic Packages

by

Arnaud L. Amadjikpè

CHAPTER 2

BACKGROUND

2.1 Challenges

2.1.1 Performance

One of the major challenges for millimeter-wave (mm-wave) multi-gigabit communications is the poor link budget, as radio signal propagating in the mm-wave frequency band experiences significant path loss (attenuation increases quadratically with frequency), reflection loss, multipath interference, and other degradation [104]. In addition, non-line-of-sight (NLOS) propagation makes the link budget even poorer in many cases. Also, the 60-GHz band happens to operate in the so-called oxygen absorption spectrum, which means that transmitted energy is quickly absorbed by oxygen molecules in the atmosphere (15 dB/km) over long distances, making it unsuitable for long-range wireless communications. 60-GHz radios are also limited by their restricted transmit power levels because higher power devices dissipate much more heat, which is harmful for end users and thus incompatible with commercial devices. To overcome these challenges, directional antennas are ultimately the solution.

Directional antennas focus the radiated power in a narrow beamwidth and considerably increase the boresight gain. Fortunately, for the same physical area, a 60-GHz antenna has a much narrower pencil beam-like radiation lobe, compared to its low frequency counterpart. In fact, diffraction theory shows that the minimum angle within which radiation can be concentrated by an antenna is given by [60]

$$\theta_0 = \frac{1}{L_a/\lambda} \tag{1}$$

where θ_0 is the half-power beamwidth in radians, L_a is the antenna length and λ the free space wavelength. Hence, for an antenna with 100% radiation efficiency, one narrow major

Table 1: Combined (G_t + G_r) antenna gain in dBi required for LOS path [108]

Distance d **(m)**	**QPSK (2 Gbps)**	**16-QAM (4 Gbps)**	**64-QAM (6 Gbps)**
1	13	19	24
5	27	33	38
10	33	39	44
20	39	45	50

lobe and negligeable side lobes, we relate the antenna maximum directivity D_0 to the half-power antenna beamwidths in each principal plane, θ_0 and ϕ_0, respectively, by [24]

$$D_0 = \frac{4\pi}{\theta_0 \phi_0} \tag{2}$$

(1) and (2) thus suggest that the maximum antenna directivity is given by

$$D_0 = 4\pi \frac{A_a}{\lambda^2} \tag{3}$$

where A_a is the antenna physical aperture. Therefore, it turns out that a 60-GHz antenna is 10 dB more directive than a 6-GHz antenna that has the same physical size or aperture. Intuitively, this result stems from the fact that although both antennas have the same physical aperture, the 60-GHz one has a much larger electrical area. The narrow beamwidth property of directive antennas is essential to increase immunity to multipath effects whereas a high boresight gain is required to maintain reasonable error rate criteria under an acceptable signal-to-noise ratio (SNR). In [107], Zhang *et. al.* provided a very useful equation (4) to derive required antenna gains based on distance and expected data rates for line-of-sight (LOS) scenarios. If the transmit power level is 10 dBm, the combined transmit and receive antenna gain is given by:

$$G_t + G_r = 2 + SNR + 20 \log d \tag{4}$$

where G_t and G_r are the transmit and receive gains respectively, d is the LOS distance between antennas and SNR the signal-to-noise ratio required for proper demodulation at a specific data rate. Table 1 gives typical combined (G_t + G_r) antenna gains to achieve 2, 4 or 6 Gbps data rates at different ranges in the LOS path.

Table 2: Frequency bands and limits on transmit power and antenna gain levels

Region	Frequency Band (GHz)	Maximum Tx Power (mW)	Maximum Antenna Gain (dBi)
USA/Canada	57-64	500	-
Japan	59-66	10	47
Europe	57-66	20	37

Besides, 60-GHz antennas would ideally cover the entire wireless personal area network (WPAN) spectrum (57-66 GHz) making them compatible with regulations in the USA, Canada, Europe and Japan. Table 2 summarizes performance specifications for 60-GHz antennas, as defined in the IEEE 802.15.3c standard [7].

2.1.2 Cost

The 60-GHz technology will penetrate the highly competitive wireless consumer electronics market only if its cost is similar to other technologies such as wireless-fidelity (Wi-Fi), ultra wideband (UWB), global positioning system (GPS), or global system for mobile communications (GSM). An example of 60-GHz enabled product is the Cables-to-Go TruLink 1-Port 60 GHz WirelessHD Video Kit. It comes as a set of two boxes (one transmitter and one receiver) and the overall kit costs about $500. Nowadays, a decent liquid crystal display (LCD) HD-ready TV would cost about the same if not cheaper. How many households could really afford to get this product? In addition to that, the kit comes as a standalone device that further needs to be connected to a laptop or a TV; truely competitive 60-GHz radios will come fully integrated with laptop and TVs, and not as accessories.

Significant effort is currently being done to reduce the cost of mm-wave integrated circuits (IC), and this is essentially enabled thanks to the silicon germanium (SiGe) BiCMOS technology. This fast-growing technology integrates SiGe heterojunction bipolar transistors (HBT) together with complementary metal-oxide-semiconductor (CMOS) transistors into a single hybrid analog-digital system-on-a-chip solution using standard CMOS fabrication processes. This is exactly what brings the SiGe radios costs down, compared to gallium arsenide (GaAs) devices: SiGe BiCMOS can leverage the world's silicon foundry capacity

and respond to the market demand for on going integration of wireless connectivity into our daily lives. The other advantages of the SiGe BiCMOS technology are the much better transconductance gain and noise performance compared to CMOS transistors (ideal for analog RF circuits) and the higher linearity compared to BJT transistors.

These advancements however put hard constraints on antenna designers because the antenna packaging and integration costs must follow this die cost reduction trend. Irrespective of the technology used to make the antenna, reliable mass-producible cost-effective antenna solutions are mandatory. The antenna cost is highly dependant on the design complexity, the bill of materials (BOM) used to make the antenna and also maturity of the fabrication processes. Two technologies are currently competing to meet cost requirements: antenna-on-chip (AoC) and antenna-in-package (AiP), which will be described in details in the literature survey paragraph.

2.1.3 Form-Factor

In order to fit into slim smartphone platforms such as the Apple iPhone, 60-GHz antennas would need to occupy small-form factors. Typically, this means that the antenna package thickness may not exceed 2 mm. Moreover, the density of electronics circuits in mobile devices is already extremely high, which leaves almost no room to any additional circuitry. Fortunately, 60-GHz radios operates well beyond the 800 MHz-6 GHz range thus avoiding co-existence and interference issues. For smallest form factors, 60-GHz antennas may be directly integrated on-chip (AoC or wafer-level integration); otherwise, they will be integrated in-package (AiP). Care should be taken with the AoC approach because the ICs costs increase with die area and it is well known that large area antenna are better for higher directivity. With the AiP technology, the antenna size can quickly increase so that care should be taken to keep the package size within 4 cm^2 or less. As a matter of fact, reflector, lens and horn antennas are undoubtedly not an option (for consumer electronics devices) because they are expensive, bulky, heavy, and more importantly they can not be integrated with solid-state devices.

2.2 Literature Survey

60-GHz antenna solutions for the wireless consumer electronics market, and in particular mobile devices, will nearly always be integrated with the chip or chip package because of the increased level of integration required to achieve small-form factors. Also, highly integrated radio transceivers take advantage of minimized antenna-to-IC interconnects losses. This paragraph discusses the state-of-the-art mm-wave antenna solutions.

2.2.1 Antenna-on-Chip

The AoC solution features the integration of antennas or arrays together with other front-end circuits on the same chip in mainstream Si (SiGe BiCMOS or CMOS) or GaAs technologies. The fundamental advantages of AoC are reliability (entire circuitry fabricated on a single wafer), extremely high-integration level (avoidance of chip-to-antenna interconnects such as vias, bond wires or flip-chip) and cost. However, the high relative permittivity (ϵ_r = 11.9) and low resistivity ($\rho = 10\ \Omega{\cdot}\text{cm}$) of silicon-based substrates used for active devices drastically degrade the antenna impedance bandwidth and radiation efficiency [109]. Sophisticated designs and fabrication processes based on the use of high-resistivity Si ($\rho \geq 1$ k$\Omega{\cdot}$cm), polyimide or benzo cyclo butene (BCB) thin-film between the silicon and antenna layers, silicon bulk-micromachining, superstrate focusing or artificial magnetic conductor (AMC) as the antenna ground plane can be effectively used to improve the antenna bandwidth and efficiency at the price of higher fabrication complexity and cost [12, 14, 32, 45, 56]. A more advanced technique based on wafer-scale integration of a quartz superstrate elevate antenna on top of silicon substrate has been proposed in ([22]) and offers excellent antenna performance. Willmot *et. al.* recently demonstrated a highly efficient Yagi-Uda antenna on silicon using bond wires. It is worth mentioning that this approach is cost-effective and guarantees good yield [101]. Alternatively, high-k dielectrics mounted on top of slot line patterned on-chip may be excited to resonate and behave as antennas, thus the dielectric resonator antenna (DRA) appellation [73]. The main issue with DRAs is thermal sensitivity of the dielectric material. Another challenge with on-chip antenna is chracterization and measurements of radiation performance. In fact, coaxial connectors may not be soldered

Table 3: Summary of most recent mm-wave AoC solutions from the literature

Freq. (GHz)	**Technology**	**Topology**	**Gain (dBi)**	**Efficiency (%)**	**Size** (mm^2)	**Ref.**
55-65	0.18 μm CMOS	Yagi-Uda	-14	-	1.1 × 1.34	[36]
55-67.5	post BEOL	Inverted F	-19	3.5	0.1 × 2	[109]
57-66	90 nm CMOS	Patch-AMC	-3	20	1.1 × 1.3	[56]
55-70	0.15 μm pHEMT	Dipole	3.6	-	0.9 × 1	[33]
86-100	0.13 μm BiCMOS[1]	Pyramid horn	8	55	3.2 × 3.2	[78]
89-99	GaAs MMIC[2]	Patch	-	58	9 × 9	[45]
24	SiGe MMIC[3]	Patch	7	-	13 × 13	[12]
36-37	SiGe/CMOS[4]	Yagi-Uda	8	82	0.4 × 1.1	[101]
33-37	SiGe MMIC[5]	DRA	3	51	1 × 1.15	[73]

[1] Antennas elevated on quartz and electromagnetically coupled to on-chip microstrip line.
[2] Bulk micromachined antenna.
[3] BCB thin-film between antenna and silicon substrate.
[4] Bond wire loop antennas direclty bonded onto silicon chip.
[5] DRA using a high-k dielectric excited by on-chip slot line.

to the chip because of the the ground-signal-ground (GSG) pitch mismatch between the die and the connector. Therefore, the most common measurement technique relies on GSG probes. Needless to say, the proximity of the GSG probes does affect the measured radiation pattern, thus creating measurement errors. Murdock *et. al* tried to address this issue in [72] using matrix inversions techniques to de-embed the probes effects. Table 3 recapitulates the most recent published work on mm-wave AoCs.

2.2.2 Antenna-in-Package

The AiP solution realizes the antenna or arrays in the package that carries highly integrated mm-wave radios in a packaging technology. Although FR4-epoxy ($\epsilon_r = 4.4$ and $\tan\delta = 0.02$) has extensively been used at low frequencies as an antenna substrate, its dissipation losses are intolerable at mm-wave frequencies. Most common packaging materials for AiP solutions are fused silica (or quartz), high-resistivity Si, low-temperature co-fired ceramics (LTCC), teflon (or PTFE), and liquid crystalline polymer (LCP). In [110], air-suspended superstrate antennas were assembled on top of a metal frame cavity with excellent performance. In

this design, the flip-chip antenna element is printed on a fused silica substrate ($\epsilon_r = 3.8$ and $\tan\delta = 0.0003$) and the bottom metal frame cavity used as a reflector to increase the antenna directivity (8 dBi peak gain) while maintaining a wide impedance bandwidth (13%). This was the first generation integrated 60-GHz antenna developed at IBM T. J. Watson Research Center. This design unfortunately could never penetrate the market because of the complex assembly technique that limited its mass producibility. Costs related to this packaging solution were also unaccpetable. A similar cavity-backed concept using high-resistivity Si ($\epsilon_r = 11.9$ and $\rho = 1$ kΩ·cm) as the superstrate and the cavity material was demonstrated in [50]. The bottom Si cavity is fabricated using deep reactive ion etching (DRIE) and metallized afterwards with sputtered and electroplated Cu. This antenna exhibits higher than 10% bandwidth and 6 to 8 dBi gain at boresight. Although this AiP solution uses existing semiconductor processing, it involves complex and costly steps such as DRIE and critical alignment of the superstrate to the cavity. The same factors prevented this type of packaging solution to flourish.

Table 4 succintly compares LTCC, PTFE, and LCP that are all quite attractive for multilayer (ML) type of packages. But to start with, why would one need an ML package for mm-wave antennas? The advantages of going ML are the following:

- one can route RF and DC control lines on separate layers to mitigate crosstalk issues;
- one can embed chips into the package using embedded interconnects. Enclosed dies are thus protected from external world;
- one can reduce the package form factor by stacking multiple chips similar to system-in-a-package or package-in-package approaches;
- one can build reliable printed circuit boards thanks to the progress accomplished in via and lamination processing; and
- one can build high-Q passives by taking advantage of the depth of the package.

Ferro A6-S LTCC ($\epsilon_r = 5.9$ and $\tan\delta = 0.002$) is an excellent packaging ceramic material provided by Kyocera and that has been present in the field of microwave engineering for a

Table 4: Comparison of LTCC, PTFE, and LCP

Criteria	**LTCC**	**PTFE**	**LCP**
ϵ_r	5.9	2.1	3
$\tan\delta$	0.002	0.0008	0.004
CTE (ppm/°C)	9	24	(x,y)=17, (z)=150
Bond temperature (°C)	850	343	285
Hermeticity (%)	≤ 0.1	0.015	0.02-0.04
Thermal conductivity (W/mK)	2.0	0.25	0.2
High volume cost ($/mm^2)	***	***	***

while. The main advantage of LTCC is multilayer capability and good thermal conductivity to provide heat dissipation. Since it is a ceramic material, it is a hard substrate and thus layer-to-layer alignment is fairly easy to achieve. Via fabrication on LTCC has also been proved to work very well. There are really many good reasons for using LTCC as a packaging material, and as the literature survey proves it, there is currently a lot of work being done with this package material [54, 57, 93, 94, 108]. However, there are also some good reasons why one has to think carefully before adopting LTCC. The first one is that multilayer lamination with LTCC requires to fire the stack up as high as 850°C, which exceeds by far temperatures sustained by ICs. This means that ICs can not be embedded into the LTCC package before a final lamination step that would cover the chips. The second reason is that LTCC's high relative dielectric constant tends to penalize antenna efficiency. LTCC's coefficient of thermal expansion is also much less than the one of Cu, and this is particularly bad because interconnects breakage may occur if the package was to be exposed to high temperatures. Finally, LTCC as a ceramic may easily break or it will certainly not absorb any shock if it falls: this becomes a concern especially for large area packages (4 cm^2) made with LTCC.

PTFE as well as organic LCP have much lower relative diecltric constant and are very low loss materials. They can also be laminated at much lower temperature than LTCC, which makes them highly competitive. LCP however surpasses PTFE because of its CTE that matches the one of Cu (17 ppm/°C). The main challenges with PTFE and LCP are heat

dissipation and substrate flexibility. Thick ground planes and heat sinks are clearly required to provide enough path for heat flow. Flexibility of these materials makes them hard to process as they can curl very easily, thus provoking voids formation during lamination unless pressure and heat are properly controlled during bonding. The biggest challenge with LCP though is registration between layers: in fact, the Ultralam 3908 prepreg used to laminate core Ultralam 3850 LCP layers flows a lot and forces core layers to slide on each other during lamination. Process parameters (heat and pressure under vaccum) control is so critical at this point and reliability may be very easily affected as a result. When cavity are required in core LCP layers, because LCP is so soft, it tends to suck into the opened cavity during lamination thus deforming the substrate and metal traces. Alternatively, cavities may be drilled afterwards (after lamination) with precise depth control. Overall, processing ML packages with LCP has demonstrated to be a substantial challenge and this is one of the reasons why it has not been able to penetrate the low-cost printed circuits boards yet. Industry and research institutions are working hard to improve processes and it is worth being optimistic. Because core LCP is mainly available in thicknesses of 1, 2, and 4 mils, one may use other organic materials such as Rogers®RO3003 material ($\epsilon_r = 3.0 \pm 0.04$ and $\tan\delta = 0.002$) that has very similar properties although slightly more expensive. Rogers®RO3003 is available in 5 up to 60 mils thicknesses with 5 mils increments. LCP prepreg is available in 1 and 2 mils thicknesses. When multiple lamination sequences are required (as is the case in one of the designs proposed in this dissertation), a lower temperature prepreg may be used subsequently to the first press at 285°C. The Taconic *fast*Rise™27 prepreg that melts at about 121°C is a great choice. Its electrical properties are $\epsilon_r = 2.58$-2.74 and $\tan\delta = 0.0017$. Table 5 recapitulates most recently published work on in-package mm-wave antennas. Most of the reported designs except [92] have a broadside radiation pattern. The particularity in [92] is also the use of a high-frequency MCL-LZ-71G epoxy material that has much better loss properties than standard epoxy. Although the cost of this material was not disclosed in the paper, it would be interesting to inquire more about it because the material seems to be compatible with standard PCB fabrication processes. In [55], the research group at IBM T. J. Watson Research Center presented their second generation integrated antenna package

Table 5: Summary of most recent mm-wave AiP solutions from the literature

Freq. (GHz)	**Technology**	**Topology**	**Gain (dBi)**	**Efficiency** (%)	**Size** (mm^3)	**Ref.**
59-65	LTCC[1]	Slot	7-11	94	12.5×8×1.3	[108]
50.5-62	LTCC[2]	Patch array	17	-	20×13×1.4	[94]
56.3-65	LTCC[3]	Grid array	14.5	88	13.5×8×1.3	[93]
60	LTCC[4]	Patch array	5/patch	-	28×28×1.46	[54]
60-65	Epoxy[5]	PWW	6	-	8.7×6.4×1.0	[92]
57-66	LCP&RO4000[6]	Patch array	5/patch	80	28×28×-	[55]
61-62.6	PTFE[7]	Patch array	8.5-11	91	10×10×1.1	[89]

[1] Passive slot antenna.
[2] Active antenna package including wire bonded LNA, 4×4 circularly polarized patch array. The active antenna gain is 35 dBi.
[3] Passive microstrip grid array.
[4] Active antenna package including either flip-chip Tx or Rx ICs, 16 antenna elements for phased-arrays.
[5] Passive post-wall-waveguide antenna built using high-frequency MCL-LZ-71G epoxy material.
[6] Active antenna package including either flip-chip Tx or Rx ICs, 16 antenna elements for phased-arrays.
[7] Passive multilayer parasitic patch array.

using multilayer organic (MLO) packaging. It utilizes a combination of Rogers®RO4000 and LCP organics where LCP is selectively added to minimize losses on the 60-GHz RF lines that feed each patch antenna element.

For AoC or AiP designs, conductive films such as Cu, Ni, Ag, Al, or Au are very often used. In the mm-wave band, 2 μm ($\geq 5\delta_{skin}$) thick metal traces are usually enough to provide a good conductive layer. Besides, Ti, Cr or TiW are very often used as adhesion promoters for the thicker metal layers. Adhesion layers contribute considerably less to an overall conductor loss increase even at 100 GHz owing to their low layer thickness, typically below 1000 Å.

We mentioned previously that in AiP designs, interconnects are required to connect the chip to the antenna port. It is thus worth reminding key challenges pertaining to interconnects designs for mm-wave applications. Different chip-to-package interconnects are bond wires, flip-chip, electromagnetically coupled strip lines, and short-via transitions. Bond

wires are usually modeled as a low-pass filter (a series inductor connected to a shunt capacitor). At mm-wave frequencies, the inherent low-pass function of bond wires is pronounced because of the shorter wavelengths. For instance, practically realizable bond wire lengths of 100, 150 and 250 μm are equivalent to series reactances of $+\jmath 0.27$, $+\jmath 0.5$ and $+\jmath 1$ Ω respectively, in a 50 Ω impedance system: the shorter the wire the higher its cut-off frequency. Also, the air-bridge height of the wirebond must be minimized to about 100 μm to ensure that image currents cancel out the direct radiation currents of the bond wire. In general, it is recommended to mount dies inside recessed cavities to level the die and package top surfaces. Bond wires compensation using shunt capacitive stubs connected to a series inductive transmission line may be used and is described later in this work. Flip-chip interconnects are usually modeled as a Π-network including two shunt capacitances and a series inductance. The capacitive effect is usually larger because of the strong fringing fields that are confined between the overlapping pads on both the die and the package [52]. Proximity of the die transmission lines to the package dielectric also tends to de-tune the chip performance, especially when the top surface of the package is metalized. As a result, minimum bump-pad sizes (50 μm $\times$ 50 μm) with minimum bump diameter (25 μm) are usually recommended at millimeter-wave frequencies. Although, the bump height plays a less significant role (when the top side of the package is not metalized), it was found that higher bumps increase the antenna quality factor, which means that a tradeoff between the impedance bandwidth and the radiation efficiency is necessary [44]. 20 to 30 μm thick bumps realized by selective Au electroplating shall usually be suitable. Further compensation scheme using a series high-impedance line may be used as suggested in [52, 61]. Electromagnetic coupling between the chip and package pads is an alternative interconnect solution that uses surface-to-surface vertical transitions [66]. Precise alignment (both lateral and vertical) are extremely critical in this type of interconnects. Short-via transitions for embedded chips are another solution. In this case, a thin benzocyclobutene−BCB (or LCP) layer is spun (or laminated) on top of the chip; then, short vias are carefully ablated using an excimer laser and sputtered to establish a physical connection between the chip pads and the vias that can be eventually electroplated [31, 82]. BCB and LCP are the materials of choice because

of their low relative dielectric constant (2.7 for BCB and 3 for LCP), which is important not to significantly de-tune the embedded chip. To date, these last two approaches are unfortunately not as mature as wire bonding and flip-chip for mass production, especially in mm-wave band and beyond. In-package interconnects such as through vias, blind vias and micro-vias are nowadays pretty well controlled. Micro-vias though that require laser processing of holes increases manufacturing costs. Alignment tolerances (not better than 25 to 50 μm) between internal layers usually force designers to implement large landing pads that may affect the mm-wave transition performance. Another type of in-package interconnect is the electromagnetically coupled surface-to-surface transition [42]. It is highly sensitive to alignment.

2.3 Proposed Approach

Table 6 summarizes key aspects of each technology, AoC and AiP. Based on the cost, gain and bandwidth requirements for efficient 60-GHz antenna systems, the AiP solution undoubtedly prevails. Cost-effective mm-wave antennas will not achieve the required performance on-chip unless substrate modifications techniques are used, but to date, processing costs to modify the silicon substrate are still high. AiP is thus the most promising approach and is believed to be a key enabler of commercial 60-GHz integrated radios.

In this dissertation, organic materials such as LCP and Rogers®RO3003 are utilized to build various AiP solutions at low cost. Two, three and five metal layers antenna packages on organics are demonstrated. Single compact organic packages including multiple antenna elements and switching devices are designed. Power amplifiers and low-noise amplifiers may also be integrated in the same package for the sake of increasing the transmit and/or receive power levels. ICs are mounted inside recessed cavities and wire bonded to the package.

Ideally all 60-GHz communication links would be in the line-of-sight (LOS), that is, both the transmitting and the receiving radios are perfectly aligned. Although this is not always the case, there still is a number of applications where LOS links do exist. A good example is downloading a Blu-ray movie from a kiosk in a few seconds with 60-GHz enabled devices. Another LOS scenario is streaming uncompressed high-definition Audio/Visual (AV)

Table 6: Comparison between AoC and AiP solutions

Criteria	**AoC**	**AiP**
Impedance bandwidth	Poor	Excellent
Radiation efficiency[1]	Poor	Excellent
Directivity[2]	Poor	Excellent
Cost[3]	Good	Excellent
Size[4]	Excellent	Good
Reliability	Excellent	Good
Fabrication[5]	Excellent	Good
Integration level[6]	Excellent	Good
Testability	Poor	Good

[1] AoC efficiency may be increased to more than 30% using substrate modification techniques.
[2] AoC directivity may be increased to about 5 dBi using substrate modification techniques.
[3] Higher AoC cost associated with substrate modification techniques. Best cost with AiP implemented on LCP.
[4] Increased size in antenna arrays implementations.
[5] AoC fabrication complexity increases with the need for substrate modification techniques.
[6] AoC solutions do not need interconnects. AiP solutions do require proper compensation of bond wires or flip-chip parasitics.

content between a portable device (laptop computer, smartphone, tablet) and a graphics display (monitor, projector or HDTV) or sound systems. In some cases, the LOS path may be obstructed and this often happens when a human body appears in the LOS path. In [43], it was found that in general the maximum indoor shadowing loss is around 40 dB and this occurs when the human body blocks the LOS path completely. The only way to overcome this is to steer the antenna beam in a non-line-of-sight (NLOS) path with the intent to bounce it off the walls or the ceiling to finally close the link at the receiver. As one may anticipate, 60-GHz is a serious candidate to enable truely wireless communications systems for home entertainment. In this dissertation, we address the LOS type of links scenarios using the following antenna architectures:

- Passive antennas: the antenna has a static beam (usually a single beam) and the device housing the antenna must be moved or oriented to point toward the target.

The obvious limitation of this type of antennas is that the end user has to manually point the portable device. This is less critical with small devices like smartphones but unacceptable with larger size devices (laptop computer, tablets).

- Switched-beam antennas: if the end user on a laptop computer intends to stream high-definition video to an HDTV (in the front), the antenna system would need to point its main beam toward the HDTV. If he desires to stream the video to a projector (on the ceiling) that would further display the content on a wall, the antenna system would need to point its main beam toward the projector. There is virtually 90° between both link paths, which would require the ability of the antenna system to switch its main beam between these two paths. This type of antennas is suitable for LOS scenarios with a limited number of links in a piconet.

- Simultaneous-beam antennas: if the end user on a gaming platform intends to stream high-definition video to an HDTV (in the front) and at the same time stream high-definition audio from the gaming platform to sound systems (on the front and sides), the transmit antenna system must have the simultaneous-beam option implemented to reach out to the HDTV and sound systems. This type of antennas is suitable for LOS scenarios with a limited number of links in a piconet.

CHAPTER 3

PLANAR END-FIRE ANTENNAS ON ORGANIC PACKAGES

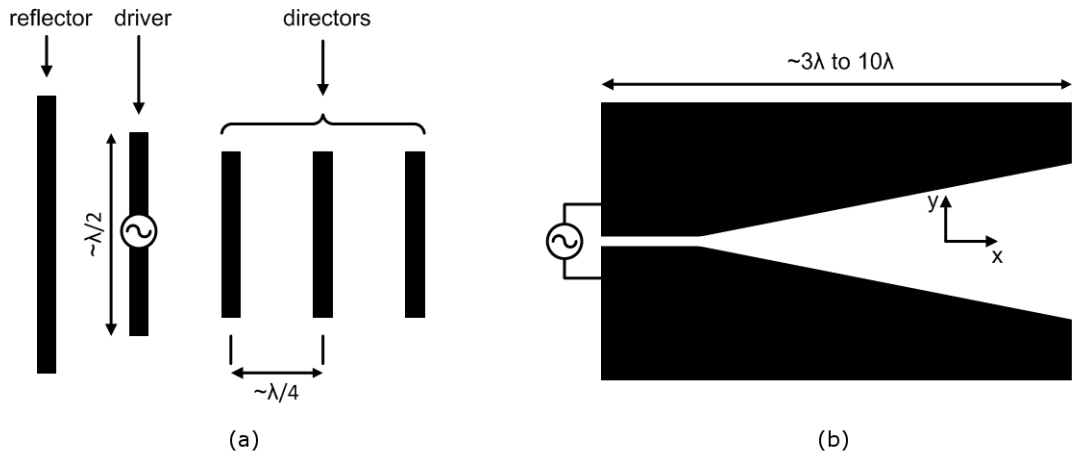

Figure 1: Schematics of (a) Yagi-Uda antenna; (b) Tapered slot antenna.

Planar end-fire antennas are a class of antennas that radiate in the direction of the antenna substrate. These antennas are useful for portable devices such as tablets and smartphones because they can be easily mounted inside the chassis and radiate from the surrounding edges of the chassis. The planar Yagi-Uda antenna and the tapered slot antenna (TSA) are two examples of planar end-fire antennas. The planar Yagi-Uda (Figure 1a) is composed of a printed driver, one printed reflector and one or more printed directors dipoles. The driver dipole is about half of the guided wavelength λ_g. The reflector dipole is slightly longer than $\lambda_g/2$ while the director dipoles are slightly shorter than $\lambda_g/2$ and spaced at about $\lambda_g/4$ from each other. This distribution of the director dipoles makes them behave as a dipole array with approximately equal current magnitude and equal progressive phase shift between subsequent directors. From basic array theory, it is known that an array with equal amplitude and progressive phase shift radiates at end-fire if the phase at the origin of each element of the array β and the element spacing d satisfy the condition given by

$$\beta \pm kd = 0, \tag{5}$$

where k is the wave number. It is thus apparent from (5) that with a quarter wavelength spacing, the progressive phase shift must be about 90°. This phase shift is achieved with a surface wave on the substrate that feeds each director dipole as it travels along the planar Yagi-Uda and thus excites currents in a sequential and progressive fashion. The result of this behavior is that fields radiated from each dipole of the planar Yagi-Uda reinforce each other in the end-fire direction.

The TSA (Figure 1b) is composed of a printed metal ground plane from which a tapered slot is etched off. The tapering of the slot is either linear, exponential or an optimized shape $y = f(x)$, where f is an arbitrary function or polynomial of x that defines the slot profile. Just as the planar Yagi-Uda antenna, the TSA fundamentally operates based on a surface wave that travels progressively along the tapered slot. Unlike the planar Yagi-Uda where each dipole element is resonant, the TSA is a broadband antenna in the sense that it conserves its radiation properties over a wide frequency range. This property stems from the fact that edge currents propagate along the slot with minor reflections (owing to the progressive impedance profile of the slot line). By the time edge currents reach the open end of the slot line, their amplitude has diminished by a significant order of magnitude such that reflections at the open end discontinuities have minor effects on the input impedance of the TSA.

As it can be inferred from the previous analysis, both antennas tend to be electrically long (3 to $10\lambda_g$) since the more directors you have the higher the directivity of the Yagi-Uda is, and the longer and less abrupt tapering of the slot line the broader the bandwidth and the higher the directivity of the TSA are. This is the main drawback of this class of antennas known as *traveling wave* antennas. In the following sections, a switched-beam planar Yagi-Uda antenna array and a switched-beam TSA are developed.

3.1 Switched-Beam Planar Yagi-Uda Antenna Array Module

3.1.1 Single Element Planar Yagi-Uda Antenna

The topology of a single element planar Yagi-Uda antenna is inspired from [40]. Figure 2 illustrates the antenna topology. The antenna is decomposed into two parts. The driver

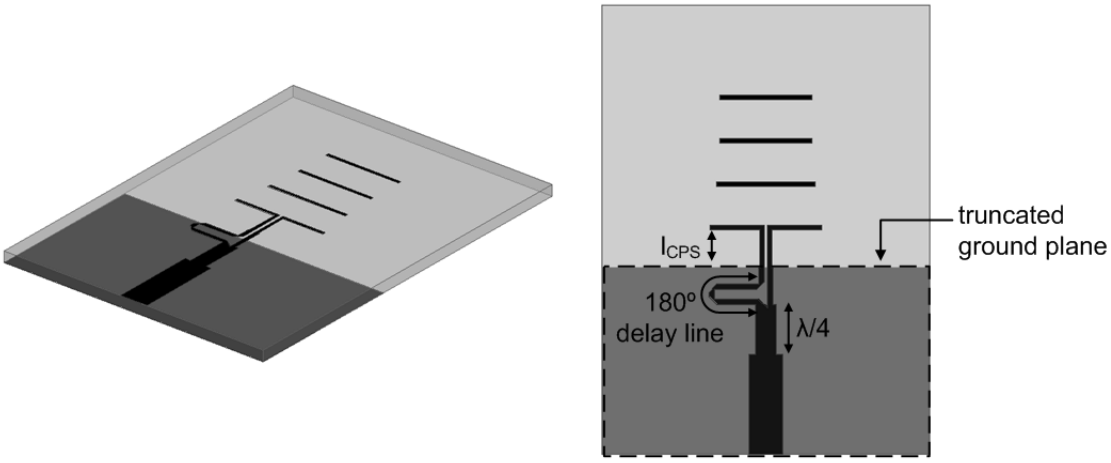

Figure 2: Planar Yagi-Uda antenna with three directors.

dipole and the directors are printed on the top layer along with the feed network. Note that there is no reflector dipole because of the presence of the feed network. However, the bottom layer of the substrate is patterned with a truncated ground plane that plays the role of the reflector. The driver dipole is fed with a coplanar stripline (CPS) that excites the zero cut-off TE_0 dielectric slab (not grounded dielectric section) surface wave mode. Radiation from this structure is fundamentally produced from the TE_0 surface wave. The truncated ground acts as a reflector because the TE_0 mode is cut-off by the grounded dielectric slab which cut-off frequency is at 265 GHz. In other words, the backward propagating surface wave can not propagate in the grounded slab. The two significant parameters of the CPS line are its characteristic impedance Z_{CPS} and its length l_{CPS}. The CPS spacing has a significant effect on Z_{CPS}, and the spacing must be decreased to minimize the impedance of the CPS line. l_{CPS} is adjusted to about a quarter wavelength from the edge of the truncated ground plane. For correct feeding of the driver dipole, each strip of the CPS line must carry currents with equal amplitude but opposite phase. The topology of this antenna shows that the input of the feed network is a 50 Ω microstrip line. Thus, a balun is inserted between the microstrip line and the CPS line to provide both mode conversion and impedance matching. The structure of the microstrip balun starts with a T-junction that splits the microstrip mode into two equal amplitude microstrip modes. A 180° phase delay is introduced between the splitted microstrip lines. These lines are further coupled

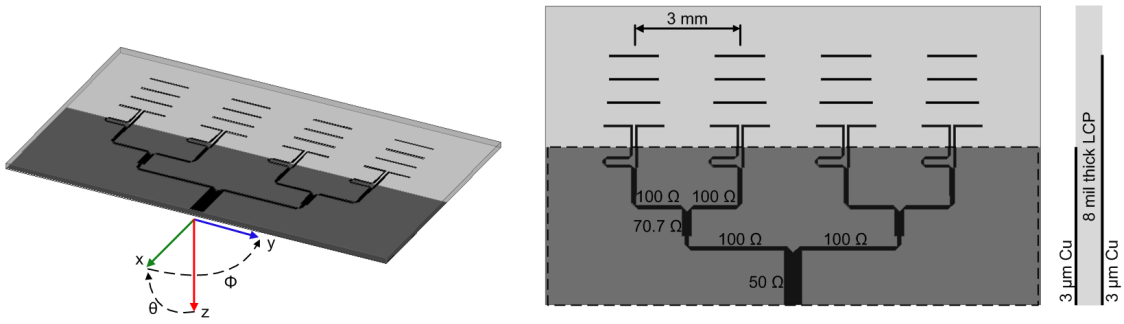

Figure 3: Four-element planar Yagi-Uda antenna array.

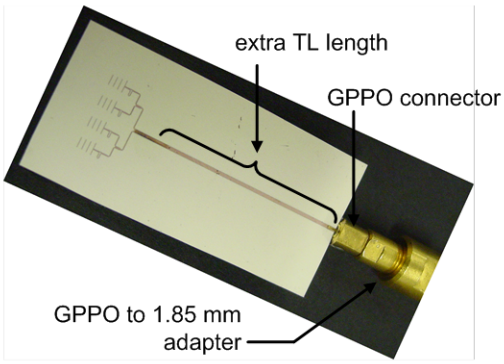

Figure 4: Fabricated four-element planar Yagi-Uda antenna array.

to each other to form a coupled microstrip line structure that carries both odd and even mode currents. The mode of interest here is the odd one that will drive the CPS line. The odd mode impedance Z_{odd} is thus another optimization parameter to insure a smooth impedance matching at the input of the CPS line. Using an 8-mil thick LCP substrate, the planar Yagi-Uda antenna was simulated with Ansys's HFSS [1]. For optimum impedance matching in the band of interest, it was found that $Z_{CPS} = 131\ \Omega$ and $Z_{odd} = 86\ \Omega$. The simulated impedance at the input of the balun is 86 Ω at resonance. This justifies the need for a section of quarter-wave transformer for impedance matching purpose. The simulated gain of the single element antenna is about 7 dBi when three directors are utilized.

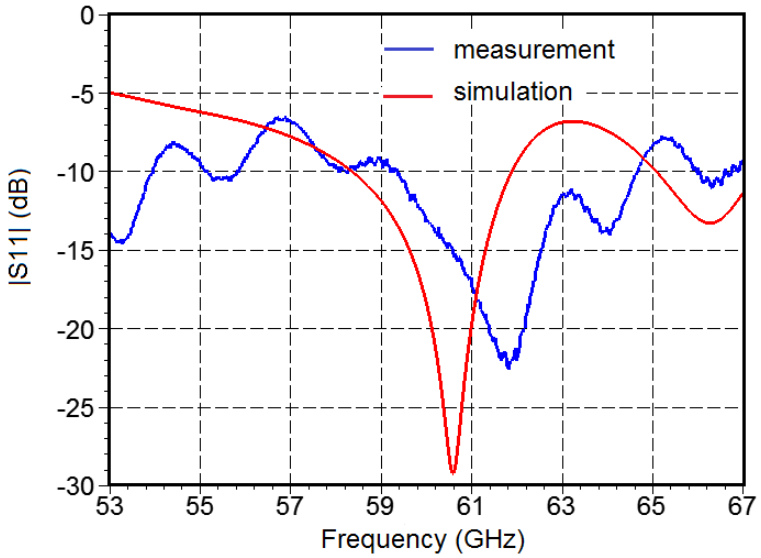

Figure 5: Simulated and measured magnitude of S_{11} of the four-element planar Yagi-Uda array.

3.1.2 Four-Element Planar Yagi-Uda Antenna Array

To increase the antenna directivity thus the gain, a four-element linear array with a corporate feed network is designed. Figures 3 and 4 illustrate the structure of the planar Yagi-Uda array. For this purpose, each single element antenna is first matched to a 100 Ω input impedance. A four-way power splitter is designed to equally distribute power to each antenna element. Simple T-junctions are used to split power from a one-way to a two-way path. The power splitter lines are all designed to be 100 Ω such that the feeding network size is kept small. Then, it suffices to add two 70.7 Ω quarter-wave transformers to convert the 50 Ω modes coming from each two-element array into 100 Ω. Finally, a four-element array is formed by combining the two-element arrays with a T-junction with a 50 Ω input impedance, suitable for testing of the device. Note that each right angle is optimally mitered to minimize corner reflections. A rule of thumb is to miter the corners such that the length of the mitered edge is about 1.8 times the width of the microstrip line. The array spacing follows the traditional rule, that is, about half the free space wavelength to constructively combine fields radiated from each antenna element in the far-field range.

Characterization of this antenna was done and presented in [17]. The 50 Ω input microstrip line is extended by 2.91 cm to prevent interactions between the fields radiated from the antenna and from the coaxial aperture of the connector. Edge launch GPPO connectors from Corning Gilbert are used to probe the antenna. A GPPO to 1.85 mm adapter is used to match connections between the antenna and the 1.85 mm cable going to a PNA. For one's interest, a PNA is an advanced version of a vector network analyzer that corrects for frequency-offsets errors, an additional feature that standard VNAs do not have. Also, both PNA and VNA measure magnitude and phase of an electrical network, which basically allows the equipment to generate complex points in the smith chart. After performing an SOLT (Short-Open-Load-Through) calibration of the PNA with calibration standards, the antenna reflection coefficient or S_{11} is measured. Figure 5 shows both simulated and measured reflection coefficients.

The radiation pattern and gain of the antenna were measured at 60 GHz in a calibrated anechoic chamber. The measurement setup is the one of the GTRI research center and Figure 6 illustrates the full setup. Figure 7 is a photograph of the antenna chamber. Two standard gain horn antennas were initially used to calibrate the path loss in the system. A 1.85 mm to U-band waveguide adapter (0.8 dB loss) was required to connect the antenna to the measurement system. A 1.85 mm to 1.85 mm adapter (0.3 dB loss) was also used to match the polarities between the GPPO to 1.85 mm adapter, and the 1.85 mm to U-band waveguide adapter. The 2.91 cm feed line also adds 1.46 dB loss, given that the simulated attenuation constant in a 50 Ω microstrip line patterned on an 8 mil thick LCP substrate is 0.5 dB/cm. Overall, losses are compensated for about 2.56 dB up to the reference plane of the antenna, that is, at bout 1.5 mm from the T-junction. Once this compensation is done, the simulated and measured gains in the peak direction are 10.9 and 10.3 dBi respectively. Figure 8 shows the E and H plane radiation patterns. The E plane cut corresponds to $\theta = +90^\circ$ while the H plane corresponds to $\phi = +0^\circ$.

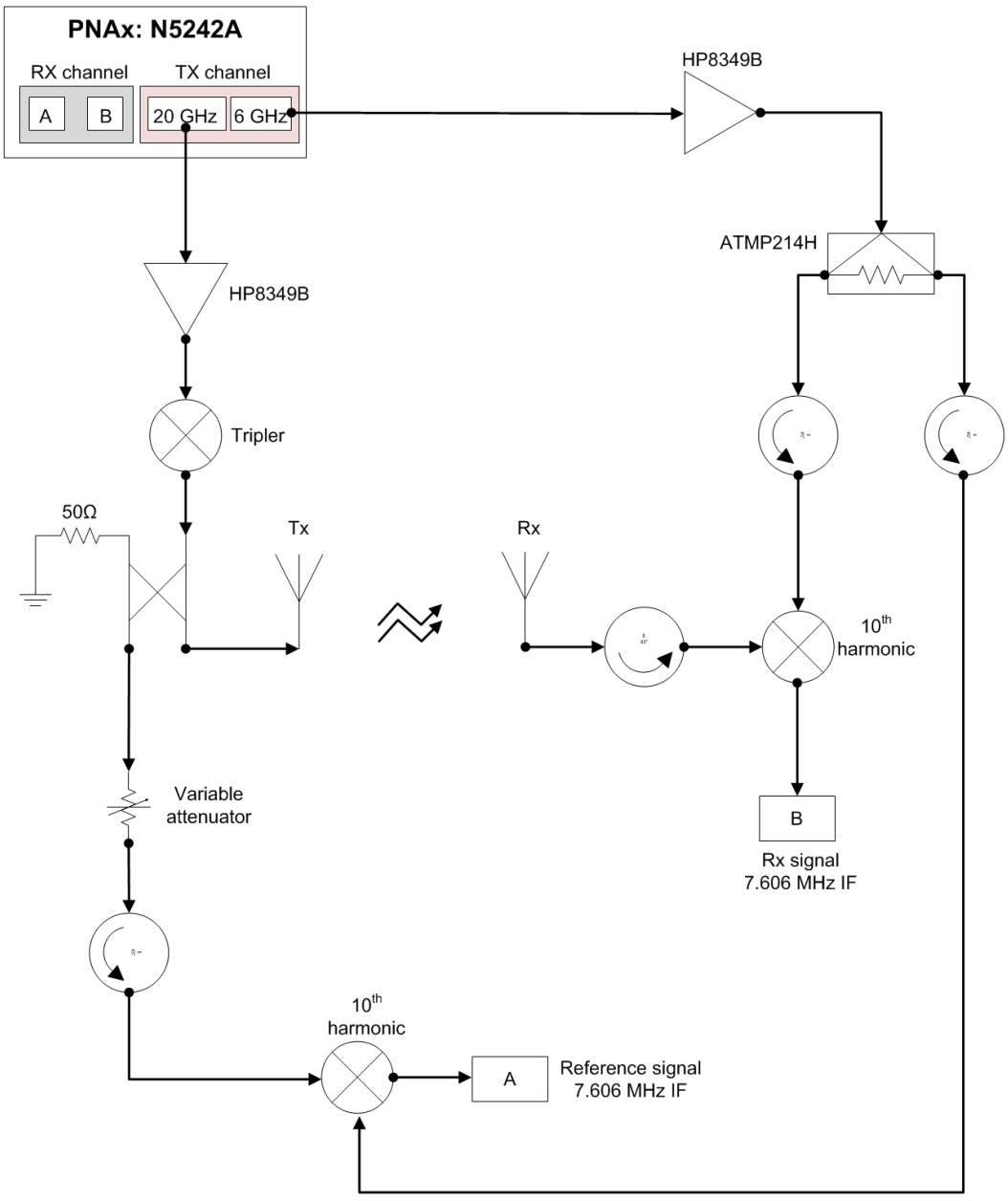

Figure 6: Antenna radiation pattern measurement setup from the GTRI.

3.1.3 Switched-Beam Planar Yagi-Uda Antenna Array

In this section, two planar Yagi-Uda antenna arrays are arranged orthogonally to each other in the substrate plane (θ = +90°) in an effort to create two orthogonal beams at ϕ = -45° and ϕ = +45°. Each beam is selected with a single pole double throw (SPDT) switch, one beam at a time. Because the switch is a bilateral device, this switched-beam

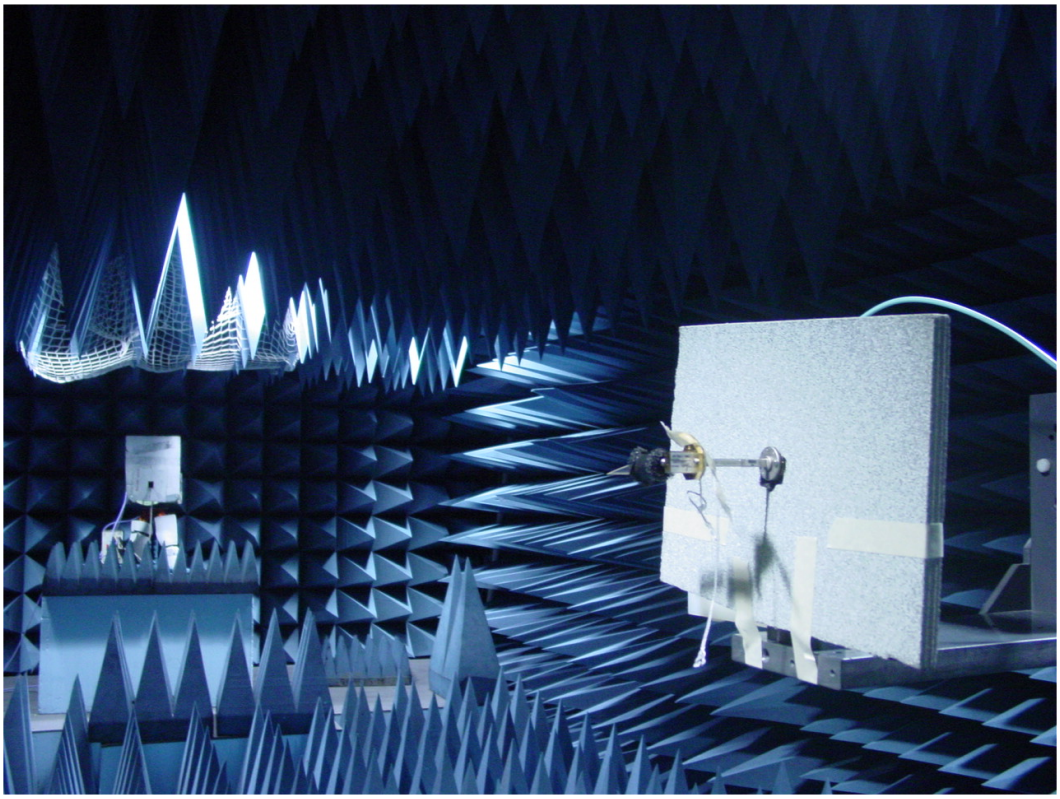

Figure 7: Photograph of the GTRI far-field range setup.

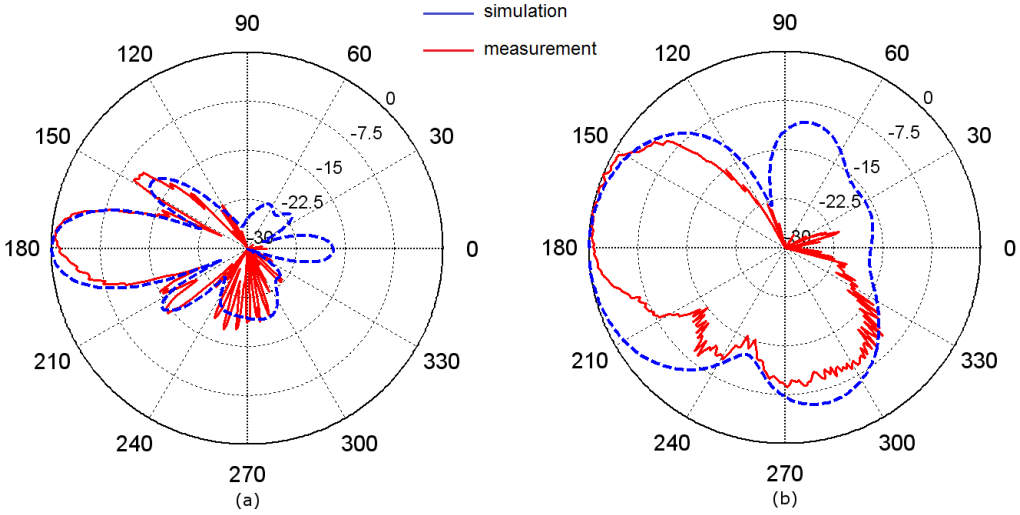

Figure 8: Normalized radiation pattern of the four-element Yagi-Uda array: (a) E plane; (b) H plane.

array can operate either as a transmit or receive antenna with either of the two orthogonal beams. The structure of the switched-beam array is shown in Figure 9. The switched-beam

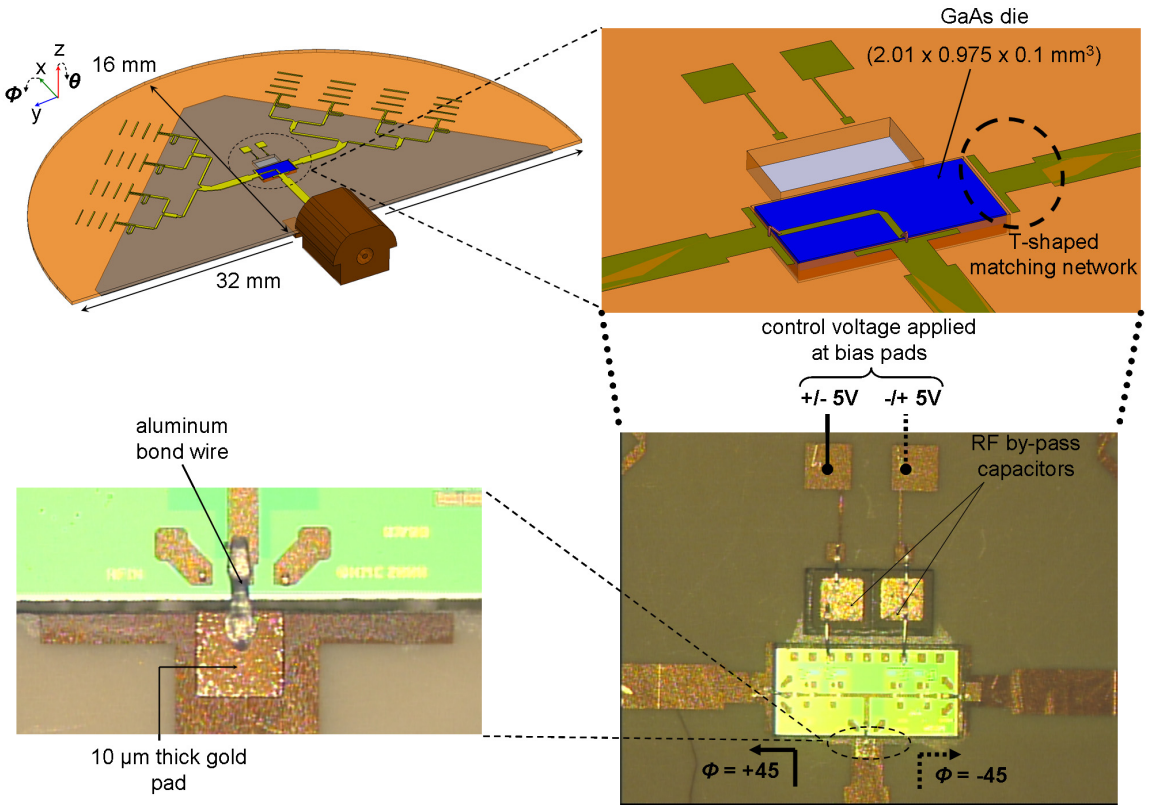

Figure 9: Schematic of the switched-beam planar Yagi-Uda array fabricated on LCP and integrated with the HMC-SDD112 SPDT GaAs switch.

array is designed on an 8 mil thick LCP substrate. On the bottom layer is patterned a ground plane with truncations for both 4×1 arrays. This layer is made of $\frac{1}{4}$ oz thick bare Cu. On the top layer, Yagi-Uda dipole elements, feed lines and bias lines for the switch are patterned in a two-step process: a thin 1.5 μm gold (Au) layer is first evaporated and patterned to define the entire top layer metallization; 10 μm thick Au pads are then selectively electroplated close to the switch pads to enhance bond wires adhesion to the soft LCP substrate and prevent scratching of the thin Au seed layer during the bonding process. A detailed description of the Au pads creation involving thick mold patterning is provided in the appendix.

The cavity for the GaAs PIN die (Hittite: HMC-SDD112) is opened in the LCP substrate with a UV excimer laser. The cavity size is precisely controlled owing to the narrow laser beam spot (5 μm diameter). Using a vector mode, a rectangular shaped cavity can be created with 10 to 25 μm gaps between the die edges and the cavity contour. Note that the

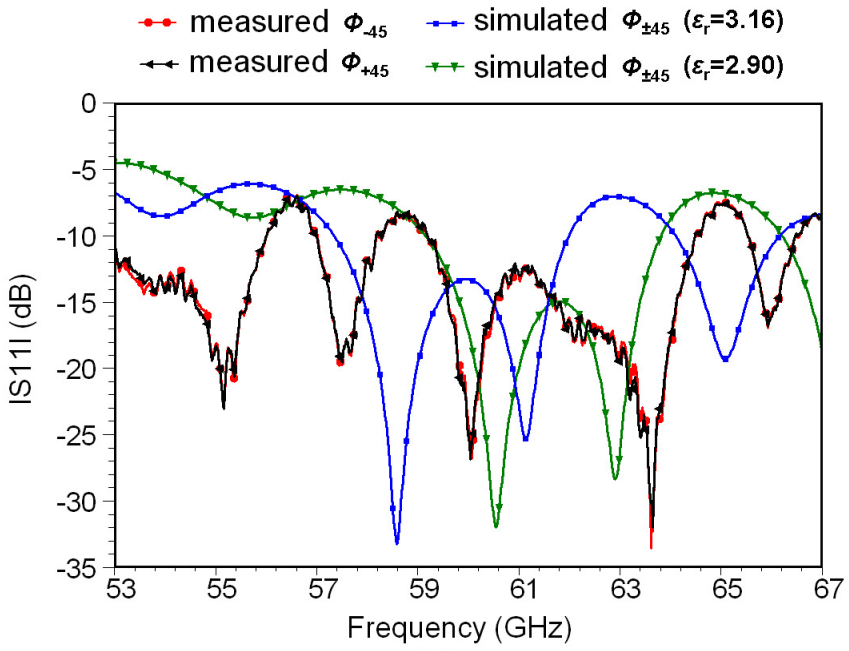

Figure 10: Simulated and measured magnitude of S_{11} of the switched-beam planar Yagi-Uda antenna array.

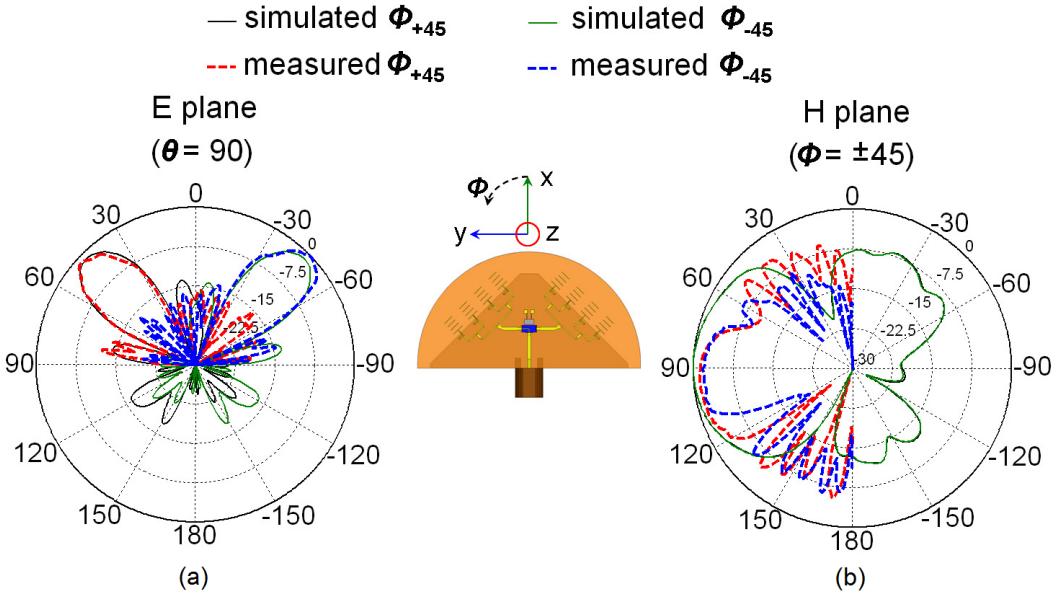

Figure 11: Simulated and measured normalized radiation pattern of the switched beam planar Yagi-Uda antenna array at 60 GHz: (a) E plane; (b) H plane.

$\frac{1}{4}$ oz thick Cu ground plane is also used as a stop layer while ablating the LCP material. The power of the laser beam should be controlled to prevent melting of the Cu layer. It is important to keep the surface of the Cu remaining after LCP ablation to maintain the die flat inside the cavity and thus minimize bond wires length. Because the LCP is as thick as 8 mil and the die is only 4 mil thick, a 4 mil thick conductive silver epoxy film adhesive (ESP8660-WL) from AI Technology is used to attach the die to the RF ground. Under this configuration, both the die and the patterned top metal layer share a common RF ground plane. Bond wires lengths of 150 and 250 μm are achieved. The SPDT switch has two control lines used to bias shunt PIN diode switches. Hence, a positive potential (+5V) between a control pin and the DC ground makes a shunt diode conductive forcing RF currents to flow through the diode to the RF ground plane. Likewise, a negative potential (-5V) makes the shunt diode capacitive forcing RF currents to flow through the transmission line. It is then obvious to see how the SPDT switch is biased to provide a through path to one output port while the other output port is isolated. Note that each control line must be properly designed with bypass capacitors (100 pF typical) to short any 60 GHz signal that may have coupled to the bias lines. Because the bypass capacitor has a series lead inductance, it will resonate at a frequency called the series resonant frequency (SRF). The impedance of the capacitor is then minimal at resonance, and this is where the capacitor will provide effective short circuit to any parasitic RF signal. Note that if the lead inductance is increased, the same capacitor will resonate at a much lower frequency, thus it will no longer provide a good short at the frequency of interest. This is fundamentally the reason why the 100 pF capacitor must be mounted as close as possible to the die to minimize the series inductance of the control line between the die bias pad and the capacitor. In this circuit, we utilized single layer chip capacitors from Presidio Components. These are vertical capacitors that are also cavity-mounted inside the antenna substrate. The bottom metal of the capacitor is directly connected to the DC/RF ground, while the top metal pad is wire bonded to the die bias pad. Although the bond wires length was kept minimum, the equivalent series inductance of the bond wires adds significant reactance thus shifting the ports input impedance away from the 50 Ω impedance. To compensate for the parasitic

reactance, a T-matching network is added at each RF port. Basically, the T-network acts as a matching network with a shunt capacitor between two series inductors. Figure 9 illustrates how the matching network is realized. Two shunt stubs act as capacitors followed with a narrowed section of transmission line that provides enough inductance to move back to the 50 Ω impedance on the smith chart. At the time this circuit was designed, the switch S-parameters file were not available from Hittite, and ideal 50 Ω microstrip lines on a 4 mil thick GaAs substrate are used instead to model the switch packaging in HFSS. For reference, the Hittite switch has a typical 1.5 dB insertion loss (including DC blocks and matched ports), better than 30 dB isolation and 12 dB return loss at 60 GHz.

Figure 10 shows the simulated and measured magnitude of S_{11} for the switched-beam antenna in free space. The measured operating bandwidth spans from 59.2 to 64.5 GHz versus a simulated 57.3-62 GHz bandwidth. A frequency shift of 1.9 GHz (3%) is noticed between the simulated and measured plots: an adjustment of the ϵ_r value from 3.16 to 2.9 would be the major source of discrepancy. In fact other literature has reported some variability ($\epsilon_r = 3.0 \pm 0.2$) in the relative dielectric constant of LCP [107]. Note that the dominant excited mode in the planar Yagi-Uda antenna is a TE_0 surface wave mode that is parallel to the substrate, in which case anisotropy of the relative permittivity might also influence the frequency shift. Recall that the simulated model does not use S-parameters files of the switch, which might be an additional source of error. Parasitic resonances that are partially attributed to the connector transition can be suppressed once this transition is de-embedded. This was verified by simulating the model with a waveguide port feeding instead of the GPPO launcher, in the HFSS environment.

Excellent agreement is achieved between the simulated and measured E plane patterns (See Figure 11). The E plane 3-dB beamwidth is in all cases $20° \pm 1°$. The measured H plane patterns are narrower than expected and this is essentially attributed to nulls formation in the $\phi \leq 60°$ and $\phi \geq 120°$ directions. These nulls result from interference between the antenna main beam and the fields radiated upward or downward from the coaxial aperture of the connector and a 26 mm long (not shown in Figure 9) microstrip feed line (that is used for clearance between the antenna element and the GPPO launcher). Also, the slight curvature

of the LCP substrate justifies why the measured beams point a bit downward. After de-embedding the connector loss (0.9 dB) and the 26 mm microstrip line loss (0.5 dB/cm), the simulated and measured peak gain values are found to be 9.9 dBi and (10.1 dBi at $\phi = +45°$ and 11 dBi at $\phi = -45°$) respectively, at 60 GHz. The fundamental shortcomings of this design are the total antenna array size and the poor bandwidth. Indeed, the proposed switched-beam antenna array arrangement does not exploit efficiently the surface area of the package, and more importantly, the antenna needs to operate at least in the 57-64 GHz band for compliance with the United States regulation, or up to 66 GHz for worldwide usage. The next section presents a different design with improved performance and significantly reduced surface area.

3.2 Switched-Beam Tapered Slot Antenna Module with Novel Microstrip to Slot Transition

Significant efforts are being made in the development of both antenna-on-chip (AoC) and antenna-in-package (AiP) solutions [107]. Owing to the limited performance and increased die cost of on-chip antennas, numerous AiP solutions realized in polytetrafluoroethylene (PTFE), glass cloth resin, low-temperature co-fired ceramics (LTCC) and liquid crystal polymer (LCP) susbtrates have recently been proposed in [77,92,108], and [18] respectively. In [77, 108], and [18] the antenna element has a broadside radiation pattern whereas Suga *et. al.* proposed a post-wall waveguide aperture antenna with end-fire radiation in [92]. The post-wall waveguide antenna package integrating two antenna elements and a recessed cavity for a CMOS chip occupies a volume of 14.4 $\times$ 14.4 $\times$ 1.0 mm^3 while achieving only 2.2 dBi gain per antenna element in the 59-66 GHz frequency range. A modified design with 6 dBi gain was also mentioned but it required to increase the length of the package by 4 mm. Besides, the full CMOS chip/antenna package performance was not evaluated. In this section, a compact end-fire antenna module solution with broader bandwidth and higher gain performance is demonstrated (see Figure 12). Furthermore, the proposed design includes a novel microstrip-to-slot transition (see Figure 13) that is a key to achieve the wide bandwidth performance for this small-size tapered slot antenna.

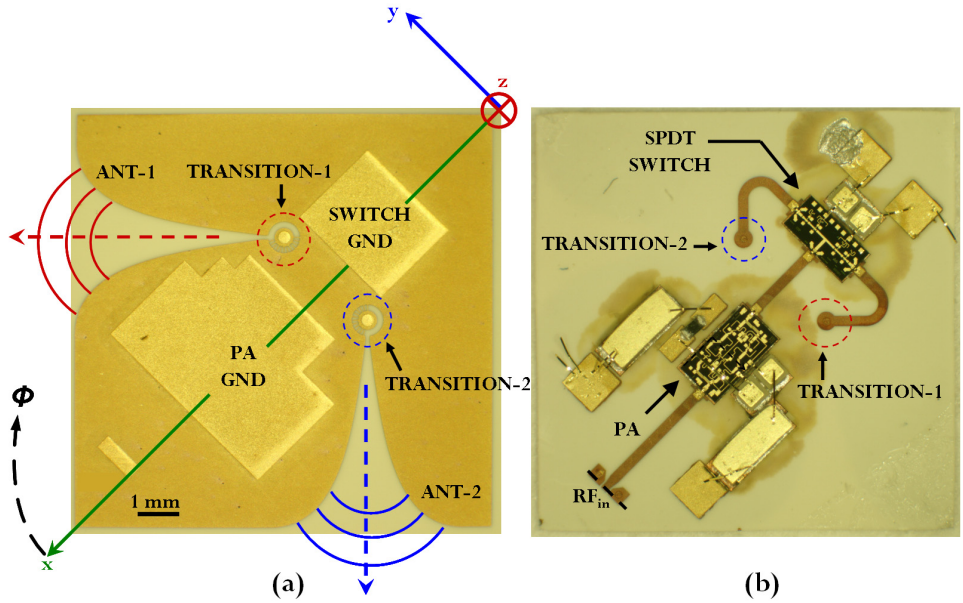

Figure 12: Proposed 10 mm × 10 mm end-fire tapered slot antenna module with switch and power amplifier recessed in a 4 mil thick LCP substrate: (a) bottom layer with patterned slot antennas in the ground plane; (b) top layer with integrated chips and feed/bias networks.

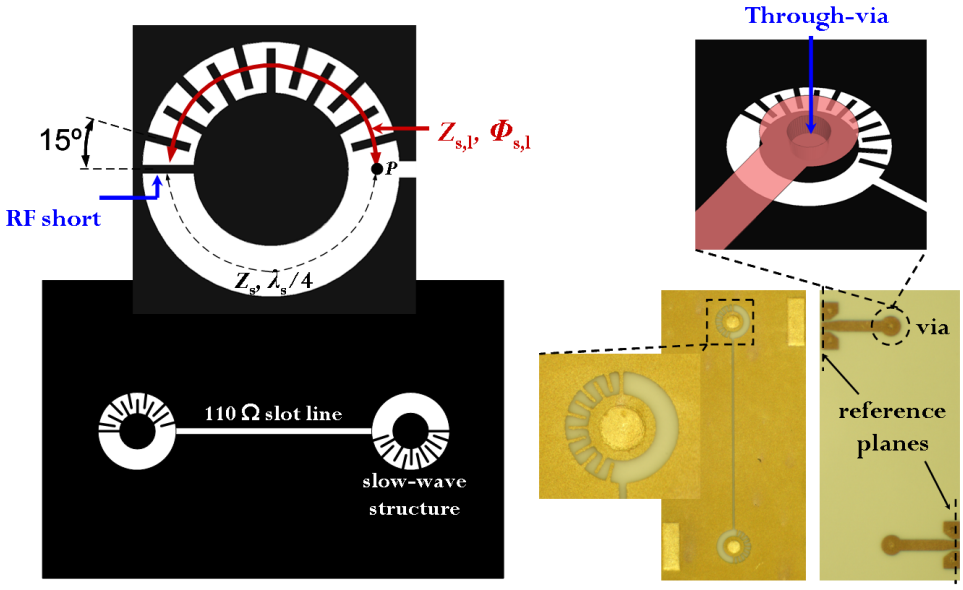

Figure 13: Proposed novel microstrip-to-slot transition: schematic and photograph of the transition structure.

3.2.1 Novel Microstrip-to-Slot Transition

Figure 14 shows the bandwidth of a conventional transition from a uniform open ended 50 Ω microstrip line to a $Z_{s,th}$ slotline when $Z_{s,th}$ varies between between 60 Ω and 110 Ω. It

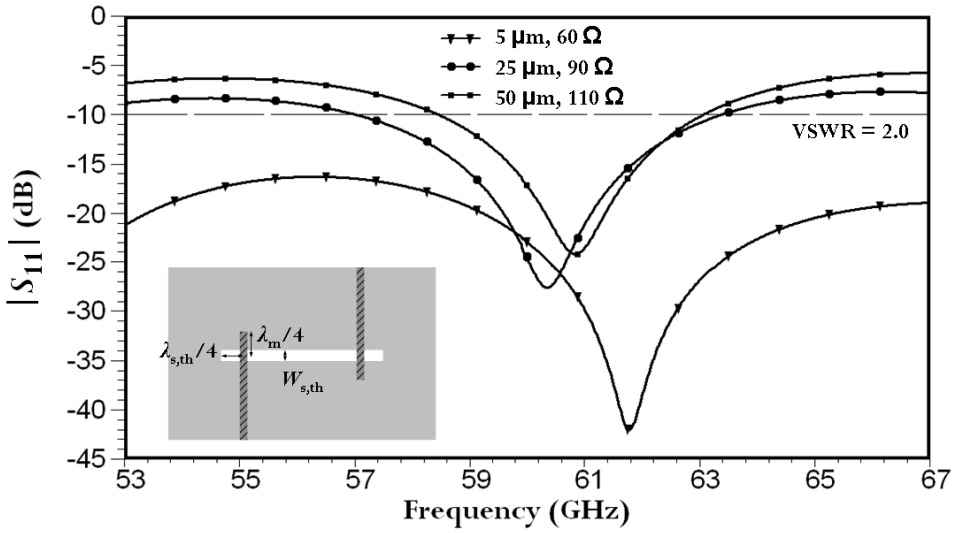

Figure 14: Simulated magnitude of S_{11} of a conventional transition from a uniform open ended 50 Ω microstrip line to a $Z_{s,th}$ slot line: $Z_{s,th}$ varies from 60 to 110 Ω.

is clear that if $Z_{s,th}$ is too large, the limited bandwidth of the conventional transition will degrade the initially wide bandwidth of the tapered slot antenna (TSA). Also, achieving a near 50 Ω slot line impedance on a 4 mil thick LCP substrate requires that the width $w_{s,th}$ of the through slot line is about one fifth of a mil, which falls below the limitations of standard printed circuit board (PCB) manufacturing processes. Therefore, it is proposed in this work to design a novel transition that covers the entire 60−GHz bandwidth with a 110 Ω through slot line ($w_{s,th}$ = 2 mil is a reasonable feature size). Furthermore, a shorter tapered slot length can be achieved by matching the TSA impedance from its open end down to 110 Ω at its input while keeping a large bandwidth.

Figure 13 shows a back-to-back configuration of the proposed microstrip-to-slotline transition. Figure 16 illustrates the microstrip-to-slot mode conversion using edge currents flow. The top layer is patterned with a 50 Ω microstrip line that is connected to the bottom layer using a 5 mil diameter and 4 mil height through-via. The via catch pad size is 18 mil. The bottom layer is composed of a one wavelength long through slot line ($Z_{s,th}$ = 110 Ω) that is connected at its open ends to a slow-wave slot line structure. Half of this structure is a simple quarter-wavelength long slot line (Z_s, β_s) while the second half is a periodically loaded slot line ($Z_{s,l}$, $\beta_{s,l}$) with open stubs used as loading capacitors. β_s and $\beta_{s,l}$ are the

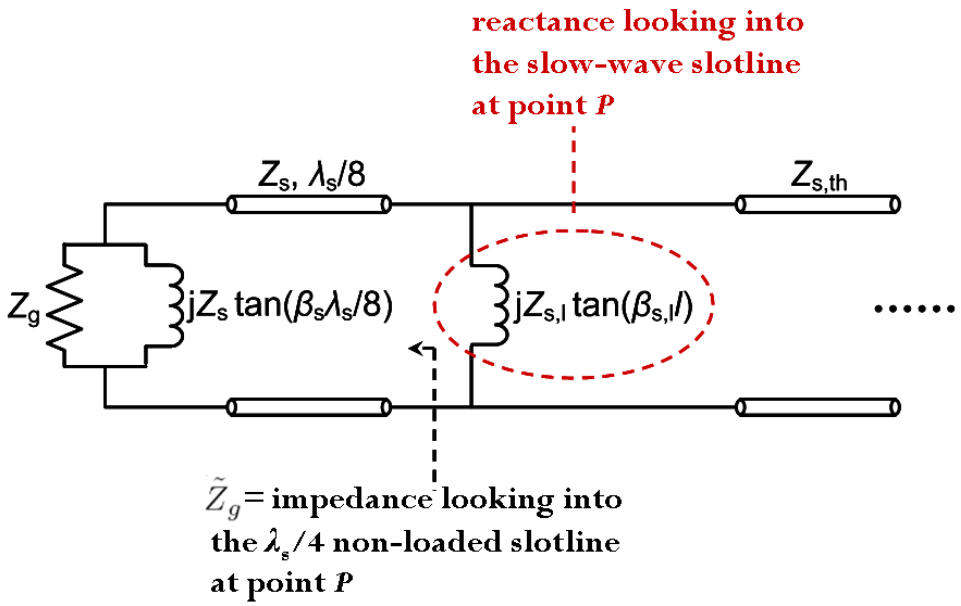

Figure 15: Equivalent circuit model of the proposed microstrip-to-slot transition.

Figure 16: Edge currents flow on the microstrip-to-slot transition.

propagation constants of the simple and loaded slot lines respectively (lossless lines are assumed to show the operating principle of this structure). Because fields propagate *slower* through the periodic path, it is possible to generate currents on both edges of the 110 Ω slot line that are out-of-phase. Starting from the RF short, the impedance looking from P into the slow-wave slot line is a reactance $jZ_{s,l}\cdot\tan(\beta_{s,l}l)$, where l is the physical length of the loaded slot line. Likewise, the impedance looking from P into the unloaded slot line is $\tilde{Z}_g$ that is obtained from a $\lambda_s/8$ rotation of $Z_g||(jZ_s\cdot\tan(\beta_s\lambda_s/8))$, where Z_g denotes the source impedance. Figure 15 shows the equivalent circuit model of the proposed microstrip-to-slot

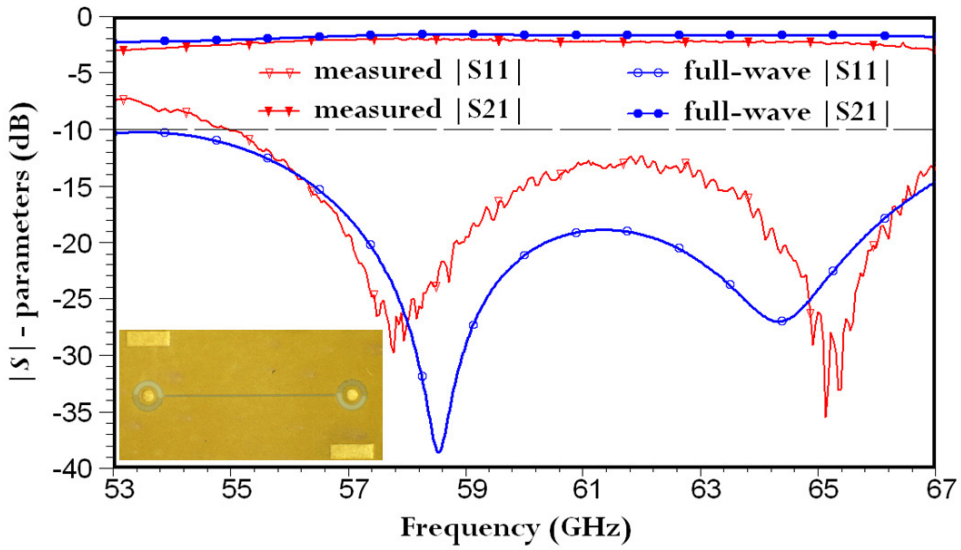

Figure 17: Simulated and measured magnitude of S-parameters of the proposed microstrip-to-slot transition.

transition. Thus, the matching condition at P can be derived as

$$\tilde{Y}_g + \frac{1}{jZ_{s,l} \cdot tan(\beta_{s,l} l)} = Y_{s,th}. \tag{6}$$

According to [85], $\beta_{s,l}$ can be expressed as a function of $Z_{s,l}$. Also, $\tilde{Y}_g$ and $Y_{s,th}$ are known parameters. Therefore, (6) can be solved by finding the roots of the imaginary part of the left-hand side in (6) and setting its real part equal to $Y_{s,th}$. The suggested structure was optimized in HFSS ([1]). Eleven loading stubs (1 mil width and 1 mil capacitive gap) with an angular spacing of 15°, in a 6 mil wide slotline, were required to achieve the performance shown in Figure 17. A good agreement is found between the simulated and measured S-parameters. Measurements were performed using a standard SOLT calibration with 250 μm GSG probes. The measured back-to-back transition is matched from 55 to 67+ GHz (VSWR = 2.0) and has better than 2.3 dB insertion loss over the entire bandwidth. The simulated insertion loss is better than 1.6 dB. It is worth mentioning that these calculated and measured values include the conductor backed coplanar waveguide (CB-CPW) to microstrip transitions that are not de-embedded (See Figure 13).

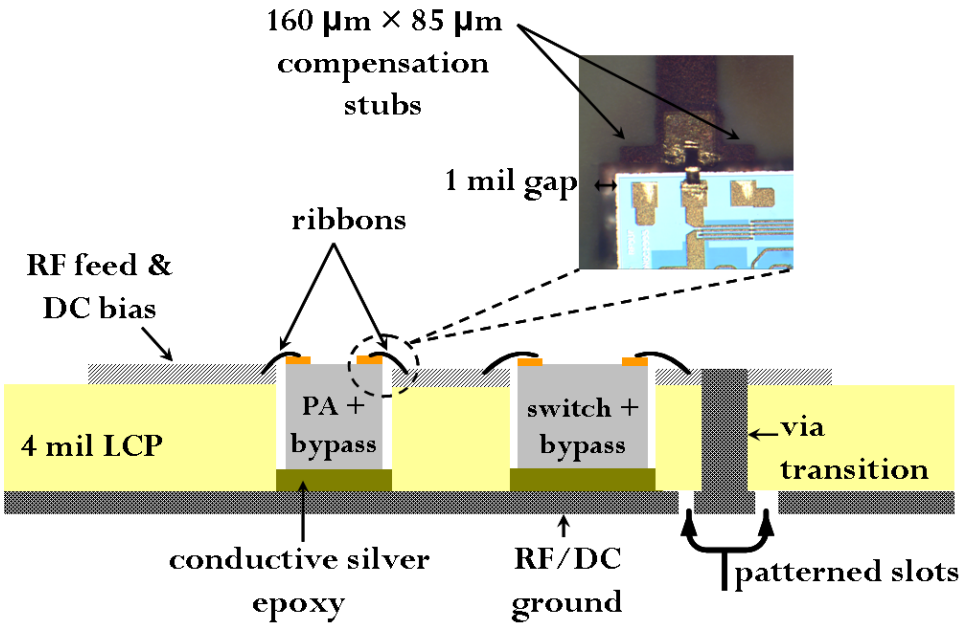

Figure 18: Conceptual drawing of the proposed end-fire antenna module.

3.2.2 End-Fire Tapered Slot Antenna Module

As shown in Figure 12, the proposed end-fire antenna module is composed of two orthogonally arranged tapered slots patterned in the common chip/antenna ground on the bottom side of a 4 mil thick LCP substrate ($\epsilon_r = 3.0 \pm 0.2$ and $\tan\delta = 0.004$ at 60 GHz [97]) while a microstrip feeding network along with the IC biasing network are patterned on the other side of the substrate with ribbon bonds interconnects from chips to package. The profile of the tapered slot is optimized in HFSS to match the TSA input impedance from $Z_{air} =$ 377 Ω down to 110 Ω, where each TSA is further connected to the microstrip-to-slot transition. As explained previously, this transition transforms the 110 Ω TSA input impedance into 50 Ω (over the entire 60−GHz bandwidth) to ease integration with 60−GHz ICs. To compensate for the ribbon bonds parasitic inductance, shunt stubs (165 μm × 85 μm) are connected to the 50 Ω microstrip line at each bonding pad location (see Figure 18).

The entire antenna package fabrication and assembly was performed at the Nanotechnology Research Center cleanroom facility. The fabrication starts with patterning the TSA profile and slow-wave structure using a standard lithography process (photoresist developing followed by wet-etching of copper). Next, 5 mil diameter vias are ablated from the top

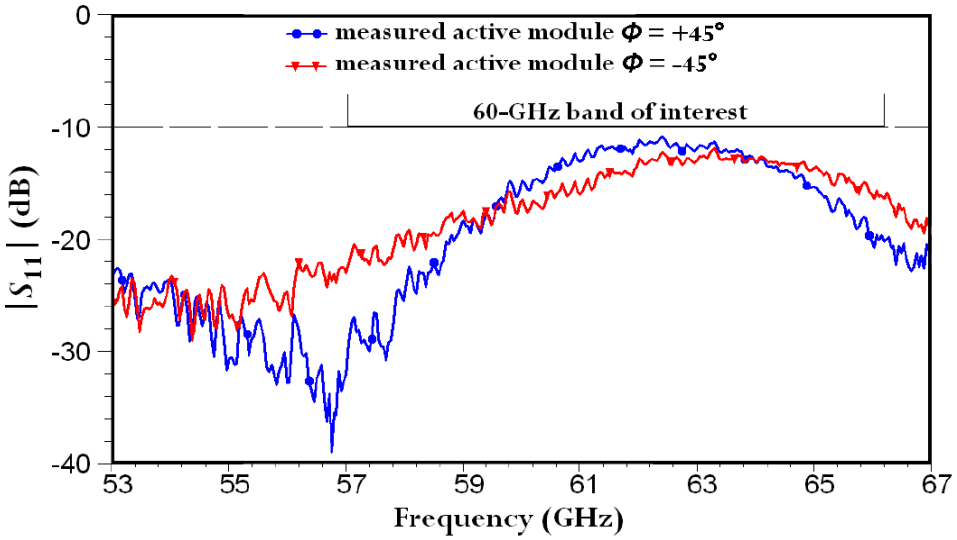

Figure 19: Measured magnitude of S_{11} of the active antenna module in both $+45°$ and $-45°$ transmit modes.

of the substrate with enough laser power to go through the 4 mil thick LCP and also stop at the bottom metal layer (the laser power is controlled to prevent the bottom metal layer from melting). The opened via holes are then electroplated with copper all the way through the 4 mil thick LCP substrate, using the bottom metal as a seed layer. Subsequently, the top side of the substrate is sputtered and patterned using a standard lithography process. Finally, a 10 μm thick gold layer is selectively electroplated at the bonding pads locations. Detailed fabrication steps are provided in the appendix. Precisely controlled size cavities are ablated in the LCP substrate using an excimer laser that has a spot size as small as 5 μm. Cavities for the switch (Hittite HMC-SDD112), power amplifier (Hittite HMC-ABH209), and single layer chip bypass capacitors (Presidio Components) are all ablated with a 1 mil gap between chip edges and cavity edges. This allows us to properly align the chips in the cavities during assembly but also minimize the ribbon bonds lengths on the high-speed signal lines. A thorough O_2 plasma cleaning of the wafer is performed before mounting the chips inside the cavities to remove polymer residues that back deposit on the substrate. Note that since the antenna is patterned on the bottom LCP layer, the top layer is entirely available to easily route the RF and DC lines without any cross-talk concern.

In order to measure the S_{11} of the active antenna, a thick piece of Rohacell®HF foam is

mounted underneath the antenna module to isolate it from the metal chuck of the probing station. Figure 19 shows the measured magnitude of the reflection coefficient of the fully integrated antenna module at the input of the CB-CPW port. Measurements are performed using a 250 μm GSG probe with a standard SOLT calibration. A CS-5 calibration substrate from Cascade is utlized. The active antenna is demonstrated to be matched beyond the required 57-66 GHz bandwidth for commercial 60−GHz gigabit applications. The plots for the $+45^\circ$ and -45° states are more or less similar.

The antenna module radiation patterns and gains are measured in a 60−GHz anechoic chamber with a 25 dBi standard gain horn receive antenna that rotates in a radius of 52 cm around the antenna under test (AUT). The AUT and the standard gain horn are both connected to the ports of a power network analyzer (PNA). The gain calibration is performed using the substitution method. The measurement system was limited to 60 GHz, thus patterns and gains measurements were performed at 56, 58 and 60 GHz. Also, to alleviate the measurement setup, a GPPO connector was mounted onto the CB-CPW port of the antenna module. A GPPO to 1.85 mm adapter was used to connect the antenna to the 1.85 mm cables from the PNA. The GPPO connector and its adapter have a total 0.9 dB insertion loss, as mentioned in the datasheet [2]. In [5], it can be found that the HMC-SDD112 switch has about 1.2 dB insertion loss while the HMC-ABH209 power amplifier has about 13 dB gain in the frequency band of interest.

Figures 20 and 21 show the measured normalized E plane and H plane radiation patterns respectively. Note that since the transmit antenna module is symmetric with respect to the x-axis, only one set of H plane scans was measured. The transmission measurement corresponds to the H plane scan at $\phi = +45^\circ$ when ANT-1 is ON and ANT-2 is OFF (the module effectively radiates towards $+45^\circ$). The isolation measurement corresponds to the H plane scan at $\phi = -45^\circ$ when ANT-1 is ON and ANT-2 is OFF (no radiation is expected from ANT-2).

The measured E plane patterns suggest that the beams point toward $\phi = \pm 20^\circ$ instead of $\pm 45^\circ$ as expected from the antenna layout. First, it is seen from Figure 12 that each tapered slot antenna element has at its open end one side larger than the opposite one. This

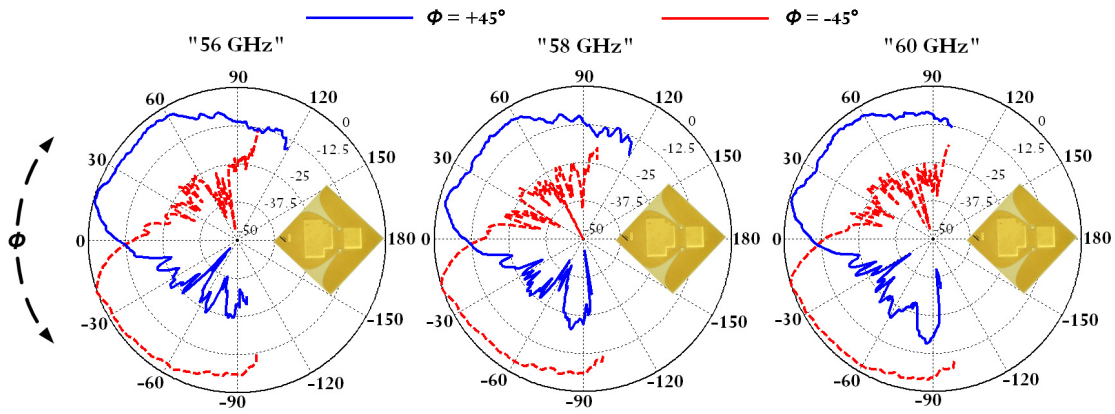

Figure 20: Measured normalized E plane radiation pattern of the active antenna module at 56, 58 and 60 GHz: the E plane is parallel to the antenna module plane, that is $\theta = 90°$.

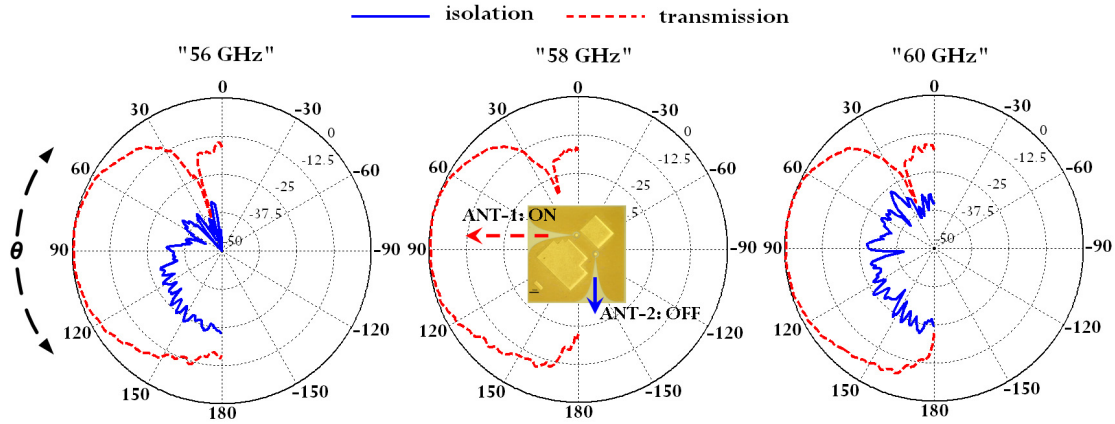

Figure 21: Measured normalized H plane radiation pattern of the active antenna module at 56, 58 and 60 GHz: only the $\phi = +45°$ transmit mode is measured (ANT-1 is ON and ANT-2 is OFF) with the isolation corresponding to the H plane scan looking into ANT-2.

layout creates unequal current flow on the open end edges of the slots. Besides, the GPPO connector and cables that are aligned in the x-axis tend to obstruct fields emanating from the antenna module, and eventually contribute to the observed skewed E plane radiation patterns. Nonetheless, the measured E plane patterns are very consistent over the measured bandwidth and we do observe a spatial beam switching in the antenna module plane with about 55° half-power beamwidth in each direction. The measured H plane patterns are much better and very consistent over the measured frequency bandwidth. The corresponding H plane half-power beamwidth is 68° over the frequency range. The measured isolation levels better than 23 dB suggest that the proposed switched-beam transmit antenna module has

a discrimination level higher than 23 dB between each direction of radiation. This is crucial to prevent radiation toward undesired directions.

The measured active antenna peak gain is 19.5, 19.2 and 18.2 at 56, 58 and 60 GHz respectively. An average 19 dBi active antenna gain is thus achieved, after de-embedding the 0.9 dB insertion loss in the GPPO connector and adapter. Given the 13 dB PA gain, the 1.2 dB insertion loss of the switch, and the microstrip lines losses between the chips, it is estimated that the average passive antenna gain is slightly above 7.2 dBi. Full-wave simulation of the standalone passive element (without chips) gives a 7.7 dBi passive gain for each tapered slot antenna element of the module. This performance along with the demonstrated wide bandwidth characteristics of the proposed antenna module make the proposed solution more competitive than the post-wall waveguide design presented in [92]. To our knowledge, this solution is also the smallest size (10 mm $\times$ 10 mm) highest gain (19 dBi active and 7 dBi passive) end-fire antenna module on organic material with such a wide impedance bandwidth (beyond 55-67 GHz).

CHAPTER 4

BROADSIDE ANTENNA ON MULTILAYER ORGANIC PACKAGES

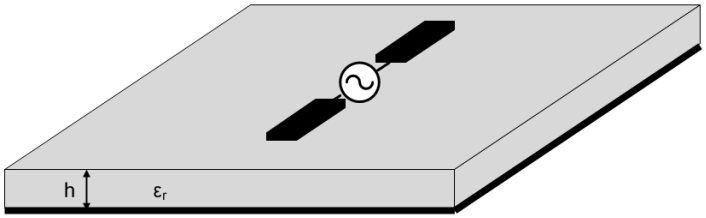

Figure 22: Schematic of a horizontal dipole antenna printed on top of a grounded dielectic substrate.

The radiation mechanism of the antenna paradigm called broadside radiator is such that the direction of maximum radiation occurs at boresight, that is, normal to the antenna substrate and ground plane. To understand the mechanism of broadside radiation, its is essential to get some insight into some more general concepts such as standing wave antennas and image theory.

Let us take the example of a dipole antenna formed by bending two wires away from each other orthogonally to the feeding transmission line (t-line). This particular antenna is classified as a standing wave antenna because of the standing wave nature of currents flowing on each open ended wire. The currents on both wires are of equal magnitude but out-of-phase. To reinforce the fields radiated from each wire and thus maximize the dipole antenna efficiency, the phase of the currents on each single wire must be the same throughout its entire length. This condition is met when the length of the dipole is less than a wavelength at the frequency of the RF signal, that is, the length of each wire is less than half of a wavelength. Beyond that value, the standing wave currents on each wire have alternate phase (0° or 180°), and the fields radiated from each half-wavelength section of a single wire cancel each other and thus create nulls of radiations. On the other side, if the dipole length is too small compared to the wavelength, the aperture of the antenna will

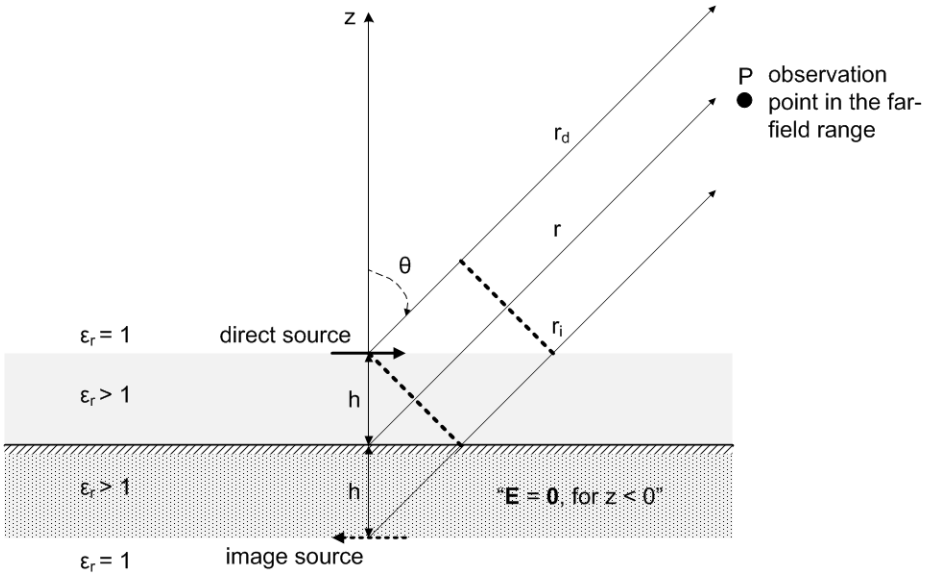

Figure 23: Image theory as applied to an infinitesimal horizontal dipole above a grounded dielectric medium.

be too small to intercept fields. Now, one may bring the dipole antenna in proximity to a ground plane, as is the case of antennas for wireless communication platforms. Although the dipole may be arranged vertically, this solution is disregarded here because the total height of the vertical antenna-ground plane would literally exceed 3 to 5mm, which is not suitable for mobile platforms integration. The dipole is thus arranged horizontal and parallel to the ground plane at a finite height h above the ground plane, as illustrated in Figure 22. The energy radiated toward the ground undergoes a reflection and the amount of reflected energy and its direction are controlled by the geometry and constitutive parameters of the ground and medium separating the dipole from the ground plane. The most appropriate technique to analyze such an antenna system is image theory. The basis of image theory consists in finding an equivalent model where the dipole and its virtual image combined together have same radiation properties as the dipole above a ground plane. In image theory analysis, the first assumption is that the ground plane is perfectly conductive. Another assumption is that the ground plane size is infinite. The former one is an ideal condition that can neverthless be easily approached with traditional good metal conductors such as copper,

aluminum, gold or silver. The second assumption is less trivial and necessitates more in-depth analysis of ground plane surface currents distribution (surface currents exist indeed on a lossy metal ground plane). In general, when the magnitude of surface currents has ebbed off, the ground plane can be truncated with minor effect on the radiation characteristics. A typical rule of thumb would suggest to truncate the ground plane at about five guided wavelengths ($5\lambda_g$) from the antenna edges, but this value may be further optimized with electromagnetic analysis on CAD tools. From Maxwell's equations, it is fundamentally understood that the tangential components of the electric fields are null at the ground interface ($h = 0$). Therefore, at the ground interface, the sum of the direct and virtual tangential electric fields is null. Continuity at the limit of $h = 0$ thus requires that the electric fields above the ground plane are out-of-phase with the electric fields below the ground plane as shown in Figure 23. Combining the fields radiated from both sources in the far-field result in the total electrical field $|E_\psi|$ magnitude proportional to

$$\frac{|\sin(k_0\sqrt{\epsilon_r}h\cos(\theta))|}{r} \tag{7}$$

where the argument of the sin function is half of the phase delay between the direct and image plane waves paths. k_0 is the propagation constant in free space. From (7), the radiation intensity is derived as

$$U(h,\theta) \propto r^2\frac{|E_\psi|^2}{2\eta} = \frac{1}{2\eta}|\sin(k_0\sqrt{\epsilon_r}h\cos(\theta))|^2 \tag{8}$$

where $\eta = 120\pi$ is the free space impedance. The condition for maximum radiation at boresight ($\theta = 0^\circ$) is thus

$$k_0\sqrt{\epsilon_r}h = \frac{\pi}{2} \tag{9}$$

or

$$h = \frac{\lambda_0}{4\sqrt{\epsilon_r}} \tag{10}$$

where λ_0 is the free space wavelength. This is an important and well-kown result. At 60 GHz, (10) means that antenna substrate thicknesses may range from 700 to 900 μm for relative permittivity between 2 and 6. These values are very appropriate for antenna package manufacturing at 60 GHz, unlike at VHF frequencies. This is the reason why it

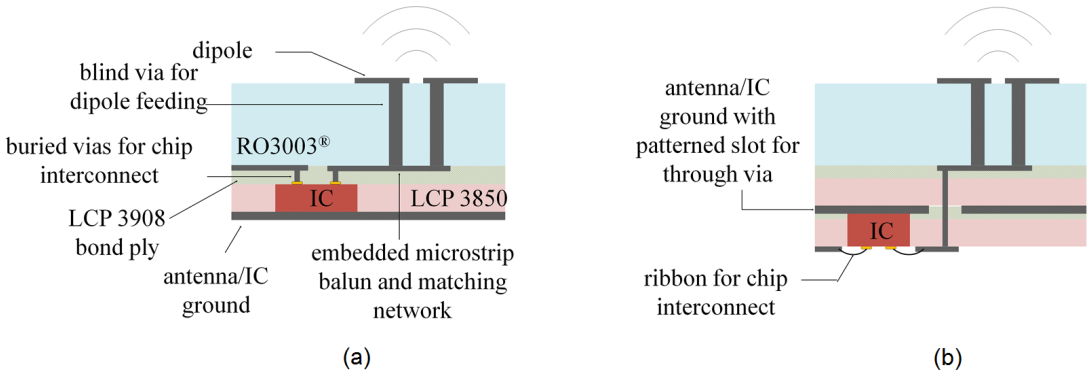

Figure 24: Conceptual drawing of the proposed dipole antenna integrated with a 60-GHz chip: (a) flip-chip or embedded die; (b) wire bonded die.

is extremely attractive to take advantage of image theory to design high directivity dipole antennas at 60 GHz. Moreover, the quarter-wave thick antenna substrate contributes to a high enough frequency bandwidth, as will be shown later in this chapter. As expected, the efficiency of such an antenna design is very high because the dipole is far enough from the ground plane such that return currents do not cancel direct currents. Based on this foundation, high gain and wide bandwidth broadside antennas on multilayer organic (MLO) packages are developed. For advanced theory on printed microstrip antennas with broadside radiation, it is recommended to review the cavity-model and transmission line model analysis techniques in [25].

4.1 High Directivity Dipole Antenna on MLO Package

The proposed design is an enhanced directivity dipole antenna via fed with a substrate embedded balun and matching network densely packaged in a multilayer assembly. The antenna can be built and laminated in an organic stack-up containing embedded or wire bonded chips, as illustrated in Figure 24. The chip packaging approach in Figure 24a is attractive because heat can be easily dissipated from the backside ground plane by conduction and by attaching a heat sink to the ground plane if necessary. Also, interconnects lengths are reduced as a consequence of direct contact between the chip pads and the board traces. The use of C4 bumps for flip-chip assembly is also feasible. A couple of aspects that need to be accounted for though are mechanical stability of the packaged die as well

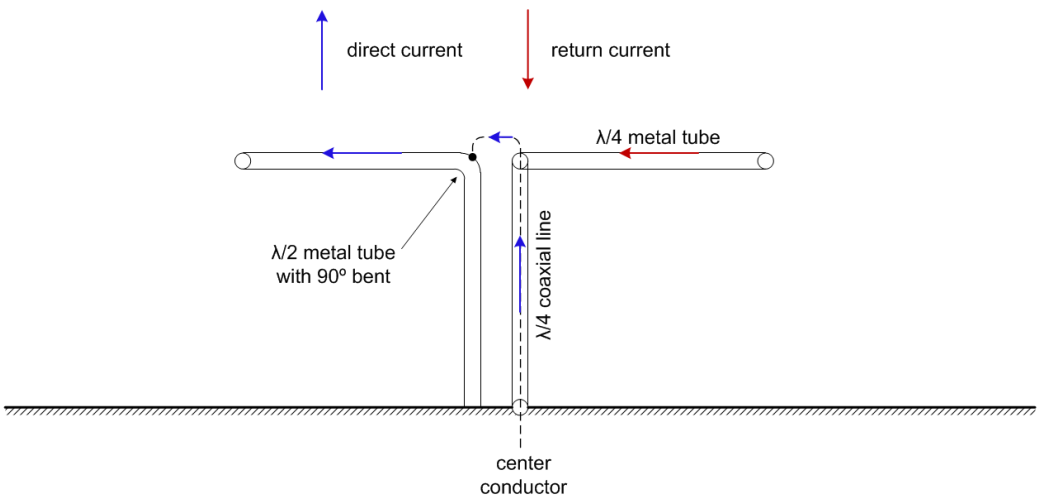

Figure 25: Conventional dipole antenna above ground plane with integrated balun.

as the effect of a higher relative dielectric constant seen from the top side of the die. The approach presented in Figure 24b has the advantage that the die sees air on its top side thus the die performance will not be affected by the package material. The use of bond wires or ribbons require compensation for parasitics. Compensation stubs may be added on die or on package. Advancements in via manufacturing using PCB materials allow for successful development of such antenna packages. The main concern though is heat dissipation that becomes very challenging in this scenario due to the poor thermal conductivity of LCP and Rogers®RO3003. Heat may neverthless be dissipated from the top side of die by convection and radiation. A heat sink may also be attached after encapsulating the die inside an additional layer of LCP material.

Figure 25 illustrates a conventional dipole antenna above a ground plane with enhanced directivity at boresight. The dipole is supported by a pair of metal tubes of length $\lambda/4$ which are electrically connected to the ground plane at one end and to the arms of the dipole at the other. A center conductor is brought up inside one of these tubes and looped over to connect electrically to the junction of the other tube with the other dipole arm. The resulting coaxial line is seen to feed two elements in parallel: (a) the dipole, and (b) a two-wire line of length $\lambda/4$, shorted at its other end by the ground plane. The dipole antenna−feed network system as suggested in [41] is electrically balanced. Indeed, the

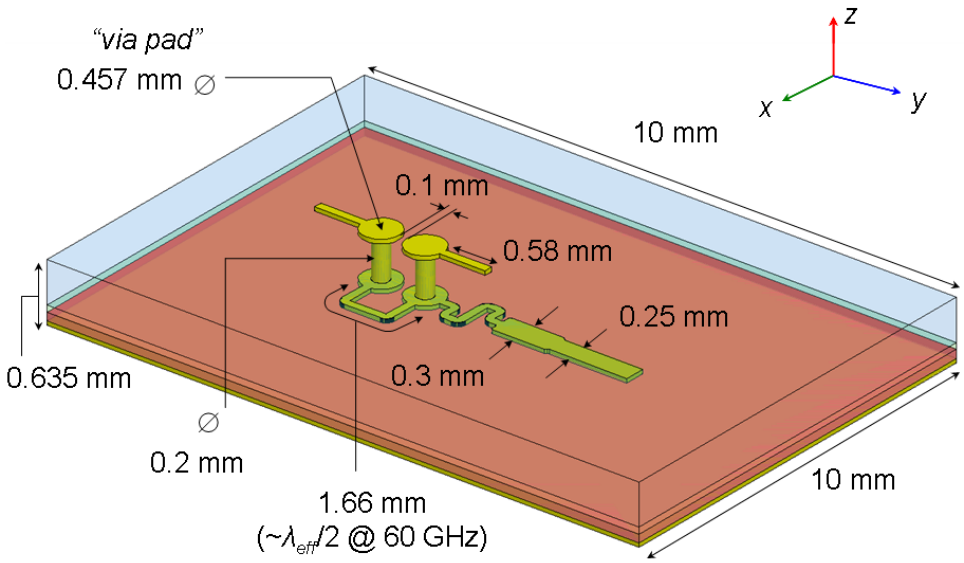

Figure 26: Schematic of the proposed package-integrated dipole.

currents flowing on the center conductor and coaxial shielding are out of phase thus forcing the currents on each branch of the dipole to be out of phase, while their magnitudes are approximately equal due to the short circuit created at the end of the two-wire line. It is worth noting that at the feeding gap between the dipole branches, the impedance looking into the two-wire line is very high because the short circuit seen by the two-wire line is transformed into an open circuit; as a result the magnitude of the current flowing into the two-wire line is negligible which insures that the two-wire line does not contribute to radiation. However, metal tubes are not suitable for integration with solid-state devices and furthermore, they are too bulky to be integrated with wireless platform devices. It is thus essential to find an alternative technique that takes advantage of multilayer printed circuits integration to model a similar structure. Even though an attempt to reproduce the exact same topology may be acceptable, one clear challenge is how to build a vertically integrated coaxial line in printed circuit board technology. In the proposed design, an affordable cost-effective approach is proposed, as illustrated in Figure 26.

It is well known that a half-wavelength dipole antenna, in free space, has a low directivity (2.15 dBi). As described above, image theory is used to design a highly directive dipole

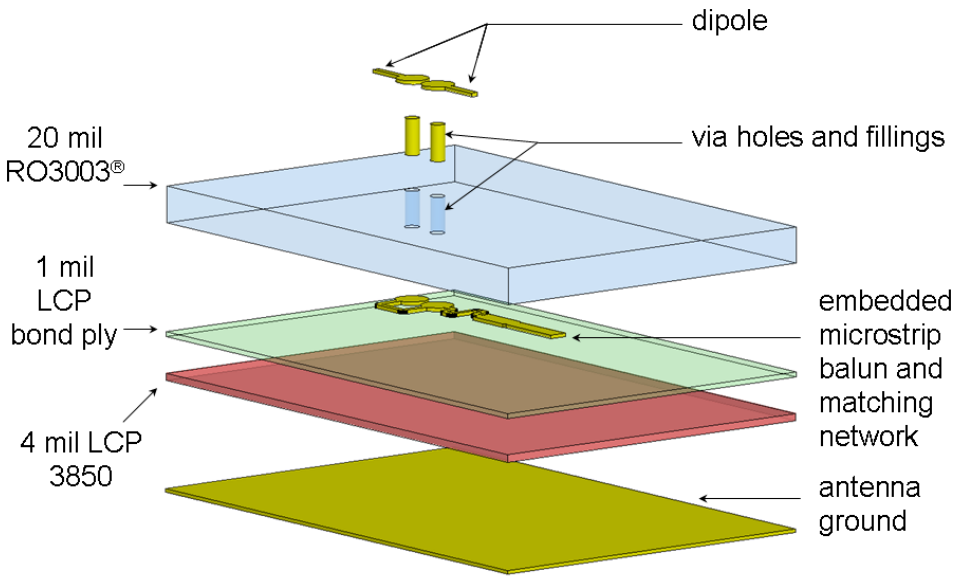

Figure 27: Stack-up of the proposed package-integrated dipole.

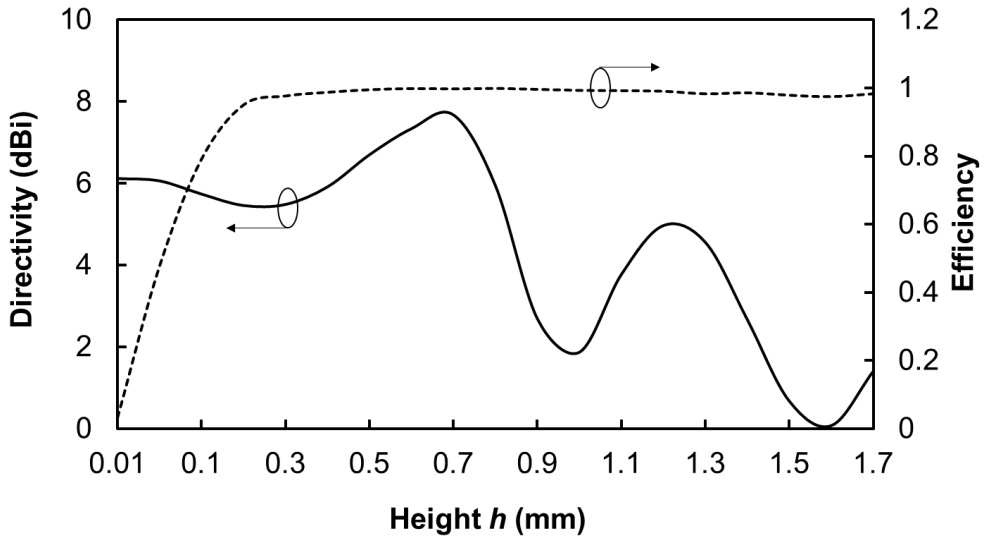

Figure 28: Variation of directivity and efficiency of the horizontal dipole at a height h above a finite ground plane.

antenna. Our goal is to have an antenna that radiates at boresight. Figure 26 shows a detailed view of the proposed antenna. The package stack-up is also shown in Figure 27. Note that because LCP does not come thicker than 4 mil in general, it is best to combine

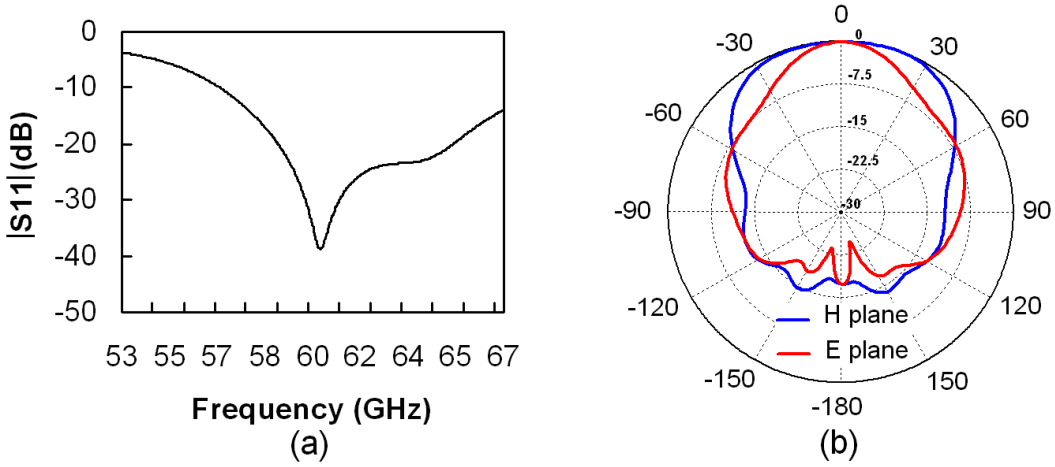

Figure 29: Simulated antenna parameters of the package-integrated dipole: (a) Magnitude of S_{11}; (b) Normalized radiation pattern at 60 GHz.

LCP with another organic material Rogers®RO3003 that bonds very well to LCP using standard LCP bonding process. Also, electrical properties of both materials match very well at mm-wave frequencies. Full wave simulations on the multilayer integrated antenna structure using Ansoft's HFSS [1] are performed. The simulated boresight directivity of a half-wavelength dipole at a height h above a finite ground plane (10 mm $\times$ 10 mm) is shown in Figure 28. It is seen that the directivity peaks at 7.67 dBi when $h = 0.7$ mm ($\approx \lambda_g/4$). λ_g is the guided wavelength inside the package dielectric medium of relative permittivity 3, at 60 GHz. The radiation efficiency is higher than 99 % above 0.5 mm.

After establishing the optimal dipole height, a feeding network is designed to keep the overall antenna structure compact without altering its radiation performance. For printed dipole antennas, the feeding transmission line may be directly printed on the same layer as the dipole. However, transmission lines such as microstrips printed on a thick substrate tend to be excessively wide, and are particularly undesirable in antenna array configurations. Alternatively, the feed line can be printed on a sub-layer (hence substrate embedded), closer to the ground plane, to reduce the feed line width and the feed network form-factor. Taking advantage of multilayer capabilities of RO3003 and LCP materials, this solution can be easily implemented. A miniature substrate embedded feed network composed of two vias, a balun and a matching network for 50 Ω input impedance is designed to drive the dipole. To

closely match the simulated optimal dipole height of 0.7 mm, we use the substrate stack-up shown in Figure 27. The dipole is printed on top of a 20 mil thick RO3003 substrate that is traversed with two through vias that connect to the balanced input of a microstrip balun printed on the opposite side of this substrate. The balun is integrated with a microstrip matching network. The ground plane for the microstrip line is provided on the bottom side of a 4 mil thick LCP layer. Finally, the two above mentioned layers are bonded together using a 1 mil thick LCP bond ply at about 285 °C. The 180 ° microstrip balun feeds the two dipole arms out-of-phase with almost the same amplitude. The phase shift is achieved with a 0.1 mm wide and 1.66 mm long microstrip line. The amplitude attenuation through the phase shifter is less than 0.1 dB and that guarantees equal amplitude feeding for both dipole arms. At the unbalanced input of the balun, a 0.1 mm wide and 1 mm long meandered microstrip line acts as a series inductor to bring the resonant frequency of the dipole to around 60 GHz; the simulated input impedance is $(38.5 + 1\jmath)\ \Omega$. The antenna is then matched to 50 Ω with a quarter-wavelength transformer. The proposed dipole is matched from 56 GHz to above 67 GHz covering the entire WPAN band (see Figure 29). This design also takes advantage of the low relative permittivity of the RO3003 layer and the high elevation of the dipole above the ground plane to broaden the impedance bandwidth (56 to $\geq$ 67 GHz) [99]. The radiation pattern shown in Figure 29b is perfectly symmetric in both E (yOz) and H (xOz) planes, with a peak of 7.83 dBi at boresight, and the antenna radiation efficiency is 91.7 %. The structure of the proposed embedded feed network along with the balun is critical in the achievement of the E/H plane pattern symmetry. The peak directivity is very close to the ideally fed dipole of Figure 28 whereas the efficiency drops by only 0.08 % and this is attributed to the insertion loss through the vias and the feed network.

4.2 Dipole Antenna Array on MLO Package

The proposed single dipole antenna has a significantly high measured gain (7.68 dBi) for 60-GHz high speed communications at moderate distance ranges. However, for applications at distances of several meters, the antenna directivity needs to be enhanced, and this can

be achieved with dipole arrays. In order to increase the antenna directivity, a 22 mm $\times$ 11 mm $\times$ 0.635 mm 8-element linear array is designed. A corporate feed network is used in this antenna array. The dipoles are spaced half a wavelength from each other in the x-direction. EM simulations indicated that this spacing provides at least 18 dB isolation between adjacent elements. Figure 30 shows a schematic of the designed array with a photograph of the fabricated part. Since this antenna structure has an embedded microstrip feed line, it requires a transition to an external feed for antenna testing. A low-loss broadband microstrip-to-CPW transition is developed in the frequency band of interest, based on the approach of [42]. The theory of operation of this transition is based on magnetic coupling between the overlaying microstrip line and the orthogonal slot line, which is then appropriately bent to form a CPW line. The CPW dimensions were fixed to 1300 μm/100 μm because of the limitations in the lithography process used by the PCB circuit manufacturer. The center conductor width of the CPW line is further tapered down to 400 μm for a good transition to the GPPO connector. Manufacturing of this antenna structure is achieved using standard printed circuit board processes for high volume and low-cost production. To measure the radiation patterns of the antenna array, the embedded 50 Ω microstrip line has been extended to 25 mm long; this helps isolating the antenna and the bulky GPPO connector. Because of the long microstrip line (0.5 dB/cm), the vertical transition (0.3 dB) and the GPPO to 1.85 mm adapter (0.9 dB) used in measurements, about 2.45 dB of loss is expected from the reference plane P to the input of the 1.85 mm adapter.

The reflection coefficient of the dipole array is simulated and measured at the input of the GPPO connector. The connector is plugged to a GPPO to 1.85 mm adapter, which is connected to a calibrated Agilent network analyzer. Simulation at plane P where the antenna is to be actually connected to a chip in an integrated system is also performed (See Figure 31a). At reference plane P, the 8-element array exhibits more than 11 GHz bandwidth (56 to above 67 GHz - $S_{11} \leq$-10 dB). After inclusion of the extended microstrip line and GPPO connector, the simulated array is matched from 54 GHz to above 67 GHz, whereas the measured array has 8 GHz bandwidth (56.6 to 64.6 GHz). The narrower

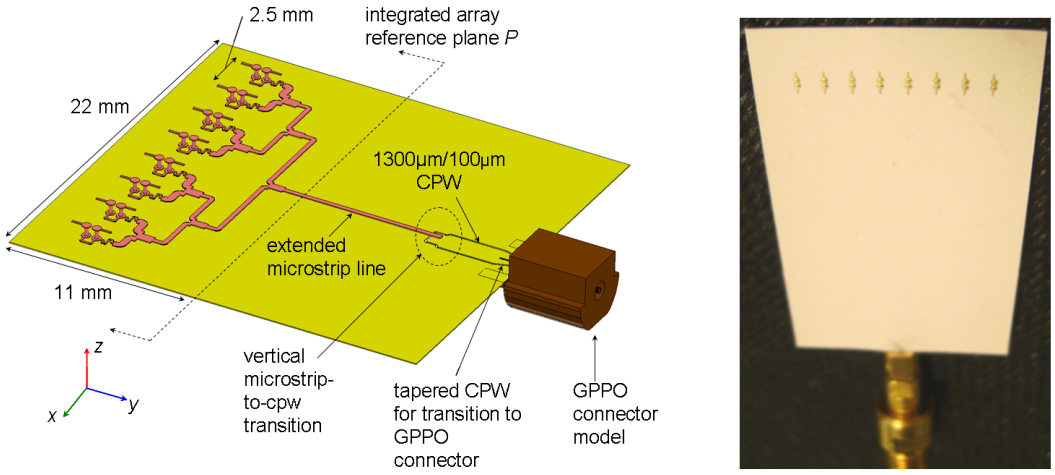

Figure 30: Schematic and photograph of the proposed package-integrated dipole array.

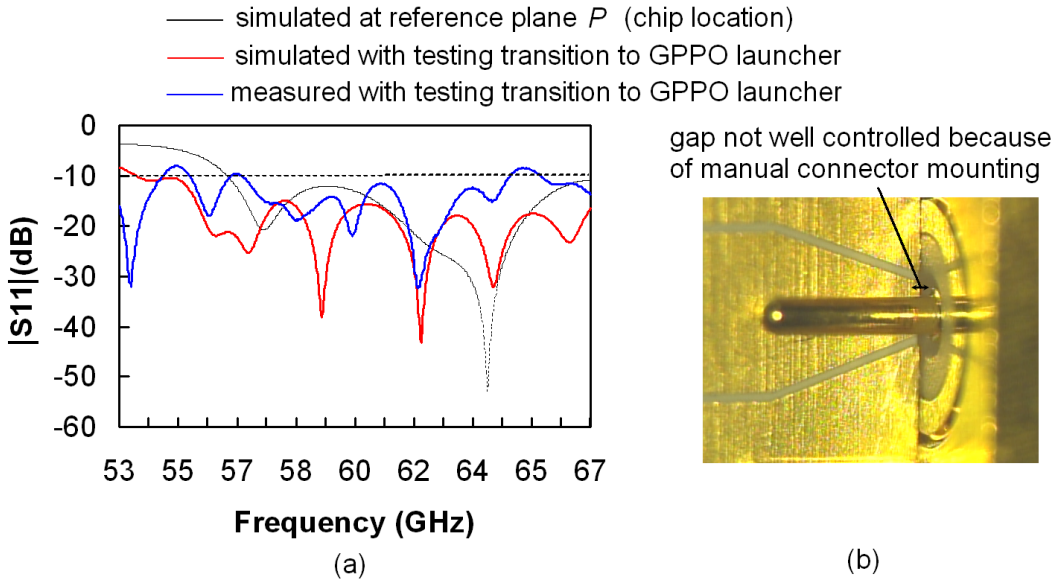

Figure 31: Eight-element dipole antenna array: (a)Simulated magnitude of S_{11}; (b) Photograph of the CPW-to-GPPO launcher transition.

measured bandwidth is attributed to mismatch through the different transitions, especially the transition to the GPPO connector that has a response sensitive to the accuracy with which the connector is mounted on the test board. Note that there is always a 50 to 100 μm (or more) gap between the actual CPW input and the connector when the connector is manually mounted (See Figure 31b). This gap may introduce a step in the transition thus affecting the fields distribution at the input of the CPW line.

The normalized radiation patterns of the antenna array are plotted at 58 GHz, 61 GHz

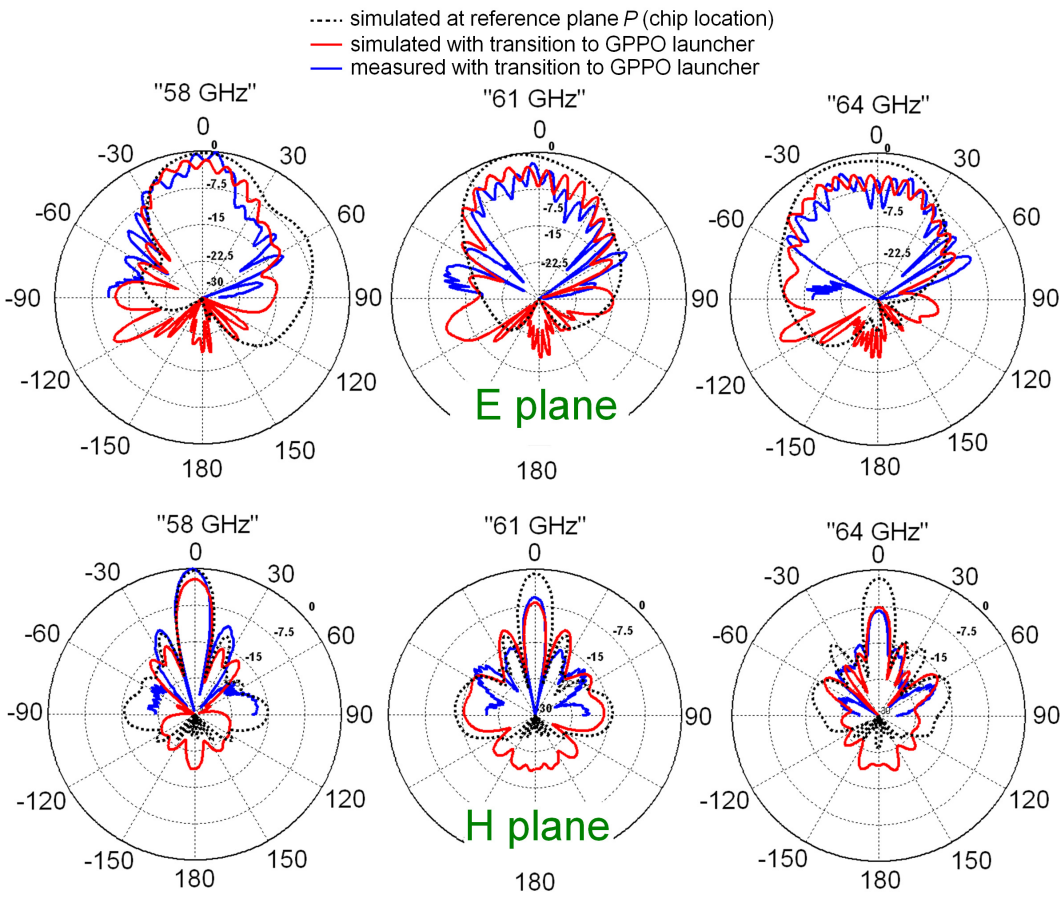

Figure 32: Simulated and measured normalized radiation pattern of the 8-element dipole array at 58, 61 and 64 GHz.

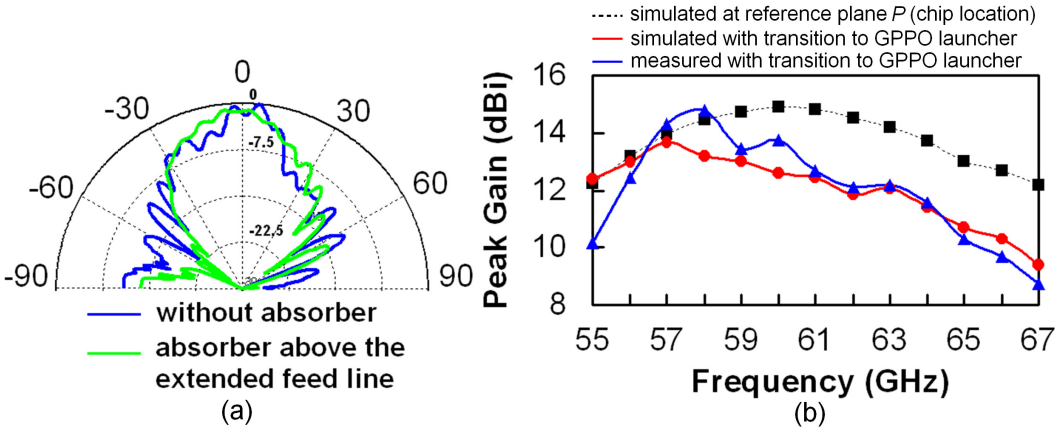

Figure 33: Dipole antenna array: (a) Measured normalized E plane pattern at 58 GHz with extended microstrip line effects; (b) Simulated and measured peak gain variation with frequency.

and 64 GHz (See Figure 32). The E and H plane simulated (with GPPO connector) and measured patterns are all in good agreement. In the E plane, several ripples with 1 to 3 dB amplitudes are observed, in both simulation and measurement with the extended feed line and the GPPO connector. By carefully covering the long feed line with a 3 mm thick millimeter-wave absorber, these ripples are smoothed to below 1 dB amplitude, as seen in Figure 33a. The out-of-phase standing wave currents between subsequent half-wavelength line sections on the electrically long microstrip feed line create a pattern with multiple nulls and lobes, that add up constructively or destructively to the main antenna beam and thus generate the ripples in the E plane pattern [70]. Since the long feed line is orthogonal to the H plane, it does not introduce any perturbation in the H plane patterns. In the E plane, we also observe a minor beam skewing over the frequency band that is attributed to amplitude and phase imbalance in the balun. Figure 33b shows the peak gain level variation over the frequency band. As expected the simulated and measured peak gain levels at the GPPO input are about 2 dB less than the simulated levels at reference plane P, above 60 GHz. From 55 GHz to 60 GHz, the difference in trends is attributed to the ripples that may either increase (or decrease) the peak gain level because of the constructive (or destructive) fields radiated from the microstrip line. After de-embedding the 2.45 dB loss in the feeding network, the 8-element dipole antenna array exhibits a measured peak gain of 17.23 dBi at 58 GHz, 15.1 dBi at 61 GHz, and 14.02 dBi at 64 GHz. The estimated radiation efficiency is 68 to 70% at the GPPO input and 75 to 83% at reference plane P.

CHAPTER 5

INTEGRATED ANTENNA ON MULTILAYER ORGANIC PACKAGES WITH BROADSIDE AND END-FIRE RADIATION

Figure 34: Example of mm-wave WPAN with Wireless HDMI and 3D sound system.

Figure 34 is an example of mm-wave piconet involving multiple devices: the central device (a 60-GHz enabled iPad for instance) transmits uncompressed video contents at high data rates to a 60-GHz enabled HDTV and audio contents at high data rates to 60-GHz enabled speakers arranged in a 3D configuration. In order to reach all these devices, the radiators inside the iPad would ideally have an omnididirectional pattern. However, omidirectional antennas suffer from very poor antenna gain that is in fact close to 0 dBi. Moreover, to increase the antenna range, it is compulsory to utilize highly directive radiators that is narrow beam width antennas. To compensate for the reduced field-of-view, multiple radiators may be mounted inside the iPad device. There exists an inherent high cost and

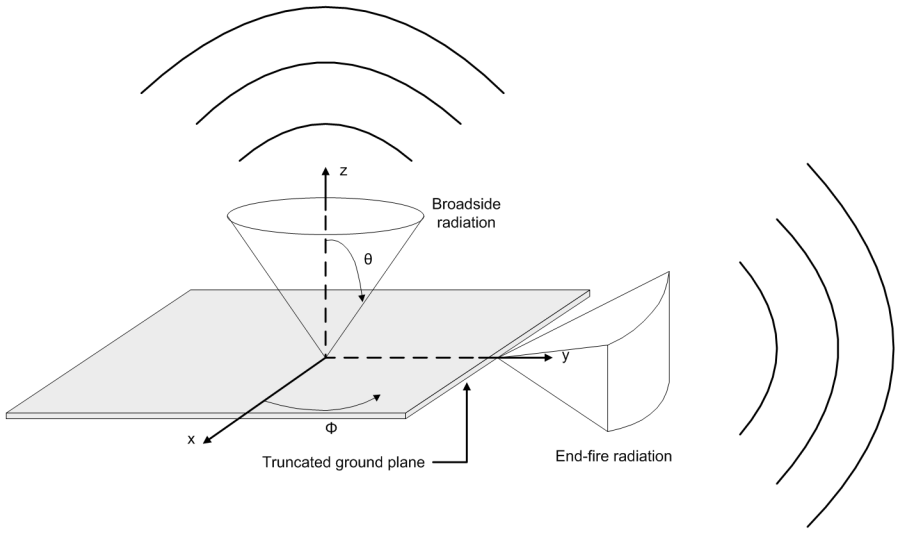

Figure 35: Spherical coordinates system showing broadside radiation at elevation angles and end-fire radiation at azimuth angles.

size to this solution that requires multiple antennas. One way to tackle this problem is to develop an integrated antenna module with multiple beams and yet reduced cost and size. The multiple-beam antenna module would thus be able to switch between various beams and reach out to any desired device. The choice of the antenna topology determines its capability to synthesize beams at various directions. Existing printed mm-wave radiators for high-speed 60 GHz PHY may be categorized into two groups: broadside and end-fire. In broadside radiators, a main beam normal to the antenna ground is synthesized to illuminate one half-plane above the ground plane (see Figure 35 with $z \geq 0$) and reach out to other devices that radiate in the same line-of-sight. The energy radiated by an optimal broadside radiator above a ground plane decreases at small elevation angles and vanishes at grazing angles. Thus, an optimal broadside radiator is a very poor radiator at $\theta = \pm 90^{\circ}$. Likewise, in printed end-fire radiators a main beam parallel to the antenna ground is synthesized to illuminate one half-plane beyond the truncated ground plane (see Figure 35 with $y \geq 0$) and reach out to other devices that radiate in the same line-of-sight. The energy radiated by an optimal end-fire radiator decreases at higher elevation and azimuth angles and vanishes at grazing angles. Thus, an optimal end-fire radiator is a very poor radiator at $\theta(\phi) = 0^{\circ}$ or $\theta(\phi) = 180^{\circ}$. A single antenna module that integrates both types of antennas however

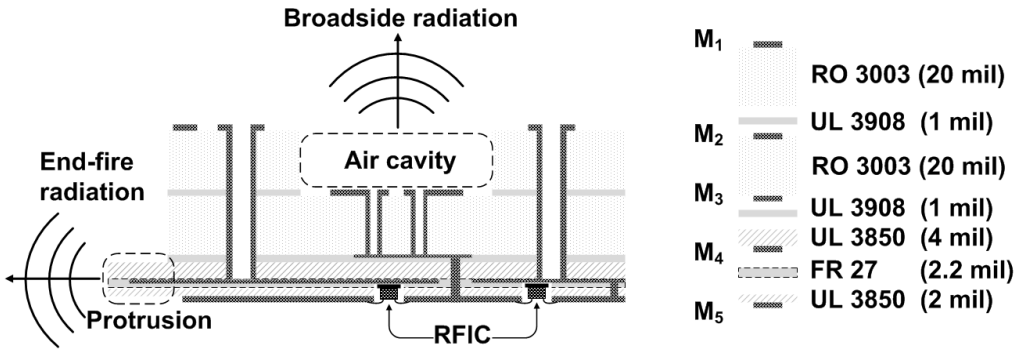

Figure 36: Conceptual drawing of the integrated antenna on MLO package with broadside and end-fire radiation.

overcomes these limitations. The single antenna module uses active devices such as switches to select each radiator. Challenges in designing this type of antenna module are size, cost, beam switching speed, antenna gain and beam width, frequency bandwidth, as well as isolation between radiators. Figure 36 illustrates the architecture of such an antenna module that realizes both broadside and end-fire radiation in a single package yet maintaining a compact size, low cost, and high performance. A detailed representation of the antenna structure is given in Figure 37.

5.1 Integrated Antenna Design on MLO Package

5.1.1 Broadside Dipole Radiator

The antenna design presented in section 4.1 is used as a prelude to design a higher directivity broadside radiator while keeping significant bandwidth. In fact, it was demonstrated earlier that a theoretical 7.83 dBi directivity could be achieved when image theory is invoked. Another common technique used to enhance either a slot, dipole or patch antenna directivity is the cavity-backed concept [41, 46, 95]. When a dielectric substrate separates the radiator from its ground plane, a substantial amount of surface waves is excited in the dielectric. Thus, a metallic cavity surrounding the radiator forces substrate mode fields to reflect off the metallic walls in which case the fields that exist in the cavity are predominantly of a TE_{10} standing wave type. Hence, the cavity may be seen itself as a resonant antenna which radiation occurs from the cavity aperture. If the cavity size with respect to the slot, dipole

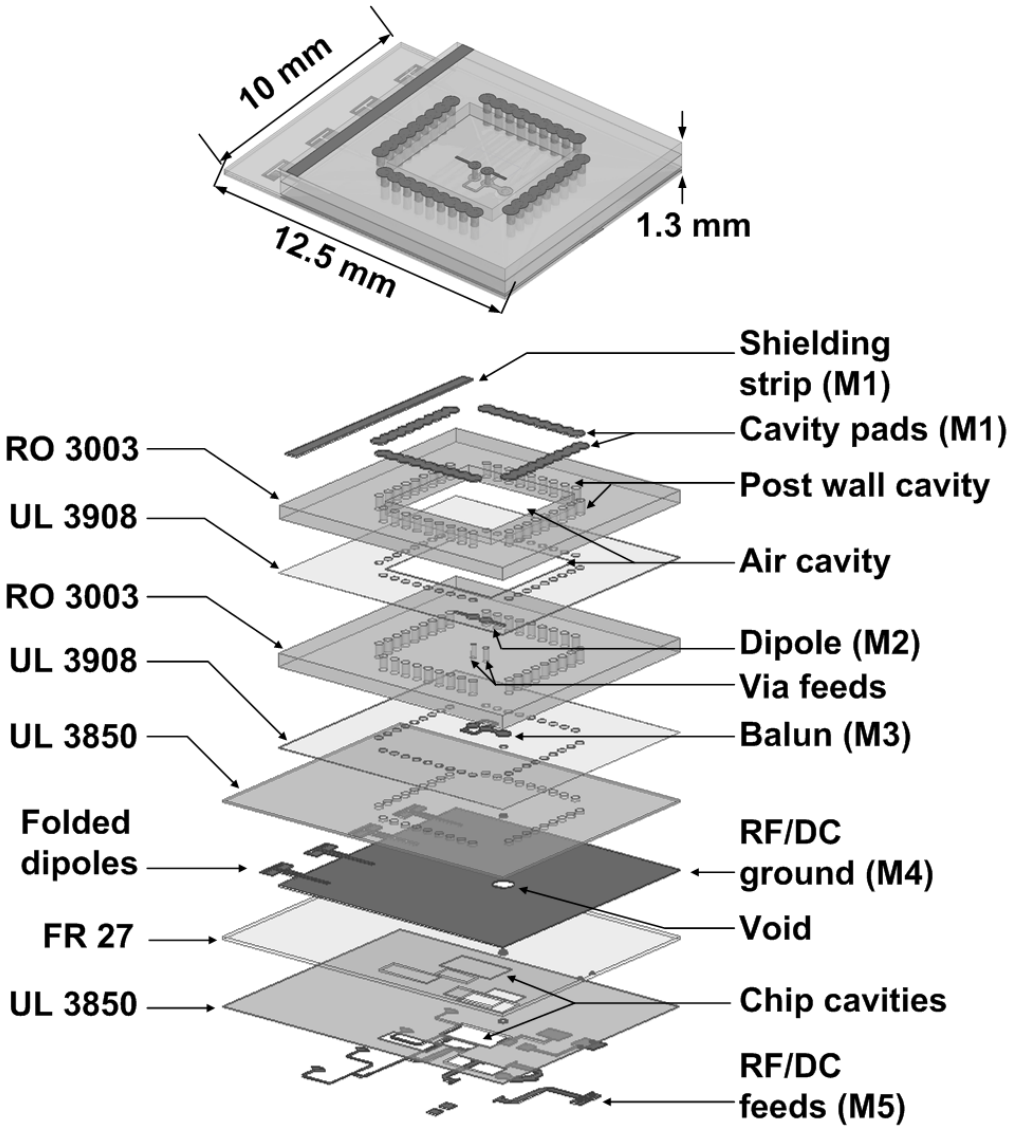

Figure 37: Stackup of the integrated antenna on MLO package.

or patch radiator is properly designed, the fields radiated from the cavity aperture will reinforce with the main radiator fields at boresight thus enhancing the antenna directivity. Wong and King published a design of a cavity-backed antenna to enhance the directivity at boresight by about 2 dB. Their radiator was however made of bulky metallic rods and cylinder for MHz range satellite communications [103].

Dipole on Vias: The antenna design starts with the definition of the dipole height above the finite size ground plane. This step was covered in the previous chapter, and it was

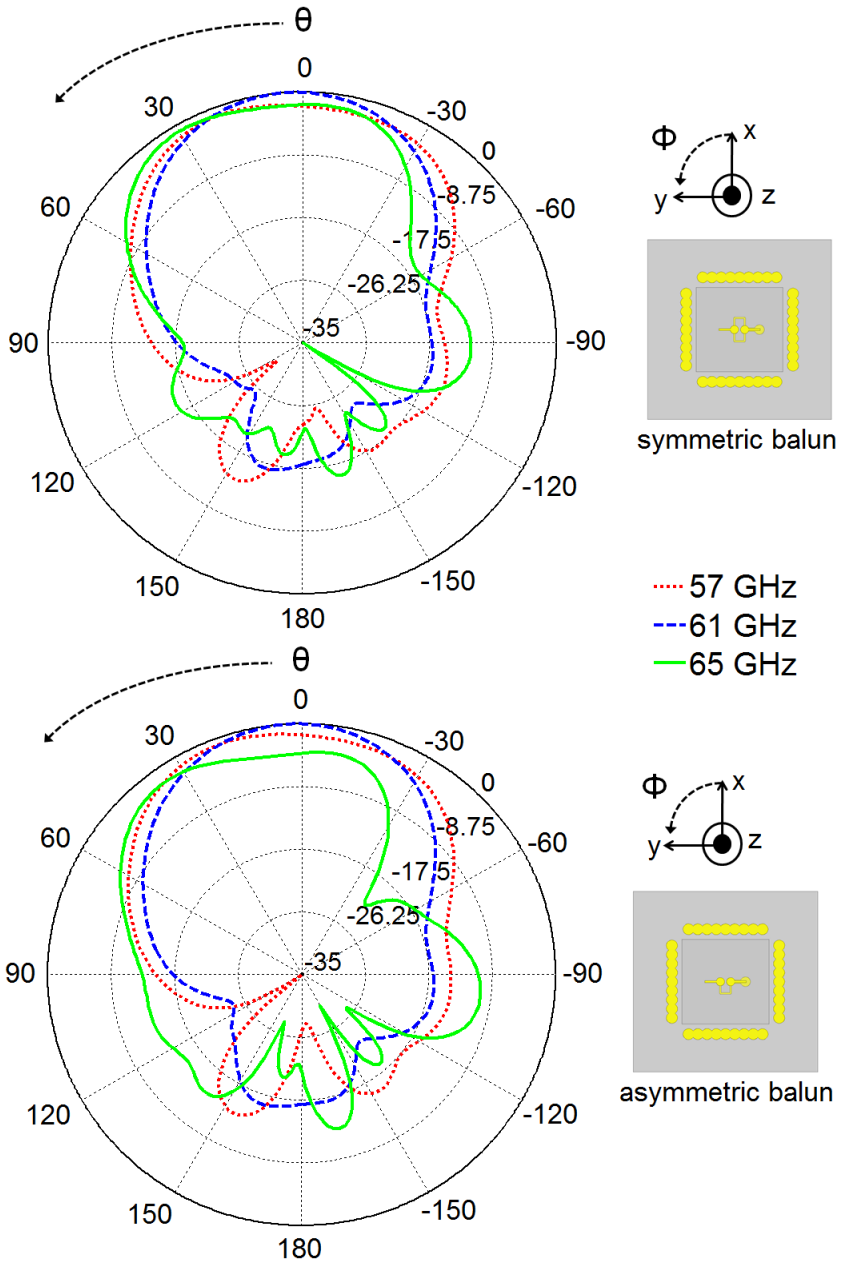

Figure 38: Simulated normalized E plane radiation pattern of the broadside radiator: effects of balun symmetry on E plane (ϕ=90°) pattern over frequency.

found that a dipole printed on a 20 mil thick RO3003 grounded substrate provides near optimal directivity at boresight. The ground plane size could be larger than 10 mm × 10 mm to approximate an infinite one but minimizing the antenna package adds constraints on this parameter. The ground plane size is neverthless optimized to minimize current densities near the ground edges, therefore mitigating edge diffraction that could distort the

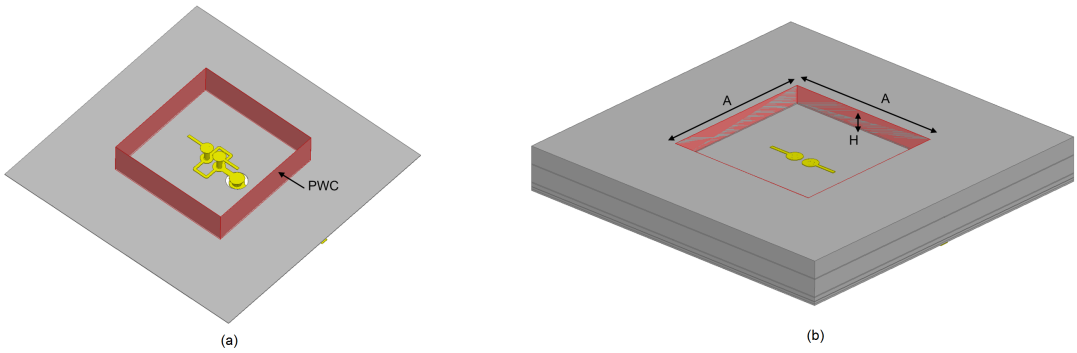

Figure 39: Schematic of broadside dipole antenna with a post wall cavity: (a) view of the dipole on vias, balun, and micro-via through ground plane; (b) view of air cavity created inside the superstrate layer.

patterns. Each dipole branch is about quarter of the effective wavelength of a conductor printed on a 20 mil thick RO3003 grounded dielectric. The branch width is set to 100 μm and this is the minimum achievable line width to comply with standard PCB manufacturing processes. Two metallic posts or vias are then created to connect the dipole branches on M2 to a microstrip balun on M3. M2-M3 vias are mechanically drilled and end up in a near cylindrical shape of 8 mil diameter. Catch pads on M2 and M3 have 18 mil diameter and this gives enough room for misalignment tolerances (2 to 4 mil typical). To excite each dipole branch with out-of-phase currents, 180° delay lines connect to the vias on layer M3. The delay lines are microstrip lines on top of a 4 mil thicl LCP substrate. A pair of delay lines is utilized to maintain symmetry of the structure as well as improve the balun frequency bandwidth. In fact the balanced dipole has a uniform E plane radiation pattern over a large frequency bandwidth when the balun is symmetric, as shown in Figure 38. A microstrip T-junction on M3 splits power equally at the input of the two-section delay line and feeds each dipole branch with almost equal amplitude. The dipole on vias is thus electrically balanced.

Post Wall Cavity: A square shaped post wall cavity (PWC) surrounds the dipole (see Figure 39). Two parameters are essential in the design of the PWC: the height H and the aperture A. Both parameters are optimized using the HFSS finite element method (FEM)

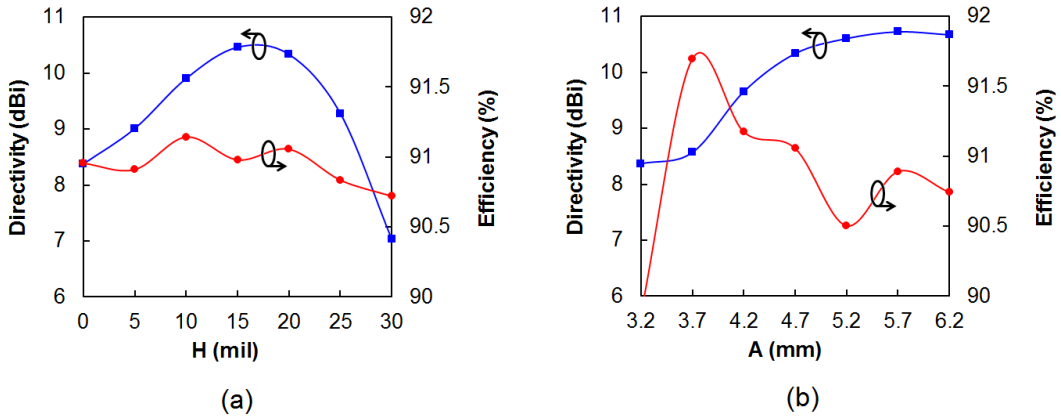

Figure 40: Effects of PWC height and aperture size on boresight directivity and radiation efficiency: (a) variations with H; (b) variations with A.

tool. Figure 40 illustrates the effects of cavity size on the dipole antenna directivity and radiation efficiency. It is clear that increasing the PWC height substantially improves the directivity at boresight. If the PWC has 0 mm height (that is the PWC is only as high as the dipole), the directivity at boresight increases from 7.83 to 8.4 dBi compared to a dipole without PWC. Then, as the PWC height H increases the directivity also increases and peaks at about 10.5 dBi for a fixed cavity aperture (A = 4.7 mm). Beyond 20 mil height, the directivity starts dropping and it is believed that as the depth (or height) of the cavity increases its quality factor increases and the amount of energy stored inside the cavity increases which translates into smaller radiated power. It is not surprising to observe that as the aperture size (A) of the cavity increases the directivity also increases. This is a fundamental result that results from a wider capture area of the radiator. However, the directivity versus aperture curve saturates beyond 5.7 mm and it is understood that if the aperture increases even further, higher order standing wave modes excited in the cavity will also contribute to radiation and may interfere with the main beam. Note that the efficiency is at least 90 % over the entire sweeping range for both tuning parameters. A practical and cost-effective way to implement the PWC is to drill via holes between M1 and M4, as illustrated in Figure 41. The vias height is determined from the previous parametric study. M1-M4 vias are supported by an additional 20 mil thick RO3003 dielectric. These

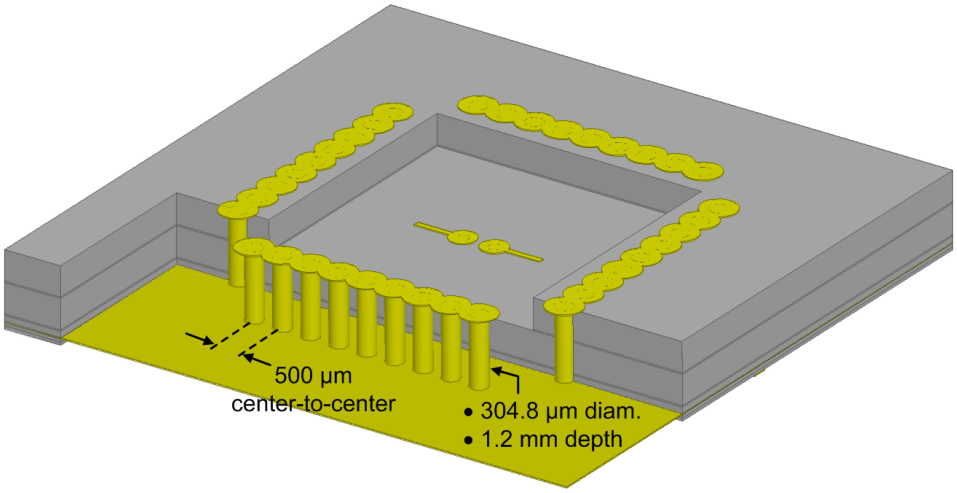

Figure 41: Implementation of a PWC with 4:1 aspect ratio through vias.

vias are mechanically drilled and thus form a hollow cylinder grounded to M4 layer. Each M1-M4 via has 12 mil diameter and the catch pad on M1 has 24 mil diameter. To ensure that the fields radiated from the dipole and its image reinforce at boresight, the 20 mil thick dielectric right above the dipole is removed to form an air-cavity. In fact, without the air-cavity the electric paths followed by the direct and image radiated fields differ from the free space path and this may result in undesired patterns variations. Furthermore, an advantage of the air-cavity is that the dipole does not get loaded with the thick superstrate layer, and the dipole radiates directly into air thus avoiding surface waves excitation and energy dissipation into the lossy superstrate.

Feed Network and Impedance Matching: To prevent coupling from the standing wave fields radiated from microstrip lines and thus radiation patterns distortion, the feed network must be isolated and shielded below the antenna ground plane. It is therefore necessary to have a micro-via hole created with a laser from M3 to M5 and going through a metal void in M4 (See Figure 42). Because the M3-M5 via hole is laser created starting from M5, it has a wide base diameter on M5 (13 mil) and a narrow base diameter on M3 (10.5 mil). The catch pad size on both layers is 21 mil diameter. The metal void in M4 has 30 mil diameter and this leaves enough room to avoid any short circuit between the

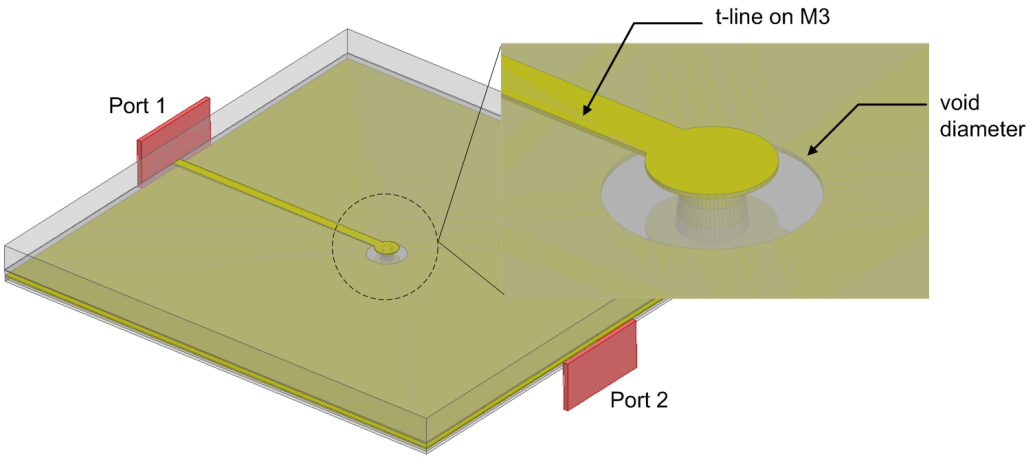

Figure 42: Micro-via transition between layers M3 and M5 with a ground plane void.

micro-via and the ground plane metallizations during the via plating process. This layer-to-layer microstrip line transition was optimized with HFSS to account for reflections occuring through the via transition as well as the large void discontinuity in the ground plane. Figure 43 shows the return and insertion losses for various values of the void diameter. It is clear that at 30 mil diameter, the transition exhibits excellent matching as well as less than 0.5 to 1 dB insertion loss from 53 to 67 GHz, and beyond. The input impedance of the broadside dipole antenna as evaluated from the input of the micro-via transition on layer M5 at resonance is 22.5 Ω. A single section of quarter-wavelength transformer is then utilized to bring the impedance to 50 Ω for matching with any arbitrary 50 Ω device (a mimic for instance). Input impedance matching results are presented later in comparison with measured data.

5.1.2 End-Fire Folded Dipole Radiator

The end-fire antenna must be designed as part of the package for future integration with the previously designed broadside radiator. One may either design a planar Yagi-Uda antenna on layer M5 with a truncated ground plane on M4, or pattern a tapered slot antenna in M4. The former idea is attractive but as it was studied earlier in section 3.1, the structure of that planar Yagi-Uda antenna limits the impedance bandwidth. Besides, the tapered slot

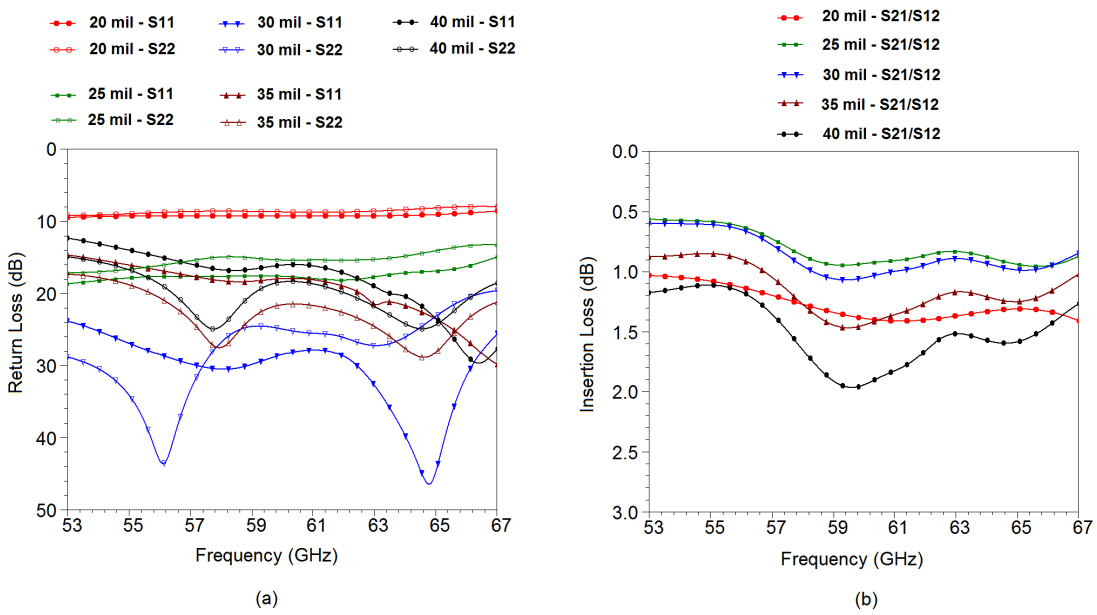

Figure 43: Impedance matching of the micro-via transition between layers M3 and M5 as a function of the void diameter: (a) Return loss; (b) Insertion loss.

antenna introduced in section 3.2, although it occupies a 10 mm $\times$ 10 mm surface area, is unacceptable to integrate with the broadside radiator as it would almost double the size of the package. A more elegant design that consists of a linear array of four folded dipoles constructed in the M4 ground plane is hereby described.

5.1.2.1 End-Fire Half-Wavelength Folded Dipole

Concept and Theory: The asymmetric folded dipole structure shown in Figure 44 is chosen for a couple of reasons: (1) It can be patterned on M4 in the area beyond the PWC and because it is so compact it would extend the actual size of the package by only a small fraction of a wavelength; (2) Compared to a planar end-fire dipole, the asymmetric folded dipole offers the flexibility to match the input impedance of the folded dipole to a high impedance (ideal for array configurations) that is function of the step-up ratio as well as the impedance of the equivalent straight dipole. The folded dipole in this figure may be decomposed into three parts: the asymmetric folded dipole of length l_{dipole} followed by a finite width coplanar strip line of length l_{CPS} and a slot line of gap s_{CPS}. The presence

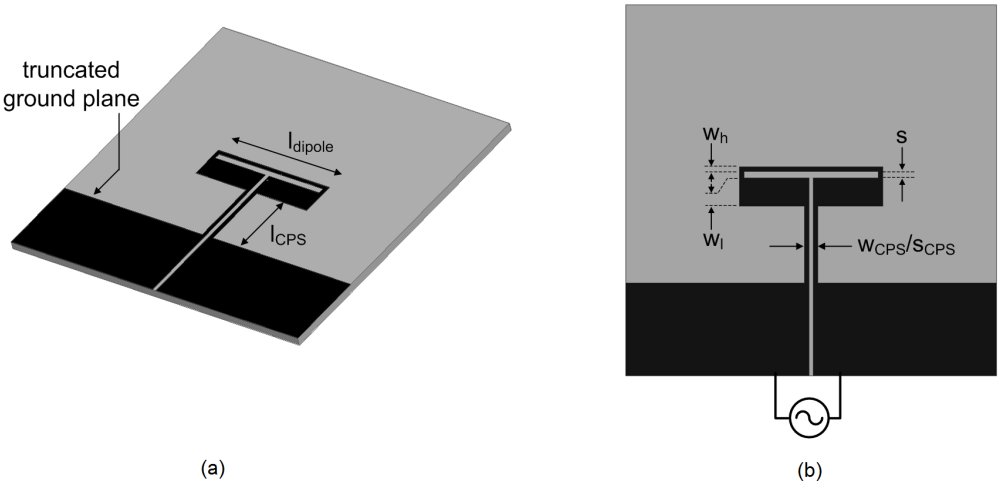

Figure 44: Schematic of a printed asymmetric folded dipole: (a) Perspective view; (b) Planar view.

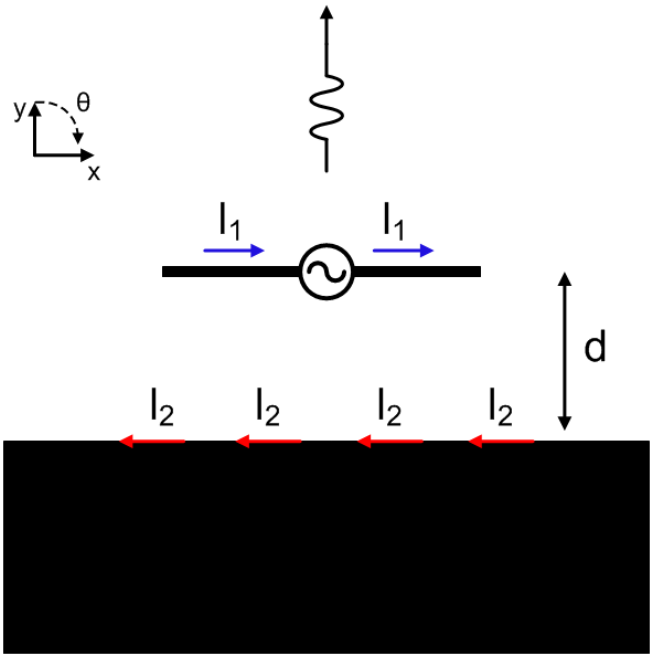

Figure 45: Schematic of a uniplanar end-fire dipole backed with a truncated ground plane.

of a truncated ground plane (that is part of the slot line) at slightly less than one quarter-wavelength from the folded dipole is essential to create an end-fire type of radiation. In fact, the slot line may be seen as an almost continuous ground plane provided that $s_{CPS} \ll \lambda_g$, the guided wavelength. The justification for end-fire radiation is thus found by analyzing

source currents on the dipole and induced currents on the truncated ground plane edge, similar to Elliot's work in [41]. Consider the scenario shown in Figure 45, where the dipole is at a distance d from the ground plane. The time varying voltage source V_1 creates a current I_1 on the source dipole. This current induces a return current flow on the ground plane edges and we denote this current as I_2. The voltage V_1 is thus given by

$$V_1 = Z_{11}I_1 + Z_{12}I_2, \tag{11}$$

where Z_{11} is the self impedance of the dipole and Z_{12} is the mutual impedance between the dipole and the ground plane. Likewise, and because the ground plane provides an RF short circuit, a similar equation relating I_1 and I_2 can be derived and is given by

$$0 = Z_{21}I_1 + Z_{22}I_2. \tag{12}$$

The array factor for this antenna is given by

$$AF(\theta) = 1 + \frac{I_2}{I_1}e^{-\jmath kd\cos\theta} = 1 - \frac{Z_{12}}{Z_{22}}e^{-\jmath kd\cos\theta}, \tag{13}$$

where k is the propagation constant of the surface wave. (13) may also be expressed as a function of the phase delay between $I_1 = |I_1|\,e^{\jmath\phi_1}$ and $I_2 = |I_2|\,e^{\jmath\phi_2}$ and is given by

$$AF(\theta) = 1 + \left|\frac{I_2}{I_1}\right| e^{\jmath(\phi_2-\phi_1-kd\cos\theta)}. \tag{14}$$

To maximize the magnitude of the array factor in the direction $\theta = 0°$, one must satisfy the following condition

$$\phi_2 = \phi_1 + kd = \phi_1 + 2\pi\frac{d}{\lambda_g}. \tag{15}$$

(15) means that to create an end-fire beam at $\theta = 0°$, I_1 must lead I_2 by $kd = 2\pi\frac{d}{\lambda_g}$. One adequate solution occurs when d is slightly less than $\lambda_g/4$. In the previous description, it was assumed that the antenna is in free-space. However, one may further enhance this antenna directivity at end-fire by having it printed on a dielectric slab, where a TE_0 surface wave is intentionally excited to produce radiation simultaneously with the free-space radiation [64]. The following explains how such a surface wave is excited and how it is used to enhance the directivity. A quasi-transverse electromagnetic (TEM) wave is excited in

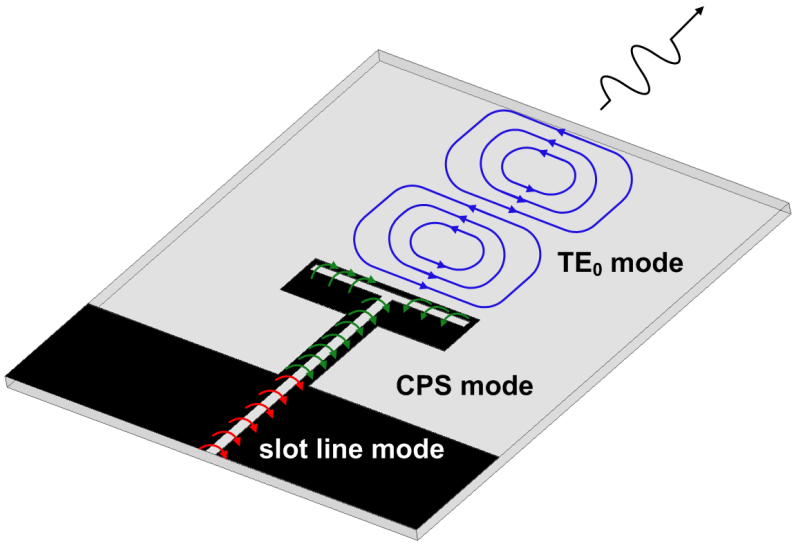

Figure 46: TE_0 dielectric slab surface wave mode excitation mechanism.

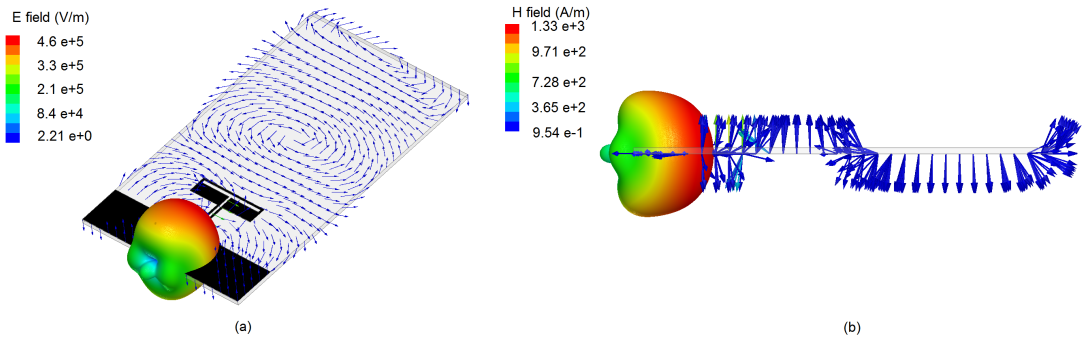

Figure 47: E and H fields distribution of the TE_0 dielectric slab surface wave mode: (a) E field; (b) H field.

the slot line (with a balanced port) and fields transition from a slot line to a finite width coplanar strip line occurs smoothly owing to the continuity of electric and magnetic fields between a slot line and a coplanar strip (CPS) line. Balanced currents on the CPS lines are used to feed a folded dipole that terminated the CPS transmission line. The entire structure composed of the CPS line and the folded dipole is utilized to excite the zero cut-off TE_0 and TM_0 surface wave dielectric slab modes with a higher proportion of TE_0 mode that couples to the CPS mode because both TE_0 and CPS modes electric fields are parallel to the dielectric [15, 40, 49, 69]. Note that because the TM_0 electric field is normal

to the dielectric, it is indeed barely coupled to the CPS mode and it will contribute to a very low level of cross polarization, a desired feature in the design of linearly polarized antennas. Besides, when the surface wave TE_0 mode is excited, it produces both forward ($x \geq 0$) and backward ($x \leq 0$) fields. Because the TE_0 mode is parallel to the dielectric, it undergoes reflection at the ground plane edge that acts as an RF short circuit, that is, a reflector. The backward surface wave propagation is therefore cancelled, and the remaining energy is forward radiated, from which it is inferred that the proposed antenna is an end-fire radiator. Figure 46 illustrates the mechanism of TE_0 dielectric slab surface wave excitation. The radiator is simulated in the HFSS environment and the simulated E and H fields distributions are shown in Figure 47. Note that the TE_0 surface mode E fields are parallel to the dielectric while the H fields are normal to its surface, as expected for a TE_0 dielectric slab mode.

Design for Optimal Directivity and Efficiency: As indicated in Figure 36, the end-fire radiator is to be integrated with the broadside radiator into a single package. A closer view at Figure 37 shows that from a manufacturing standpoint, it is straightfoward to directly pattern the end-fire radiator inside the PWC ground plane (layer M4) supported by the top 4 mil thick LCP substrate. However, the folded dipole must be fed and have input ports accessible from outside the package (that is on layer M5). This requires the folded dipole to be covered on both sides with dielectric layers. In other words, the folded dipole is now substrate embedded. From a radiation point of view, it is worth examining the effect of a single layer and a double layer folded dipole. A single layer design is just as shown in Figure 45 while the double layer utilizes the same dielectric on both sides of the folded dipole. Our previous analysis indicated that the folded dipole excites the TE_0 dielectric slab surface wave mode that enhances radiation at end-fire. The amount of energy transfered from the CPS mode to the surface wave mode is evidently dependent on how strong the coupling is between the two modes. Then, the stronger that coupling the stronger the surface wave energy and the produced end-fire radiation is enhanced. It is well known that at a fixed frequency coupling to surface wave modes increases with slab thickness.

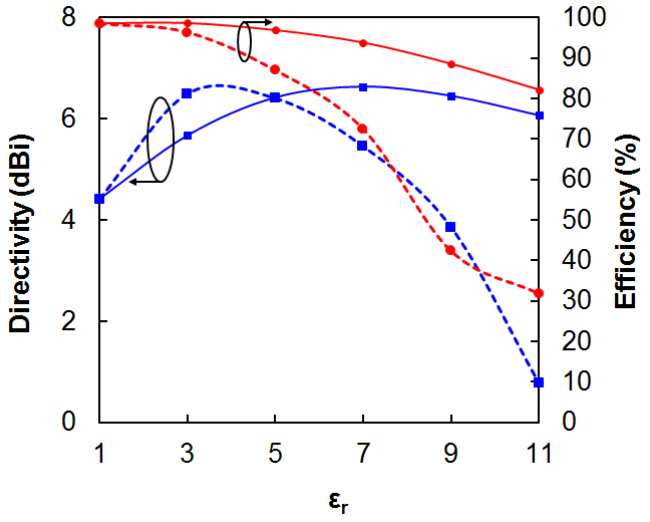

Figure 48: Effects of dielectric slab relative permittivity (or effective thickness) on radiator directivity and efficiency: solid lines correspond to dipole with single slab layer; dotted lines correspond to dipole with slab layers on both sides.

However, if the dielectric becomes too thick the energy actually gets trapped inside the slab and it would be hard to get that energy radiated from the dielectric. Therefore, there is an optimal thickness (at a given frequency and for a given relative dielectric permittivity) to excite enough surface wave energy while allowing this energy to be radiated. The folded dipole length l_{dipole} is set to about $\lambda_g/2$ at 60 GHz and the the dipole to truncated ground spacing l_{CPS} is set to 800 μm, that is slightly less than $\lambda_g/4$ at 60 GHz. This value is very easily optimized using HFSS.

Figure 48 shows the directivity and radiation efficiency plots versus the dielectric relative permittivity for a fixed physical thickness of 4 mil. Note that as ϵ_r increases at a fixed frequency for a fixed physical thickness, the effective thickness (d_{eff}) of the dielectric actually increases. Thus the plots may also be analyzed as a variation with increasing slab thickness. A comparison of the solid and dotted lines suggest that the dielectric slab waves quickly get trapped inside the double layer thick structure but the optimum directivity occurs for a smaller ϵ_r (about 3 in this case) and this corresponds to each slab layer being $0.04\lambda_g$ thick. As ϵ_r increases beyond 3, the directivity of the substrate embedded dipole starts decreasing along with the efficiency. The single dielectric dipole however has a decent

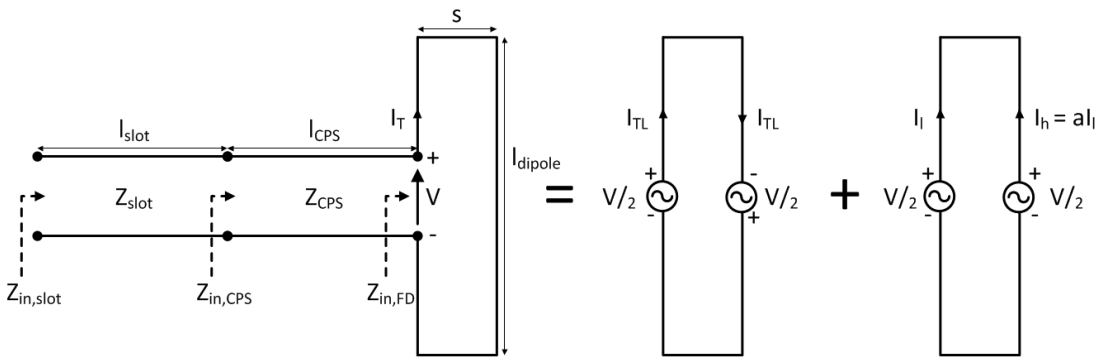

Figure 49: Equivalent transmission line circuit model of the asymmetric folded dipole antenna; V represents the voltage at the input of the folded dipole branch.

directivity but it also starts dropping beyond $\epsilon_r = 7$. In both cases, it is clear though, that the dielectric slab enhances the end-fire directivity for moderate slab thicknesses. For our design, the dielectric chosen is LCP with $\epsilon_r = 3$ and this value matches pretty well with the simulated optimal ϵ_r value and 4 mil dielectric thickness at 60 GHz. For the substrate embedded dipole, a simulated directivity of 6.5 dBi is achieved at end-fire along with 96.3 % efficiency at 60 GHz.

Design for Impedance Matching: The folded dipole serves both as a source of excitation for the dielectric slab mode but also as an impedance transformer. The asymmetric design is chosen in this work because it offers flexibility for impedance matching purpose. Lampe in fact demonstrated that the input impedance of an asymmetric coplanar strip folded dipole depends on three quantities: (1) the impedance of the transmission line mode, (2) the impedance of the dipole mode, and (3) the impedance step-up ratio [63]. Inspired from the work accomplished in [63, 96] and provided that the gap s is much smaller than the guided wavelength in the medium (necessary condition for validity of transmission line model), the equivalent transmission line circuit model of the folded dipole is derived as shown in Figure 49. Note that V represents the voltage at the input of the folded dipole branch. Currents flowing on the folded dipole branches can be decomposed into two currents modes: the transmission line mode and the antenna mode. In the transmission line mode, the folded branches on each side of the source act as shorted coplanar strip lines with

asymmetric width w_l and w_h and length $l_{dipole}/2$. Thus the transmission line impedance at the source reference plane looking into each half branch is given by

$$Z_{TL} = \jmath Z_0 tan\left(\frac{k_0 l_{dipole}}{2}\right), \tag{16}$$

where Z_0 is the characteristic impedance of an asymmetric CPS line of widths w_l and w_h and gap s, k_0 is the propagation constant of the medium. The derivation of Z_0 is found in [63]. The transmission line current I_{TL} is the current flowing through a line with two series reactive impedances Z_{TL} and two series voltage sources $V/2$. Therefore, I_{TL} is given by

$$I_{TL} = \frac{V/2 + V/2}{Z_{TL} + Z_{TL}} = \frac{V}{2Z_{TL}}. \tag{17}$$

On the other hand, in the antenna mode the two parallel branches of width w_l and w_h are closely spaced and have the same potential at the source reference planes. The narrow branch of width w_h carries a current I_h while the wider branch carries a current I_l. Because both branches are fed with the same voltage source V/2 and the narrow line has a higher impedance it is then clear that $I_l \geq I_h$. If $a \leq 1$ defines the impedance ratio between the wide and narrow branches, then $I_h = aI_l$, and the total current flowing in the equivalent single dipole formed by merging both branches is

$$I_D = I_l + I_h = (1+a)I_l = \frac{V/2}{Z_D}. \tag{18}$$

The equivalent dipole is an ordinary dipole of same length l_{dipole} and radius ρ. The derivation of the single dipole input impedance Z_D may be found in [26] but it does not include the proximity effects of the truncated ground plane. The values are however not too much different and the impedance may be further optimized with a full-wave solver. From (17) and (18), the actual current flowing into the the wider branch of the folded dipole is

$$I_T = I_{TL} + I_l = \frac{V}{2Z_{TL}} + \frac{V}{2\left(1+a\right)Z_D}. \tag{19}$$

Therefore, the input impedance $Z_{in,FD}$ of the folded dipole is given by

$$Z_{in,FD} = \frac{V}{I_T} = \frac{2\left(1+a\right)Z_{TL}Z_D}{Z_{TL} + \left(1+a\right)Z_D}. \tag{20}$$

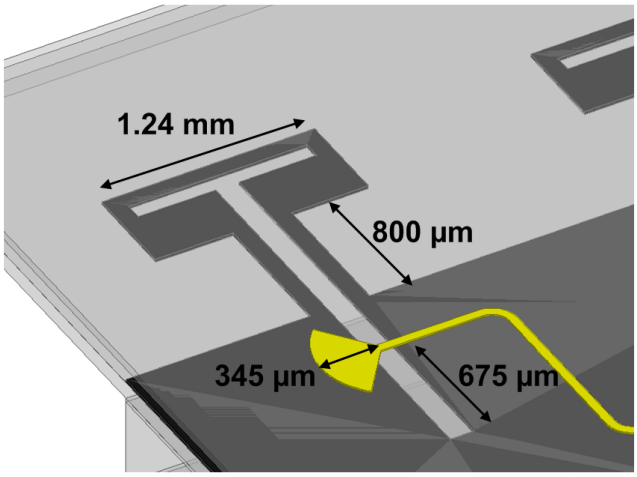

Figure 50: Microstrip-to-slot transition used to provide an external feed on layer M5 for the end-fire radiator.

If the folded dipole is half-wavelength long then from (16) the transmission line impedance Z_{TL} becomes infinite and (20) reduces to

$$Z_{in,FD} = 2\,(1+a)\,Z_D, \tag{21}$$

where $2(1+a)$ is defined as the step-up impedance ratio. For a symmetric folded dipole, $a = 1$ and the folded dipole input impedance is $Z_{in,FD} = 4Z_D$, the well-known step-up impedance ratio of 4. Equation (21) suggests that in fact two quantities may be adjusted to match the asymmetric half-wavelength folded dipole impedance to a desired level. In our case, given that a single folded dipole achieved only 6.5 dBi, it is necessary to have an array of these elements to increase the end-fire directivity. Hence, it is desired to match each element to a high input impedance that will minimize the required number of impedance transformers in the feed network. In fact, only two quarter-wavelength transformers are needed to match the 4-element array to 50 Ω using this approach, instead of six if each element of the array is individually matched to 50 Ω. An ordinary dipole backed with the same truncated ground plane is simulated with HFSS and it has about 64 Ω input impedance.

A target $Z_{in,CPS} = 130$ Ω impedance is chosen to be achieved at the input of the CPS line. Recall that l_{CPS} was set to 800 μm from the previous section. The CPS line impedance

Z_{CPS} may be thus be judiciously chosen to serve as a quarter-wavelength impedance transformer. Inside the medium seen by the folded dipole, the effective wavelength of the coplanar strip line is $\lambda_g = 3.2$ mm (computed with HFSS). To make the radiator resonant at 60 GHz, the dimensions in Figure 44b are optimized as follows: $w_h = 100$ μm, $w_l = 400$ μm, $s = 100$ μm, and $l_{dipole} = 1.24$ mm. A minimum feature size of 50 μm is required by the circuit board manufacturer and these dimensions are compliant. It is apparent that the impedance ratio between the wide and narrow branches is 0.25, thus applying a 2.5 (Equation 21) step-up ratio to the 60 Ω ordinary dipole results into $Z_{in,FD} = 160$ Ω. This impedance is then converted to the desired $Z_{in,CPS} = 130$ Ω through a 145 Ω CPS line ($w_{CPS} = 100$ μm and $s_{CPS} = 140$ μm). Note that the impedance of the slot line following the CPS transformer section is about 130 Ω while keeping the same slot width for both slot and CPS lines. To feed the slot line from layer M5, it then suffices to magnetically couple a microstrip line to the slot line. This type of coupling is a standard technique that requires that about a quarter-wavelength is kept between the open end of the microstrip line and the thin slot line, and between the short end of the slot line and the microstrip line. The width of the microstrip line is 50 μm which makes the line about 100 Ω. This is enough to guarantee a good transition from the slot to the microstrip mode.

5.1.2.2 4 × 1 End-Fire Folded Dipole Array:

Since the folded dipole radiator is substrate embedded, it is interesting to verify how adjacents elements are isolated to mitigate loading of nearby elements in a linear array. In fact, the fields radiated from one element couple easier to the adjacent element inside the dielectric slab than if the antenna is covered with dielectric only from one side. The mutual coupling between two adjacent elements is simulated at 60 GHz with respect to the element-to-element spacing. Figure 51 shows the isolation levels at 60 GHz. The solid line is the isolation of the substrate embedded radiator whereas the dotted line is for the radiator with dielectric only on one side. The element-to-element spacing is chosen to be 2.5 mm. The corresponding isolation for the in-package radiator is 17 dB. When four elements are equally spaced, the peak directivity at end-fire is 10.45 dBi, that is, 4 dB higher than a

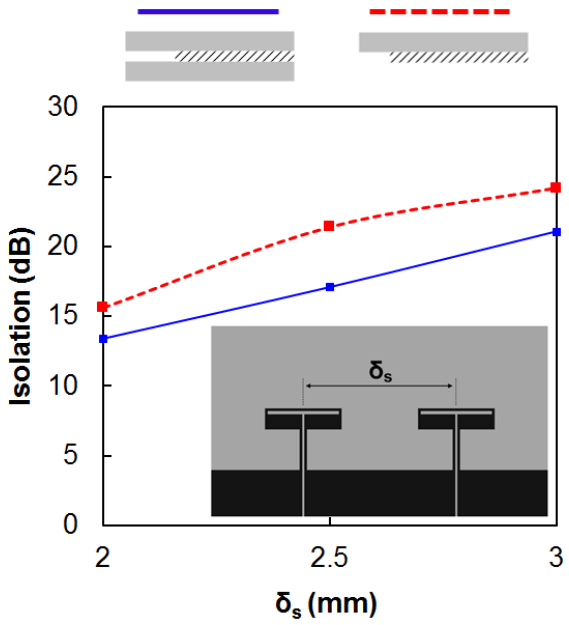

Figure 51: Isolation between two adjacents folded dipole end-fire radiators: the solid line represents the dipole with slabs on both sides; the dotted line represents the dipole with slab only on one side.

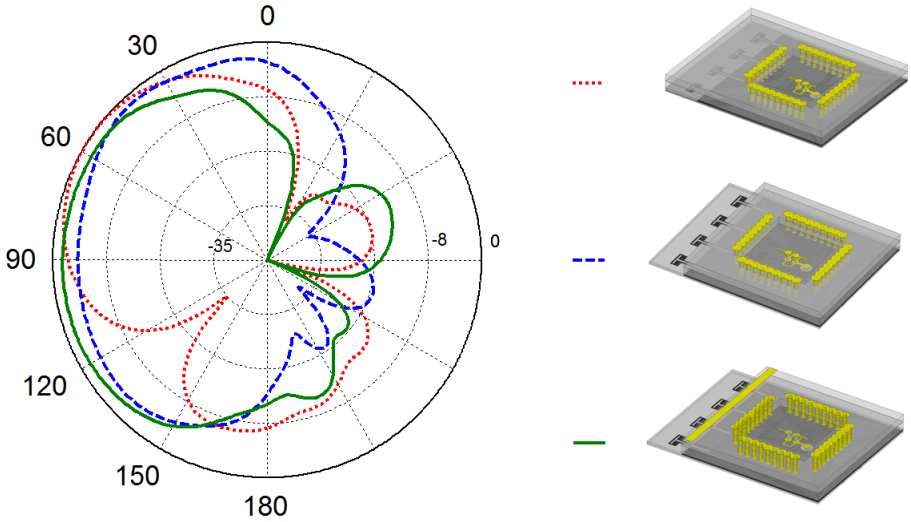

Figure 52: Compensation techniques to correct for the end-fire beam squinting: normalized H plane radiation pattern of the end-fire radiator.

single element.

During the design of the end-fire array, we found that if the top thick dielectric layers between M1 and M3 cover the end-fire array the end-fire beam is squinted toward higher

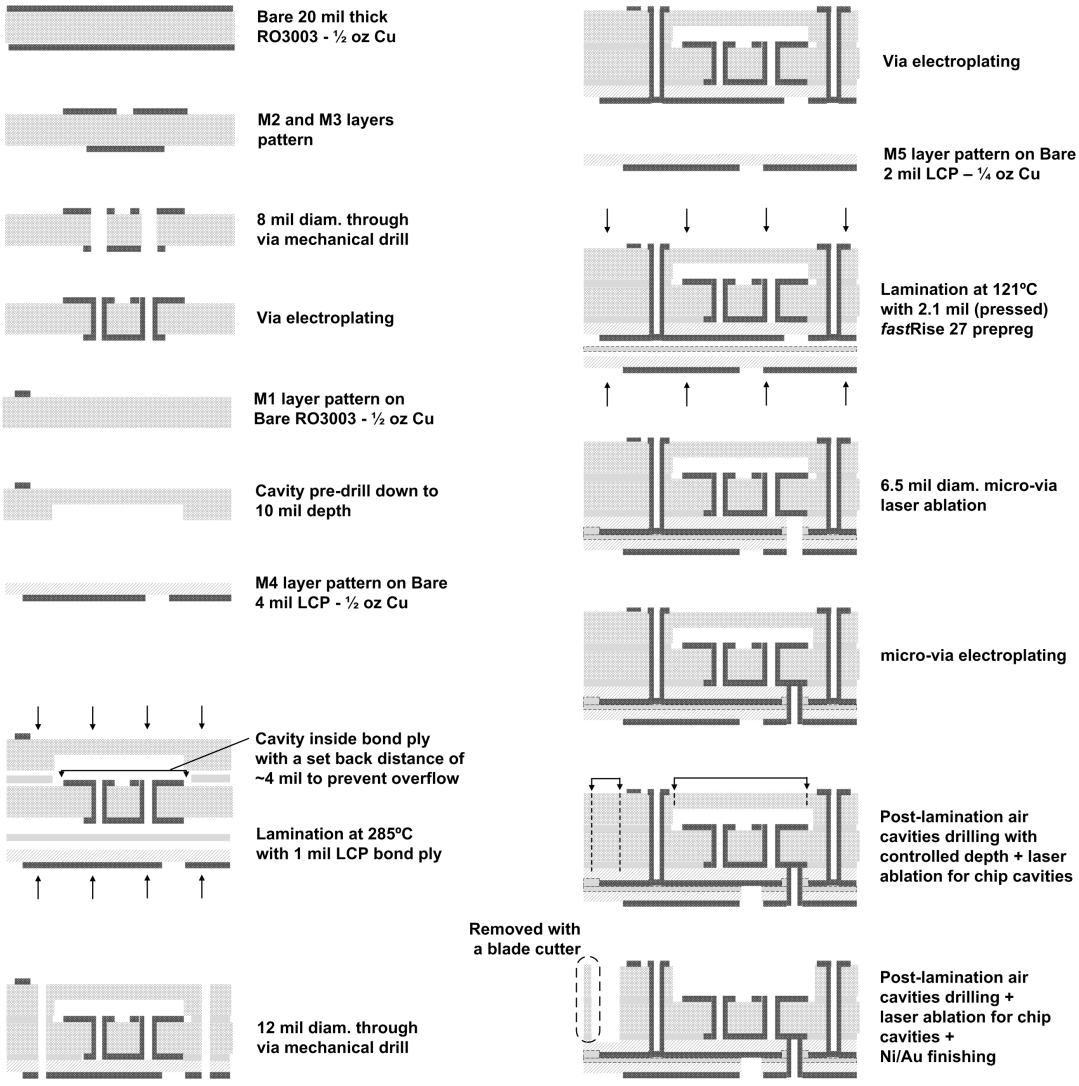

Figure 53: Multilayer integrated antenna fabrication process flow with organic materials.

elevation angles. It is understood in that case that the dieelctric slab energy is stronger in the thicker layers which enhances directivity at higher elevation angles. To compensate for that error, it is suggested to remove after complete lamination the dielectric between M1 and M3 from the area above the end-fire array. In addition to that, a 500 μm wide strip is patterned on top of M1 and this helps to keep the beam pointing at grazing angles ($\theta = 90°$). Figure 52 identifies the effects of each of these design tricks.

5.2 Fabrication of the Integrated Antenna Module

The fabrication process flow is fully described in Figure 53 and it provides all the details of the process. Standard lithography, via processing, cavity processing and lamination techniques that are used by the PCB industry are applied. The circuit manufacturer is Metro Circuits. The main challenge with this process was to define if the air cavities should be drilled before or after complete lamination of the package. A first attempt was given to a pre-lamination drill and LCP being a soft material, it sucked into the air cavities during lamaination due to the high pressure. A second fabrication run was thus required and the air cavities were then opened toward the end, and actually after complete lamination of the full package. Note however that some air cavities were selectively pre-drilled to prevent from damaging the M2 layer. All air cavities drills were done through a controlled depth that was optimized after a few trials. In general, once the right process is defined, the fabrication of the entire package becomes straight-forward and cost-effective as well. When the full fabricated panel is received from the manufacturer, each sample is diced and the piece of material remaining from the air cavity drill above the end-fire radiator is simply removed with a blade cutter.

5.3 Input Impedance Characterization of the Passive Integrated Antenna Module

The integrated package is simulated in the HFSS environment with waveguide ports definitions to excite each antenna input. For return loss and input impedance measurements, a probe station is utilized with a 67 GHz Agilent PNA. The system is calibrated with a SOLT technique using a CS-5 standard substrate and 250 μm GSG probes. The antennas are also mounted on top of a high frequency Rohacell®HF foam that hungs with vacuum succion on a metal chuck. The antenna are however located on the hanging portion of the foam such as to radiate into air. Pieces of mm-wave absorbers are also attached to metallic areas of the probe station to minimize reflections. Figure 54 shows photographs of a fabricated integrated antenna module of MLO package.

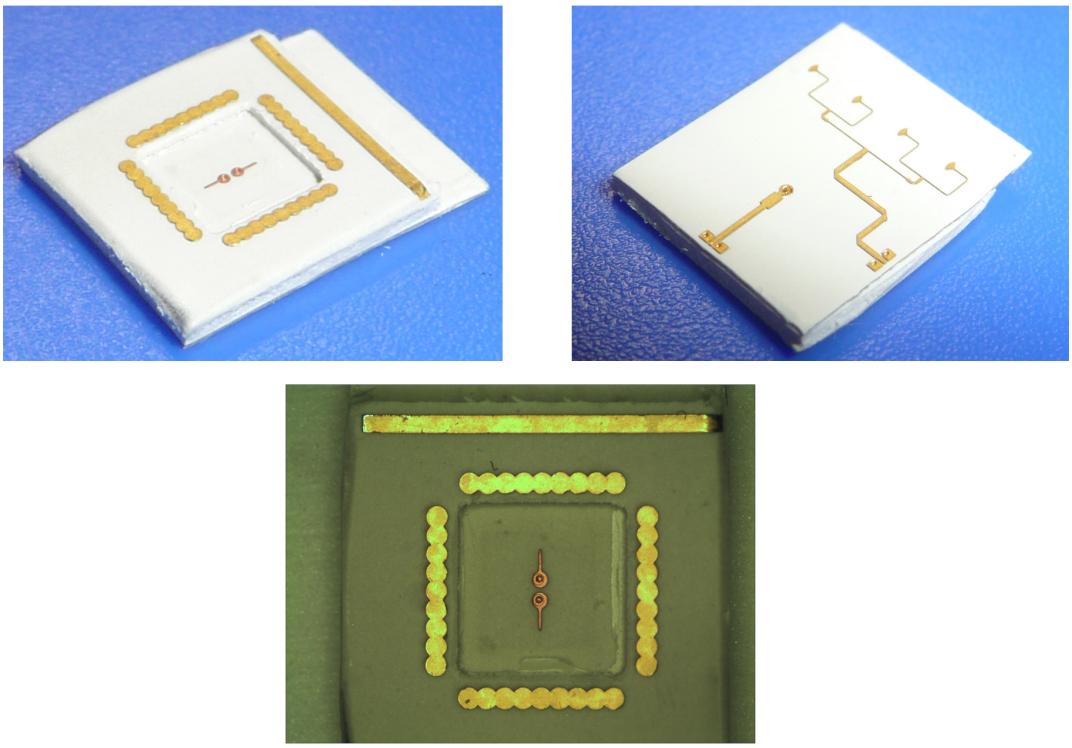

Figure 54: Photograph of the fabricated integrated antenna module on MLO package for return loss and isolation measurements.

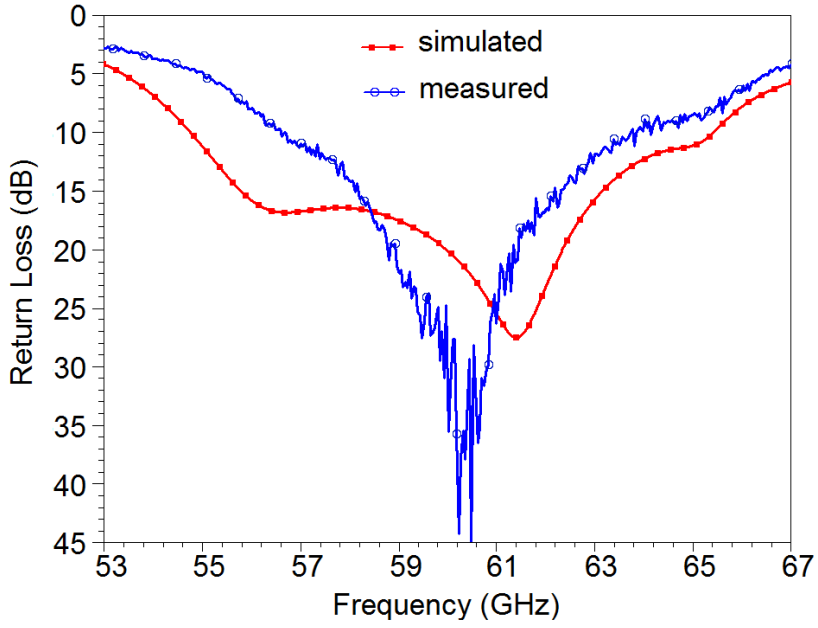

Figure 55: Simulated and measured return loss of the integrated passive broadside radiator.

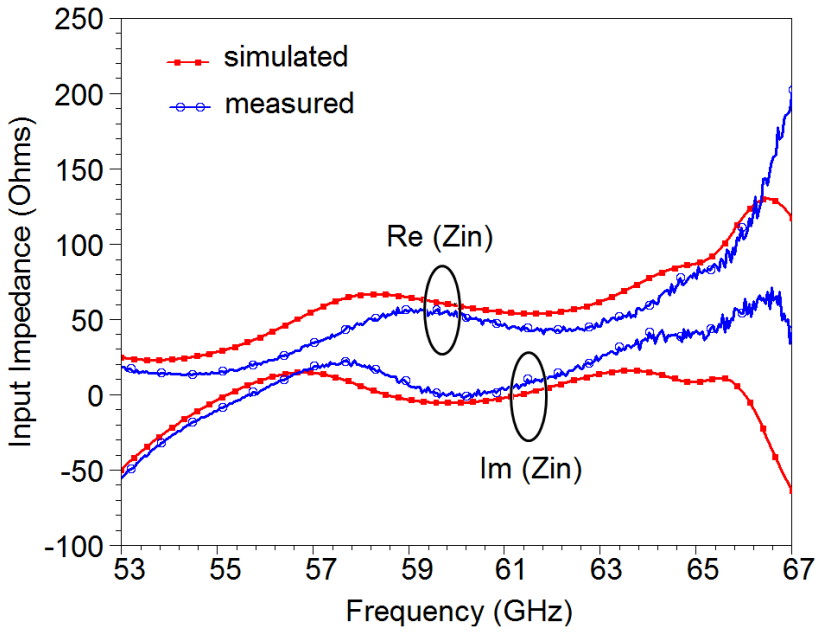

Figure 56: Simulated and measured input impedance of the integrated passive broadside radiator.

5.3.1 Broadside Radiator

Figures 55 and 56 show the simulated and measured input matching of the broadside radiator. A good agreement is observed up to 64 GHz, beyond which the measured data show an anti-resonance that causes the real part of the impedance to increase. However, the broadside radiator is well matched and measured data demonstrate that, with a 10 dB return loss reference, the proposed antenna covers the 56.4 - 64 GHz frequency range. Simulations predict a wider frequency range but due to fabrication tolerances (2 to 4 mil alignment accuracy between layers), the observed discrepancies are within an acceptable error range. Matching of this antenna is in fact sensitive to the M3-M5 micro-via transition.

5.3.2 End-Fire Radiator

Figures 57 and 58 show the simulated and measured input matching of the end-fire radiator. A good agreement is observed from 53 to 67 GHz. Both simulated and measured data demonstrate that, with a 10 dB return loss reference, the proposed antenna covers the 53 - 67 GHz frequency range.

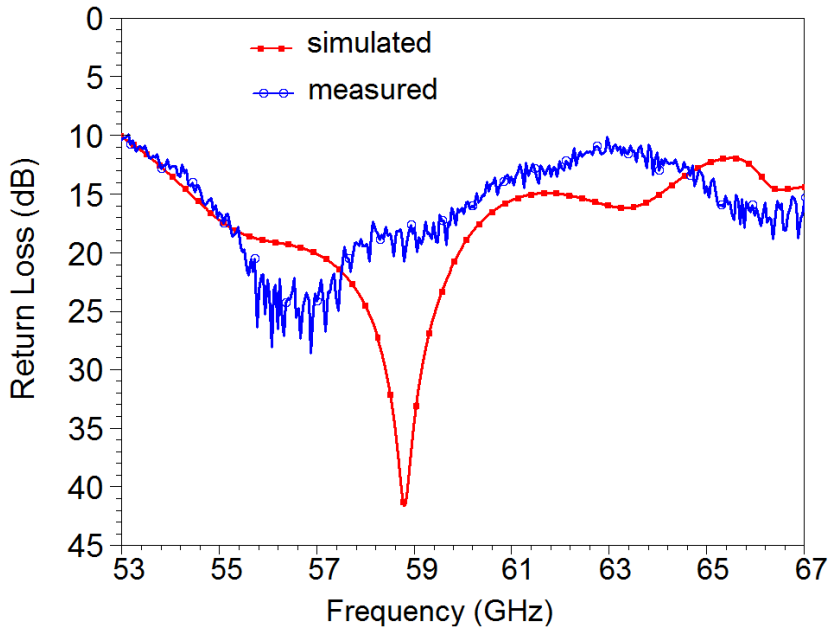

Figure 57: Simulated and measured return loss of the integrated passive end-fire radiator.

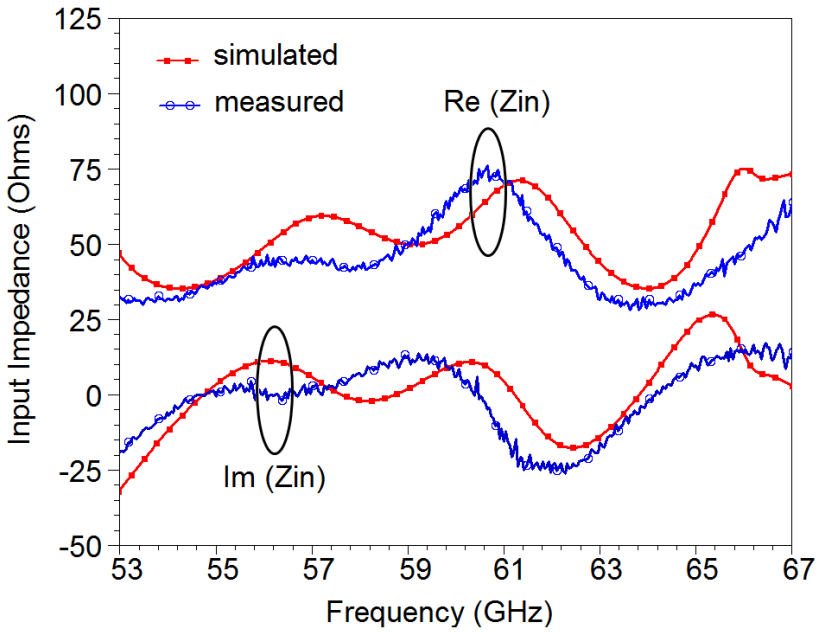

Figure 58: Simulated and measured input impedance of the integrated passive end-fire radiator.

5.3.3 Isolation Between Broadside and End-Fire Radiators

Figure 59 shows the simulated and measured isolation between both radiators. As seen from the measurements, the isolation is excellent and actually almost buried in the noise

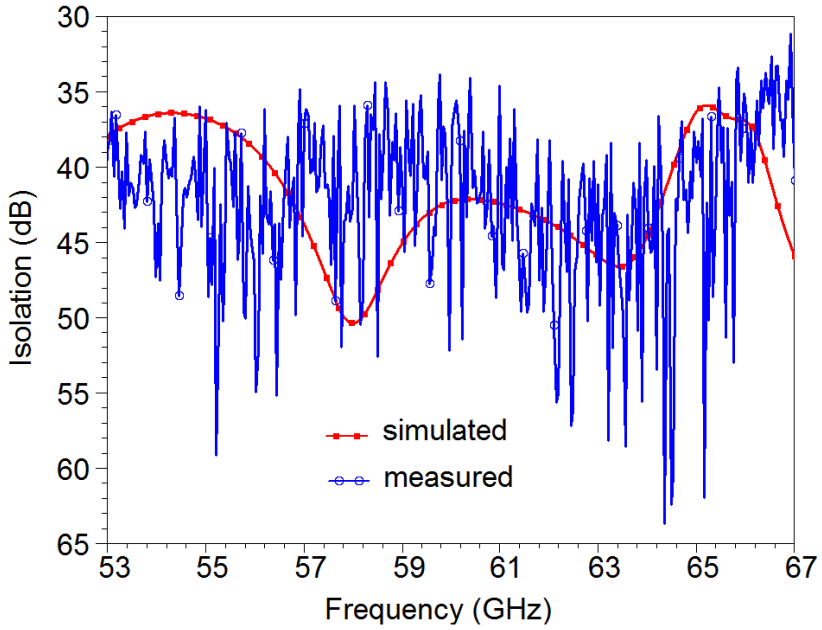

Figure 59: Simulated and measured isolation between the integrated passive broadside and end-fire radiators.

floor of the calibrated instrument. One can claim that greater than 30 dB isolation is achieved between the two antennas in the 53 - 67 GHz range, and the reasons for this are first that they are by design cross polarized to each other and second, they have very low cross polarized radiated fields. Both simulations and measurements strongly support our conclusions.

5.4 Characterization of Active Transmit and Receive Integrated Antenna Modules

5.4.1 Packaged dies performance

Integrated GaAs dies from Hittite are used to demonstrate the module approach proposed in this work. It is neverthless evident that SiGe dies are key for 60-GHz applications. Given that packaging challenges remain similar whether a GaAs or SiGe die is used, the proposed approach is essentially a validation procedure. The ICs used are the HMC-ABH209 power amplifier, the HMC-ALH382 low-noise amplifier and the HMC-SDD112 single pole double throw pin diode switch. By pass capacitors from Presidio Components are utilized to bias the gate and drain supplies. Dies are probed on package with GSG probes in a similar

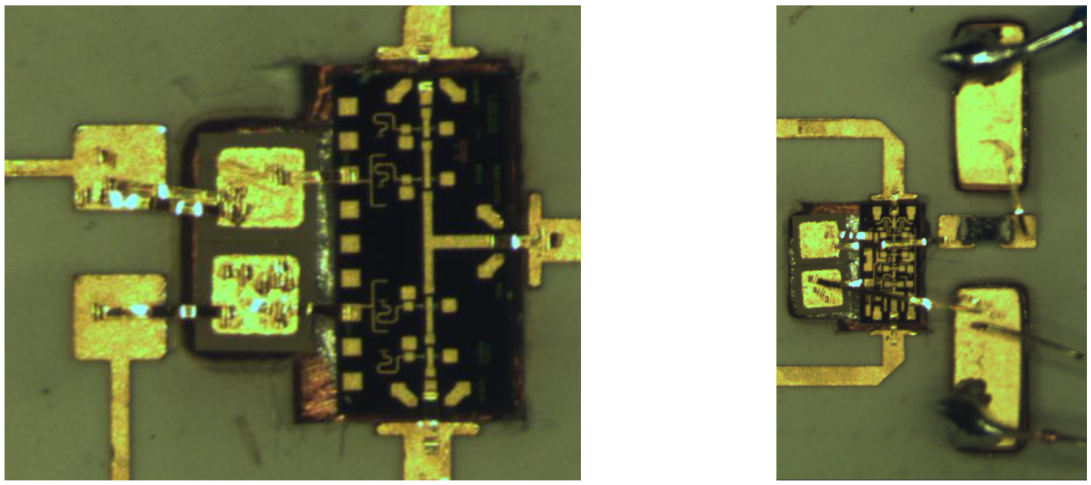

Figure 60: Photograph of packaged dies: (a) SPDT switch with by pass capacitors; (b) LNA with by pass capacitors and a series 10 Ω resistor to the gate 100 pF capacitor.

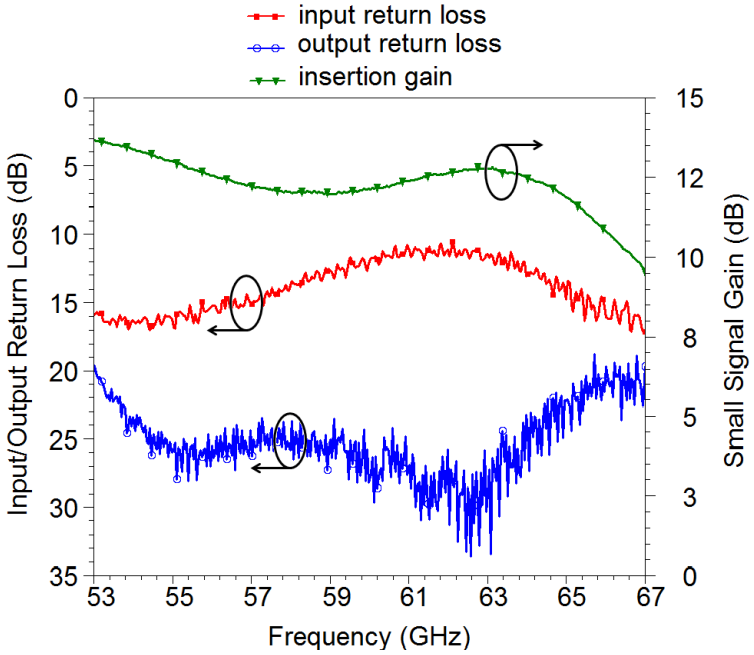

Figure 61: Measured return loss and gain of the packaged power amplifier: V_{gg} = -0.1V, V_{dd} = +5.0V, I_{dd} = 72 mA.

manner to the antenna impedance matching characterization.

Figures 61, 62, and 63 show the measured performance of the packaged dies. Except from the LNA, both the PA and the switch are very well matched in the band of interest. The LNA matching is only good from about 59 GHz to 67 GHz but the on die measurements

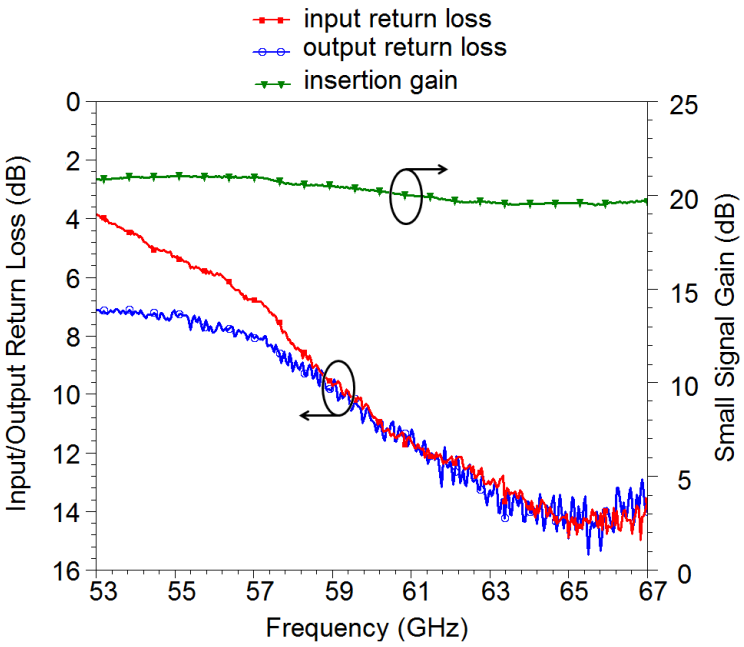

Figure 62: Measured return loss and gain of the packaged low-noise amplifier: V_{gg} = -0.2V, V_{dd} = +2.5V, I_{dd} = 67 mA.

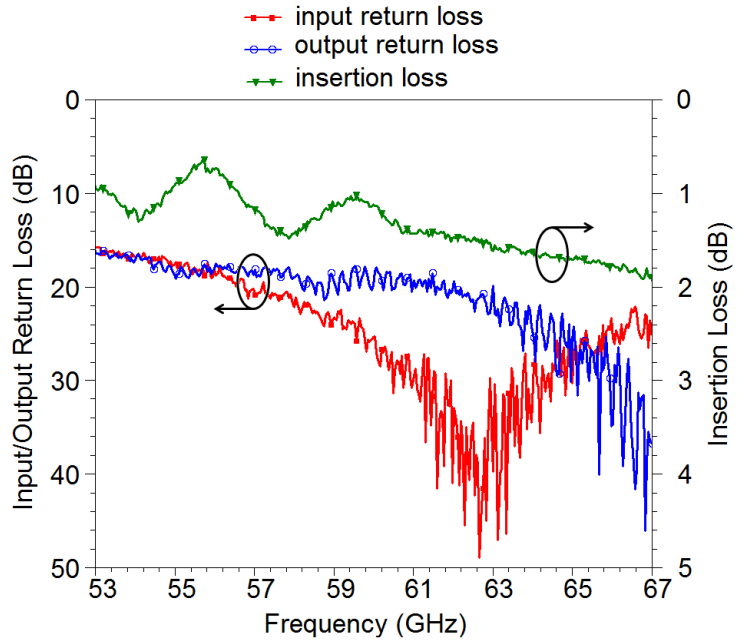

Figure 63: Measured return loss and insertion loss of the packaged single pole double throw switch: V_{dd}^{+} = +5.0V, V_{dd}^{-} = -5.0V, I_{dd} = 24 mA.

shown in the datasheet actually confirm that the die input and output matching is no better than what we observe. Therefore this confirms that our packaging approach utilizing shunt

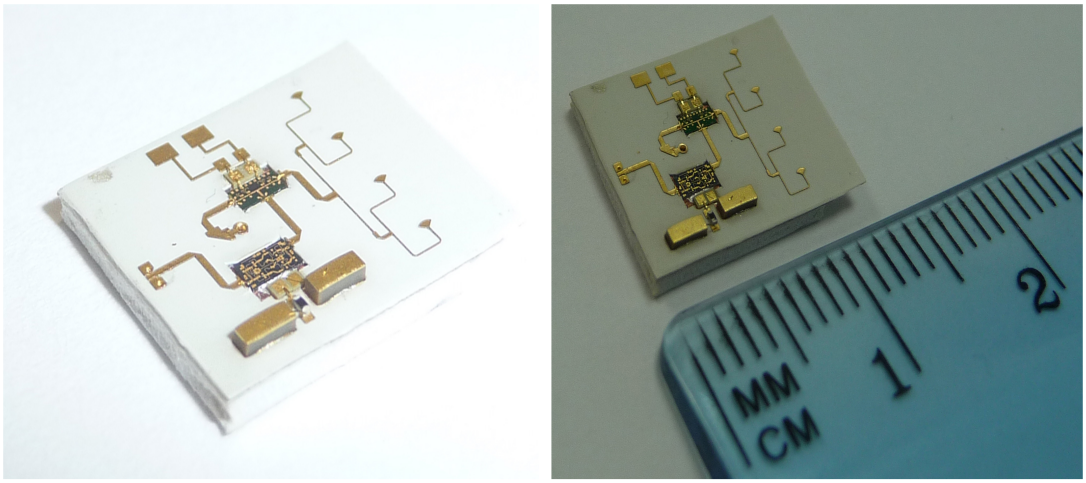

Figure 64: Photograph of the fabricated integrated transmit antenna module on MLO package.

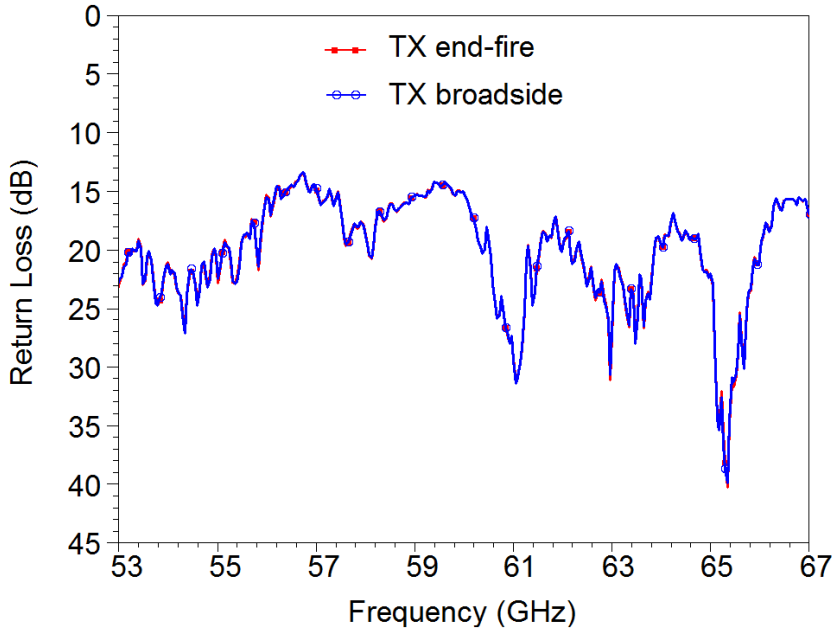

Figure 65: Measured return loss of the packaged transmit antenna module: (PA) V_{gg} = -0.1V, V_{dd} = +5.0V, I_{dd} = 72 mA; (SPDT) V_{dd}^{+} = +5.0V, V_{dd}^{-} = -5.0V, I_{dd} = 24 mA.

stubs to compensate for the parasitic inductance from the ribbon bonds is valid. This also confirms that our modeling approach to predict the parasitics effects is useful.

5.4.2 Transmit Antenna Module

Figure 64 shows a photograph of the fabricated transmit antenna module on MLO package. The antenna module is capable of switching between the end-fire and the broadside beams by controlling an SPDT switch cavity recessed on the backside of the package. A power amplifier is integrated as well to enhance the transmit antenna gain. The active circuitry bias network is designed on layer M5 along with the RF access lines. This package design is such that the broadside radiator is shielded from the other low frequency or high frequency signals owing to the ground plane in layer M4. The end-fire radiator is also decoupled from other low and high frequency signals owing to the reflective nature of the truncated ground plane to the TE_0 radiating mode. Figure 65 shows the return loss of the packaged transmit antenna module. Switching between either of the antenna states maintains the module matched over the 53 - 67 GHz range.

Figure 66 shows the antenna radiation pattern setup that we developed in our research group at Georgia Tech. It is composed of a standard gain horn antenna that rotates in a constant radius (60 cm) around the axis of a motor. The antenna under test is probed with a GSG access probe and thus requires to be carefully mounted on a high frequency Rohacell®HF foam. Four sheets of foam are utilized to make it hard as these foam materials brake very easily. Then, the foam is suspended onto a card board which is mounted to a metal plate. The metal plate (or chuck) is used to hold the magnetized probe. As one may expect, probing the antenna from top forces the broadside radiator to radiate through the foam material. To account for the loss of the foam, we calibrated the system with two standard gain horn antennas and had the foam placed in between. This should roughly compensate for the dielectric loss of the foam. The end-fire radiator also radiates through the foam in one portion of its pattern. One shall notice that it is quite challenging to prevent the card board, metal chuck, and metals on the probing system from interfering with the fields radiated from the rotating horn. This may generate some discrepancies in measurements.

Figure 67 show the simulated and measured radiation patterns at 60 GHz of the packaged transmit antenna module in broadside radiation mode. Simulated passive antenna

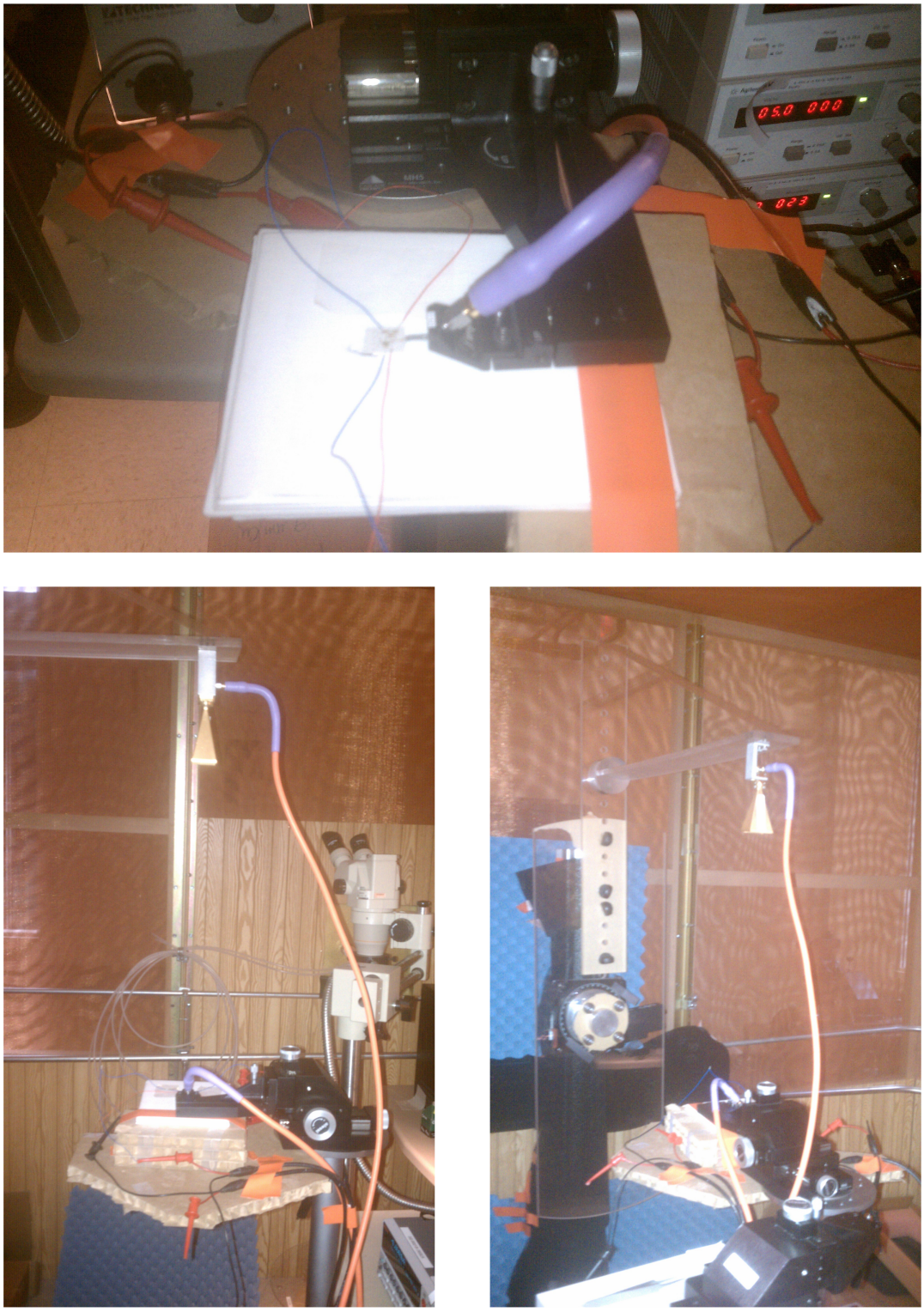

Figure 66: Photographs of the antenna pattern measurement setup belonging to the MircTech group at Georgia Tech.

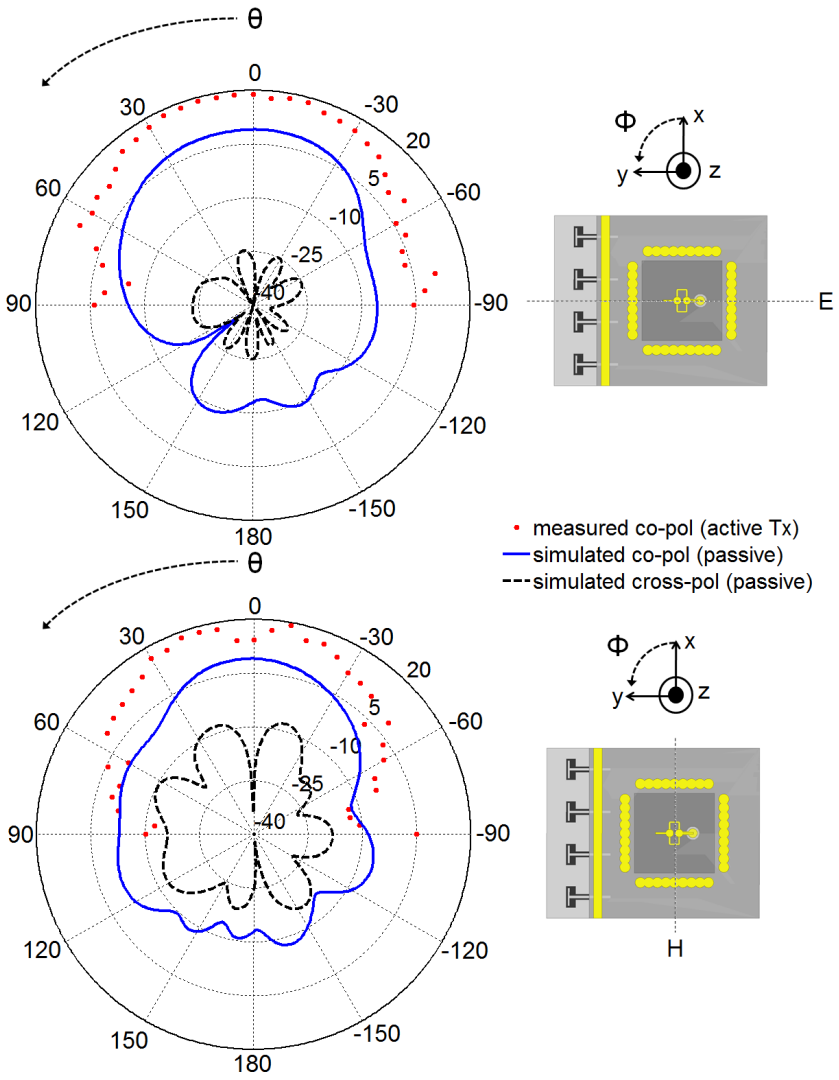

Figure 67: Simulated and measured radiation patterns at 60 GHz of the packaged transmit antenna module in broadside radiation mode: (PA) V_{gg} = -0.1V, V_{dd} = +5.0V, I_{dd} = 72 mA; (SPDT) V_{dd}^{+} = +5.0V, V_{dd}^{-} = -5.0V, I_{dd} = 24 mA.

and measured active antenna data are in good agreement. The simulated and measured boresight gains are 9.04 dBi and 19.25 dBi respectively. To estimate the passive antenna gain from the measured data, we subtract the 12 dB PA gain (at 60 GHz), and compensate for the 1.4 dB loss of the SPDT switch (at 60 GHz). This roughly gives us 19.25-12+1.4 = 8.65 dBi. We did not account for the ribbon bonds losses therefore, we can expect both simulated and measured passive antennas gain to match very well. Figure 68 shows the simulated and measured radiation patterns at 60 GHz of the packaged transmit antenna

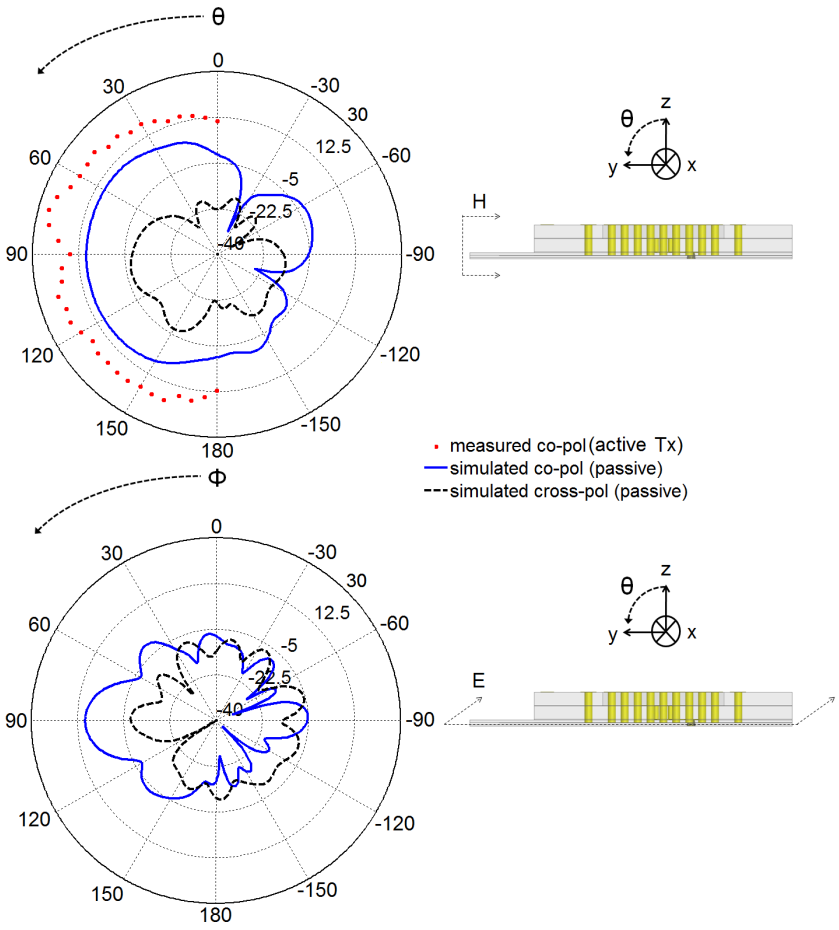

Figure 68: Simulated and measured radiation patterns at 60 GHz of the packaged transmit antenna module in end-fire radiation mode: (PA) V_{gg} = -0.1V, V_{dd} = +5.0V, I_{dd} = 72 mA; (SPDT) V_{dd}^{+} = +5.0V, V_{dd}^{-} = -5.0V, I_{dd} = 24 mA.

module in end-fire radiation mode. We noticed a gain drop of about 7 dB at end-fire but this is very localized, and in fact five degrees away, the gain rises again to a meaningful level. To measure the H plane end-fire pattern with this setup, one has to scan the horn facing the probing system and risks of metal reflections exist in that case. The broadside pattern measurement is not as sensitive to that because most of the energy is radiated downward such that the horn essentially picks up the energy radiated from the antenna. Beyond the angular region where this discrepancy occurs, the measured H plane beam agrees pretty well with the simulated one. The achieved transmit peak gain is 26.11 dBi at 60 GHz and slightly above the end-fire direction. Again, the end-fire radiator is expected to have about 9.64 dBi gain at end-fire (simulated) but there is a gain offset due to the ripple. We could

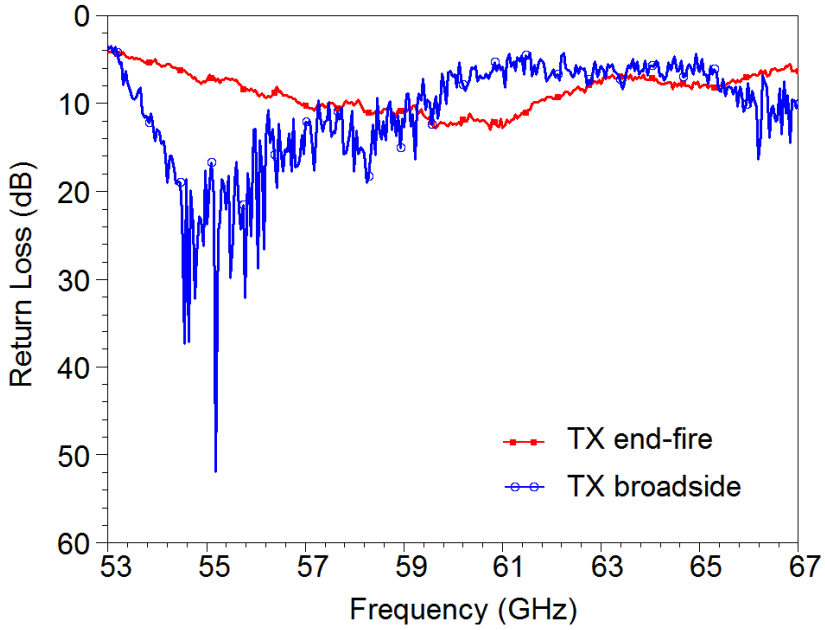

Figure 69: Measured return loss of the packaged receive antenna module: (LNA) V_{gg} = -0.2V, V_{dd} = +2.5V, I_{dd} = 67 mA; (SPDT) V_{dd}^{+} = +5.0V, V_{dd}^{-} = -5.0V, I_{dd} = 24 mA.

not measure the E plane pattern because of some limitations due to the setup. In fact, one would have to mount the antenna under test and the probe vertically to achieve this measurement.

5.4.3 Receive Antenna Module

Figure 69 shows the return loss of the packaged receive antenna module. The impedance looking at the output of the receiver is not as well matched and this may stem from the LNA output port mismatch.

Figures 70 and 71 show the same patterns at 60 GHz but for the receive antenna module. The LNA has a higher gain (20 dB) than the PA, and this results in a total receive antenna gain of 27.98 dBi at boresight and 33.39 dBi at end-fire.

Figure 72 shows the frequency variations of the measured peak gains for both transmit and receive antenna modules. The band of interest is 57 to 66 GHz. The transmit antenna module peak gain varies between 17 and 21 dBi in the broadside direction, and between 23.6 and 29.1 dBi in the end-fire direction. The receive antenna module peak gain varies between 23.8 and 31.7 dBi in the broadside direction, and between 31.2 and 38.9 dBi in the

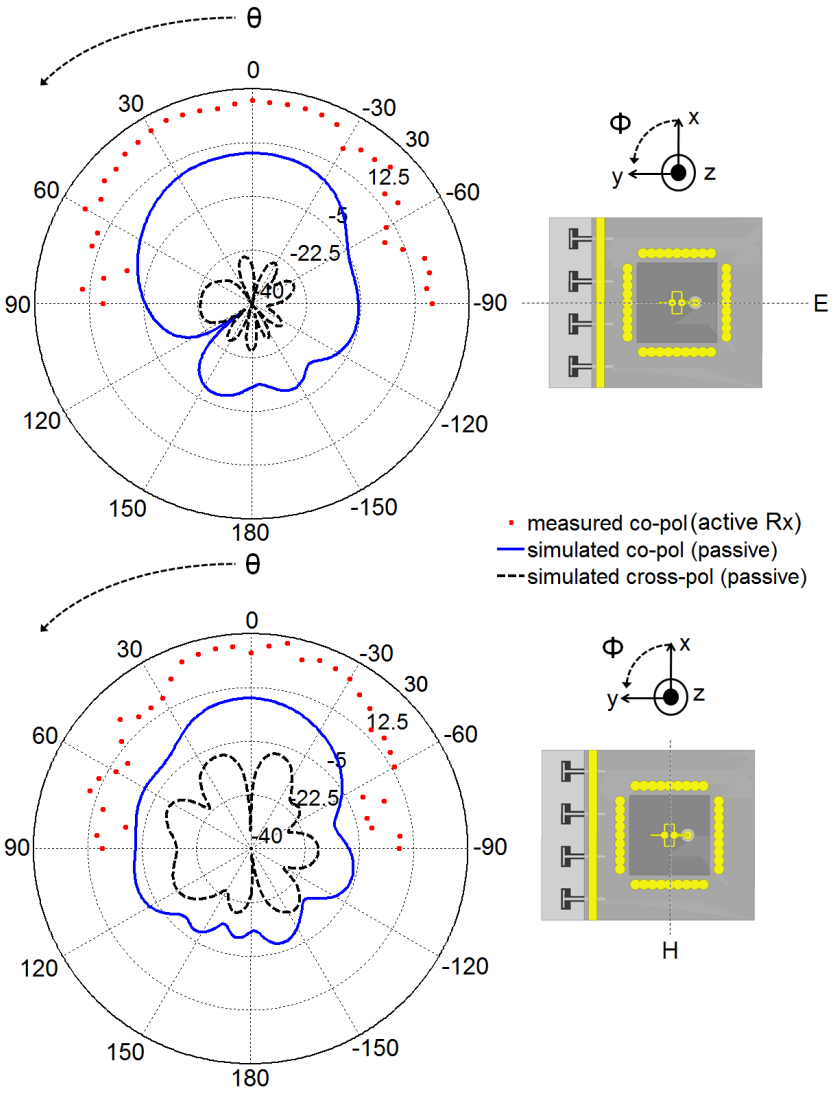

Figure 70: Simulated and measured radiation patterns at 60 GHz of the packaged receive antenna module in broadside radiation mode: (LNA) V_{gg} = -0.2V, V_{dd} = +2.5V, I_{dd} = 67 mA; (SPDT) V_{dd}^{+} = +5.0V, V_{dd}^{-} = -5.0V, I_{dd} = 24 mA.

end-fire direction.

5.5 Passive Antenna Module with Simultaneous Broadside and End-Fire Radiation

The proposed integrated antenna module may also be utilized to simultaneously generate both end-fire and broadside beams. To realize this functionality, the SPDT switch is now replaced with either a T-junction or a wilkinson power divider. The main drawback of a T-junction is that the output ports are not isolated so a leakage signal may appear on one of

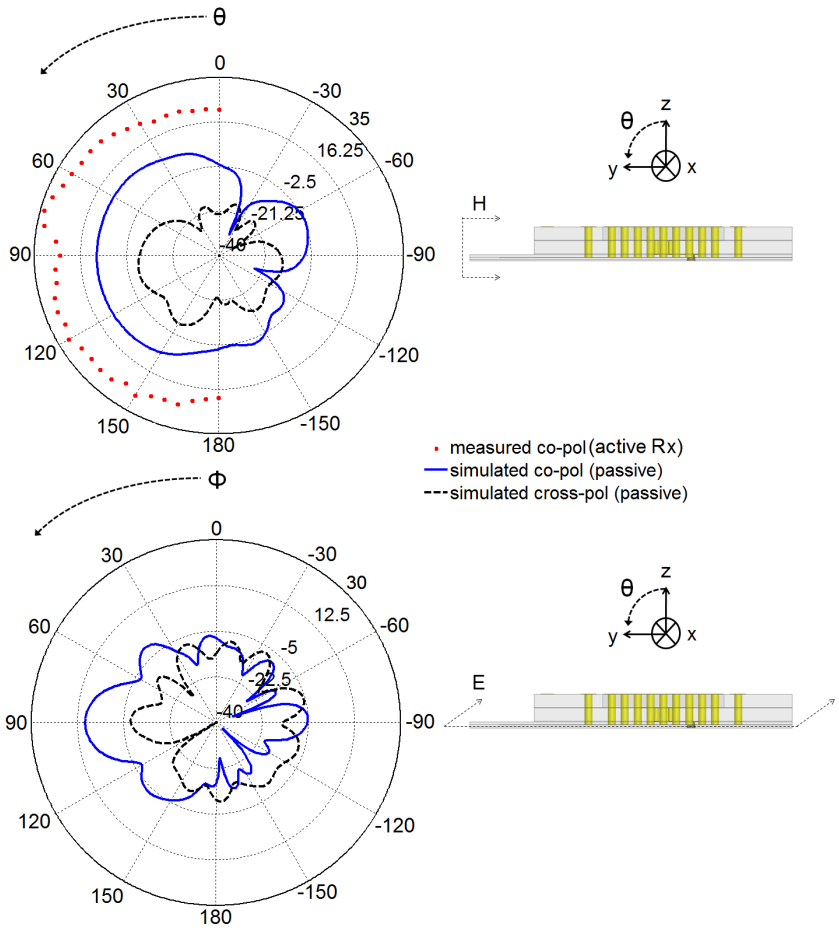

Figure 71: Simulated and measured radiation patterns at 60 GHz of the packaged receive antenna module in end-fire radiation mode: (LNA) V_{gg} = -0.2V, V_{dd} = +2.5V, I_{dd} = 67 mA; (SPDT) V_{dd}^{+} = +5.0V, V_{dd}^{-} = -5.0V, I_{dd} = 24 mA.

the output ports. A wilkinson divider solves this problem with the use of a 100 Ω resistance between the outputs.

5.5.1 Wilkinson Divider Design and Fabrication

In this work, the 100 Ω resistor is created by patterning a Nickel/Phosphorus (NiP) alloy with 50 Ω/□ sheet resistance. Rogers supplies LCP with a thin layer of NiP below 1/2 oz Cu that is laminated to the LCP material. A four-step process was developed to fabricate the wilkinson circuit with the NiP resistor in our cleanroom facility at Georgia Tech.

1. Selectively electroplate 8-10 μm Au pads on top of the Cu to provide adequate adhesion condition for ribbon bonds during assembly of the wilkinson chips with the

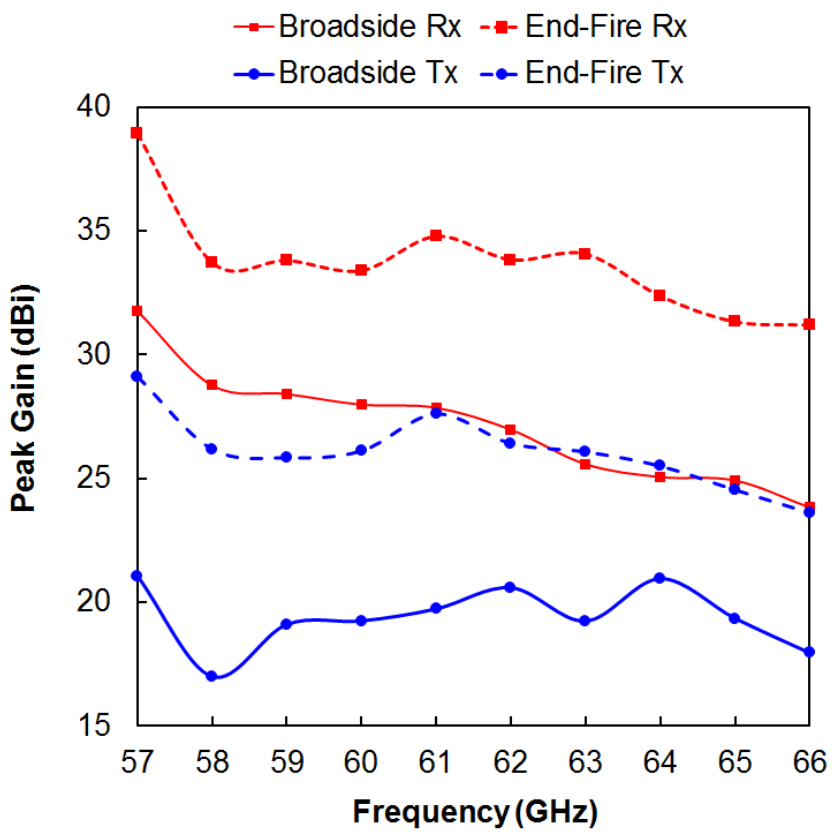

Figure 72: Measured peak gains of the integrated transmit and receive antenna module on MLO package: (PA) V_{gg} = -0.1V, V_{dd} = +5.0V, I_{dd} = 72 mA; (LNA) V_{gg} = -0.2V, V_{dd} = +2.5V, I_{dd} = 67 mA; (SPDT) V_{dd}^{+} = +5.0V, V_{dd}^{-} = -5.0V, I_{dd} = 24 mA.

antenna package. The detailed fabrication process for creating this pads is provided in the appendix.

2. Use a clear field mask with a positive photoresist to pattern the Cu of the wilkinson circuit. A solution of 30 % ferric chloride warmed up to 45 °C is used to etch the Cu.

3. When the Cu is etched, the underlying NiP (a thin gray color layer) must be removed. The wafer is then dipped into a solution containing 250 grams per liter of copper sulfate pentahydrate and 3 to 5 milliliters pre liter of sulfuric acid at 90 °C, as recommended by Ohmega Technologies Inc. the developer of NiP-based embedded resistor technologies. It typically takes less than five minutes for the NiP alloy to strip in an agitated solution.

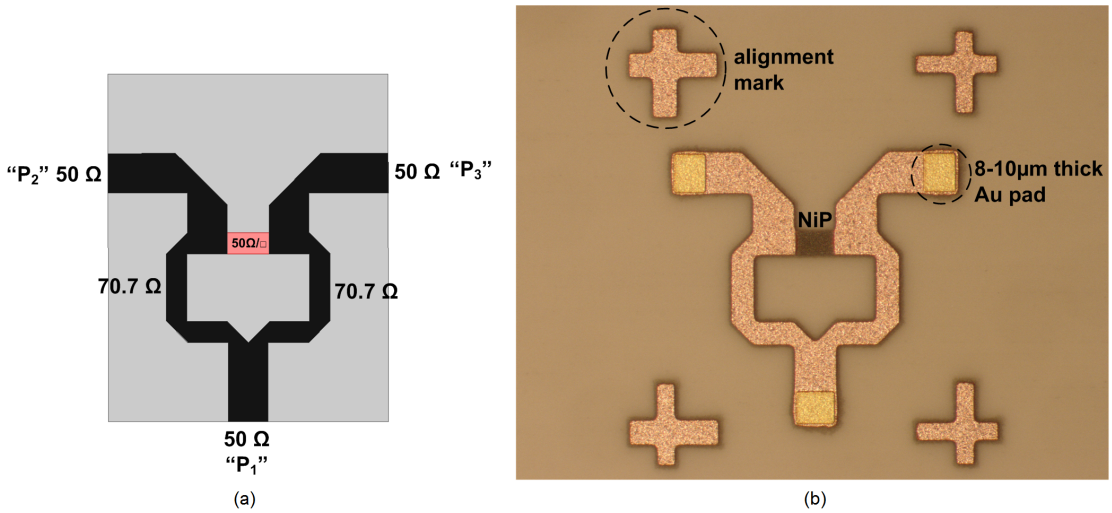

Figure 73: Design structure and photograph of the fabricated wilkinson power divider on a 4 mil thick LCP substrate.

4. The next step requires to selectivey pattern the resistors with a dark field mask and a positive photoresist. After selectively developing the photoresist, the wafer is dipped into a solution of alkaline ammoniacal Cu etchant (UltraEtch FL) that selectively etches Cu but has a slow attack rate on the NiP alloy. Thus, Cu on top of the resistive material is removed at the location of the 100 Ω resistor. Care must be taken at this step because the alkaline etchant still etches the NiP material although at a much slower rate than Cu.

Figure 73b shows a photograph of the fabricated circuit. Alignment marks are used for precision dicing of the wilkinson circuit. The circuits are manufactured on a 5 cm × 3cm wafer to accommodate multiple samples. The simulated S-parameters of the designed wilkinson divider are shown in Figure 74. Better than 20 dB isolation is achieved between the two output ports and this design results in less than 0.4 dB insertion loss.

5.5.2 Characterization of the Packaged Simultaneous Beam Antenna Module

The wilkinson divider chips are mounted inside recessed cavities just as the GaAs chips. Since the pad traces are wide enough to accommodate two 3 mil wide ribbon bonds, it is preferred here to use two parallel ribbons instead of a single one (see Figure 75). In fact, a single ribbon requires the addition of compensation stubs. In this case, one can realize

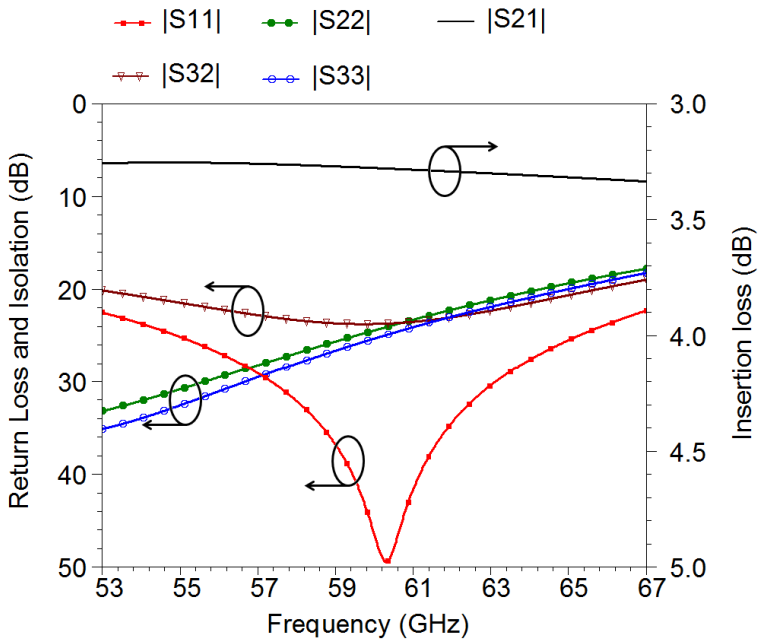

Figure 74: Simulated magnitude of S-parameters of the wilkinson power divider.

from Figure 76 that when the bonding pads allow for it two parallel ribbons are enough to maintain a good matching. In fact, both solutions result in a good matching within 56 - 64.5 GHz. The radiation patterns and gains for these antennas were not measured at the time this dissertation was submitted, but it is evident that the radiated power will drop by about 3.5-4 dB: (1) 3 dB because only half power is now injected into each radiator and (2) about 0.5-1 dB to account for the insertion of the divider.

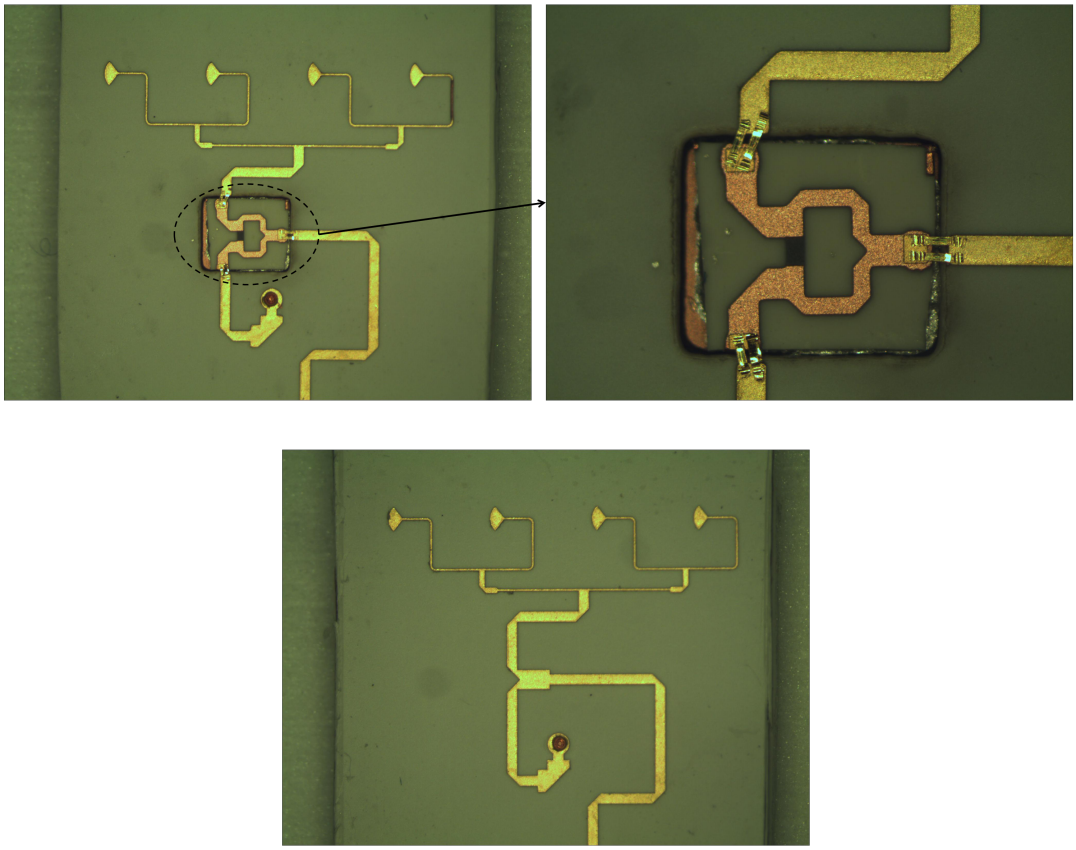

Figure 75: Photograph of the fabricated antenna package module integrated with a wilkinson power divider or a regular T-junction.

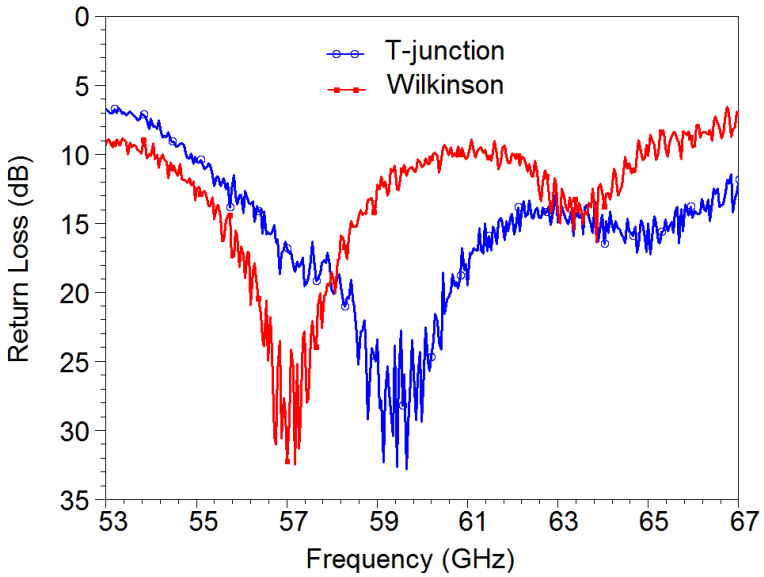

Figure 76: Measured return loss of the simultaneous beam antenna module with a wilkinson power divider or a regular T-junction.

CHAPTER 6

LOCATION SPECIFIC COVERAGE WITH WIRELESS PLATFORM INTEGRATED 60-GHZ ANTENNA SYSTEMS

Multi-gigabit short-range wireless communications for the consumer market is becoming a reality with the recent advancements in 60-GHz integrated system technologies. This fast-growing technology with unlicensed broadband frequency range shows tremendous potential for integration with most consumer electronic devices such as smartphones, tablets, e-books, netbooks and laptop computers [10, 11]. 60−GHz wireless network environments are extremely dense, and thus link reliability and robustness in such environments will critically depend on the ability of the antenna systems to provide effective coverage between different nodes. In the consumer electronics industry, aesthetic and packaging reasons have forced designers to embed antennas inside the host chassis, as opposed to the older, external monopole type of antenna approach.

Various antenna system integration with the platform chassis has been extensively studied using measurement as well as modeling approaches, starting with AM and FM antennas for automobiles ([13, 68]), followed by VHF antennas for civil aircrafts ([27, 29, 74]), and more recently GPS, GSM, Bluetooth, UMTS, UWB and Wi-Fi antennas for mobile platforms [35, 47, 51, 59, 65, 98, 106]. The behavior of internal antennas inside electrically small chassis, resonant chassis, and electrically large chassis has been characterized up to 10 GHz using different modeling approaches such as the geometrical optics (GO), the physical optics (PO), the finite difference time domain (FDTD) technique, the boundary element method (BEM), the finite element method (FEM), or integral equation (IE) formulations of the electric and magnetic fields. Most of these methods are implemented in commercial software packages such as FEKO, NEC, HFSS, and CST [1, 3, 4, 8]. The chassis integration of 60-GHz antennas can be categorized as an electrically large problem because of the very small wavelength compared to the typical wireless platform sizes. For such problems, there

is a common understanding that, at low frequencies, internal antenna characteristics are mainly affected by objects that obstruct the path of the rays emanating from the antenna element. However, this is yet to be verified and demonstrated at 60 GHz. Moreover, some studies recently conducted with 60-GHz antennas in proximity of plastic cover materials showed that small size discontinuities such as thin cover edges can significantly deteriorate the antenna performance due to space wave diffraction [16,17]. This behavior has been less significant at low frequencies because the same cover edges are electrically small and thus less apparent, if not invisible at those frequencies. This emphasizes the necessity to account for the effects of small size features composing the geometry of platform environments at 60 GHz.

For the first time, a comprehensive analysis of internal 60-GHz antenna radiation characteristics in a wireless platform environment is investigated. In this work, a laptop computer is utilized as the host platform for embedded 60-GHz antennas. The laptop chassis modeling with the specific antenna locations is described. A review of some antennas used for the experiement is provided for reference. Thereafter, the radiation performance of these antennas mounted inside the laptop computer chassis is evaluated. The last part of this chapter is devoted to discuss the major results from this study and their direct implications in the design of wireless platform integrated 60-GHz antennas.

6.1 Wireless Platform Chassis Modeling

It is necessary to mention that modeling of real-life internal antennas requires the exact model constructed by the platform chassis manufacturer. Failing to use such a model may affect simulations accuracy. In this work, however, the entire laptop chassis was created from scratch in the HFSS graphics modeler because the exact model from the manufacturer was not available. Differences between the model and the real laptop are carefully emphasized. A sensitivity study to the chassis environment is carried out later in this work to determine the pertinence of chassis structural details in the design of 60−GHz internal antennas.

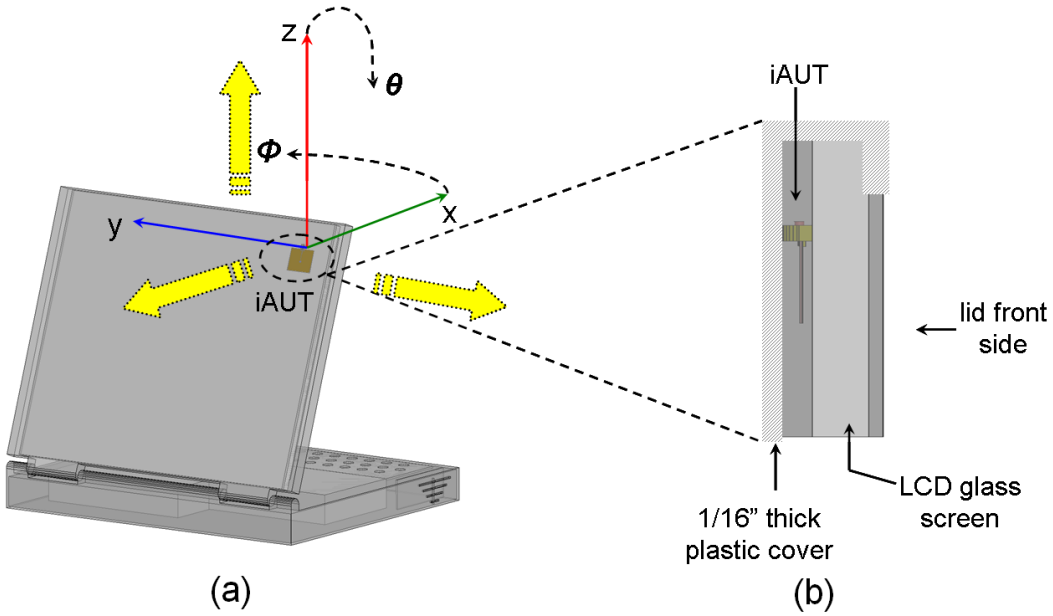

Figure 77: Antenna integration in the laptop lid: (a) back view with the center of the coordinates system aligned with the iAUT location; (b) lateral zoom on the antenna mounted behind the LCD screen. Large arrows indicate possible directions of radiation. iAUT denotes the internal antenna under test.

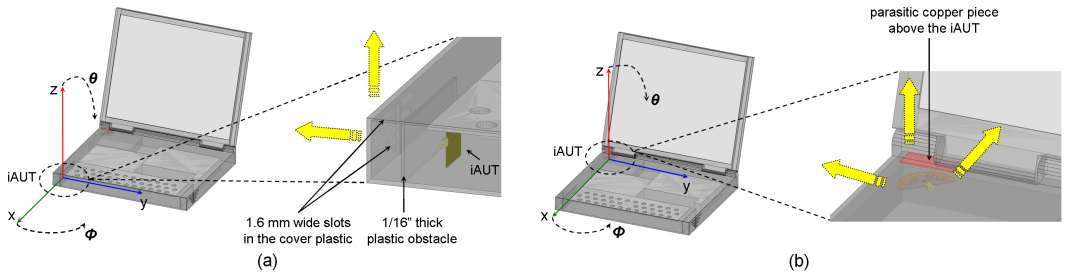

Figure 78: Antenna integration in the laptop base: (a) the antenna is mounted in the front left corner; (b) the antenna is mounted in the back left corner. In all cases, the antenna location coincides with the center of the coordinates system. Large arrows indicate possible directions of radiation.

6.1.1 Laptop Computer Lid Mounted Antenna

Internal antennas are generally integrated inside the laptop lid, close to the top edge as well as side rims around and away from the LCD screen. For the location shown in Figure 77, radiation may occur either toward -x, -y or in the +z direction. The first one represents the very familiar scenario where the antenna communicates with a spot located behind the laptop screen. The two other scenarios emulate an antenna communicating with wireless spots located on the front left hand of the laptop base or above the computer (a wireless spot

on a ceiling for instance). Radiation toward $+x$ is here considered to be odd as it would mean that the antenna points toward the laptop user. In the simulation tool, the chassis cover material is defined as a dielectric material (with no metal particle) of relative permittivity 3.45 and loss tangent 0.025, at 60 GHz [16]. Although plastic covers with conductive coatings are a very common practice in the industry for electromagnetic interference (EMI) mitigation, this model excludes these types of covers. Indeed, preliminary measurements with a metal coated plastic cover (from a real laptop computer) show that the radiated power is attenuated by at least 40 to 50 dB at 60 GHz, which clearly prevents the use of such coatings, at least, in a small area facing the radiating element. The experimental laptop also uses a plastic cover with no metal particles. The LCD screen is defined as a glass material.

6.1.2 Laptop Computer Base Mounted Antenna

The backside and lateral sides of the laptop base are other areas where internal antennas can be mounted. Figure 78a shows an antenna in the front and left corner of the base that may radiate either in the -y or $+z$ direction. For this particular laptop, the specific location originally contained the audio speaker which was removed, except for the 1/16" thick plastic obstacle and the very thin slots in the plastic. These discontinuities are included in the simulation model of the antenna placed in the surrounding laptop environment. Figure 78b shows an antenna in the back and left side of the base, from where the internal antenna under test (iAUT) can radiate toward -x, -y or $+z$. The laptop used for the experiments has some in-line apertures in the cover where VGA, USB and other connectors were located. These connectors were removed, and the apertures covered from the inside with small pieces of the same plastic material. In the model and the experimental laptop, a large (30 mm $\times$ 12.5 mm) parasitic copper piece is attached 4 mm above the iAUT to investigate the proximity effects with metal obstacles.

6.2 Review of 60-GHz Antennas for Wireless Platform Integration

Before presenting the antennas used in this work, a figure of merit based on the average $3dB$ gain of the iAUT is introduced as a more effective evaluation quantity compared to

the usually calculated or measured antenna peak gain.

6.2.1 3-dB Average Gain

As will be discussed later in this chapter, the iAUT radiation pattern at 60 GHz may be significantly distorted because of constructive and destructive interference from scattered fields throughout the host chassis. In some cases, the resulting patterns have ripples of more than 3 dB magnitude and it becomes complex to define the antenna peak gain and beamwidth in such a case. The method proposed in this work consists in:

1. smoothing rippled patterns using the MATLAB moving average method. The purpose here is to obtain data with less than 1 dB magnitude ripples in the antenna main beam. The function *smooth* is used to generate the smoothed data;

2. a 3-dB beamwidth for the smoothed patterns can then be determined, in both E and H planes; and

3. the average gain G_{3dB} of the AUT is finally defined as

$$G_{3dB} = \frac{1}{N_E} \sum_{\theta_{3dB}} G_{E_{plane}}(\theta) + \frac{1}{N_H} \sum_{\theta_{3dB}} G_{H_{plane}}(\theta) \tag{22}$$

where N_E and N_H are the number of angular points in a 3-dB beamwidth span of the E and H planes respectively, $G_{E_{plane}}(\theta)$ is the E plane gain at angle θ, and $G_{H_{plane}}(\theta)$ is the H plane gain at angle θ. The advantage of this method is that it smoothes the gain ripples and gives an estimate of the average radiated power within the $3dB$ beamwidth of the antenna, hence taking into account the gain decrease due to nulls in the antenna main beam. Ideally, if we keep θ as the sweep angle, the average gain should be computed over a full $3dB$ solid angle (that is, the solid angle integrated over all ϕ angles and within θ_{3dB}); but from a practical point of view, it is reasonable to limit to the E and H plane cuts.

6.2.2 Rectangular Patch Antenna

An inset-fed patch with broadside radiation is here designed and fabricated on an 8 mil thick liquid crystal polymer (LCP) substrate, whose relative permittivity ϵ_r and loss tangent $\tan\delta$ are defined to be 3.16 and 0.004 respectively, at 60 GHz [97]. Standard lithography

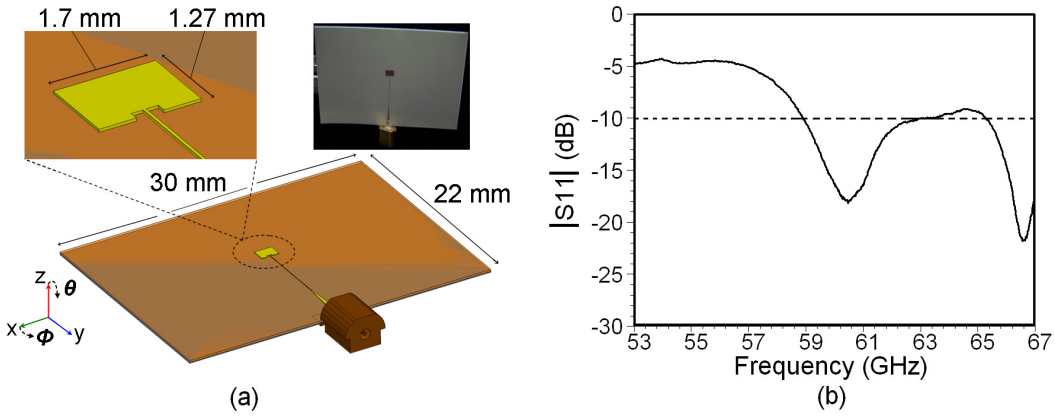

Figure 79: Rectangular patch antenna: (a) Schematic of the patch antenna; (b) Measured magnitude of S_{11} for the rectangular patch antenna in free space.

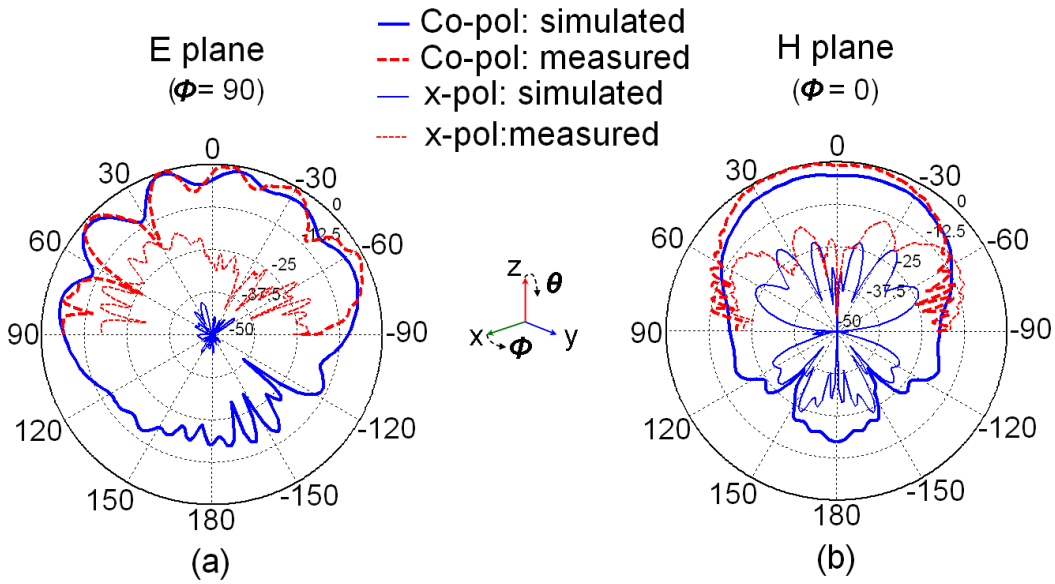

Figure 80: Simulated and measured normalized radiation pattern of the rectangular patch antenna in free space, at 60 GHz: (a) E plane; (b) H plane.

patterning of a bare $\frac{1}{4}$ oz thick copper (Cu) layer is performed to define the patch antenna geometry and feed lines on the top layer, while the bottom layer is covered with a bare $\frac{1}{4}$ oz Cu. Testing of the antenna is done with a GPPO connector edge-mounted to the microstrip feed line (Figure 79a). The fabricated patch resonates at 60.6 GHz with about 4.5 GHz frequency bandwidth (Figure 79b). The higher resonance above 65 GHz stems from the launcher over-moding. The simulated and measured radiation patterns are very similar, including the E plane ripples that are attributed to radiation from the microstrip

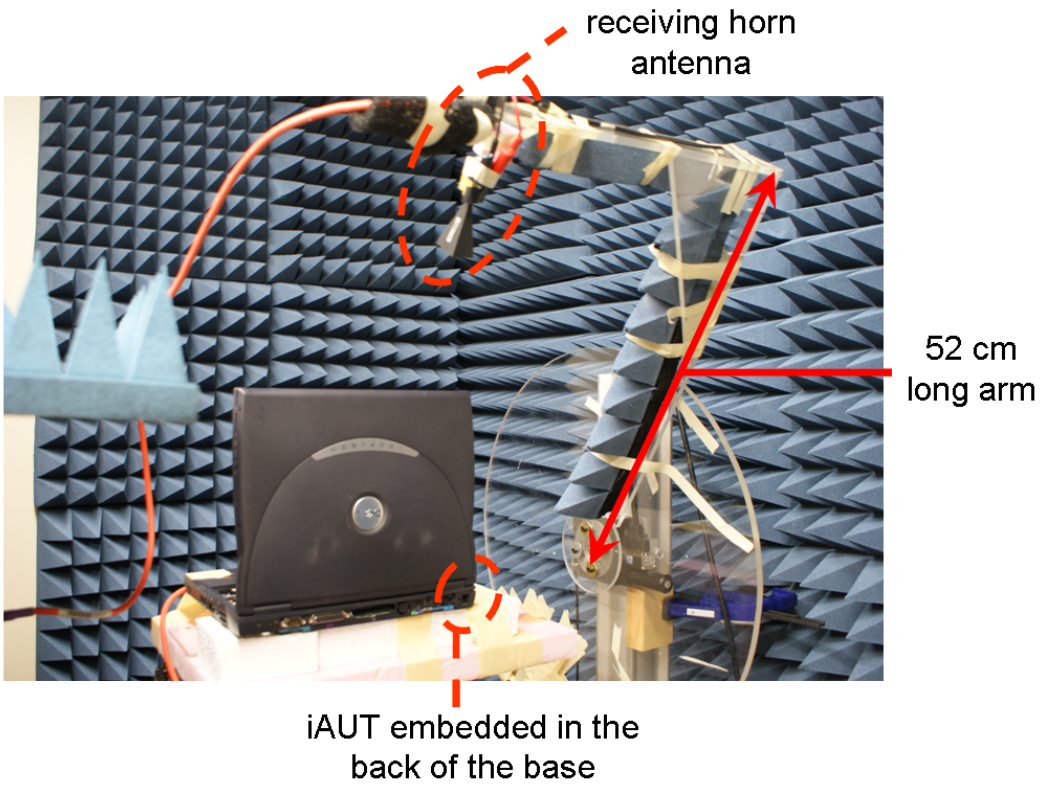

Figure 81: Photograph of measurement setup. This picture was taken during the measurement of the embedded switched-beam antenna. The laptop is re-positioned each time for a new measurement run to align the iAUT with the receiving horn antenna.

feed line and reflections from the launcher. After smoothing the pattern, the calculated and measured 3-dB average gain values are 3.8 and 5.8 dBi respectively. The measured value is slightly higher because the measured H plane cut level coincides with a higher gain level in the $\theta = 0°$ direction, owing to a slight pattern tilt in the E plane (Figure 80). This pattern tilt could be easily due to the curvature of the flexible LCP substrate. To remain consistent, these discrepancies in gain values are taken into account in the embedded antenna characterization.

6.2.3 Switched-Beam Directive Planar Yagi-Uda Antenna Array

This antenna is fully described in chapter III, section 1.

6.3 Characterization of 60-GHz Platform Embedded Antennas

6.3.1 Measurement Setup Description

The platform embedded antennas were characterized in a 60-GHz antenna characterization system that holds the iAUT fixed at the center of the coordinates system, where it acts as the transmitting antenna. The receiving antenna rotates in an arc with a radius of 52 cm around the iAUT. This distance is close enough to the far-field range given that the internal antennas illuminate only a localized area of the platform (and not the entire chassis as is the case at low frequencies), in such a way that the effective aperture of the chassis-mounted antenna is limited to 4 cm (8λ at 60 GHz) in average. Note that this aperture size is specific to the type of antenna used in this study and might slightly increase if the internal antenna is larger and thus illuminate a larger portion of the chassis. An Agilent Vector Network Analyzer, a V-Band low noise amplifier on the receiving port, and a pair of 1.85 mm cables are used for the measurements. The receiving antenna is a V-Band, 25 dBi standard gain horn, and a similar antenna is used for the gain measurements performed by the substitution method. A 1.85 mm coaxial to WR-15 adapter and a 1.85 mm coaxial to GPPO microstrip launcher are used for interconnects between the cables and the horn, and the iAUT, respectively. The entire system is controlled by a Labview program. Although the standalone antenna can be aligned accurately when it is characterized in free space, it is more difficult when the antenna is placed inside the laptop because the iAUT is hidden from view for most of the measurements. Thus, this must be considered a source of error. The measurement setup is shown in Figure 81. For all these measurements, the keyboard, lid, and all components of the computer are placed in their proper locations except for the CD-Rom drive and the battery to facilitate the antenna placement with the testing cables. The presence of the laptop battery and CD-Rom drive, in a real case scenario however, may alter the observed results if these metal blocks obstruct the path of the radiated fields because the induced surface currents radiate from obstacles discontinuities and add constructively or destructively to the antenna main beam. In addition, the flexible LCP substrate has a slight curvature that could not be eliminated or corrected for by placing the antenna into a fixture; this also introduced a source of error.

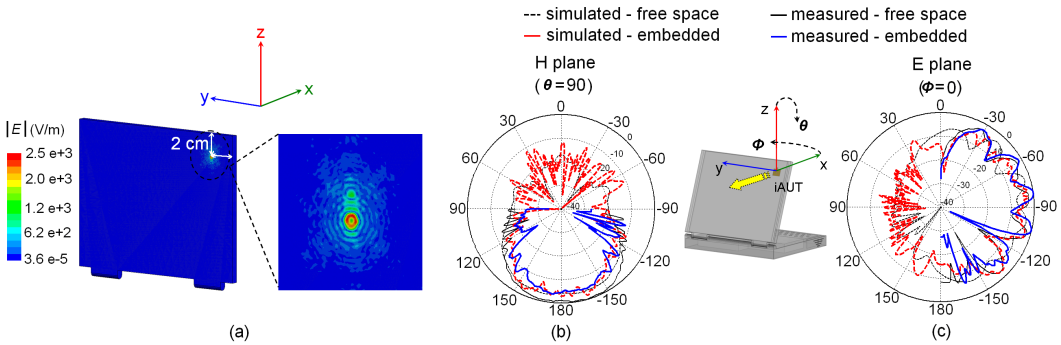

Figure 82: Rectangular patch antenna inside the laptop lid: (a) Magnitude of electric field distribution on the surface of the laptop lid, showing surface waves excitation on the interface of the plastic cover. This is a view from the back of the laptop with a zoom into the area surrounding the patch; (b) Normalized H plane co-pol radiation pattern of the patch antenna; (c) Normalized E plane co-pol radiation pattern of the patch antenna. The antenna beam is directed toward -x.

6.3.2 Rectangular Patch inside the Laptop Lid

Figure 82a shows the simulated magnitude of the electric field on the surface of the laptop lid (HFSS is used to model the laptop-mounted antennas). Concentric field lines that spread out in a cylindrical fashion around the main radiator (the patch in this case) remind of surface wave modes ($\frac{1}{\sqrt{r}}$) that are always excited in dielectrics [23, 87, 100]. Excitation of surface waves on the surface and in the bulk of the chassis cover material is particularly enhanced at 60 GHz because of its large effective thickness (1/16" $\approx \frac{\lambda_{eff}}{2}$ at 60 GHz). Surface waves usually contribute to radiation when they reach discontinuities from where reflection and/or diffraction occur. In this particular scenario, the rectangular patch is mounted 2 cm away from the lid cover edges (in the y and z directions) and the distance between the patch and the frontal cover surface is only 2 mm. Because of the 2 cm clearance distance, surface waves propagating in the cover dielectric vanish before before they reach discontinuities at the lid cover edges. Therefore, there is very limited surface wave radiation and this explains why both E and H plane patterns are similar to the free space case, as shown in Figures 82b-82c. There is a good agreement between the simulated and measured data. The H plane pattern also remains symmetric despite the large LCD glass screen behind the patch. Pattern symmetry is much more difficult to achieve at low frequencies because low frequency internal antennas require a much larger physical ground plane. Here,

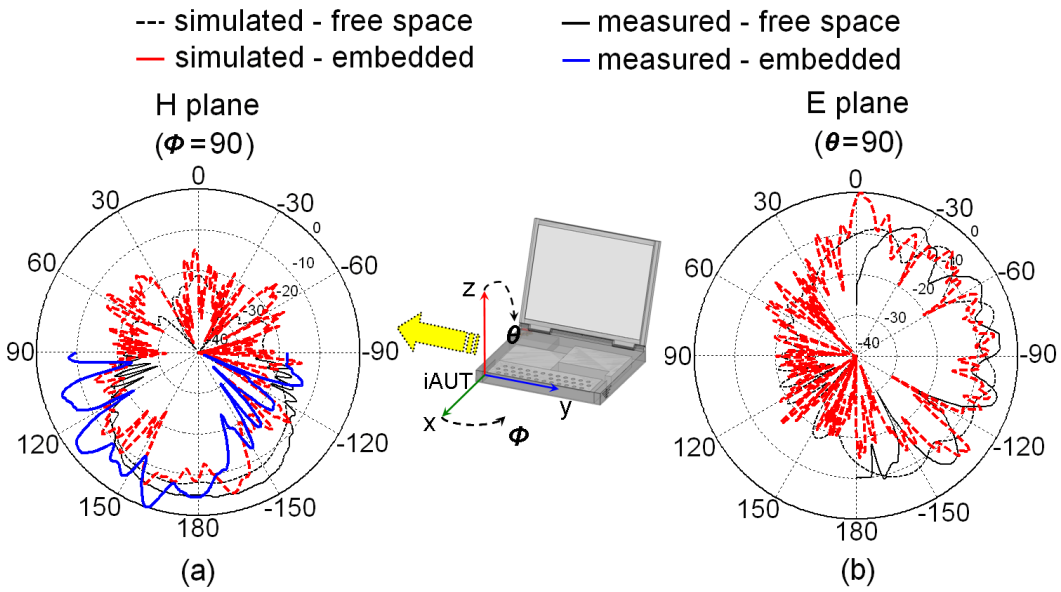

Figure 83: Simulated and measured normalized radiation pattern of the patch antenna: (a) H plane co-polarization; (b) E plane co-polarization. The antenna beam is directed toward -y. The E plane cut could not be measured. Standalone and integration in the front of the base are compared.

a $5\lambda \times 5\lambda$ wide patch ground plane is found to be large enough to hide the antenna from the LCD screen effect. The same radiation characteristics are thus expected to be observed if the patch is moved along the top or side edges of the lid. Because the fields are essentially confined in the vicinity (inside a disk of radius 4λ centered on the patch) of the patch antenna, only the lid chassis is incorporated in the simulation model. The calculated and measured power levels (averaged $3dB$ gain values) are 2.16 and 3.65 dBi respectively; total gain attenuations of 1.64 dB (simulation) and 2.15 dB (measurement) are extracted from the corresponding free space values. Calculated and measured attenuation levels are within 0.5 dB, which is acceptable for simulation and measurement tolerances. Here, the average gain is attenuated because part of the fields radiated from the patch are reflected at the cover interface and a more important part dissipated inside the plastic cover. Although not shown here, the cross-polarization levels were also measured and found to be better than 12 dB, same as for the standalone antenna. The limited diffraction of surface waves helps maintaining a reasonable cross-polarization level, in this specific scenario.

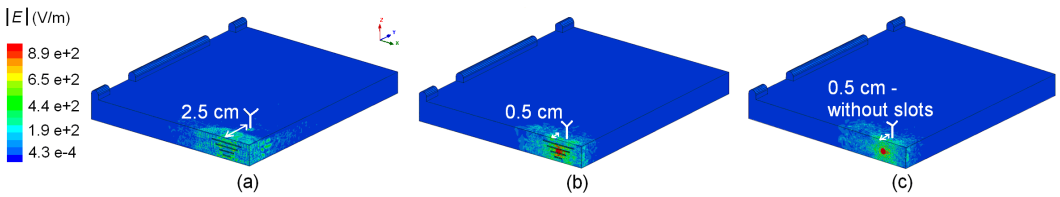

Figure 84: Magnitude of electric field distribution on the surface of the laptop base: (a) patch at 2.5 cm from the inner vertical plastic obstacle; (b) patch at 0.5 cm from the base vertical wall; (c) patch at 0.5 cm from the base vertical wall without slots in the cover. The antenna location in the coordinates system is represented by a "ϒ" in the plots.

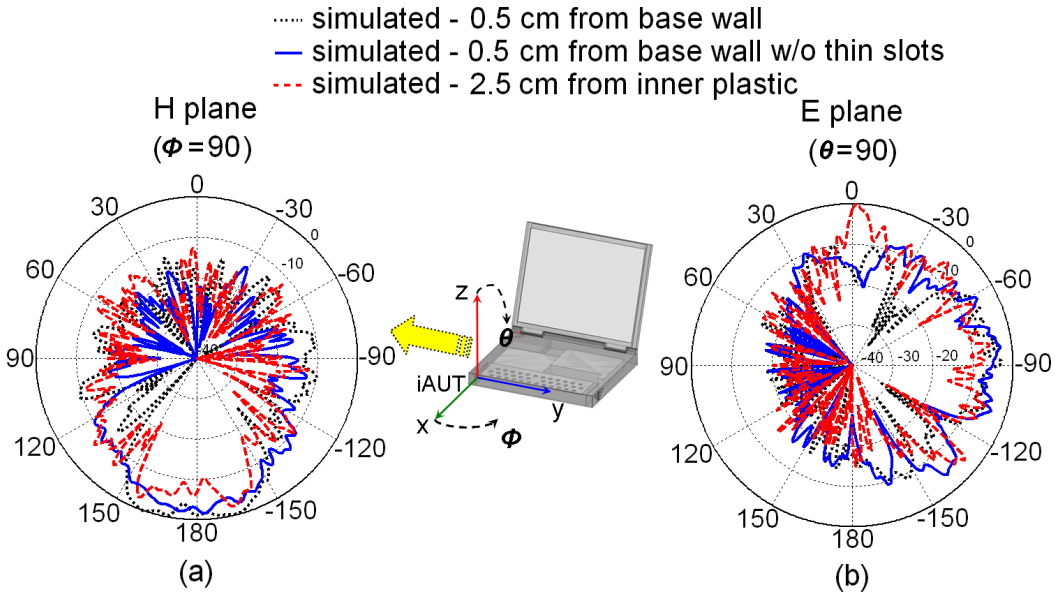

Figure 85: Simulated normalized radiation pattern of the patch antenna for different configurations: (a) H plane co-polarization; (b) E plane co-polarization. The antenna beam is directed toward -y.

6.3.3 Rectangular Patch in the Front of the Laptop Base

The measured radiation pattern of the base-mounted patch (see Figure 78a for mounting scenario) shows significant degradation compared to the standalone case (Figure 83a). To better understand the behavior at this location, the patch is placed 0.5 cm from the base sidewall (closer to the base sidewall-Fig. 84b) and 2.5 cm from the inner plastic (away from the base sidewall-Figure 84a). In the former case, the thin slots are also removed to assess their contribution (Figure 84c). In the Figure 84a case, a large area in the corner of the laptop base is illuminated and important surface waves are thus excited on adjacent cover surfaces. Diffracted surface waves from the sharp junction edges, corners and the

thin slots radiate on one side, and reflected space waves from the inner plastic piece and surrounding cover faces interfere with the main radiated waves on the other side, which in turn significantly affect the total radiated fields (Figure 85). In Figure 84b, the thin slots are the essential discontinuities that create surface wave diffraction since the fields are more confined in that area. This infers that to achieve better performance from patch like antenna at this location, it first needs to be mounted as close as possible to the base sidewall to minimize the illuminated area. Moreover, the sidewall should be free of discontinuities such as apertures or thin slots. Discontinuities in the order of a wavelength significantly diffract the excited surface waves. Although not shown here, simulations with smaller than 0.5 cm distances between the antenna and the base sidewall resulted in very consistent pattern shapes. The base-mounting scheme of Figure 84c is therefore recommended for such antennas.

6.3.4 Switched-Beam Planar Yagi-Uda Array in the Back of the Laptop Base

The measured radiation patterns of the base-mounted switched-beam array (See Figure 78b for mounting scenario) show some minor rippling along with a slight decrease in the average gain, in both -x and -y directions (Figure 86). The $3dB$ gain values are 5.9 and 5.7 dBi respectively, which corresponds to an average 2.5 dB gain decrease in both end-fire directions, compared to the standalone antenna. These results show that end-fire antennas mounted in the back of the base have satisfactory radiation characteristics although there are minor ripples that could be avoided as explained below.

Recall that the back-left (or right) corner of the laptop base is a very complex environment where connectors or power plug-ins are usually installed. The lid proximity further makes the antenna integration problem challenging at this location. The impact on the end-fire antenna is studied here by moving the iAUT close to (0.5 cm) or far from (2.5 cm) the base sidewalls. The calculated radiation patterns turn out to significantly degrade as the antenna moves away from the base sidewalls (Figure 87). In fact, the antenna element illuminates a larger area of the chassis when it is located 2.5 cm away from the base sidewalls. In Figure 88b for instance, surface waves are excited not only on the surface of the

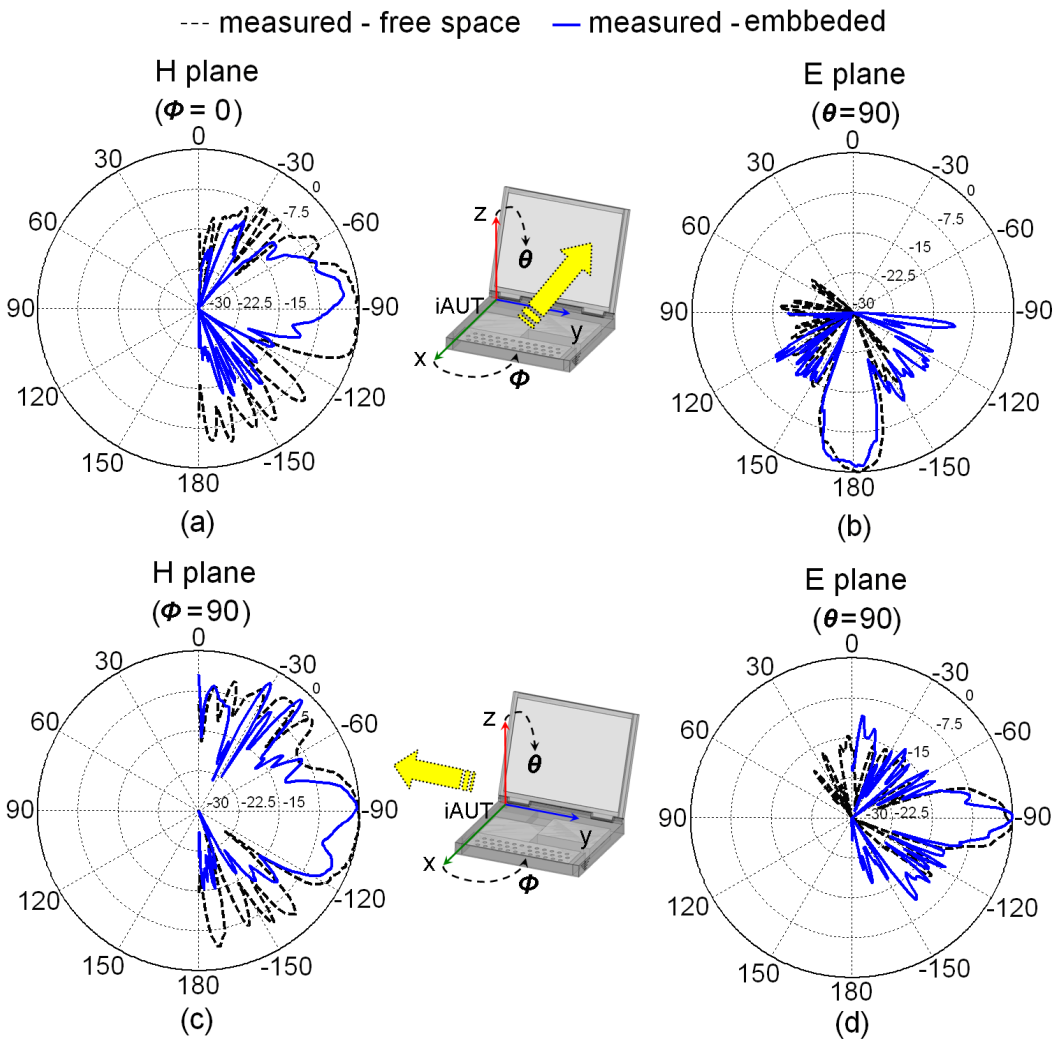

Figure 86: Measured normalized radiation pattern of the switched-beam array mounted in the back left corner of the laptop base: (a) H plane co-polarization -x; (b) E plane co-polarization -x; (c)H plane co-polarization -y; (d) E plane co-polarization -y.

base, but also on the surface of the lid; diffraction and/or reflection of these parasitic waves from the lid-base junction and also the lid and base edges and corners dramatically distort the H plane pattern (Figure 87a). The pattern ripples result in an average 2.6 dBi gain level at boresight, that is, 5.8 dB less than the free space gain. Ripples in the patterns can thus significantly reduce the internal antenna gain, and ultimately reduce the antenna range (a 5 dB gain drop at both the transmitter and the receiver reduces the antenna range by $\frac{2}{3}$−Friis equation). In Figure 87c, it is observed that the main beam direction can also be significantly tilted (20° off the end-fire direction), while the gain in the plane of the end-fire

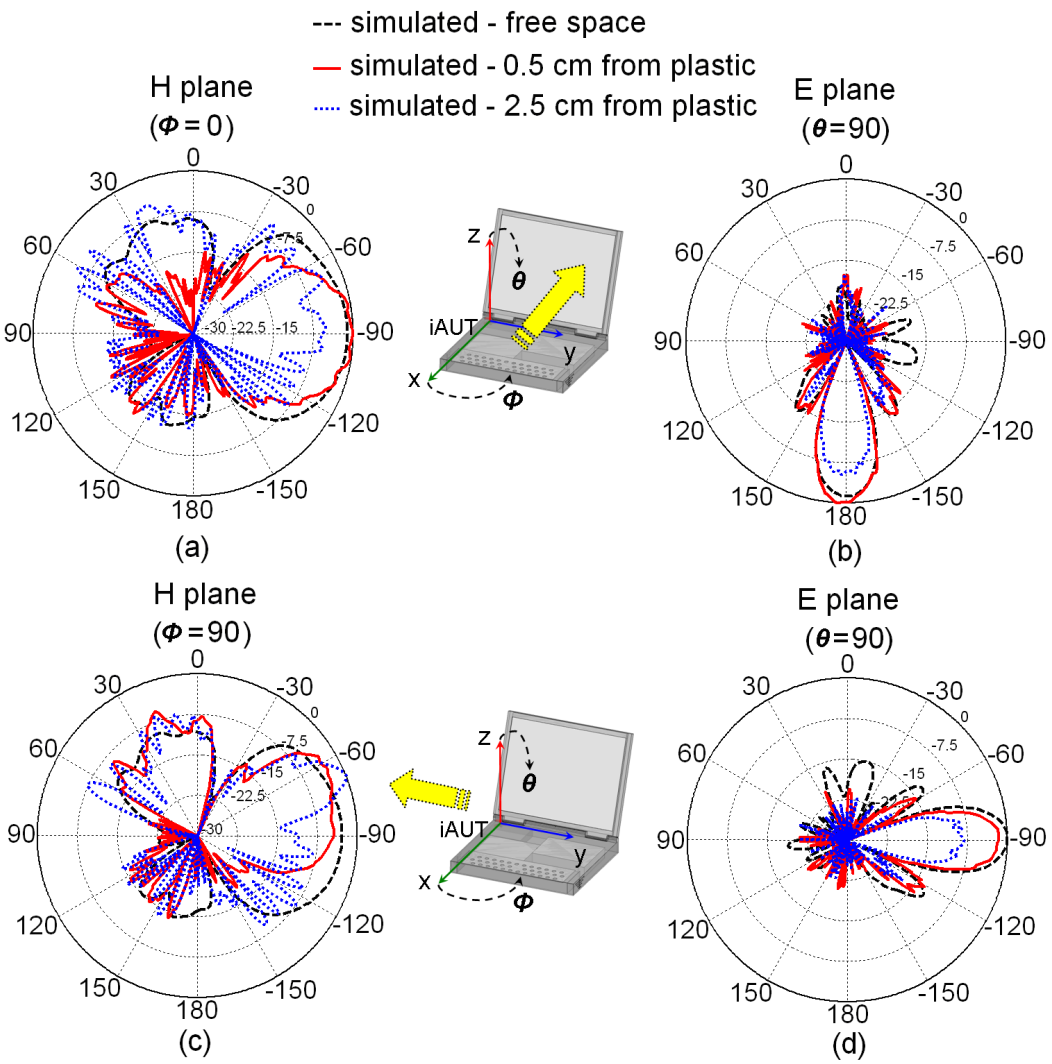

Figure 87: Simulated normalized radiation pattern of the switched-beam antenna array when located 0.5 or 2.5 cm away from the vertical plastic cover of the base: (a) H plane co-polarization -x; (b) E plane co-polarization -x; (c)H plane co-polarization -y; (d) E plane co-polarization -y.

antenna decreases by more than 10 dB; in this case, the plane of the end-fire antenna is just a shadow region, which leaves the antenna completely blind in its end-fire direction.

The best performance of the end-fire antenna is however achieved when the antenna is closer to the base sidewalls (0.5 cm antenna edge to base sidewall distance). The radiation patterns in that case are very similar to the free space case. The beam in the -x direction is even better than the -y direction because of the piece of copper mounted 4 mm above the antenna element radiating in -x: the copper piece first cancels upward radiation in the

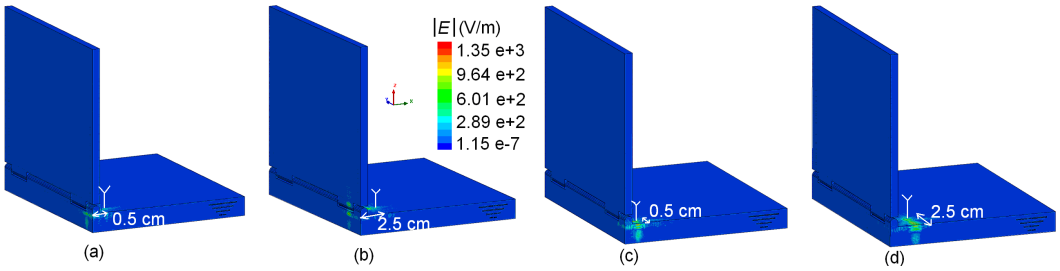

Figure 88: Magnitude of electric field distribution on the surface of the laptop lid and base: (a) switched-beam array "-x" at 0.5 cm from the base vertical wall; (b) switched-beam array "-x" at 2.5 cm from the base vertical wall; (c) switched-beam array "-y" at 0.5 cm from the base vertical wall; (d) switched-beam array "-y" at 2.5 cm from the base vertical wall. The antenna location in the coordinates system is represented by a "Υ" in the plots.

H plane (side lobe attenuation by more than 10 dB), and second, serves as a reflector that narrows the H plane main beamwidth and increases the directivity of the antenna element in the end-fire direction. For instance, the simulated directivity of the internal antenna radiating toward -x is 14.5 dBi, compared to 12.1 dBi in free space. More generally, it can be interpreted that the top and bottom surfaces of the base chassis form a structure similar to a parallel plate waveguide (in the end-fire direction) where space waves are subject to multiple reflections, therefore resulting in a more directive beam. Note that the copper piece is electrically large (30 mm $\times$ 12.5 mm) enough not to create a parasitic resonance at 60 GHz.

6.4 Summary and Discussion

This work is the first to bring insight into the integration of 60-GHz antennas with wireless platforms for consumer electronics applications. Without loss of generality, this study investigates the challenges of integrating a 60-GHz planar patch and an end-fire switched-beam planar Yagi-Uda array inside the lid and the base of a laptop computer chassis. The results and observations derived from this study are not solely specific to the laptop chassis problem and are easily transposable to various wireless platforms such as smartphones, tablets, netbooks and e-books where 60-GHz radios are very likely to be integrated. Electromagnetic analysis of the different integration scenarios has shown that with low-profile antennas, only a very limited area of the chassis surface (disk of radius 4λ centered on the

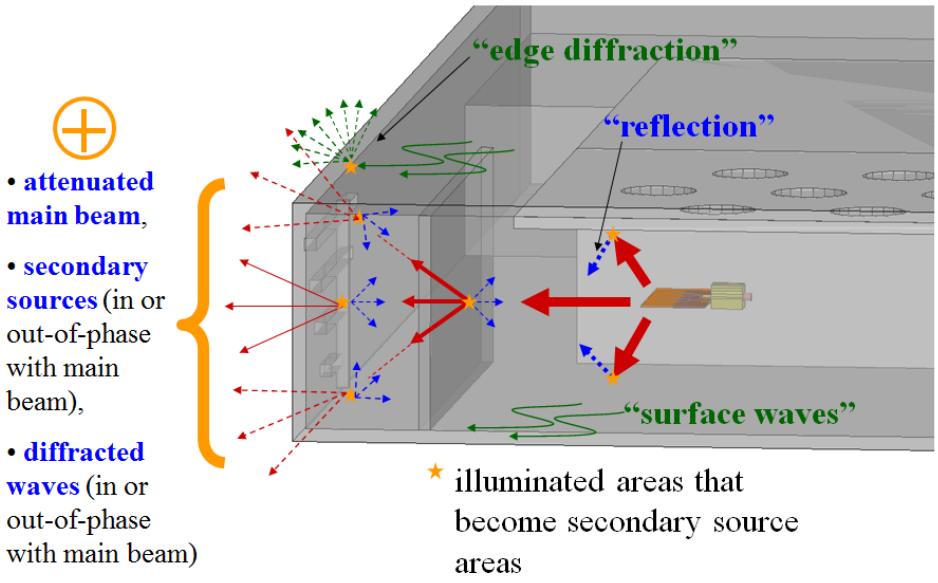

Figure 89: Summary of waves scattering phenomena that occur with platform integrated 60-GHz antenna systems.

antenna) is illuminated and effectively contributes to the entire system radiation performance, in contrary to low frequency laptop-mounted antennas. The first conclusion is that a near-field interaction assessment between the antenna element and the host platform is a useful approach to determine the chassis areas where induced surface currents are relevant to the overall antenna-platform system performance. Moreover, this suggests that platform components such as batteries, speakers, connectors and other electronic parts can be safely mounted in the host platform as long as they are isolated from the illuminated area. The illuminated area may get slightly larger than found in this work, if larger size antennas such as arrays with multiple elements are utilized. The second important point is the necessity to illuminate the smallest area of the chassis (or confine fields in an obstacle-free area of the chassis) in the boresight direction to prevent unwanted surface waves radiated from the chassis discontinuities from interfering with the antenna main beam. Indeed, it is observed that when a larger area of the chassis is illuminated, it is more likely that surface waves excited on the chassis get diffracted or reflected from surrounding chassis edges, corners or apertures. The investigations carried out in this work show that in practice, the illuminated

area on the chassis can be enough confined by simply keeping the internal antenna element within a wavelength (5 mm) or closer to the frontal cover surface. Satisfactory radiation characteristics (close to the standalone antenna) along with good cross-polarisation levels are observed under these considerations. Otherwise, improper antenna placement may lead to antenna beamwidth reduction, boresight gain decrease, boresight angle tilt and shadow regions formation. These distortions of the radiation pattern may directly impact the quality of service (QoS) by drastically reducing the antenna range (a 5 dB boresight gain drop at both the transmitter and the receiver reduces the antenna range by approximately $\frac{2}{3}-$Friis equation). It is also obvious that the internal antenna should not point toward the chassis edges and corners. Surface waves effects are thus effectively mitigated at 60 GHz with the use of low-profile antennas properly mounted inside the platform chassis. It is worth mentioning that surface waves mitigation is achieved in this work without the need for resistive thin-film coatings that have been suggested for lower frequencies applications [88]. Besides, it is also beneficial to keep the frontal cover surface (portion of cover facing the antenna boresight) as a dielectric with no metal particles because metal coated covers attenuate the $60-$GHz signal by more than 40-50 dB. Even with dielectric covers with no metal coating, reflections and dissipation losses from the plastic cover will attenuate the antenna boresight gain by 2 to 4.5 dB [16]. From a location specific point of view, both the lid and base can accommodate 60-GHz internal antennas. Lid-mounted broadside patch-like antennas with electrically large ($5\lambda \times 5\lambda$) ground planes are insensitive to the screen display back reflections and can thus be easily attached anywhere along the top or side edges of the lid, while keeping perfect pattern symmetry, in contrary to low frequency similar location scenarios [51]. Broadside and end-fire antennas (including switched-beam arrays for increased versatility) mounted along the laptop base sidewalls show satisfactory radiation characteristics when they are closely mounted to the base sidewalls. It is however expected that end-fire types of antennas may have their beamwidth reduced when their main beam is arranged parallel to the top and bottom surfaces of the base: in fact, the top and bottom cover surfaces form a structure similar to a parallel plate waveguide (in the end-fire direction) where space waves are subject to multiple reflections, therefore resulting in a more directive

beam. Because the top and bottom surfaces of the cover are not conductive, space waves may leak through these lateral boundaries with potential boresight angle tilt. Electrically large (that is non-resonant) parasitic metal patches are effectively incorporated with the platform to preserve the desired boresight angle. Figure 89 summarizes the fundamental scattering phenomena that occur with platform integrated 60-GHz antenna systems.

The main observations derived from this study on laptop-embedded 60-GHz antennas may also be compared to the problem of low frequency antennas flush-mounted on the fuselage of an aircraft and thus analyzed in a similar fashion. Indeed, in terms of wavelengths a 60-GHz antenna to laptop size ratio is very comparable to a VHF antenna to aircraft size ratio. It is thus not surprising to observe that in many aircraft mounted antenna modeling approaches, the analysis starts with an identification of the currents induced on the surface of the aircraft body ([76]) or the different source, reflected and diffracted fields components ([27, 39, 58]) that are used to generate the overall antenna-platform radiation pattern. In both problems, induced surface wave currents that are reflected or diffracted from the platform discontinuities are found to significantly distort the antenna main beam. The illuminated area of the platform also matters in terms of evaluating the pertinent portions of the platform geometry that contribute to the system performance. In references [27] and [58] for instance, dominant energy regions that are associated to the relevant induced surface currents are used to determine the critical region of the aircraft body in the vicinity of the antenna element. In reference [75], electrically large obstacles in the near-field region of an aircraft antenna are effectively incorporated to increase the antenna directivity. Finally, in the thick-radome enclosed antenna problem for aircrafts, analogous recommendations are derived: the optimal location to mitigate the resonance effects in the thick-radome corresponds to an antenna located closer to the radome apex, in which case the near-fields interactions are limited to a smaller area on the radome surface [38, 84].

This work has essentially focused on the radiation characteristics of 60-GHz internal antennas, which is certainly the most challenging study on platform integrated antennas. It is however reminded that embedded antennas also need to be characterized with respect to their voltage standing wave ratio (VSWR), and therefore their impedance bandwidth within

the respective platform environment. It will be essential to maintain the internal antenna matched in the entire WPAN frequency band (57-66 GHz). Resonant frequency shifts that are often attributed to the loading effect of the chassis cover can be easily adjusted by detuning the standalone antenna accordingly. Changes in bandwidth are typically observed at low frequencies (GSM$-$[59,98]) when the chassis starts resonating (chassis size $\approx \frac{\lambda}{2}$) and hence easily couples with the internal antenna. At 60 GHz, the chassis is expected not to affect the antenna bandwidth as much because the chassis resonant frequency is much smaller than the internal antenna resonant frequency. Finally, it is reminded that this work considered the laptop in an open environment; additional studies were later carried out with the laptop laid on a conference table with other laptops, books, pens, and coffee cups in a 60-GHz environment [83].

CHAPTER 7

CONTRIBUTIONS

- Planar end-fire switched beam antenna modules that can easily conform to various surfaces inside a wireless device platform are developed. The planar antenna package is realized on thin flexible LCP dielectrics. A low-loss microstrip-to-slot via transition is designed to provide wide impedance matching for end-fire antenna paradigms. The novel transition utilizes the slow-wave concept to provide unbalanced to balanced mode conversion as well as impedance matching. It is demonstrated that the planar antenna package may be even integrated with active circuits that are cavity recessed inside the thin dielectric.

- The first-ever integrated mm-wave active antenna module on organic package capable of generating both broadside and end-fire radiation is demonstrated. Both broadside and end-fire radiators are co-designed and integrated into a single multilayer package to achieve optimal directivity, efficiency and frequency bandwidth and yet maintain excellent isolation between the two radiators. Post-wall cavities, image theory and dielectric slab modes concepts are invoked to optimize these functions. Active circuitry are integrated into the same package to add control functions such as beam switching, and also amplify the packaged-antenna gain when operated either as a transmitter or a receiver. The versatile multilayer integration approach that is presented paves the way to smart high-performance mm-wave antenna systems and yet cost-effective owing to the low manufacturing costs of the combined IC/antenna package.

- 60-GHz broadside and end-fire antenna systems are integrated inside wireless platform environments to evaluate chassis effects onto the radiation performance. This work, essentially experimental, identifies key design constraints and proposes solutions to mitigate the effects of electrically large chassis on 60-GHz integrated antennas. It is demonstrated that a full-wave analysis of the problem leads to accurate results when

critical design parameters such as chassis thickness, chassis to antenna distance, chassis electrical properties are properly chosen. An antenna-chassis co-design approach is also suggested to take advantage of the chassis to enhance the embedded antenna directivity when desired. This is the first comprehensive analysis of the 60-GHz platform mounted antennas problem.

INTEGRATED ANTENNAS ON ORGANIC PACKAGES AND CAVITY FILTERS FOR MILLIMETER-WAVE AND MICROWAVE COMMUNICATIONS SYSTEMS

PART II

Microwave Cavity Resonator Filters

by

Arnaud L. Amadjikpè

CHAPTER 8

BACKGROUND

8.1 Challenges

Microwave signal filtering is an unavoidable function in any radio system. In fact, filters are found in instrumentations systems, communications systems, radars systems to name just a few. Instruments such as spectrum analyzers use a pre-select filter prior to down-converting the measured RF signal. The pre-select filter is a bandpass filter with very narrow bandwidth that acts as an image reject filter and guarantees that the signal detected at the intermediate frequency (IF) is indeed the information contained in the RF signal and not from the image spectral component. Another fundamental filter found inside a spectrum analyzer is the IF filter that essentially determines the spectrum analyzer resolution, that is, the capacity to resolve two narrowly spaced frequencies. Such filters may have bandwidths as low as a few Hz while still maintaing low insertion loss for signal detection and sharp out-band rejection with very low noise floor. In communications systems, filters are often found in base stations, wireless platforms, etc ... The receiver of a base station or a mobile device uses a bandpass filter following the receiving antenna to clean the signal captured by the antenna from undesired spectral noise before mixing down the signal of interest for further processing at the IF levels. Although base stations may afford bulky components, filters for mobile devices are strictly limited by their volume despite performance requirements. Filters for mobile devices must also be easily integrated with solid-state devices whether using mainstream Si technology or PCB. Depending on the type of applications, filters are designed to meet a number of specifications such as insertion loss, return loss, fractional bandwidth, out-band rejection, form-factor, and technology. These parameters are the traditional and fundamental filter design specifications but other functionalities including frequency and bandwidth tuning range, thermal stability, power handling capability, and linearity are just as important especially when designing reconfigurable filters. This class

of filters finds more and more interest in mobile communications systems where multiple radios must coexist while mitigating interferences, adjacent channels jamming. Air traffic control radars utilized to track aircrafts often operate in the 2.7-2.9 GHz frequency band where multiple channels as narrow as 1.5 MHz and spaced by only 5 MHz are assigned for spectral sharing and various usage of the spectrum. As the specifications show, very high tight specifications can be required. In both applications, one could realize multiple filters at each frequency channel and then switches to select each filter just as it done in multiplexers. The main drawback of this approach is the increased size of the system as well as the dependence on switches toggling speeds. Instead, one could in fact have a single filter which resonant frequency or other parameter of interest could be dynamically changed. This class of filter is very attractive because they are flexible, reusable, and compact. Several methodes can be implemented to make a filter's response dynamically reconfigurable. The next paragraph lists a number of techniques.

8.2 Literature Survey

ATC radars for commercial air traffic control are usually operated in the 2.7-2.9 GHz band where high power handling (500 mW) is required along with sharp selectivity and narrow bandwidth (as low as 1%). These specifications clearly put planar technologies aside as their limited quality factor or unloaded Q_u (less than 200) will inevitably harm the in-band insertion loss. Traditionally, coaxial cavity resonator filters (with $Q_u \geq$ 1,000-5,000 depending on size) are utilized but they suffer from bad spurious response because of higher order modes excitation. Well-proven techniques to improve stopband performance include evanescent-mode cavities and the insertion of finite attenuation poles, that is, finite transmission zeros in the transfer function of the filter. Evanescent-mode resonators are chosen because of their increased spurious-free range compared to coaxial cavity resonators. An evanescent-mode resonator is composed of a waveguide loaded with a post, and operated at a frequency well below the cut-off frequency of the waveguide [37, 91]. Because the operating frequency is well below the cut-off, any higher order mode will not be excited unless it is higher than the cut-off frequency. In other words, wide sprurious-free bandpass filters can be designed with

evanescent-mode cavity resonators, and the lower the operating frequency with respect to the cut-off, the wider the spurious-free range. On the other side, filters with transmission zeros have the unique feature of increasing the frequency selectivity with control of the zeros location. Among techniques available in the literature, source-load cross coupled filters are particularly attractive because compact size canonical filters with sharp roll-off can be designed [21, 28, 30, 71]. Practical implementations of source-load cross coupled resonator filters often utilize an electric source-load cross coupling scheme where the resonators are magnetically coupled to each other [62, 79, 90]. Alternatively, the source-load cross coupling is magnetic while the inter-resonator coupling is electric [34]. In the literature, it has so far been necessary to add either surface mount devices (SMDs) or sections of transmission lines to properly implement the required source-load cross coupling. Although SMDs can be easily added to planar filter topologies, they are not recommended for cavity filters because of their limited quality factor. Besides, additional lengths of transmission lines (or waveguide sections) increase the size and complexity of the filter topology, especially when it comes to prototyping mass-producible cavity filters at low costs. Besides design techniques related to filtering functions, a recent and necessary trend is the development of frequency reconfigurable filters. The need for such devices is simply justified by the increased level of integration required by most wireless applications. For instance, smartphones today contain multiple RF transceivers which perform each a specific function at various frequencies. If each function is to be assigned a distinct filter to provide enough isolation between adjacent modules, the size and cost of the RF board in the mobile device could quickly increase to unacceptable limits for the consumer market. Likewise, radar systems that operate at multiple frequency channels quickly become bulky if each channel is allocated a single filter. With the recent development of tuning semiconductor and MEMS devices such as p-i-n diode varactors, schottky diodes, radio frequency micro electromechanical systems (RF-MEMS) switches, ferroelectric thin-film barium strontium titanate (BST) varactors, and piezoelectric actuators it is now possible develop frequency reconfigurable filters integrated with these devices. An appropriate comparison between these technologies (except piezoelectric actuators) is provided in [86]. It is shown that RF-MEMS switches have the

highest Q_u (about 400), linearity ($\geq$ 60 dBm) and power handling (100-1,000 mW) to date. For applications requiring greater than 1,000 quality factors, RF-MEMS and piezoelectric actuators are prominent candidates.

8.3 Proposed Approach

Evanescent-mode filter technology is chosen to design compact albeit high quality factor filters.

- To achieve frequency reconfigurability, ohmic RF-MEMS switches are monolitically integrated on low-loss fused silica substrate with fixed high-Q capacitors. Therefore, the tunable capacitor banks (diced as chips) are mounted inside a second order evanescent-mode cavity resonator filter to achieve frequency tuning.

- To achieve steep rejection near the filter frequency pass band, a novel folded cavity filter architecture with finite transmission zeros using magnetically coupled coaxial probes connectors is developed. Filters with up to three finite transmission zeros may be designed following the proposed technique.

CHAPTER 9

FREQUENCY TUNABLE EVANESCENT-MODE CAVITY FILTER WITH OHMIC RF-MEMS SWITCHES

Frequency tunable narrow band filters find many applications in space and terrestrial communications. They can be used for cost efficiency and compactness purposes in air traffic control (ATC) radars. In fact, these radars are commonly equipped with several single frequency bandpass filters operating at adjacent frequencies, which are manually selected and plugged to the antenna of the radar system. Specifications for these filters are usually a high quality factor (Q), a narrow bandwidth, and a moderate frequency tuning range of few hundreds of MHz with fine tuning capabilities (5 to 10 MHz steps between adjacent channels). The requirement for such high performance frequency tunable narrowband bandpass filters has been the major catalyst for the reported work. A feasibility study on the development of high unloaded Q narrow band bandpass filters tunable with RF-MEMS switches is carried out in this research. Electronically tunable 3D cavity resonators and filters have recently been proposed in the quest for very high quality factors as an alternative to mechanically (screw, post insertion) tuned filters [19, 37, 48, 53, 80, 81, 86, 102, 105]. In [19], the potential for achieving Q values above 880 with evanescent-mode cavity resonators containing hard-wired switched capacitors was demonstrated. Later, Park et. al. used high Q capacitive RF-MEMS switches to implement a tunable evanescent-mode metal cavity filter with an unloaded Q of 300-500 at 4-6 GHz [80, 81]. The reported 1-dB bandwidth is 0.45-0.7%. In [53], substrate integrated waveguide (SIW) filters with piezoelectric actuated flexible posts and constant absolute bandwidth achieved Q values of 225-310 over 0.8-1.43 GHz. The achieved constant absolute bandwidth is 25 MHz (1.7-3.1%). A very similar approach was implemented in reference [105] to demonstrate the first MEMS electrostatically-tunable loaded-cavity resonator that achieves Q values of 460-530 over a very high continuous tuning range (3.4-6.2 GHz). The best tunable Q (300-900) filter was however demonstrated

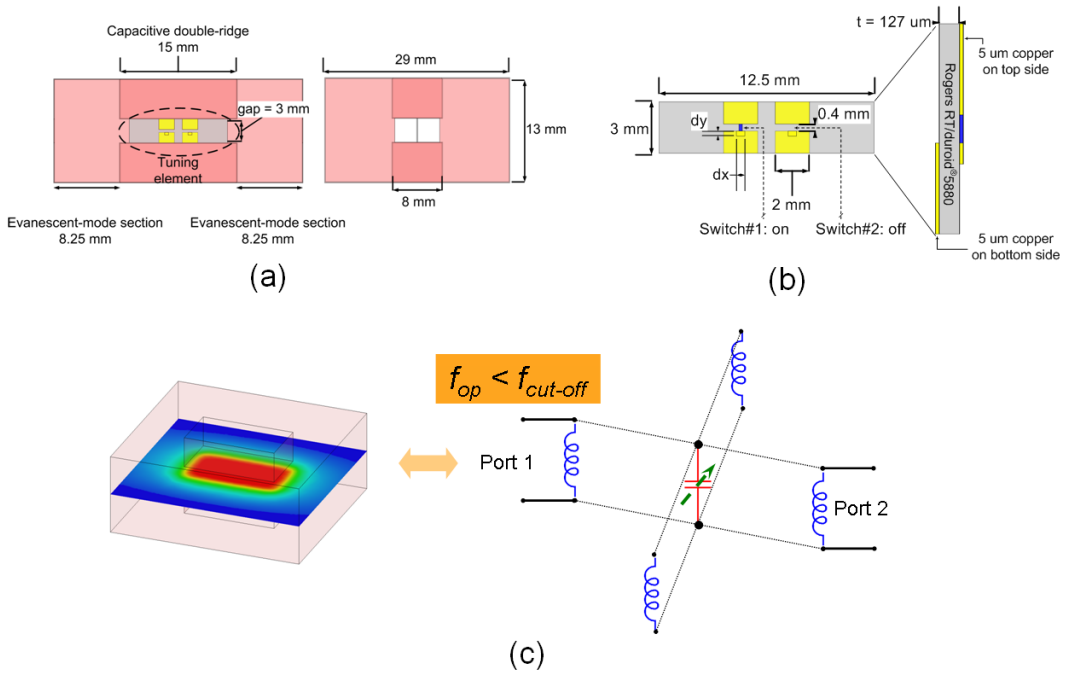

Figure 90: Proposed electronically frequency switchable evanescent-mode cavity resonator: (a) Structure of the cavity with the inserted capacitors; (b) Structure of the variable capacitor; (b) Equivalent circuit model of the proposed frequency reconfigurable resonator.

with thermally actuated RF-MEMS metal sheets above dielectric resonator materials in the 15.6-16 GHz frequency range [102]. This filter has a 1-1.3% bandwidth but a limited tuning range of 2.5%.

9.1 Evanescent-Mode Waveguide Resonator

Craven et. al previously introduced the function of a capacitive screw to mechanically tune the center frequency in evanescent-mode waveguide filters [37]. As the depth of the inserted screw increases, the loading capacitance in the cavity increases and results in frequency tuning toward low frequencies. This approach can be mimicked by replacing the mechanical screw with electronically tunable capacitors. If we denote by C_1 and C_2 the fixed capacitance of each empty cavity resonator, and ΔC_1 and ΔC_2 the contributions of the variable capacitance in each resonator, the capacitances in each tunable resonator are

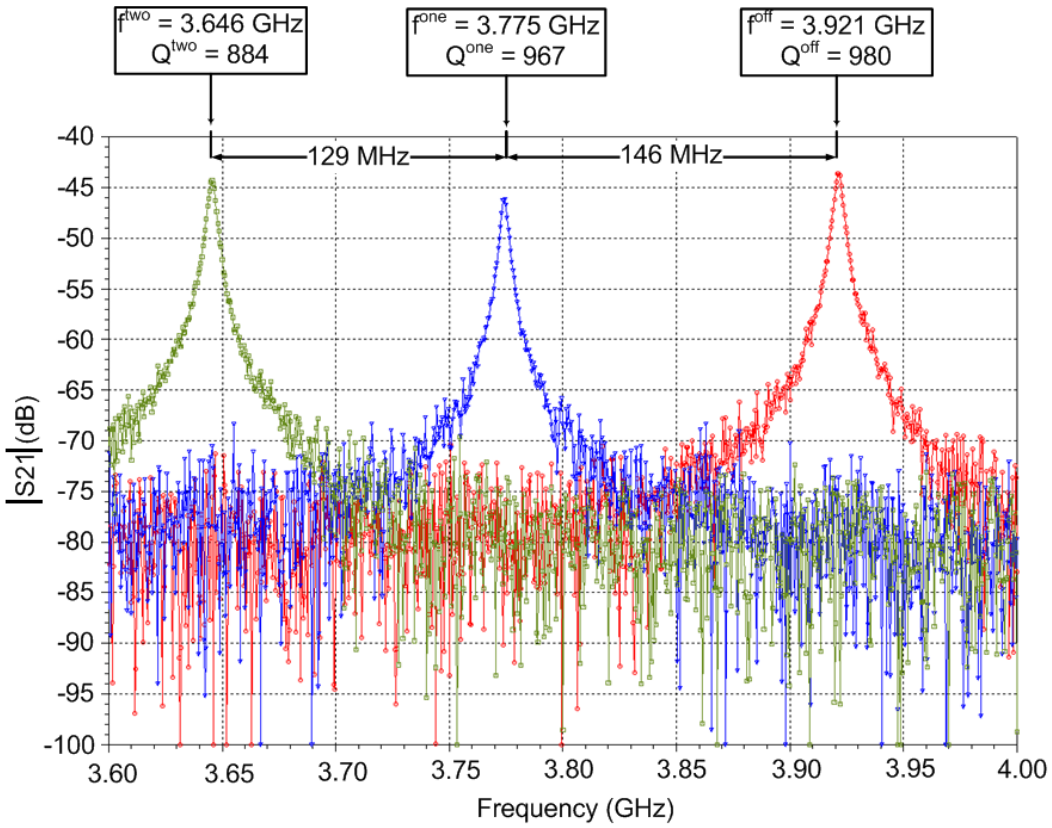

Figure 91: Measured evanescent-mode cavity resonator with three different capacitor networks inserts.

defined by C_{1v} and C_{2v} given by

$$C_{1v} = C_1 + \Delta C_1 \tag{23}$$

$$C_{2v} = C_2 + \Delta C_2 \tag{24}$$

It will be also assumed that the two-pole filter is symmetric in which case $C_1 = C_2 = C$ and $\Delta C_1 = \Delta C_2 = \Delta C$. In the case where the filter has three or more poles, the capacitances in each resonator are not necessarily the same. It is clear that to be able to tune the filter center frequency, ΔC must be of the same order as C. Moreover, if ΔC has a wide capacitance range, then in theory the filter should have a wide tuning range. Another important aspect is the loss introduced by the tuning elements. The variable capacitors should be designed to have a high unloaded Q. To demonstrate the validity of this concept, a high$-Q$ resonator with hardwired switched capacitors has been designed and fabricated [19]. An evanescent-mode double-ridged rectangular waveguide resonator houses

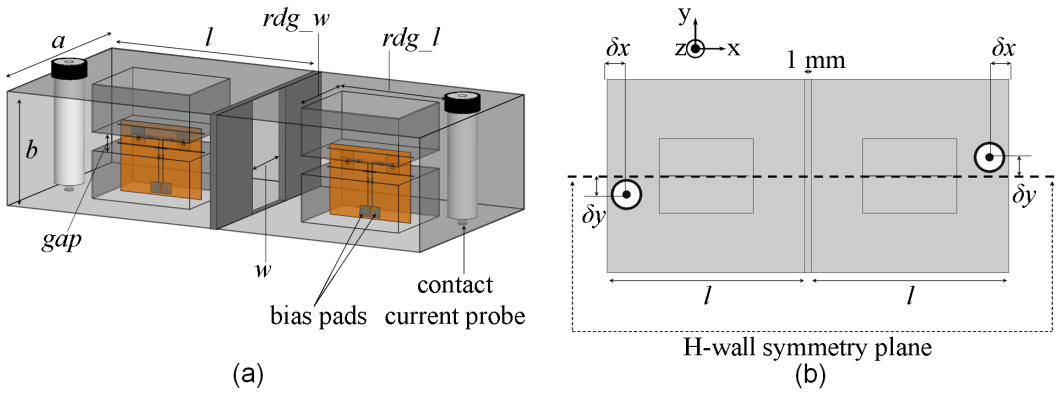

Figure 92: Proposed two-pole evanescent-mode cavity filter with inserted switchable capacitor network: (a) 3D view; (b) Top view.

a tuning element with two parasitic capacitors that are connected to or disconnected from the cavity resonator ground, in between the two ridges. Figure 90 shows the schematic of the cavity resonator with the inserted capacitive elements, along with an equivalent circuit model of the frequency reconfigurable evanescent-mode cavity resonator. To measure the quality factor Q of the resonator, two SMA to waveguide (WR284) transitions are connected to the cavity resonator where small enough rectangular apertures on the input and output faces are defined to ensure sufficient decoupling between the ports and the cavity. In that case, the measured Q is indeed almost equal to the unloaded Q given that the external Q is negligeable. Figure 91 shows the measured three frequency steps achieved when all hardwired switches are *off*, one hardwired switch *on* and the other one *off*, and both hardwired switches are *on*. This demonstrates the validity of the proposed concept to electronically switch the resonant frequency of this type of high-Q resonators.

9.2 Evanescent-Mode Filter with RF-MEMS Ohmic Switches

9.2.1 Filter design

Figure 92 shows the structure of the two-pole cavity filter, where evanescent mode resonators are formed by loading a rectangular waveguide with two back-to-back ridges. Spectral agility of this filter is achieved by inserting switchable capacitors in the waveguide H-plane, in between the two ridges. The switchable capacitor networks are designed on a 170 μm thick low loss fused quartz substrate ($\epsilon_r = 3.9$ and $\tan\delta = 5 \times 10^{-5}$). Each

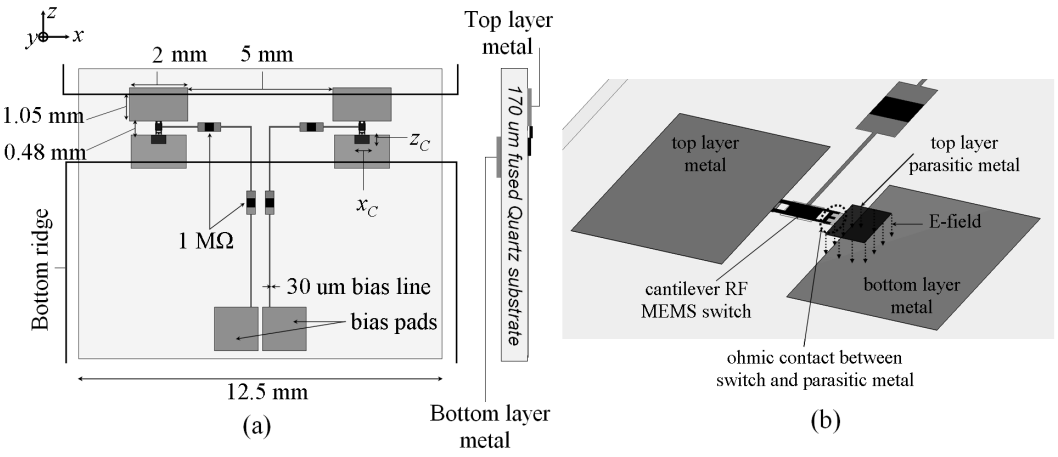

Figure 93: Switchable capacitor network: (a) Transversal view showing the capacitor network inserted between the top and bottom ridges of a resonator; (b) 3D view of one digitally switched capacitor with an RF-MEMS cantilever.

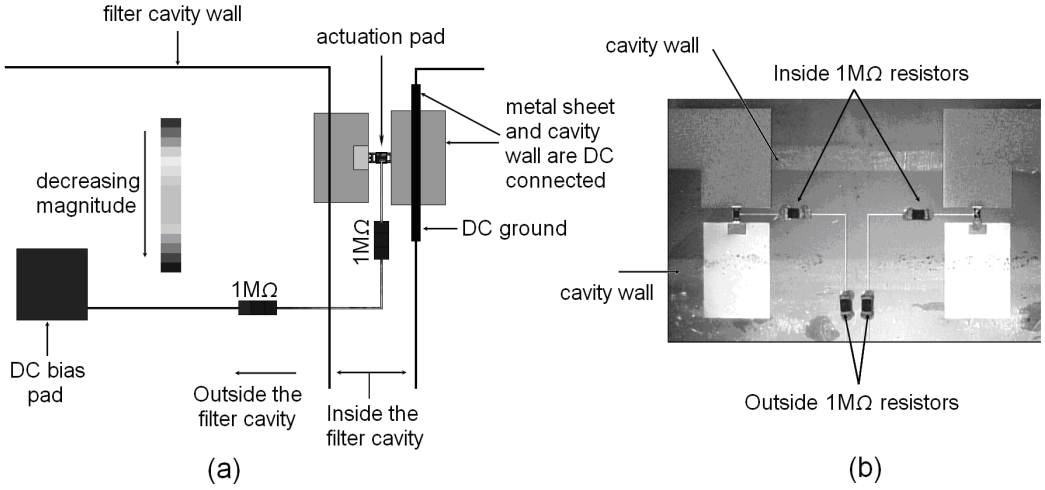

Figure 94: Biasing scheme for the switchable capacitor network: (a) Surface current distribution on the bias line of one digitally tunable capacitor; (b) Photograph of the fabricated tuning element showing the location of the resistors.

tuning element is composed of two digitally tunable capacitors monolithically integrated with ohmic cantilever RF-MEMS switches (See Figure 93). The electric field between the parasitic metal (rectangular sheet of area $x_c \times z_c$) and the bottom metal delimitates the overlapping region where a parasitic fixed capacitance C_p is defined. Actuation of each RF-MEMS switch shorts the parasitic metal, and this results in a higher loading effect inside the cavity. Each RF-MEMS switch on a tuning element requires a separate bias line. Hence, two bias lines are needed to make the DC bias pads accessible in each resonator. The bias

lines are made of 30 μm wide gold lines. The simulated surface current distribution on the bias lines is shown in Figure 94a. A strong RF current couples to the actuation pad of the switch, and then leaks through the 1.25 mm gold bias line preceding the 1 MΩ surface mount (SMT) resistor inside the cavity. Although the 1 MΩ SMT resistor blocks the RF in the bias line, it still dissipates some fringing fields that couple to the alumina package and the thin film resistive material on top of the resistor. Another important contribution to losses is the portion of the bias line inside the cavity which is parallel to the E field. Coupling to this portion of bias line is maximized in a parallel arrangement and minimized in an orthogonal one. Further improvement of the biasing network would thus consider reducing the bias line length inside the cavity and also keep the E field orthogonal to the bias lines [80]. Measurements of the filter with hardwired switched capacitors including bias lines showed that the RF decoupling resistor located right outside the cavity is necessary to prevent leakage from the cavity, especially that this external portion of bias line may be quite long to provide a reasonable location to probe the DC pads. A better way to prevent RF current dissipation into the inside portion of bias line is to use a very thin and relatively short portion of high resistive line such as chromium silicide (SiCr) or carbon-doped resistor with a sheet resistance of about 10 to 100 k$\Omega/\square$, instead of the internal SMT resistor. This was suggested in [80] where the highly resistive line was further air-bridged to isolate the SiCr from the strong RF inside the cavity.

9.2.2 Filter Fabrication

The filter cavity was fabricated at the Georgia Tech Research Institute (GTRI) machine shop. To ease the insertion of the tuning elements inside the waveguide housing, the cavity is separated into two pieces, along the H-wall symmetry plane. Thus, to test the filter, the two parts are assembled together and screws are used to tighten the cavity. The cavity should be tightened well enough to minimize field leakage. In addition, 250 μm wide irises are cut at the location of the tuning elements to leave space for the thick fused quartz substrate (tuning element), and extend bias lines outside the cavity. The empty cavity filter without any tuning element was tested to verify standalone performance. The measured

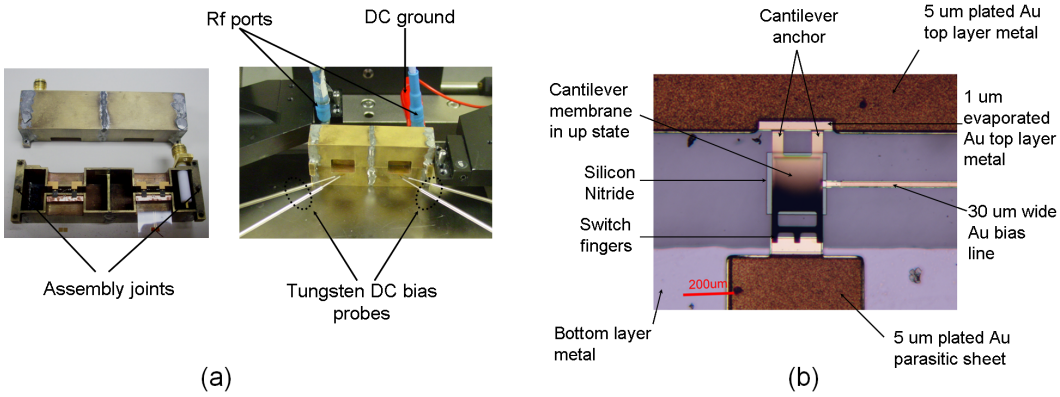

Figure 95: Evanescent mode cavity filter prototype: (a) Photograph of the fabricated tunable bandpass filter; (b) Photograph of the fabricated tuning element illustrating one of the RF-MEMS switches in up state (see color gradient).

unloaded Q drops from 1,800 to 1,080. This is essentially attributed to leakage through the H-wall cut in the cavity and quality of the brass metalization used to build the waveguide housing. To perform a realistic comparison between simulated and measured data of the tunable filter, a 40% drop in Q should and will be added to the simulated results. This will better highlight the actual impact of the inserted tunable capacitor on the overall filter performance. The fabricated RF-MEMS switches have high stress gradient that result in the cantilever curling (See Figure 95b) and thus a high isolation switch in the up state. The choice of the cantilever size (200 μm $\times$ 430 μm) and thickness (1 μm) along with the different residual stress from the Ti and Au layers of the switch membrane and the CTE mismatch between the Ti/Au cantilever and the photoresist (sacricifial layer) increase creeping of the membrane. This structure was initially designed to keep a moderate actuation voltage, but in our experiments, it turned out that the switches curl too much and a good ohmic contact could not be achieved when the switch is actuated. These switches reliability can be significantly improved by increasing the membrane thickness to 5-7 μm (at the expense of a higher actuation voltage: 60 to 110 V), and using switches with a smaller form-factor leading to a stiffer beam, less curling and longer life cycle.

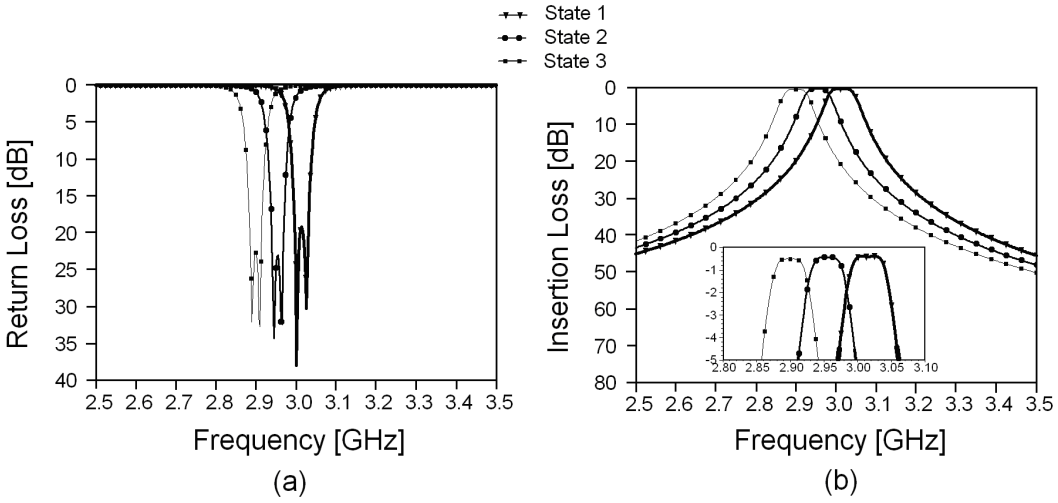

Figure 96: Simulated response of the two-pole digitally RF-MEMS tunable evanescent-mode waveguide bandpass filter: (a) Return loss; (b) Insertion Loss.

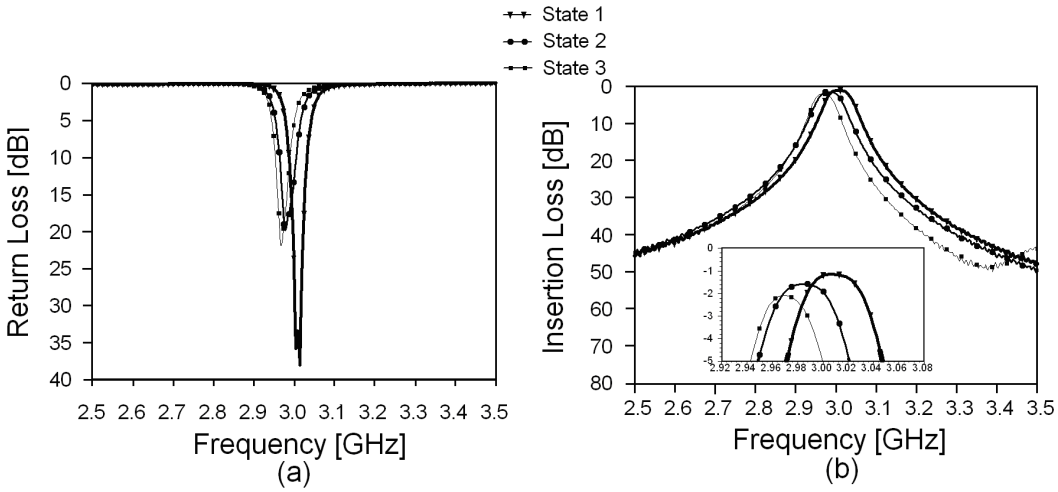

Figure 97: Measured response of the two-pole digitally RF-MEMS tunable evanescent-mode waveguide bandpass filter: (a) Return loss; (b) Insertion Loss.

9.2.3 Filter Characterization

A prototype of the proposed two-pole digitally tunable filter is simulated and measured. The specifications for the filter designed in this work require a total frequency tuning range of only a few hundreds of MHz with a 5 to 10 MHz step between each state around 3 GHz. Thus, this work does not intend to achieve very wide tuning ranges; a C_p value of 30.45 fF is thus chosen by setting $(x_c \times z_c) = (500\ \mu\text{m} \times 300\ \mu\text{m})$. It is however worth mentioning that this does not exclude the capability of the proposed approach to develop

widely tunable filters, where C_p values as high as 347 pF were found to generate up to 31% frequency tuning range. Figures 96 and 97 show the simulated and measured responses of the tunable filter. Full wave simulations predict a starting center frequency of 3.011 GHz and a tuning of 50 MHz between each state. In measurements, the starting center frequency is 6.5 MHz lower than the simulated one, and the frequency tuning is between 15 and 25 MHz. The measured filter tunes less than in simulation because of the curvature of the cantilever, which prevented an ohmic contact between the switch fingers and the parasitic metal sheet in down state. The residual capacitance C_{MEMS} between the switch fingers and the parasitic sheet (when the switch is actuated) is just enough to produce, in the worst case, a 15 MHz frequency shift but not high enough to actually short out the switch membrane with the parasitic sheet. Post-fabrication simulations show that the residual capacitance for a 25 MHz frequency shift from state 1 to state 2 is $C_{MEMS} = 135$ fF, which corresponds to approximately 0.5 μm gap between the switch fingers and the parasitic sheet. From state 2 to state 3, the frequency shift is 15 MHz and the residual capacitance is found to be $C_{MEMS} = 65$ fF, which corresponds to about 1 μm gap between the switch fingers and the parasitic sheet. The simulated 1-dB fractional bandwidth is 1.8-1.9%, and the measured fractional 1-dB bandwidth is 1.2-1.5%, which allows this filter to be categorized as narrow band. The measured filter has a good matching (better than 18 dB) and also an insertion loss of 2.1 dB in the worst case. It can be noticed that each time a switch is actuated, 0.5 dB is added to the loss of the measured filter. The major contributor to this increase in the loss is the limited Q of the loading tuning elements. The tuning elements are located right in between the two ridges where the electromagnetic (EM) field is stronger (for better tuning efficiency), and will thus affect in a significant proportion the loss performance of the filter. The simulated unloaded Q varies from 1,035 to 1,355 whereas the measured Q varies from 315 to 460. To perform a realistic comparison between the simulated and measured Q, recall that from the measurement of the empty cavity, at least 40% decrease in the Q of the filter needs to be taken into account because of the imperfect cavity assembly and leakage through the H-plane cut. Once the quartz substrate is inserted in the cavity, the H-wall opening is kept a bit wider to prevent cracking of the thin quartz chip. This will be a source

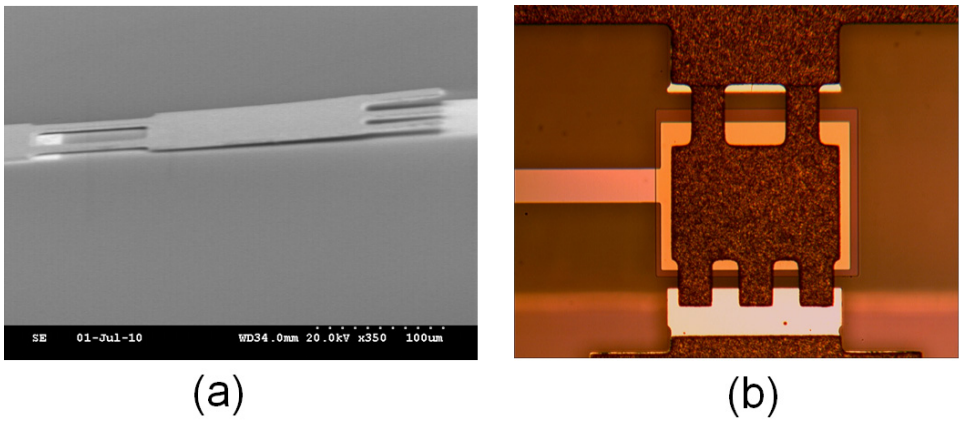

Figure 98: Fabricated low-stress gradient RF-MEMS switch: (a) SEM photograph with a side view of the released cantilever; (b) Top view of the switch.

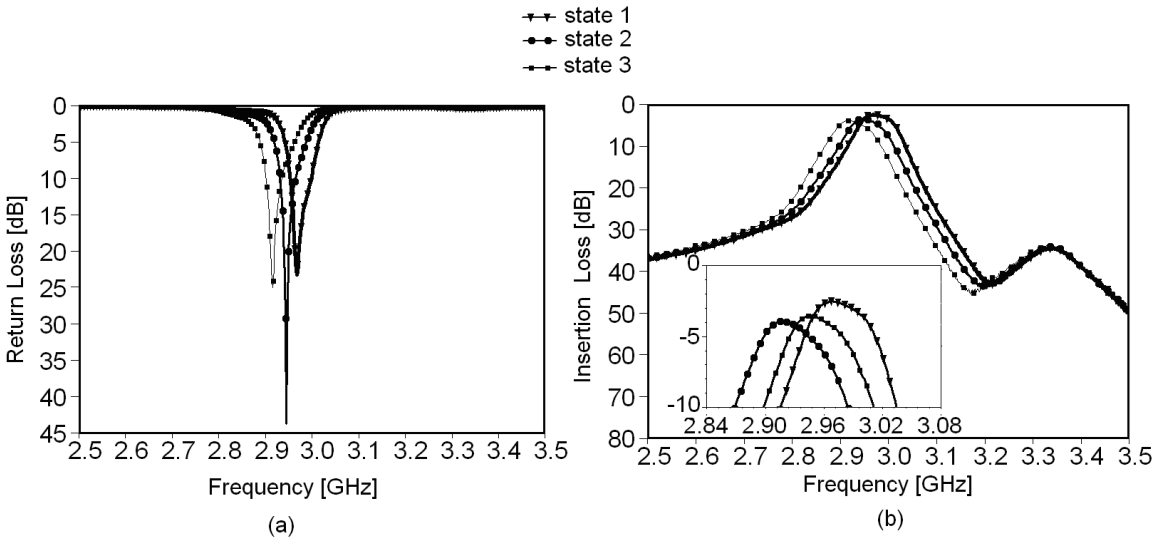

Figure 99: Measured response of the tunable evanescent-mode filter with a low stress gradient cantilever: (a) Return loss; (b) Insertion Loss.

for increased loss. The simulated Q would thus drop, at least, to effective values of 621 to 823 through the tuning range. These values are still twice as high as the measured Q (315 to 460). It is believed that the origin of this additional loss is partially due to the de-tuning of the poles from one resonator to the other one, dissipation into the bias lines, and also leakage through the H-wall plane that could not be tighten enough to avoid breakage of the quartz chips.

9.2.4 On the Improvement of the Tunable Filter Performance

In order to achieve the predicted tuning range, it is important that the RF-MEMS switch has both the desired isolation in the upstate and excellent ohmic contact when pulled down. The 1 μm thick cantilever with high stress gradient provided enough isolation in the up state but could not achieve ohmic contact due to excessive upward curling of the beam. A similar switch with a stiffer beam (See Figure 98) and a 1 μm gap between the cantilever and the actuation pad was thus fabricated to verify that the proposed filter can indeed cover the lower frequency range if a low-stress switch is used. The low stress switch has a 6 μm thick Au electroplated beam of size 320 μm $\times$ 260 μm. The measured three states are 2.97, 2.94 and 2.91 GHz (state 1, 2 and 3 respectively). Note that the state 1 frequency is 40 MHz below the expected value when all switches are up. This clearly comes from the implemented 1 μm gap between the cantilever and the parasitic metal sheet, which translates into a low isolation switch in the up state. However, the tuning step is 30 MHz between each state and has definitely been improved compared to the high stress gradient beam. Moreover, the state 3 frequency matches exactly the expected 3.1 GHz from simulation. It is thus concluded that a cantilever beam with sufficient up state isolation (2 to 3 μm gap) and a low stress gradient is necessary to achieve the expected tuning range. Recall that a higher up state isolation will necessitate a pull down voltage in the range of 70 to 110 V. The 6 μm switch pulled down at 65 V but with only 1 μm gap. The loss performance of this last filter implementation is a bit worse because of a clear de-tuning of the poles from one resonator to the other one, and also the higher loading capacitance required to reach lower frequencies. It is thus useful to implement a switch with analog tuning capabilities in order to fine tune the poles at each state [80]. The filter bandwidth can thus be adjusted at each state to keep a reasonable fractional bandwidth and a good insertion loss in the passband. Another aspect that needs significant improvement is the routing of the bias lines. In the current implementation of the tunable filter, the bias lines are right inside the strong RF region and thus contribute to important leakage inside the bias lines and through the slots made to route the bias lines outside the cavity. Unless the filter can be implemented with a self-biasing technique (bias from the RF access ports and not bias lines), the bias network

Table 7: Comparison of tunable filters technologies for Q over 400

Parameter	**[80]**	**[53]**	**[102]**	**[67]**	**This Work [20]**
Frequency range (GHz)	4-6	3-5.6	15.6-16	3.04-4.71	2.96-3
Fractional bandwidth $\Delta_{1dB}(\%)$	0.45-0.7	0.3-0.5	1-1.3	0.6-0.8	1.2-1.5
Insertion loss (dB)	3.1-4.9	3.4-5.4	1.5-4.5	2.38-3.55	1.1-2.1
Quality factor Q	300-500	500-750	300-900	470-645	315-460
Technology	Capacitive RF-MEMS switches with metal cavity	Piezoelectric disk actuator with SIW	Thermal MEMS actuator with dielectric resonator	Electrostatic SOI-based MEMS actuator with SIW	Ohmic RF-MEMS switches with metal cavity

needs to be located in a region of weakest field. Such an implementation with bias lines located at the voltage null has been shown in [80, 81]. The last aspect that also influenced the loss performance of the proposed filter is the mounting scheme of the quartz chips inside the cavity. The chips could be mounted inside pockets within the cavity walls to minimize opening of the waveguide and hence obtain a better sealed cavity.

9.3 Comparison with Other Concepts for High-Q (≥ 400) Tunable Filters

The topic on high-Q tunable filters has earned a particular interest in the recent years with the development of very robust filters structures. Table 7 identifies the most recent work reported in the literature. Tank-based filters that utilize piezoelectric, thermal or electrostatic actuators provide exceptional performance filters over a moderate to very wide continuous tuning range [53, 67, 102]. RF-MEMS (capacitive [80] or ohmic [20]) circuit-based filters have been achieved with discrete tuning, but can also be implemented for continuous tuning with the use of high capacitance ratio (100:1) capacitive switches. To

date, RF-MEMS switches have been reported with a Q as high as 400 up to 100 GHz [86], and this is the reason why they are preferred over diode varactors or BST devices for this type of application. Although the measured performance of the filter proposed in this work shows a limited tuning range, the full-wave model along with the identified improvement perspectives enhance the potential of this feasibility study on narrowband tunable filters.

CHAPTER 10

FOLDED CAVITY RESONATOR FILTERS WITH MAGNETIC SOURCE-LOAD CROSS COUPLING

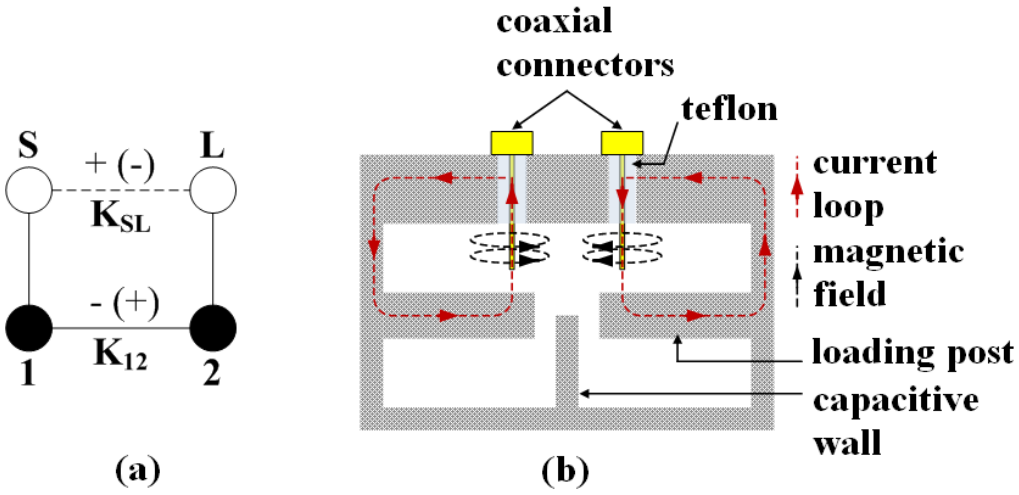

Figure 100: Folded cavity resonator filter: (a) Coupling scheme of cross coupled folded resonators filters; (b) proposed folded cavity resonator filter with magnetic source-load cross coupling.

Source-load cross coupled folded resonator filters are an attractive approach to design compact size canonical filters with sharp roll-off because n finite transmission zeros (FTZs) can be generated near the passband with only n resonators [21,28,30,71]. This result stems from the source-load coupling path K_{SL} that is provided in addition to the direct coupling path K_{12} between nonadjacent resonators while enforcing opposite polarities between K_{SL} and K_{12}, as shown in Figure 100a. Practical implementations of filters meeting this requirement often utilize an electric source-load cross coupling scheme where the resonators are magnetically coupled to each other [62,79,90]. Alternatively, the source-load cross coupling is magnetic while the inter-resonator coupling is electric [34]. In both cases, it has so far been necessary to add either surface mount devices (SMDs) or sections of transmission lines to properly implement the required source-load cross coupling. Although SMDs can be easily added to planar filter topologies, they are not recommended for cavity filters because of

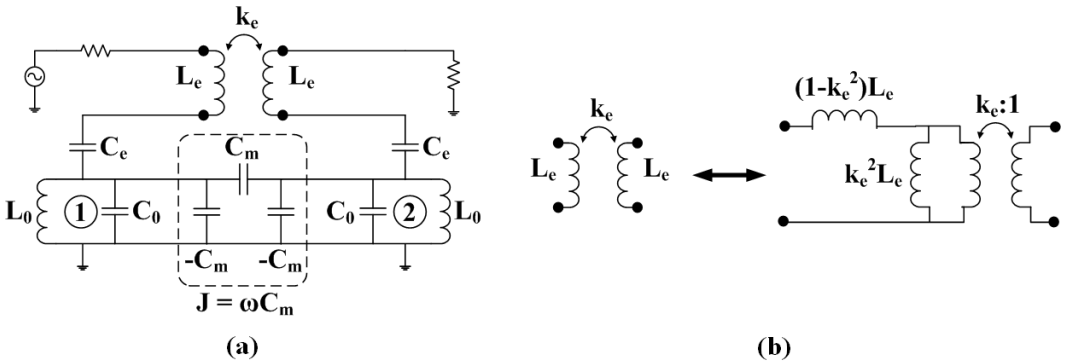

Figure 101: Circuit model of proposed filter concept: (a) Equivalent circuit model of a folded resonator filter with magnetic source-load cross coupling; (b) real transformer and its equivalent cantilever circuit model.

their limited quality factor. Besides, additional lengths of transmission lines (or waveguide sections) increase the size and complexity of the filter topology, especially when it comes to prototyping mass-producible cavity filters at a low cost.

This chapter describes a versatile technique to implement magnetic source-load cross coupling with folded cavity resonator filters. The proposed filter topology is shown in Figure 100b. It is composed of two post loaded cavity resonators that are connected in a back-to-back configuration to realize the folded architecture. The inter-resonator coupling is controlled with a capactive iris. Then, two coaxial probes used as the filter ports are proximity coupled through the iris apex to realize the source-load cross coupling. Each probe center conductor is surrounded by a magnetic field induced by the current loop. The mutual magnetic coupling between the probes thus controls the necessary amount of magnetic coupling to generate FTZs near the filter passband. The advantage of this topology is that it does not require any additional waveguide section while keeping manufacturing fairly easy to reduce costs. An equivalent circuit model is proposed to explain the behavior of such filter topologies. A second order cavity bandpass filter is fabricated to demonstrate the validity of this technique.

10.1 Theory of Magnetic Source-Load Cross Coupling

10.1.1 Admittance Transfer Function

The symmetric lossless circuit model in Figure 101a is utilized to derive the Y_{21} function of the filter's admittance matrix. The mutual coupling between the source and load inductors L_e is symbolized as a real transformer of coupling coefficient k_e, to which a simplified cantilever model is provided in Fig. 78b. The electric coupling between nonadjacent resonators is symbolized with a J-inverter ($J = \omega C_m$); note that for narrow band applications, we can assume that $C_m \ll C_0$, in which case -C_m is absorbed into C_0.

The impedance matrix of the transformer is given by

$$Z_{k_e} = sL_e \begin{pmatrix} 1 & k_e \\ k_e & 1 \end{pmatrix}. \tag{25}$$

The impedance matrix of the bottom circuit is given by

$$Z_r = sL_0 \begin{pmatrix} \frac{\omega_e^2}{s^2}\frac{N_{z,r}}{D_{z,r}} & \frac{s^2}{\omega_m^2}\frac{1}{D_{z,r}} \\ \frac{s^2}{\omega_m^2}\frac{1}{D_{z,r}} & \frac{\omega_e^2}{s^2}\frac{N_{z,r}}{D_{z,r}} \end{pmatrix} \tag{26}$$

where $N_{z,r}$ and $D_{z,r}$ are defined as follows:

$$N_{z,r} = 1 + s^2\left(\frac{1}{\omega_e^2} + \frac{2}{\omega_0^2} + \frac{2}{\omega_m^2}\right) + s^4\left[\frac{1}{\omega_0^4} + \frac{1}{(\omega_0\omega_e)^2} + \frac{1}{(\omega_e\omega_m)^2} + \frac{2}{(\omega_0\omega_m)^2}\right] \tag{27}$$

$$D_{z,r} = 1 + s^2\left(\frac{2}{\omega_0^2} + \frac{2}{\omega_m^2}\right) + s^4\left[\frac{1}{\omega_0^4} + \frac{2}{(\omega_0\omega_m)^2}\right], \tag{28}$$

with $\omega_0^2 = 1/L_0C_0$, $\omega_e^2 = 1/L_0C_e$, and $\omega_m^2 = 1/L_0C_m$.

Since the transformer and the bottom circuit are in series, the impedance matrix of the filter is given by

$$Z = Z_{k_e} + Z_r. \tag{29}$$

Equations (25) to (29) are used to derive the admittance transfer function given by

$$Y_{21} = -\frac{1}{sL_0}\frac{N_y}{D_{y,1}D_{y,2}}, \tag{30}$$

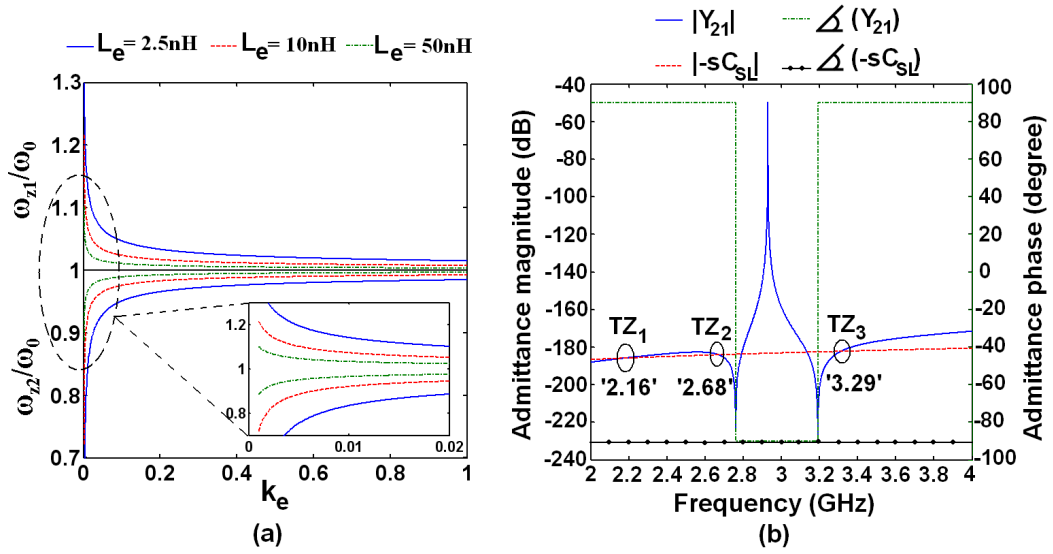

Figure 102: Circuit model filter response: (a) Variations of normalized functions of FTZs with the transformer coupling coefficient k_e: $C_0 = 0.05$pF, $C_m = 0.002$fF, $C_e = 1.4$fF, and $L_0 = 57.5$nH; (b) Transfer functions of $Y_{21}(s)$ and -$sC_{SL}(s)$: $C_0 = 0.05$pF, $C_m = 0.002$fF, $C_e = 1.34$fF, $C_{SL} = 0.037$aF, $L_0 = 57.5$nH, $L_e = 3.9$nH, and $k_e = 0.028$.

where

$$N_y = \frac{s^4}{\omega_m^4}(\frac{s^2}{\omega_m^2} + k_e\frac{L_e}{L_0}D_{z,r})D_{z,r} \tag{31}$$

$$D_{y,1} = (1+k_e)\frac{L_e}{L_0}\frac{s^2}{\omega_m^2}D_{z,r} + (\frac{\omega_e^2}{\omega_m^2}N_{z,r} + \frac{s^4}{\omega_m^4}) \tag{32}$$

$$D_{y,2} = (1-k_e)\frac{L_e}{L_0}\frac{s^2}{\omega_m^2}D_{z,r} + (\frac{\omega_e^2}{\omega_m^2}N_{z,r} - \frac{s^4}{\omega_m^4}). \tag{33}$$

10.1.2 Two Finite Transmission Zeros

The zeros of $Y_{21}(s)$ are the nontrivial roots of $N_y(s)$. After replacing s by $\jmath\omega$ and k_eL_e/L_0 by ζ_e, the two FTZs of the derived filtering function are given by

$$\omega_{z1} = \omega_0 \times \left[\frac{\omega_m^2 + (1+\frac{1}{2\zeta_e})\omega_0^2 + \omega_0\sqrt{(1+\frac{1}{2\zeta_e})^2\omega_0^2 + \frac{1}{\zeta_e}\omega_m^2}}{2\omega_0^2+\omega_m^2}\right]^{\frac{1}{2}} \tag{34}$$

$$\omega_{z2} = \omega_0 \times \left[\frac{\omega_m^2 + (1+\frac{1}{2\zeta_e})\omega_0^2 - \omega_0\sqrt{(1+\frac{1}{2\zeta_e})^2\omega_0^2 + \frac{1}{\zeta_e}\omega_m^2}}{2\omega_0^2+\omega_m^2}\right]^{\frac{1}{2}} \tag{35}$$

Figure 102a shows that a strong magnetic coupling between the source and load results in a steep roll-off near the filter passband as the two FTZs located above (ω_{z1}) and below (ω_{z2}) the resonant frequency monotonically converge. Moreover, (23) and (24) suggest that for

a fixed resonator and a fixed inter-resonator coupling, only k_e and L_e control the location of the two FTZs. In other words, the two FTZs can be tuned without affecting the filter resonant frequency and bandwidth. Note that although ω_{z1} and ω_{z2} are invariant with C_e, the resonant frequency of the filter is expected to drop with an increasing C_e because of the loading effect of the source and load.

10.1.3 Three Finite Transmission Zeros

The circuit model shown in Figure 101 assumes that there is no electric coupling between the source and load. However, there always exists some electric coupling between proximity coupled conductors though the magnetic coupling is dominant. In this section, we investigate the effect of a shunt feedback capacitor C_{SL} between the source and load to account for the parasitic electric coupling. The condition for FTZs in the stopband is now defined as

$$Y_{21}(s) - sC_{SL} = 0. \tag{36}$$

It is more challenging to derive a closed-form solution for (36). Alternatively, this problem may be solved numerically. The transfer function $Y_{21}(s)$ of the circuit without the shunt capacitor is plotted on the same graph along with the transfer function -$sC_{SL}(s)$ of the capacitor. To satisfy (36), both transfer functions must have the same magnitude but opposite phase. Therefore, looking at Figure 102b where $C_{SL} = 0.037$ aF, it can be shown that the complete circuit including the parasitic capacitor exhibits three FTZs. Figure 102b also suggests that all three transmission zeros are dependant on the value of C_{SL}. In particular, an increasing C_{SL} moves TZ_2 and TZ_3 away from the center frequency whereas TZ_1 moves closer to it. Intuitively, the out-of-phase parasitic capacitance of the transformer tends to decrease the magnetic coupling between the source and load. There also exists a maximum value of C_{SL} beyond which TZ_1 and TZ_2 are suppressed.

10.2 Folded Cavity Bandpass Filter Design and Characterization

A second order bandpass filter is designed and built based on the proposed concept. Evanescent-mode rectangular waveguide cavities are utilized to build compact resonators (see Figure 103a). A rectangular waveguide of section $w \times l$ and height h is loaded with a center

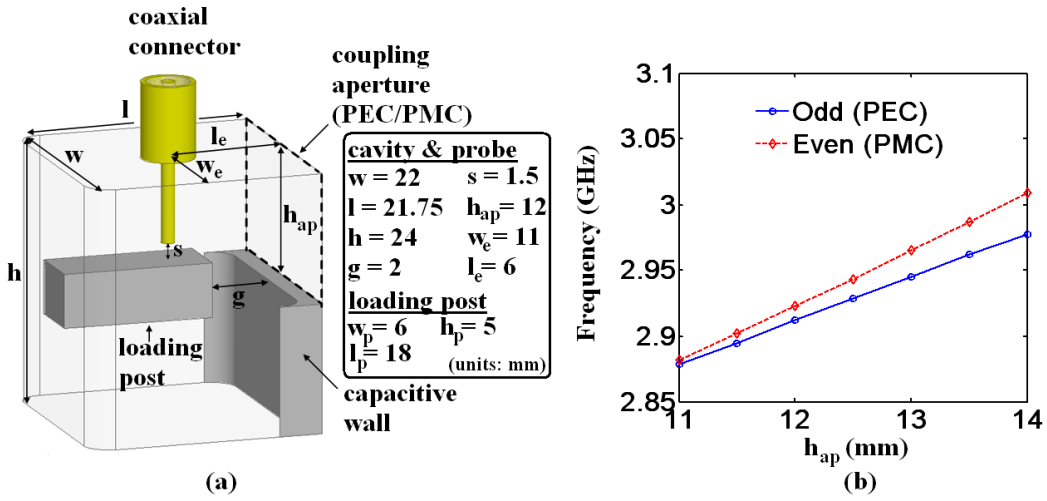

Figure 103: Folded waveguide cavity bandpass filter: (a) Half of the folded cavity filter full-wave model; (b) even and odd mode resonant frequencies as a function of coupling aperture h_{ap}.

post of gap g. The guided wavelength for this resonator is given by

$$\lambda_g = \frac{\lambda_0}{\sqrt{\left(\frac{\lambda_0}{\lambda_c}\right)^2 - 1}}, \tag{37}$$

where λ_0 and λ_c are the free space and cut-off wavelengths respectively. The size of the resonator cavity for a specific resonant frequency is optimized using the eigenmode solver in HFSS [1]. Note that the internal filter volume is only 23 cm^3. The inter-resonator coupling is controlled with a capacitive iris by tuning its height h_{ap}. Figure 103b shows the odd/even mode frequency variations with h_{ap} when the filter symmetry plane is terminated in a perfect electric conductor (PEC)/perfect magnetic conductor (PMC). Because the even mode frequency is higher than the odd mode one, one can claim that the inter-resonator coupling is in fact electric. The aforementioned magnetic source-load coupling scheme may then implemented to generate FTZs near the passband.

Two coaxial probe connectors are arranged in parallel inside the cavity housing and couple to each other through the iris apex. Each probe is located in the cavity H-symmetry plane (w_e=$w/2$) to maximize coupling to the resonator. The coupling gap s controls the I/O matching. The separation distance l_e between parallel probes is approximately $\lambda_g/4$ to provide an out-of-phase path with respect to the direct coupling path. l_e is therefore

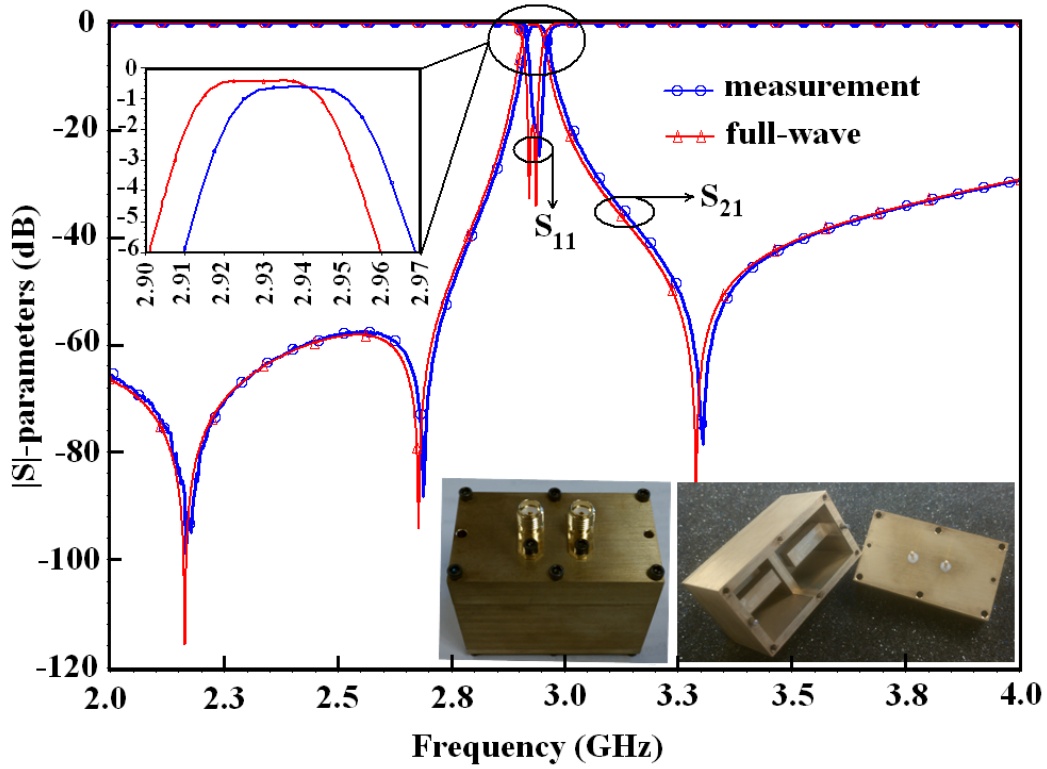

Figure 104: Simulated and measured S-parameters of the second order bandpass filter with magnetic source-load cross coupling. The filter is fabricated with brass material.

optimized with the full-wave HFSS solver keeping in mind that a decreasing l_e translates into a higher mutual magnetic coupling. Although the coupling between probes is predominantly magnetic, there exists a parasitic weak electric coupling that stems from the difference of potentials between the probes center conductors. To show the validity of the proposed concept, a second order bandpass filter is designed to resonate at 2.93 GHz with three finite transmission zeros at 2.16 GHz, 2.68 GHz, and 3.29 GHz. The filter dimensions are optimized with HFSS. Using a quasi-static approximation, the circuit parameters of Figure 101 can also be extracted. Figure 102b shows the transfer function of the circuit model where three FTZs are clearly identified. Figure 104 shows the full-wave simulated and measured S-parameters. Excellent agreement is achieved. The measured center frequency is 2.94 GHz, that is, 10 MHz higher than expected. The measured and simulated insertion losses are 0.65 dB and 0.47 dB at the center frequency. The corresponding 1dB bandwidth is 1.15% in measurement and 1.18% in simulation. As expected, three transmission zeros

are identified in the measured stopband at 2.17 GHz, 2.69 GHz and 3.3 GHz, with a 10 MHz shift compared to theory.

This work demonstrated how to generate a canonical response with folded cavity resonator filters using magnetic source-load cross coupling. A circuit model was derived to analyze the transfer function of such filter topologies. The proposed concept was validated with a second order bandpass filter and may be extended to higher order filters.

CHAPTER 11

CONTRIBUTIONS

- A frequency reconfigurable evanescent-mode cavity resonator band pass filter integrated with ohmic RF-MEMS switches is designed for operation in the S-band. The proposed design employs RF-MEMS technology to realize high quality factor filters with narrow bandwidth and improved linearity. RF-MEMS switches are monolithically integrated onto a quartz chip that is inserted into the waveguide cavities and acts as a switchable capacitor when the state of the switch is toggled. This is the first demonstration of a frequency switchable cavity resonator filter integrated with ohmic RF-MEMS switches.

- Folded cavity evanescent-mode resonator filters with magnetic source-load cross coupling that employ a pair of proximity coupled coaxial probe connectors to achieve the magnetic coupling are designed for the first time. It is shown that at least two finite transmission zeros near the passband can be generated with only one pair of resonators. A closed-form representation of the transmission zeros is derived using a circuit model where the coupled coaxial probes are represented by an equivalent transformer circuit. The developed folded source-load structure can be used as termination circuit for higher order folded cavity resonator filters.

CHAPTER 12

OPEN TOPICS FOR FUTURE RESEARCH

This dissertation can be extended into a number of different directions.

- The end-fire radiator that is integrated into the MLO packaged module is an array of four elements that currently has a fixed beam. It is suggested to integrate a phase shifter to steer the beam at end-fire. The phase shifter shall be an on-chip circuit that can be easily integrated into the package module using the proposed methodology. Moreover, three additional end-fire arrays may be added to each side of the module package for a full 360° azimuth coverage. In such a case, a single pole five throw switch is necessary to control each end-fire radiator in addition to the broadside one.

- For access point types of platforms or laptop computers that do not put as stringent limits on size as smartphone devices, the MLO package design may integrate multiple broadside radiators adjacent to each other to synthesize an array with broadside radiation and beam steering capability if desired. The previous item may be applied to this architecture as well and this ultimately results in a multi-beam antenna system.

- The next evident work that follows efforts accomplished on the proposed folded cavity resonator with magnetic source-load cross coupling is to extend the concept to higher order filters.

- The second order folded cavity resonator filter may be made tunable with the insertion of a single chip RF-MEMS switch network to load a back-to-back folded evanescent mode filter.

APPENDIX A

MICROELECTRONIC FABRICATION

This section describes the fabrication process used to selectively electroplate gold (Au) pads on top of Cu for wire bonding purposes. We noticed that due to LCP softness, it is helpful to electroplate a thick (8 to 10 μm) Au layer selectively to improve yield for wire bonding. A thick mould must be created. This process does not use the standard Ni/Au coating. It should be noted that since we plate locally to the pads, the entire plating process is actually relatively fast. This recipe has been developed for Cu on top of a 4 mil thick LCP substrate.

Mould Formation:

1. Sputter a thin 200Ålayer of titanium (Ti) on top of Cu layer (the Ti layer will help preventing underplating below the mould)
2. Dehydrate wafer in Oven at 110C for 1min
3. Spin SPR220-7 at 2000 rpm for 45 s with an acceleration of 500 to obtain roughly 9 μm PR
4. Softbake at 105°C (set on hot plate) for 6 mn
5. Cool down for 30 mn
6. Expose using the following parameters on the Karl-Suss MA6 aligner: 700/I = time with channel 2 (Soft Contact)
7. Hold for 40 mn or wait to proceed overnight
8. Post expose bake at 110°C for 5 mn
9. Cool down for 30 mn
10. Develop for about 2-5 mn with agitation (depends on hold time after exposure)

11. Hardbake in oven at 115°C for 30 mn (see resist reflow on microscope)

12. Hold for 1 hour

Au Plating:

1. Before starting the plating process, the thin Ti layer at the pad locations is etched off in a 1:20 diluted HF solution

2. Set the temperature of the 434HS-RTU Au plating solution to 125°C to get about 65°C in the solution and rotate at 200 rpm

3. With a new solution, the plating rate may be estimated from Rate (μm/mn) = 8.25 * I(mA)/S(mm^2)

4. Keeping the current density at I/S = 0.032 mA/mm^2 results in a 0.26μm/mn rate

5. Adjust the current from the power supplier to get desired rate. It is recommended to start at a low rate to prevent formation of bubbles at the interface between Cu and Au. The plating rate may the be increased but usually it drops again toward the end of the process to have a good quality Au layer on top for better bonding yield.

PUBLICATIONS

Following is a selected list of publications to date.

A.1 Invention Disclosure

"3D mm-Wave Active Antenna Modules on Organic Packages with Multi-Beam Operation," invention disclosure filed under GTRC-5573 with the Georgia Tech Office of Technology Licensing.

A.2 Journal Papers

1. **A. L. Amadjikpè** and J. Papapolymerou, "Folded Evanescent Mode Cavity Resonator Filters with Magnetic Source-Load Cross Coupling," submitted for publication in the *IEEE Microwave and Wireless Components Letters*.

2. **A. L. Amadjikpè**, D. Choudhury, G. E. Ponchak, and J. Papapolymerou, "Location specific coverage with wireless platform integrated 60-GHz antenna systems," *IEEE Transactions on Antennas and Propagation*, vol. 59, no. 7, pp. 2661-2671, July 2011.

3. **A. L. Amadjikpè**, D. Chung, S. Courrèges, P. Eudeline, A. Ziaei, and J. Papapolymerou, "Two-pole digitally tunable evanescent-mode waveguide narrow-band filter with radio frequency micro-electromechanical systems switches," *IET Microwaves, Antennas and Propagation*, vol. 5, no. 4, pp. 393-401, April 2011.

4. **A. L. Amadjikpè**, D. Choudhury, G. E. Ponchak, B. Pan, Y. Li, and J. Papapolymerou, "Proximity effects of plastic laptop covers on radiation characteristics of 60-GHz antennas," *IEEE Antennas and Wireless Propagation Letters*, vol. 8, pp. 763-766, July 2009.

A.3 Conference Papers

1. **A. L. Amadjikpè**, D. Choudhury, G. E. Ponchak, and J. Papapolymerou, "60-GHz Switched-Beam End-fire Antenna Module Integrated with Novel Microstrip-to-Slot Transition," *2011 IEEE MTT-S International Microwave Symposium Dig*, pp. 1-4, Baltimore, MD, June 2011.

2. **A. L. Amadjikpè**, D. Choudhury, G. E. Ponchak, and J. Papapolymerou, "60-GHz Antenna Integration in a Laptop Computer Base for WPAN Applications," *2011 IEEE MTT-S Radio and Wireless Symposium Dig.*, pp. 46-49, Phoenix, AZ, January 2011.

3. **A. L. Amadjikpè**, D. Choudhury, G. E. Ponchak, and J. Papapolymerou, "Highly directive package-integrated dipole arrays for low-cost 60-GHz front end modules," *2010 IEEE MTT-S International Microwave Symposium Dig.*, pp. 348-351, Anaheim, CA, May 2010. **Student paper competition finalist**

4. **A. L. Amadjikpè**, D. Choudhury, G. E. Ponchak, and J. Papapolymerou, "High gain quasi-Yagi planar antenna evaluation in platform material environment for 60 GHz wireless applications," *2009 IEEE MTT-S International Microwave Symposium Dig.*, pp. 385-388, Boston, MA, June 7-12, 2009.

5. **A. L. Amadjikpè**, D. Choudhury, G. E. Ponchak, and J. Papapolymerou,"A compact conformal end fire antenna for 60 GHz wireless applications," *2009 IEEE Antennas and Propagation Symposium Dig.*, pp. 1-4, Charleston, SC, June 1-5, 2009.

6. **A. L. Amadjikpè**, A. Vera, D. Choudhury, and J. Papapolymerou, "Study of a 60 GHz rectangular patch antenna on a flexible LCP substrate for mobile applications," *2008 IEEE Antennas and Propagation Symposium Dig.*, pp. 1-4, San Diego, CA, July 5-11, 2008.

7. **A. L. Amadjikpè** and J. Papapolymerou, "A high-Q electronically tunable evanescent-mode double-ridged rectangular waveguide resonator," *2008 IEEE MTT-S International Microwave Symposium Dig.*, pp. 1019-1022, June 2008.

REFERENCES

[1] "www.ansoft.com/products/hf/hfss/," Ansys HFSS v13.

[2] "www.corning.com/gilbert/," Corning Gilbert.

[3] "www.cst.com," CST Microwave Studio 2010.

[4] "www.feko.info," FEKO.

[5] "www.hittite.com," Hittite Microwave Corporation.

[6] "www.ieee802.org/11/reports/tgadupdate.htm," IEEE 802.11 Task Group ad (TGad).

[7] "www.ieee802.org/15/pub/tg3c.html," IEEE 802.15 WPAN Task Group 3c (TG3c).

[8] "www.nec2.org," NEC.

[9] "www.ecma-international.org/publications/standards/ecma-387.htm," Standard ECMA-387 High Rate 60 GHz PHY, MAC and HDMI PALs.

[10] "http://wirelessgigabitalliance.org/," Wireless Gigabit Alliance.

[11] "www.wirelesshd.org/news/press.html," WirelessHD consortium.

[12] Abele, P., Öjefors, E., Schad, K.-B., Sonmez, E., Trasser, A., Konle, J., and Schumacher, H., "Wafer level integration of a 24 ghz differential sige-mmic oscillator with a patch antenna using bcb as a dielectric layer," in *Proceedings of the 33rd European Microwave Conference*, (Munich, Germany), pp. 293–296, 2003.

[13] Abou-Jaoude, R. and Walton, E. K., "Numerical modeling of on-glass conformal automobile antennas," *IEEE Transactions on Antennas and Propagation*, vol. 46, no. 6, pp. 845–852, 1998.

[14] Ahmadi, M. R. N., Safieddin, S. N., and Zhu, L., "On-chip antennas for 24, 60, and 77 ghz single package transceivers on low resistivity silicon substrate," in *Proceedings of the 2007 IEEE Antennas and Propagation Society International Symposium*, (Honolulu, HI), pp. 5059–5062, 2007.

[15] Alexopoulos, N. G., Katehi, P. B., and Rutledge, D. B., "Substrate optimization for integrated circuit antennas," *IEEE Transactions on Microwave Theory and Techniques*, vol. 31, no. 7, pp. 550–557, 1983.

[16] Amadjikpè, A. L., Choudhury, D., Ponchak, G. E., Pan, B., Li, Y., and Papapolymerou, J., "Proximity effects of plastic laptop covers on radiation characteristics of 60-ghz antennas," *IEEE Antennas and Wireless Propagation Letters*, vol. 8, no. 1, pp. 763–766, 2009.

[17] Amadjikpè, A. L., Choudhury, D., Ponchak, G. E., and Papapolymerou, J., "High gain quasi-yagi planar antenna evaluation in platform material environment for 60 ghz wireless applications," in *Proceedings of the 2009 IEEE MTT-S International Microwave Symposium*, (Boston, MA), pp. 385–388, 2009.

[18] Amadjikpè, A. L., Choudhury, D., Ponchak, G. E., and Papapolymerou, J., "Highly directive package-integrated dipole arrays for low-cost 60-ghz front end modules," in *Proceedings of the 2010 IEEE MTT-S International Microwave Symposium*, (Anaheim, CA), pp. 348–351, 2010.

[19] Amadjikpè, A. L. and Papapolymerou, J., "A high-q electronically tunable evanescent-mode double-ridged rectangular waveguide resonator," in *Proceedings of the 2008 IEEE MTT-S International Microwave Symposium*, (Atlanta, GA), pp. 1019–1022, 2008.

[20] Amadjikpè, A. L., Chung, D. J., Courrèges, S., Eudeline, P., Ziaei, A., and Papapolymerou, J., "Two-pole digitally tunable evanescent-mode waveguide narrow band filter with rf-mems switches," *IET Microwaves, Antennas & Propagation Journal*, vol. 5, no. 4, pp. 393–401, 2011.

[21] Amari, S., "Direct synthesis of folded symmetric resonator filters with source-load coupling," *IEEE Microwave and Wireless Components Letters*, vol. 11, no. 6, pp. 264–266, 2001.

[22] Atesal, Y. A., Cetinoneri, B., Chang, M., Alhalabi, R., and Rebeiz, G., "Millimeter-wave wafer-scale silicon bicmos power amplifiers using free-space power combining," *IEEE Transactions on Microwave Theory and Techniques*, vol. 59, no. 4, pp. 954–965, 2011.

[23] Bahar, E., "Excitation of surface waves and the scattered radiation fields by rough surfaces of arbitrary slope," *IEEE Transactions on Microwave Theory and Techniques*, vol. 28, no. 9, pp. 999–1006, 1980.

[24] Balanis, C. A., *Antenna Theory Analysis and Design second edition*, p. 45. USA: John Wiley & Sons, 1997.

[25] Balanis, C. A., *Antenna Theory Analysis and Design second edition*, pp. 816–839. USA: John Wiley & Sons, 2005.

[26] Balanis, C. A., *Antenna Theory Analysis and Design second edition*, pp. 464–467. USA: John Wiley & Sons, 2005.

[27] Barka, A. and Caudrillier, P., "Domain decomposition method based on generalized scattering matrix for installed performance of antennas on aircraft," *IEEE Transactions on Antennas and Propagation*, vol. 55, no. 6, pp. 1833–1842, 2007.

[28] Bell, H. C., "The coupling matrix in low-pass prototype filters," *IEEE Microwave Magazine*, vol. 8, no. 2, pp. 70–76, 2007.

[29] Bogdanov, F. G., Karkashadze, D. D., Jobava, R. G., Gheonjian, A. L., Yavolovskaya, E. A., Bondarenko, N. G., and Ullrich, C., "Validation of

hybrid mom scheme with included equivalent glass antenna model for handling automotive emc problems," *IEEE Transactions on Electromagnetic Compatibility*, vol. 52, no. 1, pp. 164–172, 2010.

[30] Cameron, R. J., "Advanced coupling matrix synthesis techniques for microwave filters," *IEEE Transactions on Microwave Theory and Techniques*, vol. 51, no. 1, pp. 1–10, 2003.

[31] Carrillo-Ramirez, R. and Jackson, R. W., "A technique for interconnecting millimeter wave integrated circuits using bcb and bump bonds," *IEEE Microwave and Wireless Components Letters*, vol. 13, no. 6, pp. 196–198, 2003.

[32] Chan, K. T., Chin, A., Chen, Y. P., Lin, Y. D., Duh, T. S., and Lin, W. J., "Integrated antennas on si, proton-implanted si and si-on-quartz," in *Proceedings of the 2001 International Electron Devices Meeting*, pp. 40.6.1–40.6.4, 2001.

[33] Chen, I.-S., Chiou, H.-K., and Chen, N.-W., "V-band on-chip dipole-based antenna," *IEEE Transactions on Antennas and Propagation*, vol. 57, no. 10, pp. 2853–2861, 2009.

[34] Chen, X.-P. and Wu, K., "Substrate integrated waveguide cross-coupled filter with negative coupling structure," *IEEE Transactions on Microwave Theory and Techniques*, vol. 56, no. 1, pp. 142–149, 2008.

[35] Chen, Z. N., Liu, D., and Gaucher, B. P., "A planar dualband antenna for 2.4 ghz and uwb laptop applications," in *Proceedings of the 2006 IEEE Vehicular Technology Conference*, (Melbourne, Vic), pp. 2652–2655, 2006.

[36] Chuang, H.-R., Yeh, L.-K., Kuo, P.-C., Tsai, K.-H., and Yue, H.-L., "A 60-ghz millimeter-wave cmos integrated on-chip antenna and bandpass filter," *IEEE Transactions on Electron Devices*, vol. 58, no. 7, pp. 1837–1845, 2011.

[37] Craven, G. F. and Mok, C. K., "The design of evanescent-mode waveguide bandpass filters for a prescribed insertion loss characteristic," *IEEE Transactions on Microwave Theory and Techniques*, vol. 19, no. 3, pp. 295–308, 1971.

[38] Crone, G. A. E., Rudge, A. W., and Taylor, G. N., "Design and performance of airborne radomes: a review," *IEE Proceedings on Communications, Radar and Signal Processing*, vol. 128, no. 7, pp. 451–464, 1981.

[39] Özdemir, T., Nurnberger, M. W., Volakis, J. L., Kipp, R., and Berrie, J., "A hybridization of finite-element and high-frequency methods for pattern prediction for antennas on aircraft structures," *IEEE Antennas and Propagation Magazine*, vol. 38, no. 3, pp. 28–38, 1996.

[40] Deal, W. R., Kaneda, N., Sor, J., Qian, Y., and Itoh, T., "A new quasi-yagi antenna for planar active antenna arrays," *IEEE Transactions on Microwave Theory and Techniques*, vol. 48, no. 6, pp. 910–918, 2000.

[41] Elliott, R., *Antenna Theory & Design*, pp. 355–359. Hoboken, NJ: John Wiley & Sons, 2003.

[42] Ellis, T. J., Raskin, J. P., Katehi, L. P. B., and Rebeiz, G. M., "A wideband cpw-to-microstrip transition for millimeter-wave packaging," in *Proceedings of the 1999 IEEE MTT-S International Microwave Symposium*, pp. 629–632, 1999.

[43] Fakharzadeh, M., Nezhad-Ahmadi, M.-R., Biglarbegian, B., Ahmadi-Shokouh, J., and Safavi-Naeini, S., "Cmos phased array transceiver technology for 60 ghz wireless applications," *IEEE Transactions on Antennas and Propagation*, vol. 58, no. 4, pp. 1093–1104, 2010.

[44] Felic, G. and Skafidas, S., "Flip-chip interconnection effects on 60-ghz microstrip antenna performance," *IEEE Antennas and Wireless Propagation Letters*, vol. 8, pp. 283–286, 2009.

[45] Gauthier, G., Raskin, J., Katehi, L., and Rebeiz, G., "A 94-ghz aperture-coupled micromachined microstrip antenna," *IEEE Transactions on Antennas and Propagation*, vol. 47, no. 12, pp. 1761–1766, 1999.

[46] Grzyb, J., Liu, D., Pfeiffer, U., and Gaucher, B., "Wideband cavity-backed folded dipole superstrate antenna for 60 ghz applications," in *Proceedings of the 2006 IEEE Antennas and Propagation Society International Symposium*, (Albuquerque, NM), pp. 3939–3942, 2006.

[47] Guterman, J., Moreira, A. A., and Peixeiro, C., "Integration of omnidirectional wrapped microstrip antennas into laptops," *IEEE Antennas and Wireless Propagation Letters*, vol. 5, no. 1, pp. 141–144, 2006.

[48] Hajela, S., Xun, G., and Chappell, W. J., "Widely tunable high-q evanescent-mode resonators using flexible polymer substrates," in *Proceedings of the 2005 IEEE MTT-S International Microwave Symposium*, pp. 2139–2142, 2005.

[49] Harrington, R., *Time-Harmonic Electromagnetic Fields*, pp. 163–171. John Wiley & Sons, 2001.

[50] Hoivik, N., Liu, D., Jahnes, C. V., Cotte, J. M., Tsang, C., Patel, C., Pfeiffer, U., Grzyb, J., Knickerbocker, J., Magerlein, J. H., and Gaucher, B. P., "High-efficiency 60 ghz antenna fabricated using low-cost silicon micromachining techniques," in *Proceedings of the 2007 IEEE Antennas and Propagation Society International Symposium*, (Honolulu, HI), pp. 5043–5046, 2007.

[51] Huff, G. H., Feng, J., Shenghui, Z., Cung, G., and Bernhard, J. T., "Directional reconfigurable antennas on laptop computers: simulation, measurement and evaluation of candidate integration positions," *IEEE Transactions on Antennas and Propagation*, vol. 52, no. 12, pp. 3220–3227, 2004.

[52] Jentzsch, A. and Heinrich, W., "Theory and measurements of flip-chip interconnects for frequencies up to 100 ghz," *IEEE Transactions on Microwave Theory and Techniques*, vol. 49, no. 5, pp. 871–878, 2001.

[53] Joshi, H., Sigmarsson, H. H., Moon, S., Peroulis, D., and Chappell, W. J., "High-q fully reconfigurable tunable bandpass filters," *IEEE Transactions on Microwave Theory and Techniques*, vol. 57, no. 12, pp. 3525–3533, 2009.

[54] Kam, D. G., Liu, D., Natarajan, A., Reynolds, S., Chen, H.-C., and Floyd, B. A., "Ltcc packages with embedded phased-array antennas for 60 ghz communications," *IEEE Microwave and Wireless Components Letters*, vol. 21, no. 3, pp. 142–144, 2011.

[55] Kam, D. G., Liu, D., Natarajan, A., Reynolds, S. K., and Floyd, B. A., "Organic packages with embedded phased-array antennas for 60-ghz wireless chipsets," *IEEE Transactions on Components, Packaging and Manufacturing Technology*, vol. NA, no. NA, p. early access, 2011.

[56] Kang, K., Lin, F., Pham, D.-D., Brinkhoff, J., Heng, C.-H., Guo, Y. X., and Yuan, X., "A 60-ghz ook receiver with an on-chip antenna in 90 nm cmos," *IEEE Journal of Solid-State Circuits*, vol. 45, no. 9, pp. 1720–1731, 2010.

[57] Karim, M. F., Guo, Y.-X., Sun, M., Brinkhoff, J., Ong, L. C., Kang, K., and Lin, F., "Integration of sip-based 60-ghz 4×4 antenna array with cmos ook transmitter and lna," *IEEE Transactions on Microwave Theory and Techniques*, vol. 59, no. 7, pp. 1869–1878, 2011.

[58] Kim, J. J. and Burnside, W. D., "Simulation and analysis of antennas radiating in a complex environment," *IEEE Transactions on Antennas and Propagation*, vol. 34, no. 4, pp. 554–562, 1986.

[59] Kivekas, O., Ollikainen, J., Lehtiniemi, T., and Vainikainen, P., "Bandwidth, sar, and efficiency of internal mobile phone antennas," *IEEE Transactions on Electromagnetic Compatibility*, vol. 46, no. 1, pp. 71–86, 2004.

[60] Kozakoff, D. J., *Analysis of Radome-Enclosed Antennas second edition*, p. 35. Norwood, MA: Arctech House, 2010.

[61] Kuo, C.-C., Lin, P.-A., Lu, H.-C., Jiang, Y.-S., Liu, C.-M., Hsin, Y.-M., and Wang, H., "W-band flip-chip assembled cmos amplifier with transition compensation network for sip integration," in *Proceedings of the 2010 IEEE MTT-S International Microwave Symposium*, (Anaheim, CA), pp. 465–468, 2010.

[62] Kuo, T.-N., Deng, P.-H., Lin, Y.-S., Wang, C.-H., and Chen, C. H., "Compact stopband-extended microstrip bandpass filters with folded quarter-wavelength resonators," in *Proceedings of the 36th IEEE European Microwave Conference*, (Manchester, UK), pp. 552–555, 2006.

[63] Lampe, R. W., "Design formulas for an asymmetric coplanar strip folded dipole," *IEEE Transactions on Antennas and Propagation*, vol. 33, no. 9, pp. 1028–1031, 1985.

[64] Leong, K. M. K. H., Qian, Y., and Itoh, T., "Surface wave enhanced broadband planar antenna for wireless applications," *IEEE Microwave and Wireless Components Letters*, vol. 11, no. 2, pp. 62–64, 2001.

[65] Liu, D., Gaucher, B. P., Flint, E. B., Studwell, T. W., Usui, H., and Beukema, T. J., "Developing integrated antenna subsystems for laptop computers," *IBM Journal of Research and Development*, vol. 47, no. 2-3, pp. 355–367, 2003.

[66] Liu, D., Gaucher, B. P., Pfeiffer, U., and Grzyb, J., *Antenna Theory Analysis and Design second edition*, pp. 145–147. Torquay, UK: John Wiley & Sons, 2009.

[67] Liu, X., Katehi, L. P. B., Chappell, W. J., and Peroulis, D., "High-q tunable microwave cavity resonators and filters using soi-based rf mems tuners," *IEEE Journal of Microelectromechanical Systems*, vol. 19, no. 4, pp. 774–784, 2010.

[68] Low, L., Langley, R., Breden, R., and Callaghan, P., "Hidden automotive antenna performance and simulation," *IEEE Transactions on Antennas and Propagation*, vol. 54, no. 12, pp. 3707–3712, 2006.

[69] McLean, J. S., Wieck, A. D., Ploog, K., and Itoh, T., "Fullwave analysis of open-end discontinuties in coplanar stripline and finite ground plane coplanar waveguide in open environments using a deterministic spectral domain approach," in *Proceedings of the 21st IEEE European Microwave Conference*, (Stuttgart, Germany), pp. 1004–1007, 1991.

[70] Milligan, T. A., *Modern Antenna Design second edition*, p. 332. John Wiley & Sons, 2005.

[71] Montejo-Garai, J. R., "Synthesis of n-even order symmetric filters with n transmission zeros by means of source-load cross coupling," *Electronic Letters*, vol. 36, no. 3, pp. 232–233, 2000.

[72] Murdock, J., Ben-Dor, E., Gutierrez, F., and Rappaport, T. S., "Challenges and approaches to on-chip millimeter wave antenna pattern measurements," in *Proceedings of the 2011 IEEE MTT-S International Microwave Symposium*, (Baltimore, MA), pp. 1–4, 2011.

[73] Nezhad-Ahmadi, M.-R., Fakharzadeh, M., Biglarbegian, B., and Safavi-Naeini, S., "High-efficiency on-chip dielectric resonator antenna for mm-wave transceivers," *IEEE Transactions on Antennas and Propagation*, vol. 58, no. 10, pp. 3388–3392, 2010.

[74] Notaros, B. M., Djordjevic, M. L., Popovic, B. D., and Popovic, Z., "Rigorous em modeling of cars and airplanes," in *Proceedings of the 1999 IEEE Radio and Wireless Conference*, pp. 167–170, 1999.

[75] Obelleiro, F., Landesa, L., Rodriguez, J. L., Pino, A. G., and Pino, M. R., "Directivity optimisation of an array antenna with obstacles within its near-field region," *Electronics Letters*, vol. 33, no. 25, pp. 2087–2088, 1997.

[76] Obelleiro, F., Landesa, L., Taboada, J. M., and Rodriguez, J. L., "Synthesis of onboard array antennas including interaction with the mounting platform and mutual coupling effects," *IEEE Antennas and Propagation Magazine*, vol. 43, no. 2, pp. 76–82, 2001.

[77] Ohira, M., Miura, A., and Ueba, M., "60-ghz wideband substrate integrated-waveguide slot array using closely spaced elements for planar multisector antenna," *IEEE Transactions on Antennas and Propagation*, vol. 58, no. 3, pp. 993–998, 2010.

[78] Ou, Y.-C. and Rebeiz, G. M., "On-chip slot-ring and high-gain horn antennas for millimeter-wave wafer-scale silicon systems," *IEEE Transactions on Microwave Theory and Techniques*, vol. 59, no. 8, pp. 1963–1972, 2011.

[79] Pan, B., Li, Y., Tentzeris, M. M., and Papapolymerou, J., "A novel low-loss integrated 60 ghz cavity filter with source-load coupling using surface micromachining technology," in *Proceedings of the 2008 IEEE MTT-S International Microwave Symposium*, (Atlanta, GA), pp. 639–642, 2008.

[80] Park, S.-J., Reines, I., Patel, C., and Rebeiz, G. M., "High-q rf-mems 46-ghz tunable evanescent-mode cavity filter," *IEEE Transactions on Microwave Theory and Techniques*, vol. 58, no. 2, pp. 381–389, 2010.

[81] Park, S.-J., Reines, I., and Rebeiz, G., "High-q rf-mems tunable evanescent-mode cavity filter," in *Proceedings of the 2009 IEEE MTT-S International Microwave Symposium*, (Boston, MA), pp. 1145–1148, 2009.

[82] Patterson, C. E., Thrivikraman, T. K., Bhattacharya, S. K., Poh, C., Cressler, J. D., and Papapolymerou, J., "Organic wafer-scale packaging for x-band sige low noise amplifier," in *Proceedings of the 39th European Microwave Conference*, (Rome, Italy), pp. 141–144, 2009.

[83] Ponchak, G. E., Amadjikpè, A. L., Choudhury, D., and Papapolymerou, J., "Experimental investigation of 60 ghz transmission characteristics for wpan applications between computers on a conference table," in *Proceedings of the 2011 IEEE Radio and Wireless Symposium*, (Phoenix, AZ), 2011.

[84] Povinelli, M. J., "Finite element analysis of large wavelength antenna radome problems for leading edge and radar phased arrays," *IEEE Transactions on Magnetics*, vol. 27, no. 5, pp. 4299–4302, 1991.

[85] Rawat, D. and Ghannouchi, F. M., "A design methodology for miniaturized power dividers using periodically loaded slow wave structure with dual-band applications," *IEEE Transactions on Microwave Theory and Techniques*, vol. 57, no. 12, pp. 3380–3388, 2009.

[86] Rebeiz, G., Entesari, K., Reines, I., Park, S.-J., El-tanani, M., Grichener, A., and Brown, A., "Tuning in to rf mems," *IEEE Microwave Magazine*, vol. 10, no. 6, pp. 55–72, 2009.

[87] Roudot, B., Mosig, J. R., and Gardiol, F. E., "Surface wave fields and efficiency of microstrip antennas," in *Proceedings of the 18th European Microwave Conference*, (Melbourne, Vic), pp. 1055–1062, 2006.

[88] Sambell, A., Lowes, P., and Korolkiewicz, E., "Removal of surface-wave induced radiation nulls for patch antennas integrated with vehicle windscreens," *IEEE Transactions on Antennas and Propagation*, vol. 45, no. 1, pp. 176–176, 1997.

[89] Seki, T., Honma, N., Nishikawa, K., and Tsunekawa, K., "Millimeter-wave high-efficiency multilayer parasitic microstrip antenna array on teflon substrate," *IEEE Transactions on Microwave Theory and Techniques*, vol. 53, no. 6, pp. 2101–2106, 2005.

[90] Shin, S. and Snyder, R. V., "At least n+1 finite transmission zeros using frequency-variant negative source-load coupling," *IEEE Microwave and Wireless Components Letters*, vol. 13, no. 3, pp. 117–119, 2003.

[91] Snyder, R. V., "New application of evanescent mode wave-guide to filter design," *IEEE Transactions on Microwave Theory and Techniques*, vol. 5, no. 12, pp. 1013–1021, 1977.

[92] Suga, R., Nakano, H., Hirachi, Y., Hirokawa, J., and Ando, M., "Cost-effective 60-ghz antenna package with end-fire radiation for wireless file-transfer system," *IEEE Transactions on Microwave Theory and Techniques*, vol. 58, no. 12, pp. 3989–3995, 2010.

[93] Sun, M., Zhang, Y. P., Liu, D., Chua, K. M., and Wai, L. L., "A ball grid array package with a microstrip grid array antenna for a single-chip 60-ghz receiver," *IEEE Transactions on Antennas and Propagation*, vol. 59, no. 6, pp. 2134–2140, 2011.

[94] Sun, M., Zhang, Y.-Q., Guo, Y.-X., Karim, M. F., Chuen, O. L., and Leong, M. S., "Integration of circular polarized array and lna in ltcc as a 60-ghz active receiving antenna," *IEEE Transactions on Antennas and Propagation*, vol. 59, no. 8, pp. 3083–3089, 2011.

[95] Sun, Z. and Fay, P., "High-gain, high-efficiency integrated cavity-backed dipole antenna at ka-band," *IEEE Antennas and Wireless Propagation Letters*, vol. 5, no. 1, pp. 459–462, 2006.

[96] Thiele, G. A., Ekelman, E. P., and Henderson, L. W., "On the accuracy of the transmission line model of the folded dipole," *IEEE Transactions on Antennas and Propagation*, vol. 28, no. 5, pp. 700–703, 1980.

[97] Thompson, D., Tantot, O., Jallageas, H., Ponchak, G. E., Tentzeris, M., and Papapolymerou, J., "Characterization of liquid crystal polymer (lcp) material and transmission lines on lcp substrates from 30-110 ghz," *IEEE Transactions on Microwave Theory and Techniques*, vol. 52, no. 4, pp. 1343–1352, 2004.

[98] Vainikainen, P., Ollikainen, J., Kivekäs, O., and Kelander, I., "Resonator-based analysis of the combination of mobile handset antenna and chassis," *IEEE Transactions on Antennas and Propagation*, vol. 50, no. 10, pp. 1433–1444, 2002.

[99] Vandensande, J., Pues, H., and de Capelle, A. V., "Calculation of the bandwidth of microstrip resonator antennas," in *Proceedings of the 9th European Microwave Conference*, pp. 116–119, 1979.

[100] Waterhouse, R., *Microstrip Patch Antennas: A Designer's Guide*, p. 168. Norwell, MA: Artech House, 2003.

[101] Willmot, R., Dowon, K., and Peroulis, D., "A yagiuda array of high-efficiency wire-bond antennas for on-chip radio applications," *IEEE Transactions on Microwave Theory and Techniques*, vol. 57, no. 12, pp. 3315–3321, 2009.

[102] Winter, D. W. and Mansour, R. R., "Tunable dielectric resonator bandpass filter with embedded mems tuning elements," *IEEE Transactions on Microwave Theory and Techniques*, vol. 55, no. 1, pp. 154–159, 2007.

[103] Wong, J. and King, H., "A cavity-backed dipole antenna with wide-bandwidth characteristics," *IEEE Transactions on Antennas and Propagation*, vol. 21, no. 5, pp. 725–727, 1973.

[104] Xia, P., Qin, X., Niu, H., Singh, H., Shao, H., Oh, J., Kweon, C. Y., Kim, S. S., Yong, S. K., and Ngo, C., "Short range gigabit wireless communications systems: Potentials, challenges and techniques," in *Proceedings of the 2007 IEEE International Conference on Ultra-Wideband*, pp. 123–128, 2007.

[105] Xiaoguang, L., Katehi, L. P. B., Chappell, W. J., and Peroulis, D., "A 3.4 6.2 ghz continuously tunable electrostatic mems resonator with quality factor of 460530," in *Proceedings of the 2009 IEEE MTT-S International Microwave Symposium*, (Boston, MA), pp. 1149–1152, 2009.

[106] Zhang, C., Yang, S., El-Ghazaly, S., Fathy, A. E., and Nair, V. K., "A low-profile branched monopole laptop reconfigurable multiband antenna for wireless applications," *IEEE Antennas and Wireless Propagation Letters*, vol. 8, pp. 216–219, 2009.

[107] Zhang, Y. P. and Liu, D., "Antenna-on-chip and antenna-in-package solutions to highly integrated millimeter-wave devices for wireless communications," *IEEE Transactions on Antennas and Propagation*, vol. 57, no. 10, pp. 2830–2841, 2009.

[108] Zhang, Y. P., Sun, M., Chua, K. M., Wai, L. L., and Liu, D., "Antenna-in-package design for wirebond interconnection to highly integrated 60-ghz radios," *IEEE Transactions on Antennas and Propagation*, vol. 57, no. 10, pp. 2842–2852, 2009.

[109] Zhang, Y. P., Sun, M., and Guo, L. H., "On-chip antennas for 60-ghz radios in silicon technology," *IEEE Transactions on Electron Devices*, vol. 52, no. 7, pp. 1664–1668, 2005.

[110] Zwick, T., Liu, D., , and Gaucher, B. P., "Broadband planar superstrate antenna for integrated millimeterwave transceivers," *IEEE Transactions on Antennas and Propagation*, vol. 54, no. 10, pp. 2790–2796, 2006.